Chao-Hai Du · Pu-Kun Liu

Millimeter-Wave Gyrotron Traveling-Wave Tube Amplifiers

Springer

Millimeter-Wave Gyrotron Traveling-Wave Tube Amplifiers

Chao-Hai Du • Pu-Kun Liu

Millimeter-Wave Gyrotron Traveling-Wave Tube Amplifiers

Springer

Chao-Hai Du
Pu-Kun Liu
School of Electronics Engineering
and Computer Science
Peking University
Beijing, China

ISBN 978-3-642-54727-0 ISBN 978-3-642-54728-7 (eBook)
DOI 10.1007/978-3-642-54728-7
Springer Heidelberg New York Dordrecht London

Library of Congress Control Number: 2014940850

Printed on acid-free paper

Springer is part of Springer Science+Business Media (www.springer.com)

Preface

A gyrotron traveling-wave tube (gyro-TWT) amplifier is capable of generating high-power and broadband coherent electromagnetic radiation on the level of hundreds of kilowatts in the millimeter-wave range. It is one of the most promising candidates of the electromagnetic-wave power amplifier for the next generation of imaging radars and long-range high-data-rate wireless communications. It would play an important role in many fields, such as national security, small objects tracking in the outer space, accurate atmosphere and weather monitoring, and so on. A gyro-TWT amplifies the driving power based on the convective instability principle of the relativistic electron cyclotron maser (ECM). The amplification simultaneously suffers from competing absolute instabilities, which lead to complicated self-excited oscillations. As a result, the instability competition not only stops the system from efficient operation but also hinders practical applications. Investigating the physics of the instability competition and exploring solutions to suppress self-excited oscillations turn into primary factors essentially related to the gyro-TWT development. Hence, it is of important academic value and engineering application to study the beam-wave interaction mechanism and to reveal the instability competition physics in depth, as a way to further enhance the amplifier performance and promote its application in high-power millimeter-wave radars and communication systems.

This book focuses on the beam-wave interaction mechanisms and the competition relations between the convective instability and the absolute instability in gyro-TWT amplifiers. The book starts with a technical review of the gyro-TWT development in past decades in Chap. 1. Chapter 2 presents a comprehensive presentation of the linear theory and nonlinear theory of ECM interaction. The main content of the book is conveyed in Chaps. 3, 4, and 5, including detailed investigation of the lossy dielectric-loaded (DL) waveguide, ultrahigh gain gyro-TWT amplifier, and lossy DL gyro-TWT amplifier. Chapter 6 is arranged as an exploratory section. Three novel concepts related to amplifier interaction circuit are introduced here. Chapter 7 presents some key technologies related to developing a gyrotron amplifier.

The contents of the book originate from recent years theoretical and engineering works on developing gyrotron amplifiers in our group. We try to present them in

a comprehensive way, especially a lot of vivid figures are conceived to illustrate the complicated physics. The millimeter-wave gyrotron amplifier has experienced a tremendous advance in the past decade. We hope this book would be helpful to promote its further development.

Beijing, China

Chao-Hai Du
Pu-Kun Liu

Contents

Chapter 1
Review of Gyrotron Traveling-Wave Tube Amplifiers

Abstract The review starts with a simple introduction to the microwave electronics, and then it addresses the well-known concept of the relativistic electron cyclotron maser (ECM) and the operation principles of the gyrotron devices. The technical review of the gyrotron traveling-wave tube (gyro-TWT) amplifiers focuses on the electron beam-wave interaction schemes and a series of key techniques, including controlling instability competitions by waveguide wall loss, high-power operation based on a higher-order mode, low magnetic field operation on a higher cyclotron harmonic, and broadband operation by employing dispersion shaping. It is revealed that most of the problems in developing a high-power gyro-TWT amplifier are closely related to the instability competitions. Finally, it concludes that overcoming the challenging problem of instability competition in the interaction circuit is the key to promote the development of the high-power gyro-TWT amplifiers.

Keywords Electron cyclotron maser • Gyro-TWT amplifier • Wall loss • Cyclotron harmonic • Instability competition

1.1 Microwave Electronics

The electromagnetic wave greatly influenced the development of science and technology, and it has become an indispensable part of our daily life. The most prominent contribution to the study of electromagnetic wave was made by James Clerk Maxwell in 1860s. He formulated a complete set of equations, nowadays called Maxwell Equations, to unify electricity, magnetism, and optics into a single frame, namely, electromagnetic field [1]. In the following decades, numerous scientists devoted to develop electromagnetic wave theory and technology. The vacuum electronic device (VED), a kind of important electromagnetic wave radiation source, is a typical achievement in this field [1]. It influences the development of radar,

C.-H. Du and P.-K. Liu, *Millimeter-Wave Gyrotron Traveling-Wave Tube Amplifiers*,
DOI 10.1007/978-3-642-54728-7_1,

communication, energy, and medical field. The microwave tube is a kind of VED in microwave band. Most of the early microwave tubes are invented before or during World War II. A microwave tube was employed as the microwave source of a radar transmitter and was called the heart of the radar. Microwave tubes made an outstanding contribution to the victory of the world anti-fascist war. After the World War II, the microwave tube experienced rapid development due to expanding civilian and military requirements. Many kinds of microwave electronic devices based on various kinds of novel interaction mechanisms were proposed, and thus microwave electronic devices gradually became a huge device family. In the 1960s, competing with solid-state amplifiers, microwave tubes gradually lost their advantages in low-frequency, low-power, and integration application, but they thrived in applications related to high frequency, high power, and high efficiency [2]. At present, high-power microwave tubes play an irreplaceable role in high-power microwave imaging radar, electronic warfare, microwave weapons, satellite communication, navigation, accelerator, controlled nuclear fusion plasma heating, and so on. The power of the devices has almost covered the range between 1 W and 10 GW, and the frequency band has covered the range between 1 GHz and 1 THz [1–4]. With the development of microwave tubes and the discovery of various novel interaction mechanisms, the interaction between the electron beam and electromagnetic wave has been extensively studied. All these research activities and achievements gradually formed a thriving and prosperous research subject, namely, microwave electronics. With the rapid development of science and technology, the microwave electronics has already become an interdisciplinary subject, covering electromagnetic waves, electric engineering, applied physics, plasma physics, methods of mathematical physics, computer science, and other related fields [1–4].

The development of VEDs can be roughly divided into three phases: traditional grid-controlled electron tubes; microwave electronic tubes based on cavities or slow-wave structures; and high-power millimeter-wave, submillimeter-wave, and terahertz devices based on novel interaction mechanisms [1, 2]. In a traditional grid-controlled electron tube, the electron beam emitted from cathode is modulated by the input signal on the grid electrode, and it gradually evolves into electron bunches during transiting across the free space between the grids. Finally, the modulated electron beam induces currents in the output circuit and excites electromagnetic wave radiation. In order to achieve positive energy transferred from the electron beam to the wave, an electron bunch must leave the drifting space before the induced field reverts its direction. The limited electron transit time makes the size of the grid-controlled electron tubes become smaller at higher frequency, which imposes manufacture challenges and severely decreases power capacity [1–4].

In order to overcome the limited electron transit time and power restriction, a new kind of VED based on cavities or slow-wave circuits emerged, and the VED evolved into the second stage. A slow-wave VED uses a slow-wave circuit to reduce the electromagnetic wave phase velocity lower than the speed of the free space light, so that the electron beam in the tube is able to catch up with the phase of the slow wave, in other words, to be synchronizing with the slow wave. Thus, the electron beam can

transfer its axial energy to the electromagnetic wave and induce microwave radiation through lasting synchronizing beam-wave interaction [5]. For the microwave tubes based on cavity structures, high-frequency field is confined by cavities to interact with the electron beam and extract the beam axial energy [6]. The operating frequency of the VEDs based on slow-wave circuit or cavities can reach microwave band or even step into the millimeter-wave band. However, the development of modern radio electronics and related subjects continuously calls for microwave tubes of higher frequency and higher power. Hence, the classical VEDs once again encountered severe limitation from both size and power capacity in millimeter-wave range. In 1950s, scientists turned their interests to a series of interaction mechanisms based on relative electronics. Many new radiation mechanisms capable of radiating high power in millimeter-wave band were discovered, such as, magnetic controlled bremsstrahlung radiation, transition radiation, and wiggler field-induced radiation [2]. These discoveries greatly promoted VEDs development in millimeter and even towards THz wave band. They also made the microwave electronics become abundant and better thriving.

In recent years, with the development of radar, communication, and other related subjects, scientific research in the wave spectrum from millimeter to THz (30 GHz–3 THz) has become one of the most active topics [7]. However, on one hand, due to the comparable relation between the wavelength and VED dimension, both the size and output power of the conventional VEDs decrease sharply with the increasing frequency in millimeter-wave band. As a result, the conventional VEDs are not preferred for high-power millimeter-wave applications. On the other hand, a laser based on the energy level transition is capable of radiates intense electromagnetic wave in form of photons. But it is difficult to find out an appropriate operation material in the far-infrared band. Therefore, it is challenging to efficiently generate millimeter waves or THz waves, no matter using whichever the conventional VEDs common in low-frequency band or the quantum electronic devices in high-frequency band. This is a problem recognized as THz Gap [7].

The electron cyclotron maser (ECM) is based on the relativistic radiation mechanism. It provides a solution for "THz Gap" [7]. The ECM takes advantage of the interaction between an electron cyclotron beam and electromagnetic wave. It is inherently with the advantages of both emitting multiple photons from a single electron and long-range lasting beam-wave interaction. The axial energy of electrons provides condition for broadband Doppler-shifted synchronization, and the electron beam transfers their azimuthal kinetic energy into electromagnetic radiation through azimuthal interaction due to electron cyclotron resonance [7–9]. Studying on the ECM radiation mechanism directly leads to the inventions of gyrotron oscillator, gyrotron amplifier, cyclotron auto-resonance maser (CARM), and a series of high-power millimeter-wave-THz electronic devices, which open up a new microwave electronics branch, namely, the relativistic electronics [8]. The research in this field promotes the development of high-power millimeter-wave radar, millimeter-wave weapon, controlled nuclear fusion plasma heating, material processing, and so on. Now, the microwave electronics becomes an attractive research field [1–9].

1.2 Electrons Cyclotron Maser and Gyrotron

In an electron cyclotron maser (ECM) device, the electron beam transfers its azimuthal kinetic energy to electromagnetic radiation through azimuthal interaction [7–9]. This kind of device is capable of producing continuous wave radiation as high as to megawatt level in millimeter-wave band. Based on different beam-wave interaction structures, various kinds of gyrotron devices were developed. This section is devoted to introduce the basic principle of ECM interaction, the categories and characteristics of gyrotron devices, and their general applications.

1.2.1 The Principle of ECM

In the late 1950s, similar fast-wave radiation mechanisms were independently discovered by Australian astronomer R. Q. Twiss [10], the Soviet scientist A. V. Gaponov [11], and American scientist J. Schneider [12]. Later, J. L. Hirshfield and J. M. Wachtel proposed the concept of electron cyclotron maser (ECM) in 1964, and they verified this radiation mechanism in experiments [13]. These discoveries sparked an upsurge of research activities on fast-wave electron devices. It leads to the invention and the development of the gyrotrons, which are capable of efficiently radiating electromagnetic wave in millimeter-wave to THz wave band [7].

For a conventional VED, it is difficult to generate high power in millimeter-wave band due to limitations from small device dimension, which obeys a linear relation between the device size and the wavelength of the operating frequency. However, the interaction system based on cyclotron electron beam has unique advantages of high-order mode interaction and power capacity several orders higher than that of a conventional VED. In an interaction system based on a cyclotron electron beam, the phase synchronization condition between electron beams and electromagnetic wave is [7]:

$$\omega_{\text{eff}} \approx \omega - k_z v_z \approx s\Omega_{\text{e}}/\gamma \tag{1.1a}$$

$$\omega^2 = k_\perp^2 c^2 + k_z^2 c^2 \tag{1.1b}$$

where ω is the angular frequency of the wave; $k_\perp$ and k_z are, respectively, the transverse wave number and axial wave number; v_z is the axial traveling velocity of the electron beam; γ is the relativistic factor; s is the harmonic number; Ω_{e}/γ is the electron cyclotron frequency; and ω_{eff} is defined as the effective wave frequency seen by an electron under cyclotron motion. There are two important conclusions to be obtained from the phase synchronization Eq. (1.1a) [7]. Firstly, fast-wave interaction is possible. When the beam wave meets the synchronizing condition, $\omega/k_z = [v_z + s\Omega_{\text{e}}/(\gamma k_z)] > c$, it is fast-wave interaction. Most kinds of waveguides are capable of conveying a fast wave. Comparing with a slow-wave circuit, a

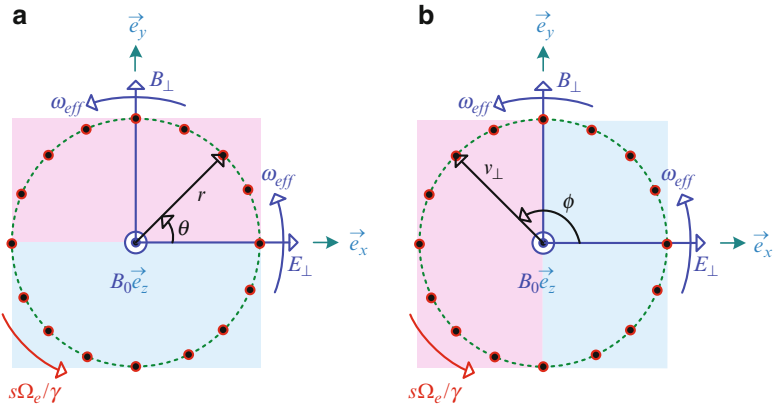

Fig. 1.1 The transverse view of the relativistic ECM of (**a**) real space and (**b**) velocity space

simple smooth waveguide is a superior candidate of fast-wave system due to simple structure and high-power capacity. Secondly, higher-order mode interaction is possible. The inherent electron cycling frequency $s\Omega_e/\gamma$ makes it possible to synchronize to a higher-order waveguide mode under low Doppler-shift condition $k_z v_z \ll \omega$. The electron cyclotron maser system is similar to a laser system where the electron beam with an inherent frequency $s\Omega_e/\gamma$, functioning as the active material, and the higher-order mode structure can be applied to select the wave frequency and increase the power capacity. The electron cyclotron interaction is based on a simple, fast-wave, and high-order mode interaction system, which makes it possible to produce high-power electromagnetic radiation from millimeter-wave to THz wave band.

The ECM based on relativistic effect of the cyclotron electron is a fast electromagnetic wave radiation mechanism [7]. Figure 1.1a, b gives the relative relations between cyclotron electrons and the electromagnetic field in real space and velocity space, respectively. When the electron beams moving along spiral trajectory in the static magnetic field and a fast electromagnetic wave meets the phase synchronization condition Eq. (1.1), the electrons in the pink half circle are under accelerating phase, and in the light-blue half circle under deceleration phase. The electrons in accelerating phase move faster under the continuous accelerating force from the transverse electric field. The kinetic energy increases and the relativistic factor γ becomes larger, as a result the effective cyclotron frequency $s\Omega_e/\gamma$ becomes lower. On the other hand, electrons in the decelerating phase move slower, the kinetic energy decreases, the relativistic factor γ becomes smaller, and effective cyclotron frequency $s\Omega_e/\gamma$ becomes higher. Thus, the electron beam bunches in the phase space. If the cyclotron frequency of electron beam is slightly lower than the effective angular frequency of the fast wave, the bunching center enters the energy decelerating phase (the light-blue half circle), as result, electromagnetic wave radiation will be excited. On the contrary, if the cyclotron frequency is slightly

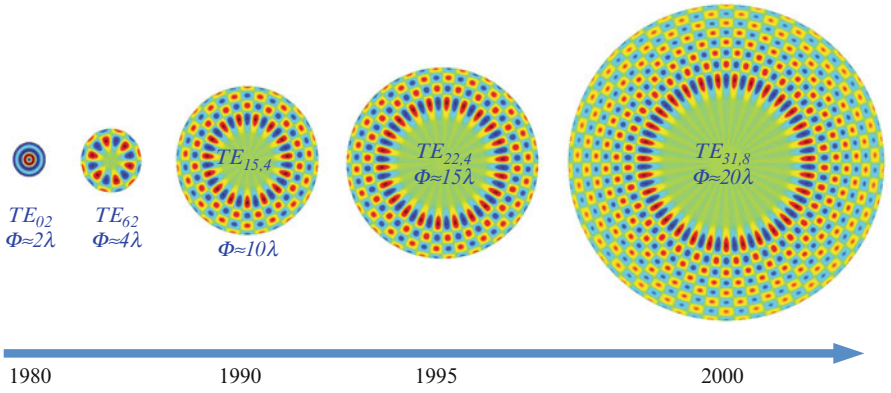

Fig. 1.2 The transverse distributions of the operation modes in gyrotrons

higher than the wave frequency, the electron bunch enters the accelerating phase (the pink half circle), electromagnetic wave will loss energy, and electron beam will be azimuthally accelerated. The relation is summarized as,

$$s\Omega_e/\gamma \leq \omega_{\text{eff}} \quad \text{(exciting radiation)} \tag{1.2a}$$

$$s\Omega_e/\gamma \geq \omega_{\text{eff}} \quad \text{(accelerating electron beam)} \tag{1.2b}$$

1.2.2 The Characteristics of a Gyrotron

The gyrotron is a general name of the gyrotron devices based on the principle of relativistic electron cyclotron maser (ECM) which employs a fast-wave interaction structure. The inherent cyclotron frequency of the electrons makes it feasible to operate on a higher-order wave mode. In other words, a high-order mode circuit can be applied. Figure 1.2 shows the conceptual evolution of the high-order mode employed in gyrotron system during the past decades. For example, the 170 GHz high-power gyrotrons for heating fusion plasma selects the operation modes of the cylindrical waveguide $TE_{31,8}$ mode [14] or coaxial waveguide mode $TE_{-52,31}$ mode [15]. Such kinds of gyrotrons are being developed toward continuous wave for one-to-several megawatt [16]. Both fast-wave interaction and high-order mode bring a gyrotron power capability in millimeter to THz band much higher than a conventional rectilinear beam VED. This is the prominent advantages of gyrotron electron devices [7, 16].

A gyrotron can operate on a higher cyclotron harmonic ($s \geq 2$) [7, 16]. The magnetic field strength of a higher harmonic gyrotron can be reduced to only $1/s$ times strength of that in a fundamental scheme [17–19]. Lower magnetic field

strength means lower cost and higher feasibility of application. Operation on a low-strength magnetic field is especially attractive for a gyrotron operating in millimeter or THz wave frequency band. For example, a fundamental harmonic 94 GHz gyrotron requires a magnetic field strength over 3.6 T, and it only can be realized by a superconducting magnet. However, on the same frequency, the third harmonic scheme requires magnetic field strength only about 1.2 T, which can be realized by a permanent magnet [20]. Such a permanent gyrotron further leads to inventing an active denial weapon for anti-terror battlefield [20]. Similarly, for a 1 THz gyrotron, the fundamental harmonic scheme only can be realized based on the pulse magnet with field strength up to 38.5 T [21], while the third harmonic 1 THz gyrotron requires magnetic field strength less than 14 T [22].

Although a gyrotron is based on the relativistic ECM, it does not decisively require high beam energy. A low relativistic electron beam, beam voltage normally less than 100 kV, can enable efficient beam-wave interaction in a gyrotron. Such a kind of low relativistic gyrotron features relatively compact size and easy application. Recently developed THz gyrotrons for Dynamic Nuclear Polarization (DNP)-NMR applications operated on voltage lower than 20 kV [23], even feasible on several kV [24]. There are also relativistic gyrotrons operating on high energy electron beam, voltage up to hundreds of kV or generated by an accelerator [19, 25–27]. A relativistic gyrotron can produce peak power of dozens of MW in millimeter-wave band.

Some of the gyrotron devices are capable of generating broadband coherent radiation [7, 16]. Other than the gyro-TWTs and gyroklystrons with broadband amplification for radar application, a gyrotron backward-wave oscillator (gyro-BWO) using backward-wave interaction is potentially capable of broad tunable bandwidth [28–30]. A step-tunable gyrotron using normal open cavity also can realize broad discrete bandwidth by tuning magnetic field strength to realize operation on a series of different modes [7, 16, 31, 32].

During the past several decades, the gyrotron with the ability of producing high-power radiation in millimeter wave to THz range makes it take a unique position in military and civilian applications. The development of gyrotron promotes the development and reformation of radar, accelerator, thermonuclear fusion plasma heating, materials processing, active denial weapon, and other related fields.

1.2.3 The Category of Gyrotron Tubes

The gyro-devices based on the relativity ECM principle are generally called gyrotron. Actually, the gyrotron includes a large family of devices, including gyrotron oscillator (gyrotron), gyrotron backward-wave oscillator (gyro-BWO), gyroklystron amplifier (gyroklystron), and gyrotron traveling-wave tube amplifier (gyro-TWT) [7].

Figure 1.3 shows the schematics of the four basic types of gyrotron devices. In the gyrotron family, both the gyrotron oscillator and the gyroklystron amplifier

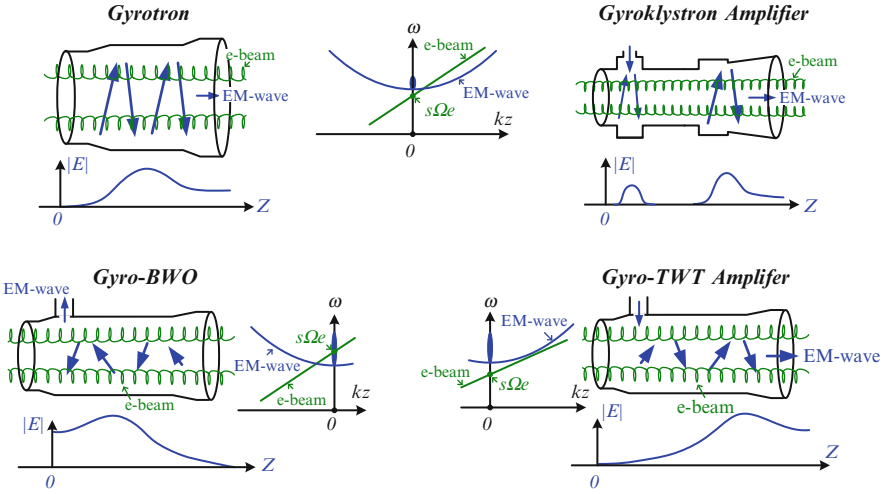

Fig. 1.3 Four types of gyrotron schemes

are cavity devices. They can excite electromagnetic radiation through the local cavity interaction. The radiation in a gyrotron oscillator originates from self-start oscillation, while radiation in a gyroklystron is induced by a low driving power. A gyro-BWO is based on the internal feedback mechanism between the forward electron beam and a backward wave, so it generates self-excite oscillation without external feedback circuit. A gyro-TWT operates on the convective instability, where electromagnetic wave is amplified along with the helical traveling electron beam, and the amplitude of the wave remains unchanged at the fixed position under stable operation. Different beam-wave synchronizations generate gyrotron devices of distinct characteristics, performance, and applications [7].

A gyrotron oscillator, traditionally called gyromonotron or simply gyrotron, employs an open cavity as interaction circuit. The oscillation frequency is quite close to the cutoff frequency, where the wave impedance is relatively higher and brings strong beam-wave coupling and interaction [7–9]. Due to simple interaction structure, high efficiency, and excellent stability in frequency spectrum, the gyrotron is the most matured one in gyrotron family [31–40]. Since Soviet scientists developed the first 6 W continuous wave gyrotron in 1964, gyrotron oscillators have been able to produce MW level continuous wave power in the 140–170 GHz frequency range, their highest working frequency have been extended to 1.3 THz [16]. The 170 GHz megawatt (MW) level continuous wave gyrotron is the candidate source for plasma heating in the International Thermonuclear Experimental Reactor (ITER) program [14, 16]. Scientists in Germany, Russia, the USA, Japan, and other countries are developing continuous wave MW gyrotron for ITER. The gyrotron also plays an important role in the anti-terrorist activities. A special system based on gyrotron oscillator called nonlethal active denial weapon

is developed. It explores the W-band millimeter-wave atmospheric transmission window, more exactly the frequency of 94 GHz. The 94 GHz millimeter wave can penetrate the surface of organism skin and reaches the nerve endings. In the active denial weapon application, when the terrorists are irradiated by a high-power 94 GHz millimeter-wave beam, they will suffer from so strong pain even to loss their resistance ability. To develop superconductor-free harmonic gyrotron for active denial weapon, application becomes attractive [20]. At present, a gyrotron is able to produce kW level power in THz band and can be used in nondestructive detection, THz communication, Dynamic Nuclear Polarization (DNP)-NMR, and many other unknown fields, waiting for further exploration [15, 20–24].

A gyroklystron is a narrow band amplifier, but there are some similarities between a gyroklystron amplifier and a gyrotron [7]. Both are based on cavity interaction and work close to the cutoff frequency, in other words, ECM interaction with low Doppler shift [7, 16, 41–53]. Other than the self-excited oscillation in a gyrotron, a gyroklystron requires a driving power. The electron beam in a gyroklystron is modulated by the driving signal in the input cavity and enhancing bunches in phase space during inertial traversing through the drift region between cavities. The modulated electron beam excites amplified high-power radiation in the output cavity [7, 16]. Based on the cavity mode operation, a gyroklystron features high-power but relatively narrow bandwidth, usually less than 1 %. In 2002, the Naval Research Laboratory (NRL) in the USA reported a W-band fundamental TE_{01} gyroklystron with 33 % efficiency, 420 MHz (0.45 %) bandwidth, 32 dB saturation gain, and average power of 10 kW [49]. Later, this gyroklystron was advanced to achieve 700 MHz bandwidth and equipped in the W-band advanced radar for low observable control (WARLOC), which can be used for high-precision imaging of clouds and tracking targets of skimming cross sea surface [49, 51, 52]. Russia developed a Ka-band radar system with a phased array radar antenna, called Ruza [53]. The power of Ruza system was combined by two power amplification chains in parallel, and each employed a TWT to drive a cascade of two Ka-band gyroklystrons. Each power amplification chain produced 500 kW peak output power and synthesized to a 1 MW power in the space. Ruza can simultaneously track 30 artificial satellites and other ballistic target with small scattering cross section. Its detection range is up to 420 km for the target with cross section larger than 0.01 m^2 [53].

A gyro-BWO is a tunable oscillator. It is essentially different from a gyrotron oscillator that the beam-wave synchronization point is in the backward-wave region [7]. When the beam-wave coupling strength exceeding a certain degree, the spiral forward electrons are modulated by the backward wave in the upstream end and continuously excite backward-wave radiation when moving toward the downstream end. At the same time, the backward wave modulates the electron beam during traveling upstream, thus when such internal beam-wave feedback is strong enough, a self-excited oscillation will be excited [7, 28–30, 54–74]. A gyro-BWO is a broadband tunable oscillator due to backward-wave interaction principle, so it may play an important role in applications, including the electronic countermeasure system or a future frequency tunable THz system.

A gyrotron traveling-wave tube (gyro-TWT) is based on the interaction between a cyclotron electron beam and a forward wave. It works on the convective instability in forward-wave region, which means it is capable of broadband coherent amplification [7]. Hence a gyro-TWT is the most proposed candidate for a high-resolution remote-imaging radar and is attractive for military application. However, the severe parasitic oscillations originating from instability competitions in the interaction structure limit its performance. The gyro-TWT experienced rises and falls, and recently it is right during the transition stage of transferring from experiment lab to applications.

1.3 Gyrotron Traveling-Wave-Tube Amplifiers

A gyro-TWT is based on the convective instability of the relativistic ECM mechanism. It can generate coherent radiation of several hundreds of kilowatts in millimeter-wave band, which makes it the most suitable candidate for transmitter source of the next-generation high-resolution imaging radar and high-data-rate remote communication system. Hence, it is of great significance in national security stratagem. After more than half a century development, the gyro-TWT is now in the transition stage from laboratory experiments to engineering applications, and there are also many problems need to be solved.

1.3.1 The Development of Gyro-TWTs

The development process of the gyro-TWT is roughly divided into three stages [75]. Between 1970s and 1980s, it was the initial exploring stage. Later, the gyro-TWT entered the stage of rapid development in 1990s, and it enters the stage of practical application from 2000 and then on. The Ref. [16] reviewed the major experiments of the world. The ECM interaction not only requires efficient and stable extraction of energy from electron beam but also effectively controls and transmits the high-power electromagnetic wave. Therefore, interaction circuit is the key component. To some extent, the development of the gyro-TWTs is the evolutionary process of the interaction circuits [7].

In early 1980s, the NRL used metal circular waveguide and TE_{01} mode in gyro-TWT experiments [76, 77]. Around 1990s, NRL successfully explored the broadband operation of the gyro-TWTs by using transverse dimension-tapered rectangular waveguide [78]. However its power, efficiency, and gain were limited by severe instability oscillation.

In 1990s, Prof. K. R. Chu from National Tsing Hua University carried out experiments on fundamental harmonic circular waveguide TE_{11} mode gyro-TWTs [79, 80]. In their experiments, the linear stage of the interaction circuit is loaded with a thin layer of lossy Aquadag, functioning as the distributed wall loss to

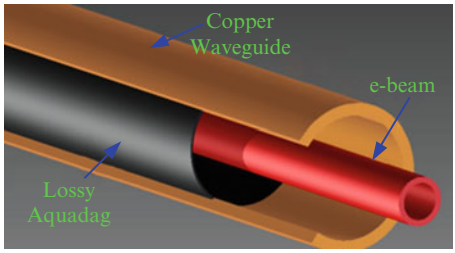

Fig. 1.4 Decomposition diagram of the Loss Aquadag coated interaction waveguide [79, 80]

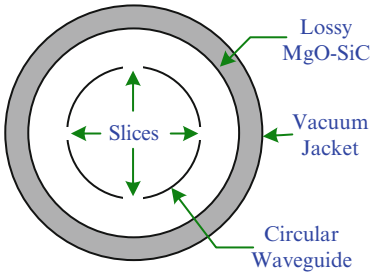

Fig. 1.5 Sectional view of the sliced interaction waveguide [81]

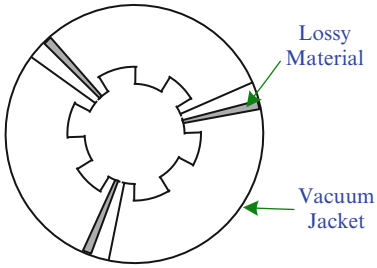

Fig. 1.6 Sectional view of the slotted waveguide [82]

boost the thresholds of self-exciting oscillation. The amplification growth rate of the operation mode is reduced, but on an acceptable level. The lossy interaction structure is demonstrated in Fig. 1.4. This scheme is of great reference for a series of following millimeter-wave gyro-TWT experiments [75].

This lossy interaction scheme can be realized via different ways. The University of California (UC) carried out gyro-TWT experiments operating at the second harmonic [81] and the third harmonics [82]. The interaction circuit in the experiments is shown in Fig. 1.5 (sliced waveguide) and Fig. 1.6 (slotted waveguide), respectively. The loss mechanisms of the interaction circuits are similar. The axial slots can truncate the induced currents of the competing modes on the waveguide wall, as a way to suppress the mode competitions.

After 2000, the NRL carried out a series of gyro-TWT experiments based on interaction circuits shown in Figs. 1.7 and 1.8. Figure 1.7 demonstrates a loss circuit iteratively loaded with dielectric rings and metal rings along the axis [83, 84]. Using the complex and ingenious design, the attenuation of the operation mode is small, while the competing modes are strongly attenuated by the lossy structure.

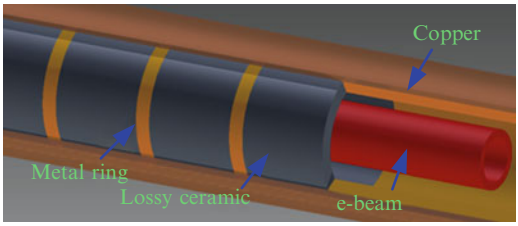

Fig. 1.7 The TE_{01} mode periodic lossy ceramic-loaded interaction circuit [83, 84]

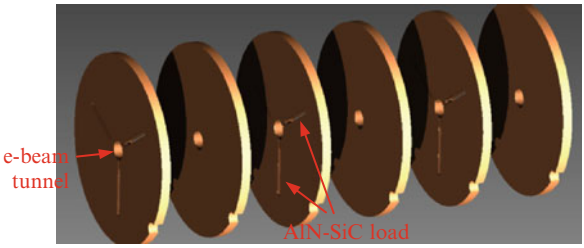

Fig. 1.8 The TE_{11} mode sliced interaction circuit [85, 86]

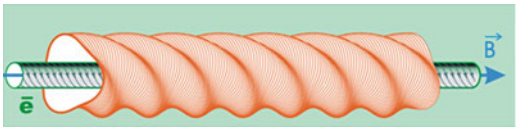

Fig. 1.9 Corrugated waveguide [90]

The structure of periodically overlapping the metal rings prevents the system from dielectric charging. The waveguide in Fig. 1.8 is also another kind of slotted waveguide. It is with the ability of selecting operating mode and generating high average power [85, 86].

In addition, harmonic interaction system based on a corrugated waveguide is another candidate of the broadband gyro-TWT interaction circuit, as shown in Fig. 1.9 [87]. The operation mode in the corrugated waveguide originates from two counterrotating modes coupling with each other under a resonance condition. In such a waveguide, the dispersion curve of the operation mode is approximately a straight line close to the region $k_z = 0$. Therefore, the coupling modes can interact with the cyclotron beam in a wide frequency band. When the corrugated circuit is compared with a conventional cylindrical waveguide, the corrugated circuit scheme is more insensitive to electron beam velocity spread. The Institute of Applied Physics (IAP) and the Strathclyde University of UK successfully carried out a series of experiments based on such corrugated circuits [28, 65, 88–90].

The confocal waveguide shown in Fig. 1.10 can also be used for a gyro-TWT [91, 92]. The open side wall reduces the mode density, which introduces scattering loss and suppresses competing modes and parasitic oscillation. In 2003, MIT successfully carried out the quasi-optical gyro-TWT experiment based on confocal waveguides. The advantages include reduced mode density, scattering loss leading to higher starting current for a parasitic oscillation, and using optical sever to achieve higher stability [92]. These factors work together to suppress the competitive modes and enhance the stability of amplification operation.

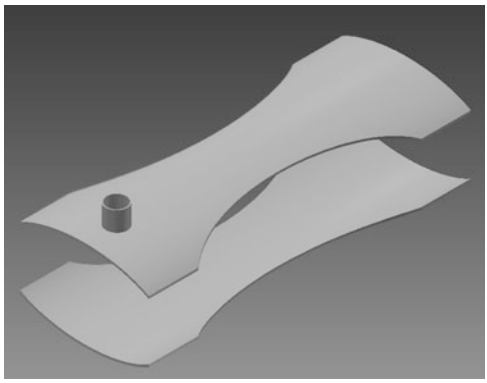

Fig. 1.10 Confocal waveguide interaction circuit [91, 92]

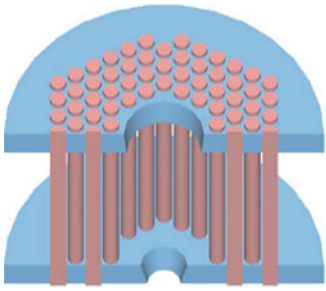

Fig. 1.11 Photonic-band-gap waveguide [38]

The photonic-band gap (PBG) is one of the active scientific research fields in recent years. Due to the band-gap characteristics, the electromagnetic waves in the band-gap range can be restricted in the photonic-band-gap defects and generate a high-order mode, while the electromagnetic waves out of the band-gap range can propagate through the PBG structure and will be scattered out. This provides the PBG waveguide the ability of over-moded operation and mode selection. In 2001, MIT launched the first cyclotron oscillator experiment based on photonic-band-gap waveguide [38]. The interaction structure is shown in Fig. 1.11. It employed the quasi-TE_{041} mode and demonstrated no competition oscillation in 30 % magnetic tuning range near the operating point. The experiment is important for future development of high-order modes and high harmonic gyrotron oscillators and amplifier.

In short, the gyro-TWT experiments were carried out based on various kinds of interaction structures during evolution process. The early interaction structures adopted smooth circular waveguides. Since there was no mechanism to suppress self-excited oscillation, these devices operated at low currents and were difficult to fully realize the advantage of high-frequency, high-power, and wide-band operation. And then, transverse dimension-tapered waveguide and gradually changed magnetic field were applied to improve the bandwidth. However, both output power and efficiency were limited due to the problem of instability oscillation. K. R. Chu and his group investigated the influence of distributed loss to system stability and

greatly improved the stability of the gyro-TWT, which promoted the development of the gyro-TWT. At the same time, the spiral corrugated waveguide was employed in the gyro-TWT, which demonstrated broadband operation, and stable to electron velocity spread. New kinds of interaction structures continually enlarged the vision of the scientists and simultaneously brought new possibilities.

1.3.2 Comments on Technologies

Various kinds of interaction circuits were applied during the past gyro-TWTs experiments [7, 75]. Each of these experiments explored solutions to the problems of certain aspect. The key technology developed during these experiments promotes the evolution and development of the amplifier. In order to better understand these technologies, we will introduce the problems in four aspects, including technology of wall loss, high-order mode interaction, harmonic interaction, and bandwidth extending.

1.3.2.1 Waveguide Wall Loss

Until now, the waveguide wall loss is the most successful solution to suppress the instability competition problem in gyro-TWTs [7, 75]. The waveguide wall loss is realized by loading a certain kind of wave dissipating material on the waveguide wall and imposing a distributed loss effect to wave mode during its propagation, while disturbance to the operating mode distribution is negligible. Through introducing propagation attenuation, it makes the convective instability-induced amplification operate on a reduced strength, and it imposes relatively stronger disturbance and attenuation to the competing modes, as a way to increase start-oscillation thresholds of the competing instabilities [7, 75, 79, 80, 93]. The technology, to some extent, is proved to be generally valid to solve the instability competitions in a series of gyro-TWTs experiments [7, 75].

In early 1980s, a series of experiments in American NRL revealed that the interaction circuits loaded with distributed wall loss were capable of improving the gain and stability of a gyro-TWT [94–97]. The first gyro-TWT based on the distributed loss interaction circuit operated in Ka band, using TE_{01} mode interaction, beam current 3 A, and pitch factor 1.5, and it achieved a linear gain of 50 dB [76].

In 1990s, Prof. K. R. Chu and his group carried out a series of Ka-band gyro-TWT experiments under strong theoretical backup [7, 75, 79, 80, 93]. In 1998, a Ka-band fundamental harmonic TE_{11} mode gyro-TWT experiment achieved ultrahigh gain up to 70 dB. It achieved saturation peak power 93 kW, the gain 70 dB, efficiency 26.5 %, and 3 dB bandwidth 3 GHz. The experimental results demonstrated that the distributed loss could effectively suppress various parasitic oscillations, and the

threshold current was increased from 0.9 to 3.5 A. These experiments demonstrated a generally valid solution to instability competition in a gyro-TWT system and also played a role of milestone during the history of gyro-TWTs.

UC Los Angeles designed a Ku-band gyro-TWT in 1996 [81]. The interaction circuit shown in Fig. 1.5 was axial sliced waveguide based on the idea of distributed loss. It operated at second harmonic of the TE_{21} mode with electron beam voltage 80 kV, current 20 A, and pitch factor 1.1. The experiment generated saturated output power of 207 kW, efficiency 12.9 %, gain 16 dB, and bandwidth 2.1 %. The American NRL also carried out experiments based on the circuit with radial deep-sliced gaps along the axis, as shown in Fig. 1.8 [85, 86]. It adopted the TE_{11} fundamental mode with beam voltage 70 kV, current 6 A, and pitch factor 0.8. It generated peak output power 78 kW with the gain of 60 dB. The most outstanding feature was the wide saturated output bandwidth up to 17 %. The American NRL also carried out another Ka-band experiment based on periodic lossy ceramic loading technology, as shown Fig. 1.7 [83, 84]. It adopted the circular TE_{01} fundamental mode. The beam voltage and current were 70 kV and 10 A, respectively. The saturated peak power was 137 kW. However, the bandwidth was seriously restricted by the velocity spread of the electron beam, simulation results showed that the electron beam axial velocity spread was $\Delta v_z/v_z \approx 8 \sim 10$ %, and the measured bandwidth was about 3.3 %. Similar interaction structures were also adopted in recent Ka-band experiments in several institutions in China, including UESTC, IECAS, and BVERI [16]. And experiments achieved peak power about 100–200 kW and bandwidth about 5 %. In 2003, MIT successfully launched a 140 GHz gyro-TWT experiment, which took advantage of quasi-optical confocal waveguide [92]. This device operated at HE_{06} mode. The amplifier obtained peak output power 30 kW, peak efficiency 12 %, and bandwidth 2.3 GHz.

From above technique review, it demonstrates that there are several ways to realize waveguide wall loss in a gyro-TWT, including loading low conductivity material in the linear stage of the circuit [76, 94–97], coating lossy material on the inner wall of the waveguide [93], using lossy material filled sliced waveguide [81, 85, 86], utilizing ceramic-loaded cylindrical waveguide [83, 84], and using quasi-optical confocal waveguide with partial open boundary [92]. From these lossy ways, the advantages of waveguide wall loss scheme are summarized as follows. Firstly, the wall loss imposes stronger attenuation to a mode when the frequency gets closer to the cutoff frequency, where normally self-exciting oscillation happens. Hence, it is inherently with the ability of suppressing absolute-instability-induced oscillation. Secondly, in a lossy interaction system, the reflected wave from the downstream port is strongly attenuated when it inversely travels through the loss circuit toward upstream end, and thus it acts little influence on the initial non-bunched cyclotron beam in the input stage and guarantees stable operation of the driving power. Thirdly, generally speaking, the wall-loss mechanism has the ability of selectively attenuation and suppressing the mode competition. Therefore, waveguide wall lossy mechanism can be widely applied in gyro-TWTs to suppress instability competition.

1.3.2.2 High-Order-Mode Interaction Circuit

The higher-order-mode operation is the prime reason that vacuum electronic devices based on the ECM principle are capable of achieving higher output power than conventional VEDs in millimeter-wave band and wave band beyond. To explore on a high-order mode interaction is one of the major tendencies of the gyro-devices [7]. Employing a high-order mode increases the interaction space, and the power capacity is accordingly boosted. Until now, the world-wide gyro-TWT experiments have employed operation modes including rectangular waveguide TE_{10} mode [78], cylindrical waveguide TE_{11} mode [85, 86], cylindrical waveguide TE_{21} mode [81], cylindrical waveguide TE_{01} mode [83, 84], helical corrugated waveguide TE_{11}/TE_{21} coupled mode [89, 90], π mode in cylindrical waveguide with six azimuthal slots [82], and HE_{06} mode in confocal waveguide [92]. It is summarized that, when compared with a gyrotron oscillator, most of the gyro-TWTs operated on relatively low-order modes and a higher-order mode interaction are also possible when special mode control technology is employed. For example, MIT carried out a gyro-TWT experiment on 140 GHz based on a confocal waveguide with opened side walls, and its mode was HE_{06} [92].

A 170 GHz gyrotron oscillator developed for plasma fusion heating is capable of producing 1 MW level continuous wave power. Usually, it employs a supper higher-order operation mode, such as $TE_{31,8}$ mode [14]. To some extent, this also indicates the potential of the high-order-mode operation for a gyro-TWT. The interaction length of a gyro-TWT is as long as dozens of the wavelength, which is fundamentally different from the interaction of gyrotron oscillators based on open cavities [7, 16]. For a gyro-TWT operating on a higher-order mode, the mode density on the dispersion map is very high, and electron cyclotron modes intersect with many waveguide modes in the backward-wave region or near the cutoff frequency. A traveling-wave circuit for a gyro-TWT is normally much longer than an open cavity of the same frequency band. When the axially accumulated feedback strength is strong enough, a self-excited oscillation based on certain instability will be induced. Each beam-wave cross point on the cold dispersion map is a potential origin of an oscillation. Other than transverse mode (TE_{mn}) competitions in a gyro-TWT, there are also axial mode competitions. Each operating mode (TE_{mn}) in the interaction may exhibit different higher-order axial modes [98, 99]. Abundant self-excited oscillations from certain instabilities are the fundamental reason preventing a gyro-TWT from operating at a high-order mode.

Effectively suppressing the absolute-instability oscillations to achieve zero-drive stability is the precondition of a gyro-TWT under high-order-mode operation [79, 80]. Summarizing the world-wide gyro-TWT experiments, interaction circuit with special transverse structure to reduce the effective mode density and mode selective attenuation mechanism is an effective solution to stabilize a high-order mode gyro-TWT [7]. Other than the lossy circuit, the gyrotron carried out by MIT employed interaction structure based on photonic crystal structure [38], and it provided a valuable mode-filter consideration for the gyro-TWTs. In addition,

the experiments of coaxial cavity gyrotron [16, 29, 100, 101] and coaxial cavity gyroklystrons [26] also proved that the mode selection capability and system stability can be enhanced by using the special coaxial interaction structure.

1.3.2.3 Higher-Order Harmonic Operation

Developing a gyro-TWT of a high-order harmonic is of great significance [7]. Firstly, the magnetic field strength is inversely proportional to the harmonic number; hence harmonic interaction reduces the magnetic field intensity. For military application, making the Ka-band gyrotron amplifier as an example, the second-harmonic scheme requires a magnetic field strength of about 0.6 T and normal coil magnet is available, while the fundamental harmonic scheme requires a magnetic field strength of about 1.2 T and superconducting magnet is the first choice. A gyrotron amplifier based on a normal coil magnet will much improve the reliability and reduce the cost. Secondly, the coupling strength of the operating mode is smaller than the fundamental interaction, which increases the threshold current of the absolute instability. Thus the device may work at higher current and achieve stronger wave radiation power [102]. Thirdly, large-orbit cyclotron beams with electron guiding center $r_c = 0$ are suggested in a higher-order harmonic interaction system. Therefore, only for the modes with azimuthal index equaling to the cyclotron harmonic number, their beam-wave coupling coefficient is nonzero. That is, in a large-orbit interaction system, TE_{mn} mode ($m = s$) can only effectively interact with the s harmonic mode, which, to some extent, suppresses the influence of mode competition.

Harmonic gyro-TWT experiments were carried out at University of California at Los Angeles [19] and Davies [81, 82]. In 1990, the University of California at Los Angeles carried out an experiment on harmonic gyrotron amplifier [19]. The gyro-TWT operated on the eighth harmonic. It used large-orbit electron beam and circular waveguide. The voltage and current were 350 kV and 150 mA respectively. The achieved output power in Ku band was 0.5 kW with efficiency of 1.35 %, and the small signal 10 dB bandwidth was 4.3 % [19]. When the operating parameters slightly diverged from the optimum parameters, the parasitic oscillations from low harmonics rose up which resulted in low efficiency and low gain.

In 1996, the University of California at Davis reported an experiment using second-harmonic interaction [81]. The interaction circuit was an axial sliced circular waveguide, and there were four slices along the axis with 90° interval. With the special structure, the circular TE_{n1} mode (n is odd) can be effectively scattered and the mode competition was also weakened. This interaction structure is shown in Fig. 1.5. The experiment utilized wall loss technology and harmonic interaction structure which successfully demonstrated that harmonic interactions were with higher current thresholds current than fundamental interactions.

In 1998, University of California at Davis launched the third harmonic gyro-TWT experiments operated at X band [82]. The interaction circuit was a slotted

waveguide: there were six slots in the waveguide wall at intervals of 60° along the axis for mode selection purpose, as shown in Fig. 1.6. There were also three slices at intervals of 120° which provided scattered loss. The device used π mode and 66 kV operating voltage. The operating current and velocity ration was 8 A and 1.05, respectively. Experimental results showed that the output power was 6 kW with 5 % efficiency, 11 dB gain, and 3 % bandwidth.

Theoretically speaking, a harmonic gyro-TWT can operate on higher current and may provide higher output power [81]. However, it is not always the experiment outcomes. The magnetic field strength for harmonic operation is several times smaller than the fundamental system. It is inevitable to encounter the mode competitions from lower-order harmonics. The issues from the three aspects should be considered for using harmonic interaction system. The first is to reduce the mode density and to suppress mode competition through appropriate mode control mechanisms. The second is to introduce appropriate lossy mechanism to improve the competing instability threshold current. Hence, the mode competition and stability problem of harmonic interaction system are still important issues to be solved. The third is to adopt high voltage to enhance the beam-wave coupling strength, as a way to improve the interaction efficiency.

1.3.2.4 Broadband Operation

The gyro-TWT demonstrated the advantage of broadband operation during its initial stage of development. From 1980s to 1990s, NRL of American developed gyro-TWTs based on interaction structure with gradually tapered cross section [78, 103]. In such a circuit, the magnetic field is also axially tapered to ensure synchronization between the cyclotron beam and waveguide mode in a wide frequency range, providing broadband amplifying. A Ka-band gyro-TWT experiment using rectangular waveguide TE_{10} mode was reported, and the output power, efficiency, gain, and bandwidth were 6.3 kW, 10 %, 16.7 dB, and 33 %, respectively. But the reflection oscillation from the output circuits hindered further advance of its performance [104]. In a later experiment, a section of under-cutoff drifting waveguide divided the single-tapered circuit into a double-tapered circuit, outward tapered toward both ends. The system stability was enhanced; however, there was still possibility of oscillation [78]. The experiment using double-tapered circuit achieves performance of relative bandwidth 20 %, gain 25 dB, efficiency 16 %, and peak output power about 8 kW. Although the tapered circuit improves the bandwidth, it confines the effective beam-wave interaction for a given frequency in a limited length of circuit, leading to relatively low efficiency and low gain. In the output stage, due to the broadband synchronism, any reflection power in the operation band would be re-amplified by the downstream up-tapered stage and possibly builds up reflection oscillation. Hence, self-excited oscillation hinders further development of such kind device.

In the middle of 1990s, the University of California, Los Angeles, carried out X-band gyro-TWT experiment using dielectric-loaded rectangular waveguide [105].

The loaded dielectric effectively reduced the dispersion characteristics of the guided mode and extended the beam-wave synchronizing bandwidth. The experiment measured output power of 55 kW, efficiency of 11 %, gain of 27 dB, and constant drive bandwidth of 11 %. Improving the mode dispersion characteristics is just one aspect of developing gyro-TWT system [106–109], and suppressing the instability competition should be considered first in order to obtain high-power and broadband operation [7].

A gyrotron amplifier based on a helical corrugated waveguide operates on a coupled mode and is capable of broadband operation [87]. This kind of gyro-TWTs was extensively studied by cooperation groups from Russia Institute of Applied Physics (IAP) and University of Strathclyde, Glasgow, UK. Since 1998, IAP and University of Strathclyde cooperated to study gyro-TWTs based on helical corrugated waveguides [87, 89, 90, 108]. The initial experiment used second-harmonic interaction operated in X band using voltage 200 kV and current 25 A [90]. It generated peak power 1 MW, efficiency 20 %, gain 23 dB, and saturated bandwidth greater than 10 %. An improved version employed voltage 180 kV. It achieved output power 1.1 MW, saturated gain 37 dB, and relative bandwidth 21 %. Another Ka-band experiment was carried out around 2002, it employed a large-orbit electron beam of 20 A and a reduced voltage about 80 kV. It achieved peak power 180 kW, efficiency 27 %, gain about 27 dB, and bandwidth about 10 %. In a recent X-band experiment using a electron beam of voltage 185 kV and current 6 A, it reported an achieve output power 220 kW, saturated gain 24 dB, and bandwidth of 2 GHz [108].

The gyro-TWT based on a helical corrugated waveguide has major advantages from two aspects. Firstly, it operates on a coupled mode close to a region with small propagation constant $k_z \approx 0$, which makes performance insensitive to electron beam velocity spread. Secondly, harmonic operation is inherently with much lower magnetic field strength than the fundamental harmonic scheme. Previous experiments proved the potential of realizing high-power and broad bandwidth by employing helical corrugated circuit. However, little publication was reported on suppressing the instability competition-related problems in such kind of interaction system.

1.3.3 Problems and Prospects

Based on the relativistic ECM principle, a gyro-TWT amplifier employs a cyclotron electron beam to interact with a fast wave, and it is with the advantage of generating high-power and broadband coherent radiation in the millimeter-wave band and beyond, which makes the gyro-TWT one of the most promising candidates for the high-power transmitter of high-resolution imaging radar. After decades of investigation, the key problems related to its development, including instability competition, higher-order mode operation, broadband operation, and high average power operation, have been investigated in depth.

The instability competition is one of the problems essentially hindering the development of the gyro-TWTs [7]. In the interaction system, when a cyclotron harmonic strongly couples with a waveguide mode near the cutoff frequency or in the backward-wave region, an oscillation originating from absolute instability would be excited. When the input and output coupler are not perfectly matched, reflected power from both ends would be re-amplified and possibly excite reflection oscillation. During the experiment of a gyro-TWT, several kinds of parasitic oscillations may be present simultaneously in the interaction system, and suppress the amplification of the driving signal, which limits the system operate on a relatively low power-level state.

The high-order mode operation is the only way to achieve high power in high-frequency band. Employing a high-order mode circuit increases the transverse dimension of the interaction circuit and improves system power capacity, which is also the basic reason that a gyro-TWT generates higher power in millimeter-wave band than a conventional linear beam amplifier. In a conventional metal waveguide interaction circuit, the higher-order mode operation encounters more severe instability competitions due to higher mode density.

High average power operation is a basic requirement for engineering application. A gyro-TWT operating in the millimeter-wave band is with relatively limited circuit dimension, which limits the capability of heating dissipation. In order to suppress the instability competition, the circuit of a gyro-TWT usually is loaded with lossy material. The thermal conductivity of the lossy material and related fabrication technology also compose the bottleneck to the system average power.

A gyro-TWT is also characterized by its broadband operation capability. However, due to instability competition and sensitivity to electron beam velocity spread, engineering realized performance is normally much inferior to the theoretical prediction. Taking suppressing instability competition into consideration, exploring the broadband operation capability is relatively challenging.

A gyro-TWT is a complicated system. Suppressing instability competition is the precondition of the normal amplification. The following prospects would be meaningful for future investigation:

The waveguide wall loss is a general valide solution to suppress self-excited oscillation. Exploring high average power circuit based on waveguide wall loss is very important to the application of high stability, high-power gyro-TWTs.

A gyro-TWT based on helical corrugated waveguide is with much improved stability to beam velocity spread. It is of great development potential for broadband and high-power operation.

The high harmonic operation reduces the magnetic strength and possibly replaces the fragile and bulky superconducting magnet by a normal compact coil magnet. A gyro-TWT based on normal coil magnet undoubtedly enhances the system reliability and shortens the start-up time of the radar system for military application. Therefore, study of high stability harmonic interaction gyro-TWT has theoretical importance and engineering significance.

Coaxial waveguide, confocal waveguide, and photonic-band-gap structure are newly emerged interaction circuits applied in gyrotrons. In addition, researchers

also proposed new interaction system using multi-electron beams [39, 40, 110]. Investigating such higher-order mode interaction system and carrying out the corresponding experiments introduce new possibility for millimeter–terahertz wave gyro-TWTs.

After developing for more than half a century, researchers tried various interaction circuits for gyro-TWTs. The instability competition exhibits to be a deciding factor hindering its way to practical applications. Recent theoretical and experimental investigations demonstrate that the waveguide wall loss scheme based on loading high-thermal-conductive lossy ceramic in the interaction circuit is greatly advanced to matured capability of engineering application [7, 83–86, 111, 112]. The coaxial waveguide and helical corrugated waveguide are increasingly attractive for gyro-TWT applications [28, 113, 114]. Therefore, combining the existed technologies and simultaneously exploring new interaction system would bring a promising future for gyro-TWTs and high-power millimeter-wave radars.

References

1. Gilmour AS (2011) Principles of klystrons, traveling wave tubes, magnetrons, cross-field amplifiers, and gyrotrons. Artech House, Incorporated, ISBN-13918-1-60807-184-5, 685 Canton Street, Norwood, UA02062
2. Liu SG, Li HF, Wang WX (1985) Introduction to microwave electronics. National Defence Industry Press, Beijing (In Chinese)
3. Zhang KQ, Li DJ (2001) Electromagnetic theory for microwave and optoelectronics. Publishing House of Electronics Industry, Beijing (In Chinese)
4. Liao FJ, Sun ZP, Yan TC (2008) Vacuum electronics the heart of information weapons. National Defence Industry Press, Beijing (In Chinese)
5. Pierce JR (1950) Traveling wave tubes. Van Nostrand, New York
6. Varian RH, Varian SH (1939) A high frequency oscillator and amplifier. J Appl Phys 10:321
7. Chu KR (2004) The electron cyclotron maser. Rev Mod Phys 76:489–540
8. Liu LSG (1987) Relativistic electronics. Science Press, Beijing (In Chinese)
9. Nusinovich GS (2004) Introduction to the physics of gyrotrons. The Johns Hopkins University Press, Baltimore/London
10. Twiss RQ (1958) Radiation transfer and the possibility of negative absorption in radio astronomy. Aust J Phys 11:567–579
11. Gaponov AV (1959) Interaction between rectilinear electron beams and electromagnetic waves in transmission lines. Izv VUZov Radiofiz 2:836–837
12. Schneider J (1959) Stimulated emission of radiation by relativistic electrons in a magnetic field. Phys Rev Lett 2:504–505
13. Hirshfield JL, Wachtell JM (1964) Electron cyclotron maser. Phys Rev Lett 12:533–536
14. Sakamoto K, Kasugai A, Takahashi K et al (2007) Achievement of robust high-efficiency 1 MW oscillation in the hard-self-excitation region by a 170GHz continuous-wave gyrotron. Nat Phys 3:411–414
15. Beringer MH, Kern S, Thumm M (2013) Mode selection and coaxial cavity design for a 4-MW 170-GHz gyrotron, including thermal aspects. IEEE Trans Plasma Sci 41(4): 853–861
16. Thumm M (2013) State-of-the-art of high power gyro-devices and free electron masers, Update 2012. KIT Scientific Report 7641, KIT Scientific Publishing

17. Bratman VL, Fedotov AE, Kalynov YK et al (1999) Moderately relativistic high-harmonic gyrotrons for millimeter/submillimeter wavelength band. IEEE Trans Plasma Sci 27: 456–461
18. Idehara T, Ogawa I, Mitsudo S et al (2004) A high harmonic gyrotron with an axis-encircling electron beam and a permanent magnet. IEEE Trans Plasma Sci 32:903–909
19. Furuno DS, Mcdermott DB, Kou CS et al (1990) Operation of a large-orbit high-harmonic gyro-traveling-wave tube amplifier. IEEE Trans Plasma Sci 18:313–320
20. Neilson J, Read M, Ives L (2009) Design of a permanent magnet gyrotron for active denial systems. In: 34th international conference on infrared, millimeter, and terahertz waves (IRMMW-THz 2009), 21–25 Sept 2009, Busan, Korea
21. Glyavin MY, Luchinin AG, Golubiatnikov GY (2008) Generation of 1.5-kW, 1-THz coherent radiation from a gyrotron with a pulsed magnetic field. Phys Rev Lett 100:015101
22. Bratman VL, Kalynov YK, Manuilov VN (2009) Large-orbit gyrotron operation in the terahertz frequency range. Phys Rev Lett 102:245101
23. Hornstein MK, Bajaj VS, Griffin RG, Temkin RJ (2007) Efficient low voltage operation of a CW gyrotron oscillator at 223 GHz. IEEE Trans Plasma Sci 35(1):27–30
24. Glyavin MY, Zavolskiy NA, Sedov AS, Nusinovich GS (2013) Low-voltage gyrotrons. Phys Plasmas 20:033103
25. Granatstein VL, Vitello P, Chu KR et al (1985) Design of gyrotron amplifiers for driving-1 Tev E-E+ linear colliders. IEEE Trans Nucl Sci 32:2957–2959
26. Lawson W, Cheng J, Calame JP et al (1998) High-power operation of a three-cavity X-band coaxial gyroklystron. Phys Rev Lett 81:3030–3033
27. Menninger WL, Danly GG, Temkin RJ (1996) Multimegawatt relativistic harmonic gyrotron traveling-wave tube amplifier experiments. IEEE Trans Plasma Sci 24:687–699
28. He W, Donaldson CR, Zhang L, Ronald K, McElhinney P, Cross AW (2013) High power wideband gyrotron backward wave oscillator operating towards the terahertz region. Phys Rev Lett 110(16):165101
29. Hung CL, Syu MF, Yang MT, Chen KL (2012) Selective mode suppression in a W-band second harmonic coaxial waveguide gyrotron backward-wave oscillator. Appl Phys Lett 101(3):033504
30. Chen NC, Chang TH, Yuan CP, Idehara T, Ogawa I (2010) Theoretical investigation of a high efficiency and broadband subterahertz gyrotron. Appl Phys Lett 96(16):161501
31. Thumm M, Arnold A, Borie E, Braz O, Dammertz G, Dumbrajs O, Koppenburg K, Kuntze M, Michel G, Piosczyk B (2001) Frequency step-tunable (114–170 GHz) megawatt gyrotrons for plasma physics applications. Fusion Eng Des 53:407–421
32. Kreischer KE, Temkin RJ (1987) Single-mode operation of a high-power, step-tunable gyrotron. Phys Rev Lett 59(5):547–550
33. Fliflet AW, Hargreaves TA, Manheimer WM et al (1989) Operation of a quasioptical gyrotron with variable mirror separation. Phys Rev Lett 62:2664–2667
34. Fliflet AW, Hargreaves TA, Manheimer WM et al (1990) Initial operation of a high-power quasi-optical gyrotron. IEEE Trans Plasma Sci 18:306–312
35. Gantenbein G, Borie E, Dammertz G et al (1994) Experimental results and numerical simulations of a high-power 140-GHz gyrotron. IEEE Trans Plasma Sci 22:861–870
36. Chang TH, Chen SH, Barnett LR et al (2001) Characterization of stationary and nonstationary behavior in gyrotron oscillators. Phys Rev Lett 87(6):064802
37. Nusinovich GS, Sinitsyn OV, Antonsen TM (2007) Mode switching in a gyrotron with azimuthally corrugated resonator. Phys Rev Lett 98:205101
38. Sirigiri JR, Kreischer KE, Machuzak J et al (2001) Photonic-band-gap resonator gyrotron. Phys Rev Lett 86:5628–5631
39. Liu SG, Yuan XS, Fu WJ et al (2007) The coaxial gyrotron with two electron beams. I. Linear theory and nonlinear theory. Phys Plasmas 14:103113
40. Liu SG, Yuan XS, Liu DW et al (2007) The coaxial gyrotron with two electron beams. II. Dual frequency operation. Phys Plasmas 14:103114

41. Lawson W, Latham PE (1987) The design of a small-orbit large-orbit gyroklystron experiment. J Appl Phys 61:519–528
42. Chu KR, Granatstein VL, Latham PE et al (1985) A 30-MW gyroklystron-amplifier design for high-energy linear accelerators. IEEE Trans Plasma Sci 13:424–434
43. Lawson W, Calame JP, Hogan B et al (1991) Efficient operation of a high-power X-band gyroklystron. Phys Rev Lett 67:520–523
44. Lawson W, Calame JP, Hogan BP et al (1992) Performance-characteristics of a high-power X-band 2-cavity gyroklystron. IEEE Trans Plasma Sci 20:216–223
45. Calame JP, Cheng J, Hogan B et al (1994) Measurements of velocity ratio in a 90 MW gyroklystron electron-beam. IEEE Trans Plasma Sci 22:476–485
46. Lawson W, Hogan B, Flaherty MKE et al (1996) Design and operation of a two-cavity third harmonic Ka-band gyroklystron. Appl Phys Lett 69:1849–1851
47. Blank M, Danly BG, Levush B et al (1997) Experimental demonstration of a W-band gyroklystron amplifier. Phys Rev Lett 79:4485–4488
48. Lawson W (2000) Design of a 70-GHz second-harmonic gyroklystron experiment for radar applications. IEEE Microw Guided Wave Lett 10:108–110
49. Blank M, Danly BG, Levush B (2000) Experimental demonstration of W-band gyroklystron amplifiers with improved gain and efficiency. IEEE Trans Plasma Sci 28:706–711
50. Lawson W, Ives RL, Mizuhara M et al (2001) Design of a 10-MW, 91.4-GHz frequency-doubling gyroklystron for advanced accelerator applications. IEEE Trans Plasma Sci 29: 545–558
51. Danly BG, Cheung J, Gregers-Hansen V, et al (2002) WARLOC: a high-power millimeter-wave radar. In: 27th international conference on infrared and millimeter waves, 22–26 Sept 2002. Conference digest, SANDIEGO, CA, USA
52. Linde GJ, Ngo MT, Danly BG et al (2008) WARLOC: a high-power coherent 94 GHz radar. IEEE Trans Aerosp Electron Syst 44:1102–1117
53. Tolkachev A (1998) A large-aperture radar phased antenna of Ka band. In: Proceedings of the 28th Moscow international conference on antenna theory and technology, pp 22–24, Moscow, Russia
54. Ganguly AK, Ahn S (1989) Optimization of the efficiency in gyrotron backward-wave oscillator via a tapered axial magnetic-field. Appl Phys Lett 54:514–516
55. Lin AT (1992) Mechanisms of efficiency enhancement in gyrotron backward-wave oscillators with tapered magnetic-fields. Phys Rev A 46:R4516–R4519
56. Kou CS, Chen SH, Barnett LR et al (1993) Experimental-study of an injection-locked gyrotron backward-wave oscillator. Phys Rev Lett 70:924–927
57. Kou CS (1994) Starting oscillation conditions for gyrotron backward-wave oscillators. Phys Plasmas 1:3093–3099
58. Basten MA, Guss WC, Kreischer KE et al (1995) Experimental investigation of a 140-GHz gyrotron-backward wave oscillator. Int J Infrared Millim Waves 16:889–905
59. Walter MT, Gilgenbach RM, Luginsland JW et al (1996) Effects of tapering on gyrotron backward-wave oscillators. IEEE Trans Plasma Sci 24:636–647
60. Chen SH, Chu KR, Chang TH (2000) Saturated behavior of the gyrotron backward-wave oscillator. Phys Rev Lett 85:2633–2636
61. Chen SH, Chang TH, Pao KF et al (2002) Linear and time-dependent behavior of the gyrotron backward-wave oscillator. Phys Rev Lett 89:268303
62. Grudiev A, Schunemann K (2002) Nonstationary behavior of the gyrotron backward-wave oscillator. IEEE Trans Plasma Sci 30:851–858
63. Yeh YS, Chang TH, Wu TS (2004) Comparative analysis of gyrotron backward-wave oscillators operating at different cyclotron harmonics. Phys Plasmas 11:4547–4553
64. Hung CL, Yeh YS (2005) Stability analysis of a coaxial-waveguide gyrotron traveling-wave amplifier. Phys Plasmas 12:103102
65. He W, Cross AW, Phelps ADR et al (2006) Theory and simulations of a gyrotron backward wave oscillator using a helical interaction waveguide. Appl Phys Lett 89:091504

66. Pao KF, Chang TH, Chen SH et al (2006) Rise and fall time behavior of the gyrotron backward-wave oscillator. Phys Rev E 74:046405
67. Chen NC, Yu CF, Chang TH (2007) A TE21 second-harmonic gyrotron backward-wave oscillator with slotted structure. Phys Plasmas 14:123105
68. Chang TH, Fan CT, Pao KF et al (2007) Stability and tunability of the gyrotron backward-wave oscillator. Appl Phys Lett 90:191501
69. Fan CT, Chang TH, Pao KF et al (2007) Stable, high efficiency gyrotron backward-wave oscillator. Phys Plasmas 14:093102
70. Du CH, Liu PK, Xue QZ et al (2008) Effect of a backward wave on the stability of an ultrahigh gain gyrotron traveling-wave amplifier. Phys Plasmas 15:123107
71. Chang TH, Yu CF, Hung CL et al (2008) W-band TE01 gyrotron backward-wave oscillator with distributed loss. Phys Plasmas 15:073105
72. Chang TH, Idehara T, Ogawa I et al (2009) Frequency tunable gyrotron using backward-wave components. J Appl Phys 105:063304
73. Yuan CP, Chang TH, Chen NC et al (2009) Magnetron injection gun for a broadband gyrotron backward-wave oscillator. Phys Plasmas 16:073109
74. Du CH, Qi XB, Liu PK, Chang TH, Xu SX, Geng ZH, Hao BL, Xiao L, Liu GF, Li ZD, Shi SH, Wang H (2014) Theory and experiment of a W-band tunable gyrotron oscillator. IEEE Trans Electron Devices, to be published in July Issue 2014
75. Chu KR (2002) Overview of research on the gyrotron traveling-wave amplifier. IEEE Trans Plasma Sci 30:903–908
76. Barnett LR, Baird JM, Lau YY et al (1980) A high gain single stage gyrotron traveling-wave amplifier. Int Electron Devices Meet 26:314–317
77. Barnett LR, Chu KR, Baird JM et al (1979) Gain, saturation, and bandwidth measurements of the NRL gyrotron travelling wave amplifier. Int Electron Devices Meet 25:164–167
78. Park GS, Choi JJ, Park SY et al (1995) Gain broadening of 2-stage tapered gyrotron traveling-wave tube amplifier. Phys Rev Lett 74:2399–2402
79. Chu KR, Barnett LR, Chen HY et al (1995) Stabilization of absolute instabilities in the gyrotron traveling-wave amplifier. Phys Rev Lett 74:1103–1106
80. Chu KR, Chen HY, Hung CL et al (1998) Ultrahigh gain gyrotron traveling wave amplifier. Phys Rev Lett 81:4760–4763
81. Wang QS, McDermott DB, Luhmann NC (1996) Operation of a stable 200-kW second-harmonic gyro-TWT amplifier. IEEE Trans Plasma Sci 24:700–706
82. Chong CK, McDermott DB, Luhmann NC (1998) Large-signal operation of a third-harmonic slotted gyro-TWT amplifier. IEEE Trans Plasma Sci 26:500–507
83. Calame JP, Garven M, Danly BG et al (2002) Gyrotron-traveling wave-tube circuits based on lossy ceramics. IEEE Trans Electron Devices 49:1469–1477
84. Garven M, Calame JP, Danly BG et al (2002) A gyrotron-traveling-wave tube amplifier experiment with a ceramic loaded interaction region. IEEE Trans Plasma Sci 30:885–893
85. Pershing DE, Nguyen KT, Calame JP et al (2004) A TE11 Ka-band gyro-TWT amplifier with high-average power compatible distributed loss. IEEE Trans Plasma Sci 32:947–956
86. Nguyen KT, Calame JP, Pershing DE et al (2001) Design of a Ka-band gyro-TWT for radar applications. IEEE Trans Electron Devices 48:108–115
87. Denisov GG, Bratman VL, Phelps ADR et al (1998) Gyro-TWT with a helical operating waveguide: new possibilities to enhance efficiency and frequency bandwidth. IEEE Trans Plasma Sci 26:508–518
88. Burt G, Samsonov SV, Ronald K et al (2004) Dispersion of helically corrugated waveguides: analytical, numerical, and experimental study. Phys Rev E 70:046402
89. Bratman VL, Cross AW, Denisov GG et al (2000) High-gain wide-band gyrotron traveling wave amplifier with a helically corrugated waveguide. Phys Rev Lett 84:2746–2749
90. Denisov GG, Bratman VL, Cross AW et al (1998) Gyrotron traveling wave amplifier with a helical interaction waveguide. Phys Rev Lett 81:5680–5683

91. Sirigiri JR (ed) (1999) Theory and design study of a novel quasi-optical gyrotron traveling wave amplifier, M.S. Thesis, Dept of Electrical Engineering and Computer Science, MIT, Oct, 1999
92. Sirigiri JR, Shapiro MA, Temkin RJ (2003) High-power 140-GHz quasioptical gyrotron traveling-wave amplifier. Phys Rev Lett 90:258302
93. Chu KR, Chen HY, Hung CL et al (1999) Theory and experiment of ultrahigh-gain gyrotron traveling wave amplifier. IEEE Trans Plasma Sci 27:391–404
94. Lau YY, Barnett LR, Granatstein VL (1982) Gyrotron traveling wave amplifier: IV. Analysis of launching losses. Int J Infrared Millim Waves 3:45–62
95. Lau YY, Chu KR, Barnett LR et al (1981) Gyrotron traveling wave amplifier: I. Analysis of oscillations. Int J Infrared Millim Waves 2:373–393
96. Lau YY, Chu KR, Barnett LR et al (1981) Gyrotron traveling wave amplifier: II. Effects of velocity spread and wall resistivity. Int J Infrared Millim Waves 2:395–413
97. Lau YY, Chu KR (1981) Gyrotron traveling wave amplifier: III. A proposed wideband fast wave amplifier. Int J Infrared Millim Waves 2:415–425
98. Chang TH, Chen NC (2006) Transition of absolute instability from global to local modes in a gyrotron traveling-wave amplifier. Phys Rev E 74:016402
99. Du CH, Liu PK (2009) Stabilization of the potential multi-steady-state absolute instabilities in a gyrotron traveling-wave amplifier. Phys Plasmas 16:103107
100. Piosczyk B, Arnold A, Dammertz G et al (2002) Coaxial cavity gyrotron – recent experimental results. IEEE Trans Plasma Sci 30:819–827
101. Hung CL (2006) Linear analysis of a coaxial-waveguide gyrotron traveling-wave tube. Phys Plasmas 13:033109
102. Wang QS, Mcdermott DB, Luhmann NC (1995) Demonstration of marginal stability theory by a 200-kW 2nd-harmonic gyro-TWT amplifier. Phys Rev Lett 75:4322–4325
103. Barnett LR, Lau YY, Chu KR et al (1981) An experimental wideband gyrotron traveling-wave amplifier. IEEE Trans Electron Devices 28:872–875
104. Park GS, Park SY, Kyser RH et al (1994) Broad-band operation of a Ka-band tapered gyrotraveling wave amplifier. IEEE Trans Plasma Sci 22:536–543
105. Leou KC, McDermott DB, Luhmann NC (1996) Large-signal characteristics of a wide-band dielectric-loaded gyro-TWT amplifier. IEEE Trans Plasma Sci 24:718–726
106. Rao SJ, Jain PK, Basu BN (1996) Broadbanding of a gyro-TWT by dielectric-loading through dispersion shaping. IEEE Trans Electron Devices 43:2290–2299
107. Rao SJ, Jain PK, Basu BN (1996) Two-stage dielectric-loading for broadbanding a gyro-TWT. IEEE Electron Device Lett 17:303–305
108. Cross AW, He W, Phelps ADR et al (2007) Helically corrugated waveguide gyrotron traveling wave amplifier using a thermionic cathode electron gun. Appl Phys Lett 90:253501
109. Guo H, Chen L, Keren H et al (1982) Measurement of gain for slow cyclotron waves on an annular electron beam. Phys Rev Lett 49:730–733
110. Fu WJ, Yan Y, Yuan XS et al (2009) Two-beam magnetron injection guns for coaxial gyrotron with two electron beams. Phys Plasmas 16:23103
111. Yan R, Luo Y, Liu G, Pu Y (2012) Design and experiment of a Q-band gyro-TWT loaded with lossy dielectric. IEEE Trans Electron Devices 59(12):3612–3617
112. Wang E, Zeng X et al (2012) Experimental study of high-power gyrotron traveling-wave tube with periodic lossy material loading. IEEE Trans Plasma Sci 40(7):1846–1853
113. Zhang SC, Ouyang ZB, Qiu CR et al (2004) Coaxial-waveguide gyrotron amplifier operating with high power and ultrahigh gain in millimeter and submillimeter waves. IEEE Trans Plasma Sci 32:981–986
114. Hung CL (2012) High-power, stable Ka/V dual-band gyrotron traveling-wave tube amplifier. Appl Phys Lett 100(20):203502

Chapter 2
Fundamental Theory of the Electron Cyclotron Maser

Abstract This chapter builds up the theoretical foundation for the book. The fundamental theories of the uniform dielectric-lined waveguide and the periodic dielectric-loaded waveguide are reviewed first. Since high-power endurable lossy waveguide becomes an indispensable component of the gyrotron amplifier circuit, it is a precondition to understand the wave properties in the waveguide system for the beam-wave interaction study. Secondly, from the point of view of the partitioning transverse plane of the interaction space, it proposes a general ECM theoretical model, which fits well most of the waveguide interaction systems. Thirdly, using the waveguide theory and the general ECM model, the linear interaction theory and the nonlinear theory of the dielectric-lined gyro-TWT is developed. When the lossy dielectric layer becomes infinitely thin, the dielectric-lined interaction theory returns to classic form of the cylindrical waveguide theory. These theories build up the theoretical foundation for further investigating the instability competition in the interaction system.

Keywords Electron cyclotron maser • Lossy dielectric-loaded waveguide • Modal transition • Absolute instability • Convective instability

2.1 Introduction

The operation principle of a gyrotron traveling-wave tube (gyro-TWT) amplifier is based on the convective instability of the relativistic electron cyclotron maser (ECM) [1]. The ECM interaction employs a cycling electron beam with an inherent gyrating frequency $s\Omega_e$, which makes it feasible to interact with a fast electromagnetic wave (EM wave), in particular, a high-order waveguide mode. Figure 2.1a shows the transverse plane of an ECM system, for simpler illustration, using an angularly polarized waveguide mode. The electron projections on the transverse plane are gyrating with the Larmor radius r_L, which is determined by the longitudinal static

C.-H. Du and P.-K. Liu, *Millimeter-Wave Gyrotron Traveling-Wave Tube Amplifiers*,
DOI 10.1007/978-3-642-54728-7_2,

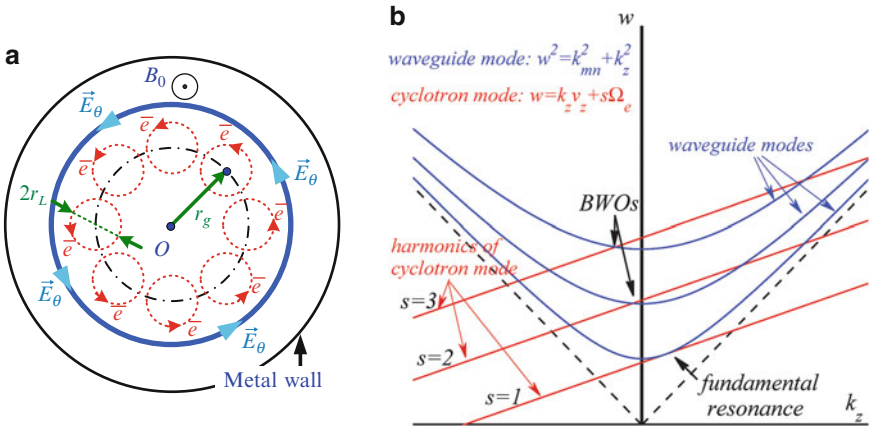

Fig. 2.1 (**a**) A schematic plot of an electron cyclotron maser interaction system based on angular polarized waveguide mode, and (**b**) the cold electron beam-wave dispersion relation

magnetic field strength $B_0\vec{e}_z$ and electron transverse velocity. The centers of these Larmor circles locate on or around a guiding circle of radius r_g. Normally, for a cycling electron beam with the guiding center radius larger than the Larmor radius $r_g > r_L$, it is called a small-orbit electron beam, which could be generated by a magnetron injection gun (MIG) [2]. On the contrary, for a cycling electron beam with relatively small guiding center radius $r_g \ll r_L$, it is called large-orbit electron beam. Usually, a large-orbit electron beam could be generated by a magnetic cusp gun (MCG) [3]. Figure 2.1b shows the dispersion relation between harmonic cyclotron modes and waveguide modes. The gyrating motion of the electron beam provides broadband Doppler-shifted cyclotron resonance between a cyclotron mode and a waveguide mode [1, 4], where the Doppler-shifted term is a product of wave number and axial velocity $k_z v_z$. The electron beam interacts with the waveguide mode through azimuthal bunching in the phase space and transfers its transverse kinetic energy to the electromagnetic (EM) wave mode, inducing high-power EM radiation.

From Fig. 2.1a, b, it is revealed that the electron beam and the waveguide mode are a pair of elements of an ECM system. On the cold beam-wave dispersion relation in Fig. 2.1b, a cyclotron resonance happens around the tangential region or a cross point between a cyclotron mode and a waveguide mode. Such a resonance is the origin of a certain kind of instability, namely, absolute instability or convective instability in plasma physics [1, 5]. Once the beam-wave feedback effect is stronger than a threshold, the instability grows into EM wave radiation. In the forward-wave region, the Doppler-shifted cyclotron resonance happens around the tangential region or cross points between a cyclotron harmonic and a forward-wave waveguide mode. It normally induces coherent radiation based on a convective instability, which amplifies the driven wave along the forward-wave propagation direction.

In the backward-wave region, a cyclotron resonance happens around the cross point between a cyclotron harmonic and a backward-wave mode. The backward-wave mode grows from the noise-level disturbance and bunches the forward moving electron beam. The electron beam in turn induces stronger radiation on the backward-wave mode. In such a way, a kind of internal feedback effect is formed. If such internal feedback is strong enough, it will induce self-excitation oscillation or the backward-wave oscillation (BWO) [1].

In order to address the fundamental theory of the ECM in a more comprehensive way in this chapter, the basic waveguide theory is reviewed first, including theory of uniform dielectric-loaded waveguide [6] and periodic dielectric-loaded waveguide [7]. And then, a frequency domain theoretical model of ECM system is developed based on the point of view of partitioning transverse plane of the interaction space, which is generally applicable to most of the ECM waveguide. Finally, the fundamental ECM theory of the lossy dielectric-lined waveguide is developed.

2.2 Theory of the Waveguides

Since 1970s, the world-wide gyro-TWT research has employed various kinds of interaction circuits [1], including cylindrical waveguides [8, 9], rectangular waveguides, transverse varying rectangular waveguides [10], dielectric-loaded cylindrical waveguides [11], distributed loss-loaded cylindrical waveguides [12, 13], radially sliced radiating lossy cylindrical waveguides [14–16], lossy dielectric-loaded cylindrical waveguides [17], helically grooved waveguides [18–20], and quasi-optical confocal waveguides [21]. Other than the abovementioned interaction circuits, open cavities employed by gyrotron oscillators, such as coaxial cavities [22], cavities with corrugated insert [23], and cavities based on photonic-band-gap defect structure [24], also provide new possibilities to mode control for the gyro-TWTs. These experiments indicated that in order to maintain broadband cyclotron resonance between the electron beam and a waveguide mode, it is specially required to pay attention to self-excited oscillations, and a certain kind of disturbance or control method should be introduced into a gyro-TWT circuit to suppress oscillations and protect the amplification [1].

Until now, the operation mode control methods in a gyro-TWT circuit mainly include waveguide wall loss (Aquadag-loaded [12] or lossy ceramic-loaded waveguide [16, 17]), dispersion relation control technology (helical grooved waveguide [18]), and mode filter technology (confocal waveguide or PBG structure [21, 24]). Controlling the propagation characteristics of the operation mode would directly influence the electron beam-wave interaction. Hence, to study the propagation characteristics of the interaction waveguide is the precondition of the ECM interaction investigation. This section reviews the theory of dielectric-loaded waveguide which provides theoretical foundation for studying the waveguide propagation characteristics.

2.2.1 Theory of Uniform Dielectric-Loaded Waveguide

According to the solution of Maxwell Equation in waveguide system, the field components of $\vec{E}$ and $\vec{H}$ can be expressed as [6]

$$\vec{E} = \frac{1}{j\omega\varepsilon}\left(k^2\vec{A} + \nabla\left(\nabla\cdot\vec{A}\right)\right) - \nabla\times\vec{F} \tag{2.1a}$$

$$H = \nabla\times\vec{A} + \frac{1}{j\omega\mu}\left(k^2\vec{F} + \nabla\left(\nabla\cdot\vec{F}\right)\right) \tag{2.1b}$$

where ω is the angular frequency of the wave, ε is the permittivity, μ is the permeability, and $\vec{A}$ and $\vec{F}$ are *magnetic potential vector* and *electric potential vector*, respectively. In cylindrical coordinate, the high-frequency field can be further expressed as

$$E_\mathrm{r} = -\frac{1}{r}\frac{\partial}{\partial\varphi}\psi^\mathrm{e} + \frac{1}{j\omega\varepsilon}\frac{\partial^2}{\partial r\partial z}\psi^\mathrm{m} \tag{2.2a}$$

$$E_\varphi = \frac{\partial}{\partial r}\psi^\mathrm{e} + \frac{1}{j\omega\varepsilon r}\frac{\partial^2}{\partial\varphi\partial z}\psi^\mathrm{m} \tag{2.2b}$$

$$E_z = \frac{1}{j\omega\varepsilon}\left(\frac{\partial^2}{\partial z^2} + k^2\right)\psi^\mathrm{m} \tag{2.2c}$$

$$H_\mathrm{r} = \frac{1}{j\omega\mu}\frac{\partial^2}{\partial r\partial z}\psi^\mathrm{e} + \frac{1}{r}\frac{\partial}{\partial\varphi}\psi^\mathrm{m} \tag{2.2d}$$

$$H_\varphi = \frac{1}{j\omega\mu r}\frac{\partial^2}{\partial\varphi\partial z}\psi^\mathrm{e} - \frac{\partial}{\partial r}\psi^\mathrm{m} \tag{2.2e}$$

$$H_z = \frac{1}{j\omega\mu}\left(k^2 + \frac{\partial^2}{\partial z^2}\right)\psi^\mathrm{e} \tag{2.2f}$$

where ψ^m and ψ^e are the distribution functions of $\vec{A}$ and $\vec{F}$, respectively, and this pair of distribution functions is the solutions of scalar Helmholtz Equation

$$\left(\frac{1}{r}\frac{\partial}{\partial r}r\frac{\partial}{\partial r} + \frac{1}{r^2}\frac{\partial^2}{\partial\varphi^2} + \frac{\partial^2}{\partial z^2}\right)\psi + k^2\psi = 0 \tag{2.3}$$

which can be solve based on the waveguide boundary condition [6].

Figure 2.2 displays the structure of the longitudinal uniform dielectric-lined cylindrical waveguide, or called dielectric waveguide. Region 1 is the vacuum region, and Region 2 is the dielectric layer. With the basic wave function from Helmholtz Equation, the distribution function in both regions are [6]

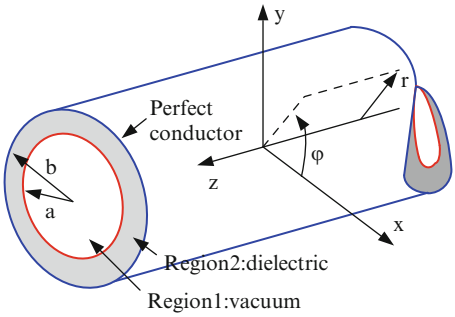

Fig. 2.2 The structure of the dielectric-loaded waveguide

$$\psi_n^{\mathrm{m1}}\left(k_{\perp 1}r\right) = AB_n^{\mathrm{m1}}\left(k_{\perp 1}r\right)\cos\left(n\varphi\right)e^{-jk_z z} \tag{2.4a}$$

$$\psi_n^{\mathrm{e1}}\left(k_{\perp 1}r\right) = BB_n^{\mathrm{e1}}\left(k_{\perp 1}r\right)\sin\left(n\varphi\right)e^{-jk_z z} \tag{2.4b}$$

$$\psi_n^{\mathrm{m2}}\left(k_{\perp 2}r\right) = CB_n^{\mathrm{m2}}\left(k_{\perp 2}r\right)\cos\left(n\varphi\right)e^{-jk_z z} \tag{2.4c}$$

$$\psi_n^{\mathrm{e2}}\left(k_{\perp 2}r\right) = DB_n^{\mathrm{e2}}\left(k_{\perp 2}r\right)\sin\left(n\varphi\right)e^{-jk_z z} \tag{2.4d}$$

where $k_{\perp 1}$ and $k_{\perp 2}$ are the transverse wave number in the vacuum region and dielectric region, respectively. The n is the order of the Bessel Functions, and the Bessel Function $B_n(k_\perp r)$ is actually a linear combination of the Bessel Functions of the 1st kind $J_n(k_\perp r)$ and 2nd kind $N_n(k_\perp r)$

$$CB_n\left(k_\perp r\right) = C_1 J_n\left(k_\perp r\right) + C_2 N_n\left(k_\perp r\right) \tag{2.5}$$

Equation 2.4 contain eight unknown variables (A_1, A_2, B_1, B_2, C_1, C_2, D_1, and D_2) in total. Due to Region 1, the axis region contains $r = 0$, where the second kind Bessel Function $N_n(0)$ is singular; hence A_2 and B_2 are naturally equal to zero. The boundary between Region 1 and Region 2 requires continuous tangential field components, $E_{z1} = E_{z2}$, $E_{\varphi 1} = E_{\varphi 2}$, $H_{z1} = H_{z2}$, and $H_{\varphi 1} = H_{\varphi 2}$. The boundary between Region 2 and the metal wall requires vanishing tangential electric field components $E_{z2} = 0$ and $E_{\varphi 2} = 0$. Boundary conditions generate equations

$$\frac{k_{\perp 1}^2}{\varepsilon_1}A_1 J_n\left(k_{\perp 1}a\right) - \frac{k_{\perp 2}^2}{\varepsilon_2}\left(C_1 J_n\left(k_{\perp 2}a\right) + C_2 N_n\left(k_{\perp 2}a\right)\right) = 0 \tag{2.6a}$$

$$\begin{aligned}&\tfrac{k_z n}{\omega\varepsilon_1 a}A_1 J_n\left(k_{\perp 1}a\right) + k_{\perp 1}B_1 J_n'\left(k_{\perp 1}a\right)\\ &- \tfrac{k_z n}{\omega\varepsilon_2 a}\left(C_1 J_n\left(k_{\perp 2}a\right) + C_2 N_n\left(k_{\perp 2}a\right)\right)\\ &- k_{\perp 2}\left(D_1 J_n'\left(k_{\perp 2}a\right) + D_2 N_n'\left(k_{\perp 2}a\right)\right) = 0\end{aligned} \tag{2.6b}$$

$$\frac{k_{\perp 1}^2}{\mu_1} B_1 J_n\left(k_{\perp 1} a\right) - \frac{k_{\perp 2}^2}{\mu_2}\left(D_1 J_n\left(k_{\perp 2} a\right) + D_2 N_n\left(k_{\perp 2} a\right)\right) = 0 \tag{2.6c}$$

$$\begin{aligned} &-k_{\perp 1} A_1 J_n'\left(k_{\perp 1} a\right) - \tfrac{k_z n}{\omega \mu_1 a} B_1 J_n\left(k_{\perp 1} a\right) \\ &+k_{\perp 2}\left[C_1 J_n'\left(k_{\perp 2} a\right) + C_2 N_n'\left(k_{\perp 2} a\right)\right] \\ &+\tfrac{k_z n}{\omega \mu_2 a}\left[D_1 J_n\left(k_{\perp 2} a\right) + D_2 N_n\left(k_{\perp 2} a\right)\right] = 0 \end{aligned} \tag{2.6d}$$

$$\frac{k_{\perp 2}^2}{\varepsilon_2}\left[C_1 J_n\left(k_{\perp 2} b\right) + C_2 N_n\left(k_{\perp 2} b\right)\right] = 0 \tag{2.6e}$$

$$\begin{aligned} &k_{\perp 2}\left[D_1 J_n'\left(k_{\perp 2} b\right) + D_2 N_n'\left(k_{\perp 2} b\right)\right] \\ &+\tfrac{k_z n}{\omega \varepsilon_2 b}\left[C_1 J_n\left(k_{\perp 2} b\right) + C_2 N_n\left(k_{\perp 2} b\right)\right] = 0 \end{aligned} \tag{2.6f}$$

where valid solution will be obtained from zero determinant of Eq. (2.6). For easier calculation, intermediate variables are introduced,

$$C_2 = -C_1 \frac{J_n\left(k_{\perp 2} b\right)}{N_n\left(k_{\perp 2} b\right)} \tag{2.7a}$$

$$D_2 = -D_1 \frac{J_n'\left(k_{\perp 2} b\right)}{N_n'\left(k_{\perp 2} b\right)} \tag{2.7b}$$

$$A_1 = \frac{k_{\perp 2}^2 \varepsilon_1}{k_{\perp 1}^2 \varepsilon_2} \frac{Q\left(k_{\perp 2} a\right)}{J_n\left(k_{\perp 1} a\right) N_n\left(k_{\perp 2} b\right)} C_1 \tag{2.7c}$$

$$B_1 = \frac{k_{\perp 2}^2 \mu_1}{k_{\perp 1}^2 \mu_2} \frac{P\left(k_{\perp 2} a\right)}{J_n\left(k_{\perp 1} a\right) N_n'\left(k_{\perp 2} b\right)} D_1 \tag{2.7d}$$

where

$$P(x) = J_n(x) N_n'\left(k_{\perp 2} b\right) - N_n(x) J_n'\left(k_{\perp 2} b\right) \tag{2.8a}$$

$$Q(x) = J_n(x) N_n\left(k_{\perp 2} b\right) - N_n(x) J_n\left(k_{\perp 2} b\right) \tag{2.8b}$$

With the intermediate variables in Eqs. (2.7) and (2.8), the expression by setting the determinant of Eq. (2.6) equal to zero is simplified into the eigen equation

$$\begin{aligned} &\left[\tfrac{1}{k_{\perp 2}} \tfrac{\varepsilon_2}{\varepsilon_1} \tfrac{Q'(k_{\perp 2} a)}{Q(k_{\perp 2} a)} - \tfrac{1}{k_{\perp 1}} \tfrac{J_n'(k_{\perp 1} a)}{J_n(k_{\perp 1} a)}\right]\left[\tfrac{1}{k_{\perp 2}} \tfrac{\mu_2}{\mu_1} \tfrac{P'(k_{\perp 2} a)}{P(k_{\perp 2} a)} - \tfrac{1}{k_{\perp 1}} \tfrac{J_n'(k_{\perp 1} a)}{J_n(k_{\perp 1} a)}\right] \\ &-\tfrac{1}{\varepsilon_1 \mu_1}\left(\tfrac{k_z n}{\omega a}\right)^2\left(\tfrac{1}{k_{\perp 1}^2} - \tfrac{1}{k_{\perp 2}^2}\right)^2 = 0 \end{aligned} \tag{2.9}$$

To solve the transcendental Eq. (2.9), the additional dispersion relations in both regions are required,

$$k_{\perp 1}^2 + k_z^2 = k^2 = \omega^2 \varepsilon_1 \mu_1 \tag{2.10a}$$

$$k_{\perp 2}^2 + k_z^2 = k^2 = \omega^2 \varepsilon_2 \mu_2 \tag{2.10b}$$

The dispersion relation (ω, k_z) of the dielectric waveguide could be solved together with Eqs. (2.9) and (2.10). The field components are given as follows:

Vacuum Region

$$E_z = -jA(z)\chi J_n\left(k_{\perp 1} r\right) e^{j(\omega t - n\varphi)} \tag{2.11a}$$

$$H_z = A(z) J_n\left(k_{\perp 1} r\right) e^{j(\omega t - n\varphi)} \tag{2.11b}$$

$$E_{\mathrm{r}} = \left[-A(z)\frac{n}{r}\frac{\omega\mu_1}{k_{\perp 1}^2} J_n\left(k_{\perp 1} r\right) - jA'(z)\frac{1}{k_{\perp 1}}\chi J_n'\left(k_{\perp 1} r\right)\right] e^{j(\omega t - n\varphi)} \tag{2.11c}$$

$$E_\varphi = \left[jA(z)\frac{\omega\mu_1}{k_{\perp 1}} J_n'\left(k_{\perp 1} r\right) - A'(z)\frac{n}{r}\frac{1}{k_{\perp 1}^2}\chi J_n\left(k_{\perp 1} r\right)\right] e^{j(\omega t - n\varphi)} \tag{2.11d}$$

$$H_{\mathrm{r}} = \left[A'(z)\frac{1}{k_{\perp 1}} J_n'\left(k_{\perp 1} r\right) - jA(z)\frac{n}{r}\frac{\omega\varepsilon_1}{k_{\perp 1}^2}\chi J_n\left(k_{\perp 1} r\right)\right] e^{j(\omega t - n\varphi)} \tag{2.11e}$$

$$H_\varphi = \left[-jA'(z)\frac{n}{k_{\perp 1}^2 r} J_n\left(k_{\perp 1} r\right) - A(z)\frac{\omega\varepsilon_1}{k_{\perp 1}}\chi J_n'\left(k_{\perp 1} r\right)\right] e^{j(\omega t - n\varphi)} \tag{2.11f}$$

Dielectric Region

$$E_z = -jA(z)\left[\tilde{\alpha} J_n\left(k_{\perp 2} r\right) + \tilde{\beta} N_n\left(k_{\perp 2} r\right)\right] e^{j(\omega t - n\varphi)} \tag{2.11g}$$

$$H_z = A(z)\left[\alpha J_n\left(k_{\perp 2} r\right) + \beta N_n\left(k_{\perp 2} r\right)\right] e^{j(\omega t - n\varphi)} \tag{2.11h}$$

$$E_{\mathrm{r}} = \begin{bmatrix} -A(z)\frac{n}{r}\frac{\omega\mu_2}{k_{\perp 2}^2}\left(\alpha J_n\left(k_{\perp 2} r\right) + \beta N_n\left(k_{\perp 2} r\right)\right) \\ -jA'(z)\frac{1}{k_{\perp 2}}\left(\tilde{\alpha} J_n'\left(k_{\perp 2} r\right) + \tilde{\beta} N_n'\left(k_{\perp 2} r\right)\right) \end{bmatrix} e^{j(\omega t - n\varphi)} \tag{2.11i}$$

$$E_\varphi = \begin{bmatrix} jA(z)\frac{\omega\mu_2}{k_{\perp 2}}\left(\alpha J_n'\left(k_{\perp 2} r\right) + \beta N_n'\left(k_{\perp 2} r\right)\right) \\ -A'(z)\frac{n}{r}\frac{1}{k_{\perp 2}^2}\left(\tilde{\alpha} J_n\left(k_{\perp 2} r\right) + \tilde{\beta} N_n\left(k_{\perp 2} r\right)\right) \end{bmatrix} e^{j(\omega t - n\varphi)} \tag{2.11j}$$

$$H_{\mathrm{r}}=\left[\begin{array}{l} A'(z)\frac{1}{k_{\perp 2}}\left(\alpha J_n'\left(k_{\perp 2}r\right)+\beta N_n'\left(k_{\perp 2}r\right)\right) \\ -jA(z)\frac{n}{r}\frac{\omega\varepsilon_2}{k_{\perp 2}^2}\left(\tilde{\alpha}J_n\left(k_{\perp 2}r\right)+\tilde{\beta}N_n\left(k_{\perp 2}r\right)\right) \end{array}\right]e^{j(\omega t-n\varphi)} \tag{2.11k}$$

$$H_{\varphi}=\left[\begin{array}{l} -jA'(z)\frac{n}{r}\frac{1}{k_{\perp 2}^2}\left(\alpha J_n\left(k_{\perp 2}r\right)+\beta N_n\left(k_{\perp 2}r\right)\right) \\ -A(z)\frac{\omega\varepsilon_2}{k_{\perp 2}}\left(\tilde{\alpha}J_n'\left(k_{\perp 2}r\right)+\tilde{\beta}N_n'\left(k_{\perp 2}r\right)\right) \end{array}\right]e^{j(\omega t-n\varphi)} \tag{2.11l}$$

where $A(z)$ is the axial field amplitude and other constants are

$$\alpha=\frac{J_n\left(k_{\perp 1}a\right)N_n'\left(k_{\perp 2}b\right)}{P\left(k_{\perp 2}a\right)} \tag{2.12a}$$

$$\beta=-\frac{J_n\left(k_{\perp 1}a\right)J_n'\left(k_{\perp 2}b\right)}{P\left(k_{\perp 2}a\right)} \tag{2.12b}$$

$$\chi=-\frac{\omega\mu_2 a}{k_z n\left(k_{\perp 2}^2-k_{\perp 1}^2\right)}\left[k_{\perp 1}k_{\perp 2}^2\frac{\mu_1}{\mu_2}\frac{J_n'\left(k_{\perp 1}a\right)}{J_n\left(k_{\perp 1}a\right)}-k_{\perp 1}^2k_{\perp 2}\frac{P'\left(k_{\perp 2}a\right)}{P\left(k_{\perp 2}a\right)}\right] \tag{2.12c}$$

$$\tilde{\alpha}=\chi\frac{J_n\left(k_{\perp 1}a\right)N_n\left(k_{\perp 2}b\right)}{Q\left(k_{\perp 2}a\right)} \tag{2.12d}$$

$$\tilde{\beta}=-\chi\frac{J_n\left(k_{\perp 1}a\right)J_n\left(k_{\perp 2}b\right)}{Q\left(k_{\perp 2}a\right)} \tag{2.12e}$$

From the field expressions, when azimuthal index $n=0$, modes in a dielectric waveguide are pure TE_{0m} or TM_{0m} and each with five wave components. While $n\neq 0$, the modes are hybrid modes HE_{nm} or EH_{nm} and each with six field components. Furthermore, if the dielectric region is a negligible thin layer, it is suitable to approximate a hybrid HE_{nm} or EH_{nm} by a corresponding TE_{nm} or TM_{nm} mode [25].

2.2.2 *Theory of Periodic Dielectric-Loaded Waveguide*

Figure 2.3 shows the sectional view of a periodic dielectric-loaded waveguide. Reference [7] presented the theory of such a waveguide in detail. A general review is included here. In the vacuum region, the field components can be decomposed into a sum of *Bloch components* according to the *Floquet's theorem*.

$$E_{z1}(r,\varphi,z)=\sum_{n=-\infty}^{+\infty}A_n^{\mathrm{I}}F_m\left(h_n^{\mathrm{I}}r\right)e^{jm\varphi}e^{-jk_nz}\qquad r<a \tag{2.13a}$$

$$H_{z1}(r,\varphi,z)=\sum_{n=-\infty}^{+\infty}B_n^{\mathrm{I}}F_m\left(h_n^{\mathrm{I}}r\right)e^{jm\varphi}e^{-jk_nz}\qquad r<a \tag{2.13b}$$

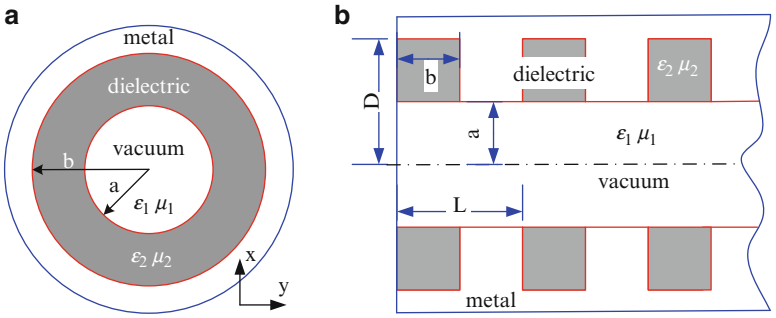

Fig. 2.3 (**a**) The transverse sectional view and (**b**) the longitudinal view of a periodic dielectric-loaded waveguide

In the periodic system, the propagation constant is $k_n = k_z + n(2\pi/L)$, where m and n indicate the order numbers of the Bessel Function and the Bloch harmonic, respectively. A_n^{I} and B_n^{I} are the unknown coefficients of fields amplitude. The Bessel Functions are

$$F_m\left(h_n^{\mathrm{I}} r\right) = \begin{cases} J_m\left(h_n^{\mathrm{I}} r\right) & \text{for } \mathrm{Re}\left[\left(h_n^{\mathrm{I}}\right)^2\right] > 0, \mathrm{Re}\left(h_n^{\mathrm{I}}\right) > 0, \mathrm{Im}\left(h_n^{\mathrm{I}}\right) > 0 \\ I_m\left(t_n^{\mathrm{I}} r\right) & \text{for } \mathrm{Re}\left[\left(t_n^{\mathrm{I}}\right)^2\right] > 0, \mathrm{Re}\left(t_n^{\mathrm{I}}\right) > 0, \mathrm{Im}\left(t_n^{\mathrm{I}}\right) > 0 \end{cases} \tag{2.14}$$

where the dispersion relations are $(h_n^{\mathrm{I}})^2 = (\omega/c)^2 - k_n^2$ and $(t_n^{\mathrm{I}})^2 = k_n^2 - (\omega/c)^2$. $J_m(h_n^{\mathrm{I}} r)$ and $I_m(t_n^{\mathrm{I}} r)$ are the first kind Bessel Function and the first kind modified Bessel Function, respectively. Because the second kind Bessel Function and the second kind modified Bessel Function are singular at $r = 0$, they are all omitted here.

Similar to the vacuum region, the field in the dielectric region can be decomposed into *standing eigenwaves*,

$$E_{z2}(r,\varphi,z) = \sum_{l=0}^{+\infty} A_l^{\mathrm{II}} G_m\left(h_l^{\mathrm{II}} r\right) e^{jm\varphi} \cos\left(\frac{l\pi z}{b}\right) \quad (a < r < D, nL < z < b + nL) \tag{2.15a}$$

$$H_{z2}(r,\varphi,z) = \sum_{l=1}^{+\infty} B_l^{\mathrm{II}} H_m\left(h_l^{\mathrm{II}} r\right) e^{jm\varphi} \sin\left(\frac{l\pi z}{b}\right) \quad (a < r < D, nL < z < b + nL) \tag{2.15b}$$

The standing eigenwaves already consider the boundary conditions of the dielectric region at $z = nL$ and $z = b + nL$. The Bessel Function $G_m(h_l^{\mathrm{II}}\rho)$ and $H_m(h_l^{\mathrm{II}}\rho)$ are

$$G_m\left(h_l^{\mathrm{II}} r\right) = \begin{cases} J_m\left(h_l^{\mathrm{II}} r\right) Y_m\left(h_l^{\mathrm{II}} D\right) - Y_m\left(h_l^{\mathrm{II}} r\right) J_m\left(h_l^{\mathrm{II}} D\right) \left(\mathrm{Re}\left[\left(h_n^{\mathrm{I}}\right)^2\right] > 0\right) \\ I_m\left(t_l^{\mathrm{II}} r\right) K_m\left(t_l^{\mathrm{II}} D\right) - K_m\left(t_l^{\mathrm{II}} r\right) I_m\left(t_l^{\mathrm{II}} D\right) \left(\mathrm{Re}\left[\left(t_n^{\mathrm{I}}\right)^2\right] > 0\right) \end{cases} \tag{2.16a}$$

$$H_m\left(h_l^{\mathrm{II}} r\right) = \begin{cases} J_m\left(h_l^{\mathrm{II}} r\right) Y_m'\left(h_l^{\mathrm{II}} D\right) - Y_m\left(h_l^{\mathrm{II}} r\right) J_m'\left(h_l^{\mathrm{II}} D\right) \left(\mathrm{Re}\left[\left(h_n^{\mathrm{I}}\right)^2\right] > 0\right) \\ I_m\left(t_l^{\mathrm{II}} r\right) K_m'\left(t_l^{\mathrm{II}} D\right) - K_m\left(t_l^{\mathrm{II}} r\right) I_m'\left(t_l^{\mathrm{II}} D\right) \left(\mathrm{Re}\left[\left(t_n^{\mathrm{I}}\right)^2\right] > 0\right) \end{cases} \tag{2.16b}$$

where $(h_l^{\mathrm{II}})^2 = (\omega/c)^2\varepsilon_r - (l\pi/b)^2$ and $(t_l^{\mathrm{II}})^2 = (l\pi/b)^2 - (\omega/c)^2\varepsilon_r$. $Y_m(h_l^{\mathrm{II}} r)$ and $K_m(t_l^{\mathrm{II}} r)$ are the second kind Bessel Function and the second kind modified Bessel Function, respectively. It needs to be stressed that the differential Bessel Functions are all differential to the *argument* $\partial J(x)/\partial x = J'(x)$. According to the relation between transverse field component and longitudinal component,

$$E_T = \frac{1}{T^2}\left(\frac{\partial}{\partial z}\nabla_T E_z + j\omega\mu\vec{z} \times \nabla_T H_z\right) \tag{2.17a}$$

$$H_T = \frac{1}{T^2}\left(\frac{\partial}{\partial z}\nabla_T H_z - j\omega\varepsilon\vec{z} \times \nabla_T E_z\right) \tag{2.17b}$$

where T indicates the transverse wave number, and the operator is $\nabla_T = \vec{e}_r\partial/\partial r + \vec{e}_\varphi\partial/(r\partial\varphi)$. With Eq. (2.17), the field components in vacuum region and the dielectric region can be obtained.

In the periodic system as given in Fig. 2.3, considering the boundary condition of tangential components continue on both the vacuum–dielectric interface (VDI) and the vacuum-metal interface (VMI).

$$E_{z1} = 0, \quad E_{\varphi 1} = 0 \quad b + nL < z < (n+1)L, \quad r = a \quad \text{(VMI)} \tag{2.18a}$$

$$E_{z1} = E_{z2}, \quad E_{\varphi 1} = E_{\varphi 2} \quad nL < z < b + nL, \quad r = a \quad \text{(VDI)} \tag{2.18b}$$

$$H_{r1} = 0 \quad b + nL < z < (n+1)L, \quad r = a \quad \text{(VMI)} \tag{2.18c}$$

$$H_{z1} = H_{z2}, \quad H_{\varphi 1} = H_{\varphi 2} \quad nL < z < b + nL, \quad r = a \quad \text{(VDI)} \tag{2.18d}$$

At first, using the boundary condition (2.18a) and (2.18b), multiplying $e^{jk_n z}$ on both sides, and integrating along the path $nL \sim (n+1)L$, it is obtained as follows:

$$A_n^{\mathrm{I}} F_m\left(h_n^{\mathrm{I}}\alpha\right) L = \sum_{l=0}^{+\infty} A_l^{\mathrm{II}} G_m\left(h_l^{\mathrm{II}}\alpha\right) R_1\left(k_n, l, b\right) \tag{2.19a}$$

$$\begin{aligned}&\left[\frac{j\omega\mu_0}{\left(h_n^{\mathrm{I}}\right)^2}B_n^{\mathrm{I}}F_m'\left(h_n^{\mathrm{I}}\alpha\right)+\frac{mk_n}{\alpha\left(h_n^{\mathrm{I}}\right)^2}A_n^{\mathrm{I}}F_m\left(h_n^{\mathrm{I}}\alpha\right)\right]L\\&=\sum_{l=0}^{+\infty}\frac{jm}{\alpha\left(h_l^{\mathrm{II}}\right)^2}\left(-\frac{l\pi}{b}\right)A_l^{\mathrm{II}}G_m\left(h_l^{\mathrm{II}}\alpha\right)R_2\left(k_n,l,b\right)\\&\quad+\sum_{l=1}^{+\infty}j\omega\mu_0\mu_r\frac{1}{\left(h_l^{\mathrm{II}}\right)^2}B_l^{\mathrm{II}}H_m'\left(h_l^{\mathrm{II}}\alpha\right)R_2\left(k_n,l,b\right)\end{aligned}\tag{2.19b}$$

where

$$R_1\left(k_n,l,b\right)=\int_{nL}^{b+nL}\mathrm{e}^{jk_nz}\cos\left(\frac{l\pi z}{b}\right)\mathrm{d}z\tag{2.20a}$$

$$R_2\left(k_n,l,b\right)=\int_{nL}^{b+nL}e^{jk_nz}\sin\left(\frac{l\pi z}{b}\right)\mathrm{d}z\tag{2.20b}$$

Using boundary conditions (2.18c) and (2.18d), multiplying $\sin(l\pi z/b)$ on both sides, and integrating along the path $nL\sim(n+1)L$, it is obtained as follows:

$$\sum_{n=-\infty}^{+\infty}B_n^{\mathrm{I}}F_m\left(h_n^{\mathrm{I}}\alpha\right)R_2\left(-k_n,l,b\right)=B_l^{\mathrm{II}}H_m\left(h_l^{\mathrm{II}}a\right)\frac{b}{2}\tag{2.21a}$$

$$\begin{aligned}&\sum_{n=-\infty}^{+\infty}\left[\frac{mk_n}{\alpha\left(h_n^{\mathrm{I}}\right)^2}B_n^{\mathrm{I}}F_m\left(h_n^{\mathrm{I}}\rho\right)-\frac{j\omega\varepsilon_0}{\left(h_n^{\mathrm{I}}\right)^2}A_n^{\mathrm{I}}F_m'\left(h_n^{\mathrm{I}}\rho\right)\right]R_1\left(-k_n,l,b\right)\\&=\frac{-j\omega\varepsilon_0\varepsilon_r}{\left(h_l^{\mathrm{II}}\right)^2}A_l^{\mathrm{II}}G_m'\left(h_l^{\mathrm{II}}\alpha\right)\frac{b}{2}\left(1+\delta_{l0}\right)+\frac{jm}{\alpha\left(h_l^{\mathrm{II}}\right)^2}\frac{l\pi}{b}B_l^{\mathrm{II}}H_m\left(h_l^{\mathrm{II}}\alpha\right)\frac{b}{2}\end{aligned}\tag{2.21b}$$

Equations (2.19) and (2.21) can be simplified into more concise forms as follows:

$$A_n^{\mathrm{I}}=\sum_{l=0}^{+\infty}A_l^{\mathrm{II}}Y_{1,ln}\tag{2.22a}$$

$$B_l^{\mathrm{I}}=\sum_{n=-\infty}^{+\infty}B_n^{\mathrm{II}}Y_{2,ln},\quad l=1,2,3,\ldots\tag{2.22b}$$

$$B_n^{\mathrm{I}}X_{2,n}+A_n^{\mathrm{I}}X_{1,n}=\sum_{l=0}^{+\infty}A_l^{\mathrm{II}}Y_{3,ln}+\sum_{l=1}^{+\infty}B_l^{\mathrm{II}}Y_{4,ln}\tag{2.22c}$$

$$A_l^{\mathrm{II}}X_{3,l}+B_l^{\mathrm{II}}X_{4,l}=\sum_{n=-\infty}^{+\infty}\left(A_n^{\mathrm{I}}Y_{5,ln}+B_n^{\mathrm{I}}Y_{6,ln}\right),\quad l=0,1,2,3,\ldots\tag{2.22d}$$

where

$$Y_{1,ln} = \frac{G_m\left(h_l^{\mathrm{II}}\alpha\right) R_1\left(k_n, l, b\right)}{F_m\left(h_n^{\mathrm{I}}\alpha\right) L} \tag{2.23a}$$

$$Y_{2,ln} = \frac{2F_m\left(h_n^{\mathrm{I}}\alpha\right) R_2\left(-k_n, l, b\right)}{H_m\left(h_l^{\mathrm{II}}a\right) b} \tag{2.23b}$$

$$Y_{3,ln} = \frac{jm}{\alpha\left(h_l^{\mathrm{II}}\right)^2}\left(-\frac{l\pi}{b}\right) G_m\left(h_l^{\mathrm{II}}\rho\right) R_2\left(k_n, l, b\right) \tag{2.23c}$$

$$Y_{4,ln} = j\omega\mu_0\mu_r \frac{1}{\left(h_l^{\mathrm{II}}\right)^2} H_m'\left(h_l^{\mathrm{II}}\rho\right) R_2\left(k_n, l, b\right) \tag{2.23d}$$

$$Y_{5,ln} = -\frac{j\omega\varepsilon_0}{\left(h_n^{\mathrm{I}}\right)^2} F_m'\left(h_n^{\mathrm{I}}\rho\right) R_1\left(-k_n, l, b\right) \tag{2.23e}$$

$$Y_{6,ln} = \frac{mk_n}{\alpha\left(h_n^{\mathrm{I}}\right)^2} F_m\left(h_n^{\mathrm{I}}\rho\right) R_1\left(-k_n, l, b\right) \tag{2.23f}$$

$$X_{1,n} = \frac{mk_n}{\alpha\left(h_n^{\mathrm{I}}\right)^2} F_m\left(h_n^{\mathrm{I}}\alpha\right) L \tag{2.23g}$$

$$X_{2,n} = \frac{j\omega\mu_0}{\left(h_n^{\mathrm{I}}\right)^2} F_m'\left(h_n^{\mathrm{I}}\alpha\right) L \tag{2.23h}$$

$$X_{3,l} = \frac{-j\omega\varepsilon_0\varepsilon_r}{\left(h_l^{\mathrm{II}}\right)^2} G_m'\left(h_l^{\mathrm{II}}\alpha\right) \frac{b}{2}\left(1+\delta_{l0}\right) \tag{2.23i}$$

$$X_{4,l} = \frac{jm}{\alpha\left(h_l^{\mathrm{II}}\right)^2}\frac{l\pi}{b} H_m\left(h_l^{\mathrm{II}}\alpha\right)\frac{b}{2} \tag{2.23j}$$

Eliminating variables A_l^{II} and B_l^{II} in Eq. (2.22), a set of simpler equations will be obtained

$$A_n^{\mathrm{I}} = \sum_{q=-\infty}^{+\infty} A_n^{\mathrm{I}} W_{1,nq} + B_n^{\mathrm{I}} W_{2,nq} \tag{2.24a}$$

$$A_n^{\mathrm{I}} X_{1,n} + B_n^{\mathrm{I}} X_{2,n} = \sum_{q=-\infty}^{+\infty}\left(A_q^{\mathrm{I}} W_{3,nq} + B_q^{\mathrm{I}} W_{4,nq}\right) \tag{2.24b}$$

where the coefficients are

$$W_{1,nq} = \sum_{l=0}^{+\infty} \frac{Y_{5,lq}}{X_{3,l}} Y_{1,ln} \tag{2.25a}$$

$$W_{2,nq} = \sum_{l=0}^{+\infty} \frac{Y_{6,lq} - Y_{2,lq} X_{4,l}}{X_{3,l}} Y_{1,ln} \tag{2.25b}$$

$$W_{3,nq} = \sum_{l=0}^{+\infty} \frac{Y_{5,lq}}{X_{3,l}} Y_{3,ln} \tag{2.25c}$$

$$W_{4,nq} = \sum_{l=0}^{+\infty} \frac{Y_{6,lq} - Y_{2,lq} X_{4,l}}{X_{3,l}} Y_{3,ln} + \sum_{l=1}^{+\infty} Y_{2,lq} Y_{4,ln} \tag{2.25d}$$

In numerical calculation, the high-order components are required to be truncated properly to obtain an equation of finite size and simultaneously to maintain accuracy high enough. A solution from zero determinant of the Eq. (2.24) corresponds to a mode. According to experience, the harmonic index could better be not smaller than 10 to keep a required accuracy.

2.3 Theory of the Electron Cyclotron Maser in Waveguide System

A gyrotron traveling-wave tube (gyro-TWT) employs an interaction circuit with a length of tens of wavelength. It requires huge computational resources to simulate such an oversized circuit based on the particle-in-cell (PIC) method. Furthermore, when a certain kind of disturbance structure is introduced into the circuit or complicate boundary, such as photonic-band-gap structure, the time consumed by full-wave 3D PIC simulation of the interaction circuit becomes unacceptable for engineering consideration. Therefore, it is required to build up an accurate and high efficient method to simulate the waveguide-based ECM system. Based on the foundation provided by the classic interaction theory, namely, the linear theory and nonlinear theory, a general applicable theoretical model based on the concept of partitioning the transverse plane of the circuit is proposed. In the interaction system, a special cylindrical region containing the electron beam is separated from the remaining complicate boundary region, as the Region 1 in Fig. 2.4. The field components of the inner cylindrical region could be expressed by accurate analytical expressions. The boundary region, as the Region 2 in Fig. 2.4, contains disturbance structure introduced to control the wave mode. The Region 2 could be solved by analytical method or by numerical simulation. This general ECM theoretical model is capable of accurately analyzing the instability competition, while maintaining the advantage of efficient simulation. Specifically, a linear theory and a nonlinear theory for ECM system based on dielectric-lined waveguide are also developed.

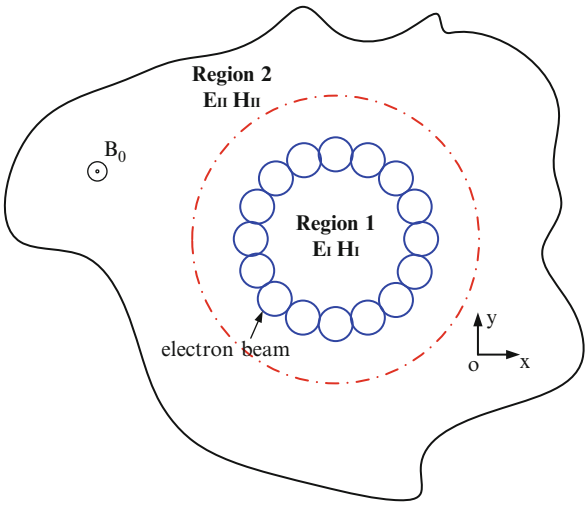

Fig. 2.4 A transverse cross view of a general ECM waveguide system, where partitioning the transverse plane by a virtual cylindrical boundary

2.3.1 Partitioning the Transverse Plane of an ECM System

The theoretical modal for ECM system developed in this section is valid with limitations. It is only valid for ECM system of longitudinal uniformity and considering only TE mode or TE mode-like hybrid mode. Three basic assumptions are made [1, 26]:

- *Single Mode Interaction* The electron beam interacts with a single mode and reaches a steady state in frequency domain.
- *Undisturbed Mode Distribution* The wave mode in the interaction circuit maintains the same transverse distribution as it is in an electron-free waveguide. The beam-wave interaction influences the wave amplitude only.
- *Omitting the Space Charge Effect* The space charge from the electron beam imposes no influence on the beam-wave interaction.

The first assumption is valid due to that when an ECM system reaches a steady state in the frequency domain analysis, the electron beam interacts with a single mode only, and other modes are suppressed. Since the electron beam for a general ECM system is not strong enough to disturb the transverse field distribution, the second assumption is valid. The third assumption is valid due to that the electron beam bunches in phase space only, other than the real space. Hence, the space charge imposes no obvious influence on beam-wave interaction [1, 26]. The above three basic assumptions are helpful for theoretical model simplification.

A general ECM waveguide system includes two elements, the electron cyclotron beam and waveguide mode. An ECM system of longitudinal uniformity, but with arbitrary transverse boundary, is shown in Fig. 2.4. The boundary of Region 1 is

with ideal axis symmetry and totally includes the electron beam, and the other region is identified as Region 2. For a waveguide system, the major field components for a TE mode or a hybrid HE mode, most energy of which is carried by TE mode components [27–29], are given by

$$H_{z\mathrm{I}} = f(z)\psi_{\mathrm{I}}(r,\varphi)\, e^{j\omega t} \tag{2.26a}$$

$$H_{z\mathrm{II}} = f(z)\psi_{\mathrm{II}}(r,\varphi)\, e^{j\omega t} \tag{2.26b}$$

$$\vec{E}_{\perp\mathrm{I}} = f(z)\frac{j\omega\mu}{k_{\mathrm{I}}^2 - k_z^2}\left[\vec{e}_z \times \nabla_\perp \psi_{\mathrm{I}}(r,\varphi)\right] e^{j\omega t} \tag{2.26c}$$

$$\vec{E}_{\perp\mathrm{II}} = f(z)\frac{j\omega\mu}{k_{\mathrm{II}}^2 - k_z^2}\left[\vec{e}_z \times \nabla_\perp \psi_{\mathrm{II}}(r,\varphi)\right] e^{j\omega t} \tag{2.26d}$$

where $f(z)$ is axial amplitude distribution and $\psi_{\mathrm{I}}(r,\varphi)$ and $\psi_{\mathrm{II}}(r,\varphi)$ are the transverse field distribution function in Region 1 and Region 2, respectively. The wave numbers are $k_{\mathrm{I}}^2 = \omega^2\varepsilon_{\mathrm{I}}\mu_{\mathrm{I}}$ and $k_{\mathrm{II}}^2 = \omega^2\varepsilon_{\mathrm{II}}\mu_{\mathrm{II}}$. With Maxwell Equation, we have

$$\left(\nabla_\perp^2 + \frac{\partial^2}{\partial z^2} + k^2\right)\vec{E}_\perp = j\omega\mu\vec{J}_\perp \tag{2.27}$$

With the Second Assumption, *Undisturbed Mode Distribution*, the transverse field component in the interaction system is

$$\nabla_\perp^2 \vec{E}_\perp + \left(k^2 - k_z^2\right)\vec{E}_\perp = 0 \tag{2.28}$$

Substituting Eq. (2.28) into Eq. (2.27), the wave equation with a disturbing current is

$$\left(k_z^2 + \frac{\partial^2}{\partial z^2}\right)\vec{E}_\perp = j\omega\mu\vec{J}_\perp \tag{2.29}$$

In plasma dynamics, the disturbing current $\vec{J}_\perp$ can be described by distribution function. Hence, operating $(\omega/2\pi)\int_0^{2\pi/\omega} \mathrm{d}t \iint_{SI+SII} \cdot \vec{E}_\perp^*/f^*(z)\mathrm{d}S$ on both sides of Eq. (2.29), the beam-wave interaction equation can be deduced as

$$\left(k_z^2 + \frac{d^2}{dz^2}\right) f(z)G = \left(\frac{\omega}{2\pi}\right)\int_0^{2\pi/\omega}\iint_{SI+SII} j\omega\mu\vec{J}_\perp \cdot \frac{\vec{E}_{\perp\mathrm{I}}^*}{f^*(z)}\mathrm{d}S\ \mathrm{d}t \tag{2.30}$$

where SI and SII indicate the transverse areas of Region 1 and Region 2, respectively. The geometry factor is

$$G = \iint_{SI} \left| \frac{j\omega\mu}{k_I^2 - k_z^2} \left[\vec{e}_z \times \nabla_\perp \psi_I (r, \varphi) \right] \right|^2 \mathrm{d}S + \iint_{SII} \left| \frac{j\omega\mu}{k_{II}^2 - k_z^2} \left[\vec{e}_z \times \nabla_\perp \psi_{II} (r, \varphi) \right] \right|^2 \mathrm{d}S \tag{2.31}$$

In real space, the real part of the wave equation with source is

$$\left(k_z^2 + \frac{\partial^2}{\partial z^2} \right) \mathrm{Im} \left(\vec{E}_\perp \right) = \omega\mu \vec{J}_\perp \tag{2.32}$$

Operating $(\omega/2\pi) \int_0^{2\pi/\omega} \mathrm{d}t \iint_{SI+SII} \cdot \vec{E}_\perp^* / f^*(z) \mathrm{d}S$ on both sides of Eq. (2.32), the beam-wave interaction equation in real space is

$$\left(k_z^2 + \frac{d^2}{dz^2} \right) f(z) \frac{G}{2j} = \left(\frac{\omega}{2\pi} \right) \int_0^{2\pi/\omega} \iint_{SI+SII} \omega\mu \vec{J}_\perp \cdot \frac{\vec{E}_{\perp I}^*}{f^*(z)} \mathrm{d}S \ \mathrm{d}t \tag{2.33}$$

Interaction Eqs. (2.30) and (2.33) are the field exciting equations for linear theory and self-consistent nonlinear theory, respectively.

In the general ECM system shown in Fig. 2.4, the transverse field distribution $\psi_I(r, \varphi)$ in the inner region can be decomposed into

$$\psi_I (r, \varphi) = \sum_m \alpha_m J_m (k_{\perp m} r) \, e^{-jm\varphi} \tag{2.34}$$

When the waveguide boundary is very simple, taking cylindrical waveguide as an example, analytical expressions can be applied to describe field components. Otherwise, numerical simulation is applicable to calculate the field distribution. Whatever the case, the above general ECM theoretical model makes integration of electron beam with analytical field expressions in the inner region, and the energy flow is considered by the geometry factor to overcome calculating complicate boundary. Hence, this general ECM theoretical model simultaneously maintains the advantages of efficiency and accuracy.

2.3.2 *The Linear Theory of Dielectric-Lined ECM System*

Generally speaking, modes in a uniform dielectric-loaded waveguide, as shown in Fig. 2.5, are hybrid ones HE_{mn} or EH_{mn}. In a gyro-TWT application, properly designed dielectric-loaded waveguide conveys an operation mode with a TE mode-like energy distribution, and this hybrid mode is quite similar to a pure TE mode in a cylindrical waveguide [17, 25, 28, 29]. According to research experience, an

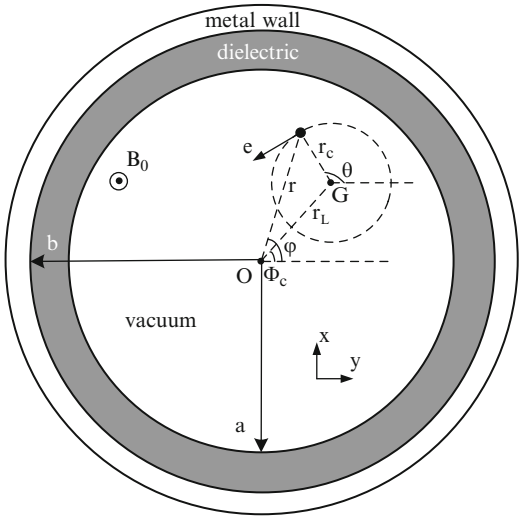

Fig. 2.5 An ECM system based on the dielectric-lined waveguide

ECM system only considers the TE mode components could evaluate the interaction performance with reasonable accuracy [30]. Substituting the field expressions of the TE component of a hybrid mode in dielectric waveguide into Eq. (2.30), it is [31, 32]

$$\left(k_{zc}^2+\frac{d^2}{dz^2}\right)f(z)G_{mn}=-\frac{1}{j\omega\mu f^*(z)}\left(\frac{\omega}{2\pi}\right)\int_0^{2\pi/\omega}\int_0^{r_w}\int_0^{2\pi}\left(\vec{J}_\theta\cdot\vec{E}_\theta^*\right)r\,\mathrm{d}r\,\mathrm{d}\phi\,\mathrm{d}t \tag{2.35}$$

where $\vec{J}_\theta$ is the disturbing current, $\vec{E}_\theta$ is field expression in the guiding center coordinate of the electron beam, the geometry factor is $G_{mn}=K_a+K_b$, and the constants K_a and K_b are

$$K_a=\frac{2\pi}{|k_{\perp1}|^2}\int_0^a\left[\left|J_m'\left(k_{\perp1}r\right)\right|^2+\left|\frac{m}{k_{\perp1}r}J_m\left(k_{\perp1}r\right)\right|^2\right]r\,\mathrm{d}r \tag{2.36a}$$

$$K_b=\frac{2\pi}{|k_{\perp2}|^2}\int_a^b\left[\begin{array}{l}\left|\left[\alpha J_m'\left(k_{\perp2}r\right)+\beta N_m'\left(k_{\perp2}r\right)\right]\right|^2\\+\left|\frac{m}{k_{\perp2}r}\left[\alpha J_m\left(k_{\perp2}r\right)+\beta N_m\left(k_{\perp2}r\right)\right]\right|^2\end{array}\right]r\,\mathrm{d}r \tag{2.36b}$$

From Eq. (2.35), it is found that when the dielectric layer is eliminated, the geometry factor becomes $G_{mn}=K_a$, and Eq. (2.35) returns to a beam-wave interaction equation of a cylindrical waveguide-based ECM system [13, 31–33].

Linearizing the relativistic Vlasov Equation and after Laplace Transform, the beam-wave coupling dispersion relation of the dielectric-loaded ECM system is [31, 34, 35]

$$D_{\text{disp}}(k_z) = \left(k_{zc}^2 - k_z^2\right) G_{mn} - \widehat{S}_1(k_z) = 0 \tag{2.37}$$

and field amplitude is

$$F(z) = \sum_{i=1}^{4} \left[F(0) \frac{\widehat{S}_0(k_{zi}) - j k_{zi} G_{mn}}{j D'_{\text{disp}}(k_{zi})} + F'(0) \frac{G_{mn}}{j D'_{\text{disp}}(k_{zi})} \right] e^{-j k_{zi} z} \tag{2.38}$$

where k_{zc} is the cold propagating constant of the waveguide, and constants $\widehat{S}_1(k_z)$ and $\widehat{S}_0(k_z)$ are respectively

$$\begin{aligned} \widehat{S}_1(k_z) = {} & \frac{4\pi^2 e^2 \mu_1}{k_{\perp 1}^2 m_0} \int_0^{r_w} r_c \mathrm{d}r_c \int_0^{\infty} p_\perp \mathrm{d}p_\perp \int_0^{\infty} \mathrm{d}p_z \frac{f_0}{\gamma} \\ & \times \sum_{s=-\infty}^{\infty} \left[\frac{-\beta_t^2 \left(\omega^2 - k_z^2 c^2\right) H_{sm}}{(\omega - s\Omega - k_z v_z)^2} + \frac{(\omega - k_z v_z) T_{sm} - k_\perp v_t U_{sm}}{(\omega - k_z v_z - s\Omega_e)} \right] \end{aligned} \tag{2.39}$$

$$\begin{aligned} \widehat{S}_0(k_z) = {} & j \frac{4\pi^2 e^2 \mu_1}{k_{\perp 1}^2 m_0} \int_0^{r_w} r_c \mathrm{d}r_c \int_0^{\infty} p_\perp \mathrm{d}p_\perp \int_0^{\infty} \mathrm{d}p_z \frac{f_0}{\gamma} \\ & \times \sum_{s=-\infty}^{\infty} \left[\frac{-k_z v_t^2 H_{sm}}{(\omega - k_z v_z - s\Omega_e)^2} + \frac{v_z T_{sm}}{(\omega - k_z v_z - s\Omega_e)} \right] \end{aligned} \tag{2.40}$$

where f_0 is the electron beam distribution function under undisturbed state

$$f_0 = \frac{I_b}{4\pi^2 e} \sum_{i=1}^{N} \frac{W_i}{r_{ci} v_{zi} p_{ti}} \delta(r_c - r_{ci}) \delta(p_z - p_{zi}) \delta(p_t - p_{ti}) \tag{2.41}$$

where the weight factor of the macro particles is given by $\sum_{i=1}^{N} W_i = 1$. The longitude and transverse normalized velocities are $\beta_z = v_z/c$ and $\beta_\perp = v_\perp/c$. Other expressions are

$$H_{sm}(x, y) = \left| J'_s(x) J_{m-s}(y) \right|^2 \tag{2.42a}$$

$$\begin{aligned} T_{sm}(x, y) = {} & 2H_{sm} + 2\mathrm{Re}\left[x J'_s(x) J''_s(x) \right] |J_{m-s}(y)|^2 - x J'^*_s(x) J_s(x) \\ & \times \left[\tfrac{1}{y} J^*_{m-s}(y) J'_{m-s}(y) + \tfrac{y^*}{y} |J'_{m-s}(y)|^2 + J^*_{m-s}(y) J''_{m-s}(y) \right] \end{aligned} \tag{2.42b}$$

$$U_{sm}(x,y)=\left(-\frac{x}{2}\right)J_s'^{*}(x)\left\{J_{s+1}(x)\left[\frac{y^*}{y}|J_{m-s-1}(y)|^2-|J_{m-s}(y)|^2\right]\right.$$
$$\left.+J_{s-1}(x)\left[\frac{y^*}{y}|J_{m-s+1}(y)|^2-|J_{m-s}(y)|^2\right]\right\} \tag{2.42c}$$

where the variables are $x=k_{\perp 1}r_{\mathrm{L}}$ and $y=k_{\perp 1}r_{\mathrm{c}}$. The linear theory takes into consideration the influence of the dielectric layer loaded to the propagation characteristics and field distribution and is capable of efficiently analyzing the ECM interaction. More details about the derivation of the linear theory are given in Appendix I.

2.3.3 *The Nonlinear Theory of Dielectric-Loaded ECM System*

Similar to the linear theory, the nonlinear theory of the dielectric-loaded waveguide considers a pure TE mode or the TE mode component of a hybrid mode. Substituting the field components into Eq. (2.33), it is obtained as follows:

$$\left(k_z^2+\frac{\mathrm{d}^2}{\mathrm{d}z^2}\right)f(z)=-\frac{2|I_b|}{G_{mn}}\sum_{i=1}^{N}W_i\frac{v_{\theta i}}{v_{zi}}\cdot\left[\frac{1}{k_{\perp 1}}\sum_{s=-\infty}^{\infty}J_s'(k_{\perp 1}r_{\mathrm{L}i})J_{m-s}(k_{\perp 1}r_{c_i})e^{j\Lambda_i}\right]^* \tag{2.43}$$

where the beam current is assumed to be

$$\vec{J}=-\frac{2\pi|I_b|}{\omega}\sum_{i=1}^{N}W_i\frac{1}{r_i}\delta(r-r_i)\,\delta(\varphi-\varphi_i)\delta(t-t_i)\frac{\vec{v}_i}{v_{zi}} \tag{2.44}$$

where the phase distribution is $\Lambda_i=\omega t_i-s\theta_i-(m-s)\phi_{\mathrm{c}i}$ and the weight factor of macro particle follows $\sum_{i=1}^{N}W_i=1$.

Equation (2.43) describes the effect of electron beam exciting EM mode. In order to self-consistently determine the electron beam-wave interaction, it is further necessary to specify the Lorentz Force to drive the electrons,

$$\frac{\mathrm{d}\vec{p}}{\mathrm{d}t}=-e\vec{E}-e\vec{v}\times\left(\vec{B}+\vec{B}_0\right) \tag{2.45}$$

In the guiding center of a cyclotron electron, the differential to time is transformed to differential to displacement via

$$\frac{1}{v_z}\frac{\mathrm{d}}{\mathrm{d}t}\vec{p}=\frac{\mathrm{d}}{\mathrm{d}z}\vec{p}=-P_\theta\frac{\mathrm{d}\theta}{\mathrm{d}z}\vec{e}_{r_{\mathrm{L}}}+\frac{\mathrm{d}}{\mathrm{d}z}P_\theta\vec{e}_\theta+\frac{\mathrm{d}}{\mathrm{d}z}P_z\vec{e}_z \tag{2.46}$$

The force acting on an electron includes EM force $\vec{F}$ and static magnetic force $\vec{R}$

$$\vec{F} + \vec{R} = \left(-e\vec{E} - e\vec{v} \times \vec{B}\right) - e\vec{v} \times \vec{B}_{\text{ext}} \tag{2.47}$$

The components of the EM force $\vec{F}$ are

$$F_{r_\text{L}} = -eE_{r_\text{L}} - e\left(v_\theta B_z - v_z B_\theta\right) \tag{2.48a}$$

$$F_\theta = -eE_\theta - ev_z B_{r_\text{L}} \tag{2.48b}$$

$$F_z = ev_\theta B_{r_\text{L}} \tag{2.48c}$$

The components of the static force $\vec{R}$ are

$$R_{r_\text{L}} = -eB_0 v_\theta + \text{ge}v_z B_0 r_\text{c} \sin\left(\theta - \phi_\text{c}\right) \tag{2.49a}$$

$$R_\theta = \text{ge}B_0 r_\text{L} v_z + \text{ge}v_z B_0 r_\text{c} \cos\left(\theta - \phi_\text{c}\right) \tag{2.49b}$$

$$R_z = -\text{ge}B_0 r_\text{L} v_\theta - \text{ge}v_\theta B_0 r_\text{c} \cos\left(\theta - \phi_\text{c}\right) \tag{2.49c}$$

where E_{r_L}, E_θ, B_θ, B_{r_L}, and B_z are the relevant field components in guiding center coordinate [1, 32]. Finally, the components of the Lorentz Force are

$$\frac{\text{d}}{\text{d}z} P_z = \frac{1}{v_z}\left(F_z + R_z\right) \tag{2.50a}$$

$$\frac{\text{d}}{\text{d}z} P_\theta = \frac{1}{v_z}\left(F_\theta + R_\theta\right) \tag{2.50b}$$

$$P_\theta \frac{\text{d}\theta}{\text{d}z} = -\frac{1}{v_z}\left(F_{r_\text{L}} + R_{r_\text{L}}\right) \tag{2.50c}$$

Other than the momentum components of an electron, the position of each particle is also needed to be determined. A transformation between the global coordinate and the guiding center coordinate is

$$re^{j\phi} = r_\text{L} e^{j\theta} + r_\text{c} e^{j\phi_\text{c}} \tag{2.51}$$

Differential to above equation generates

$$\frac{\mathrm{d}r_c}{\mathrm{d}z} = \left(\frac{1}{eB_0}p_\theta\frac{\mathrm{d}\theta}{\mathrm{d}z} - \frac{p_\theta}{p_z}\right)\sin(\theta-\phi_\mathrm{c}) - \left(\frac{1}{eB_0}\frac{\mathrm{d}p_\theta}{\mathrm{d}z} - \frac{p_\theta}{eB_0^2}\frac{\mathrm{d}B_0}{\mathrm{d}z}\right)\cos(\theta-\phi_\mathrm{c}) \tag{2.52a}$$

$$r_\mathrm{c}\frac{\mathrm{d}\phi_\mathrm{c}}{\mathrm{d}z} = \left(\frac{p_\theta}{p_z} - \frac{1}{eB_0}p_\theta\frac{\mathrm{d}\theta}{\mathrm{d}z}\right)\cos(\theta-\phi_\mathrm{c}) - \left(\frac{1}{eB_0}\frac{\mathrm{d}p_\theta}{\mathrm{d}z} - \frac{p_\theta}{eB_0^2}\frac{\mathrm{d}B_0}{\mathrm{d}z}\right)\sin(\theta-\phi_\mathrm{c}) \tag{2.52b}$$

The transformation between the time and space is

$$\frac{\mathrm{d}t}{\mathrm{d}z} = \frac{1}{v_z} \tag{2.52c}$$

In this frequency domain theory, the electron cyclotron beam is modeled by macro particles. The wave exciting equation (Eq. (2.43)) evaluates the overall contributions from the macro particles to the wave, and the state of each macro particles will be determined by the particle motion equations (Eqs. (2.50) and (2.52)). Hence, if the electron beam is modeled by N macro particles, there are $6N+1$ equations to describe the whole ECM system. The wave exciting equation (Eq. (2.43)) and together with the particle motion equations (Eqs. (2.50) and (2.52)) constitutes the complete nonlinear theory in dielectric-loaded waveguide.

2.3.4 Basic Concepts

2.3.4.1 Frequency Domain Steady State

Under a set of given operating parameters, an ECM system reaches a steady-state generating radiation at a specified wave frequency. The typical characteristic of a frequency domain steady state is a fixed longitudinal field amplitude distribution of the EM field in the interaction circuit. Theoretically, the frequency domain analysis indicates investigating all possible steady states of an ECM system to study the system performance. Actually, only the typical states need to be specified, such as the start-oscillation state, the linear amplification, the saturated states, and so on. Two major states attract attention in a gyro-TWT, namely, self-exiting oscillation and steady amplification [1]. An absolute instability is an inherent factor leading to

a self-exciting oscillation. Regenerate amplification induced by circuit discontinuity or reflection from either end of the circuit might be another factor that leads to oscillation. Steady amplification means the input power is amplified and grows along the beam moving direction in the circuit based on convective instability, and the output power will be turned off once the input power is switched off, which is also called zero-drive stability.

2.3.4.2 Instability Threshold

If the beam-wave coupling reaches a certain strength level, the ECM system turns into a state of self-exciting oscillation, and the threshold parameters of switching on this oscillation are assigned as instability thresholds. The operating parameters of a gyro-TWT are required to be below the thresholds of all potential oscillations, as a way to avoid self-exciting oscillation and to realize zero-drive stability.

The ECM system of a gyro-TWT is a semi-opening system, transverse of which is closed by waveguide wall, or with certain lossy structures, and both upstream port and downstream port exchange energy with external. Such a system may be stable under different states according to operation parameters and boundary conditions. Hence, no matter linear theory or nonlinear theory, the boundary conditions to determining both self-exciting oscillation and amplification analysis are the same. Other than the EM field boundary condition, the electron beam also could be treated as a kind of external power injected into the circuit to determine the system state.

2.3.4.3 The Weight Factor

For an ECM system, an electron beam injects into the upstream port and exits from the downstream port. The input state of the electron beam is determined by the distribution functions in Eqs. (2.41) or (2.44). The weight factor is applied to build electron beam with certain parameter distribution,

$$\sum_{i=1}^{N} W_i = A \sum_{i=1}^{N} \exp\left[\frac{-(C_i - C_0)^2}{2(\Delta C_0)^2}\right] = 1 \tag{2.53}$$

where N is the macro particle number; A is the normalized factor; C_0, ΔC_0, and C_i are the average value, variance value, and specified value of each macro particle; and this value C can be assigned to model the velocity or position distribution of the electron beam. The state for each macro particle is determined self-consistently by the interaction integration along the circuit.

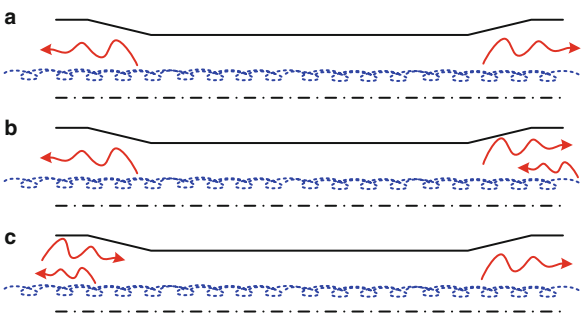

Fig. 2.6 (**a**) Outgoing wave boundary condition and (**b**) reflection oscillation boundary condition of oscillations, and (**c**) amplification boundary condition

2.3.4.4 The Boundary Condition

There are possibly multistates of an ECM system for given parameters, and each state corresponds to specific EM field boundary conditions on both ports [12]. The EM field can be described by Eq. (2.26), and its axial complex amplitude $f(z)$ can be decomposed into a sum of forward-wave component and a backward-wave component as

$$f(z) = f_+ e^{-ik_z z} + f_- e^{ik_z z} \tag{2.54a}$$

$$f'(z) = -ik_z f_+ e^{-ik_z z} + ik_z f_- e^{ik_z z} \tag{2.54b}$$

When an ECM system of length L is in a self-exciting state without external disturbance, the EM fields on both ports are outgoing waves, called outgoing wave boundary condition, as indicated by Fig. 2.6a

$$f(0) = f_-, f'(0) = ik_z f_- \quad \text{(Upstream port)} \tag{2.55a}$$

$$f(L) = f_+ e^{-ik_z L}, f'(L) = -ik_z f_+ e^{-ik_z L} \quad \text{(Downstream port)} \tag{2.55b}$$

When an ECM system is in a self-exciting state induced by the reflection $|\Gamma_L| e^{i\varphi_L}$ at the output port, without any disturbance from the upstream port, called reflection oscillation boundary condition, as shown in Fig. 2.6b

$$f(0) = f_-, f'(0) = ik_z f_- \quad \text{(Upstream port)} \tag{2.56a}$$

$$f(L) = f_+ e^{-ik_z L} \left(1 + |\Gamma_L| e^{i\varphi_L}\right), \quad \text{(Downstream port)} \tag{2.56b}$$

$$f'(L) = -ik_z f_+ e^{-ik_z L} \left(1 - |\Gamma_L| e^{i\varphi_L}\right) \quad \text{(Downstream port)} \tag{2.56c}$$

When an ECM system is in an ideal amplification state, at the upstream port, other than the driving power, there is also a backward wave due to certain factors, such as circuit discontinuity. While the downstream port is an ideal outgoing wave, called amplification boundary condition, as given in Fig. 2.6c

$$f(0) = f_+ \left(1 + |\Gamma_0| \, e^{i\varphi_0}\right) \quad \text{(Upstream port)} \tag{2.57a}$$

$$f'(0) = -ik_z f_+ \left(1 - |\Gamma_0| \, e^{i\varphi_0}\right) \quad \text{(Downstream port)} \tag{2.57b}$$

$$f(L) = f_+ e^{-ik_z L}, \, f'(L) = -ik_z f_+ e^{-ik_z L} \quad \text{(Downstream port)} \tag{2.57c}$$

2.4 Summary

The theories of uniform and periodic dielectric-loaded waveguides are reviewed first. And then a general applicable theoretical model for ECM waveguide system is proposed, which is based on partitioning the transverse plane of the interaction circuit. Finally, linear theory and nonlinear theory of the ECM system based on dielectric-loaded waveguide is developed. The theory of dielectric-loaded ECM system is based on a TE mode approximation, which is omitting the TM mode component of a hybrid mode. When the dielectric layer is negligibly thin, the theory returns to that of the ECM based on simple cylindrical waveguide, and to some extent, the theory is verified. In the last section, some fundamental concept for gyro-TWT research is clarified. By the way, although various kinds of nonlinear theories are developed for specified gyro-devices, the linear theory is still one of the most efficient theoretical solutions to estimate the preliminary characteristics of a gyro-TWT.

Appendix I: Derivation of the Linear Theory in Dielectric-Lined Waveguide

A cross view of the dielectric-lined waveguide is again displayed in Fig. A1.1. In order to better understand the linear theory, the detailed derivation of the linear theory is introduced here [1, 34, 35]. We rewrite the Eq. (2.35) in this chapter here,

$$\left(k_{zc}^2 + \frac{d^2}{dz^2}\right) f(z) G_{mn} = -\frac{1}{j\omega\mu f^*(z)} \left(\frac{\omega}{2\pi}\right) \int_0^{2\pi/\omega} \int_0^{r_w} \int_0^{2\pi} \left(\vec{J}_\theta \cdot \vec{E}_\theta^*\right) r \, \mathrm{d}r \, \mathrm{d}\phi \, \mathrm{d}t \tag{A1.1}$$

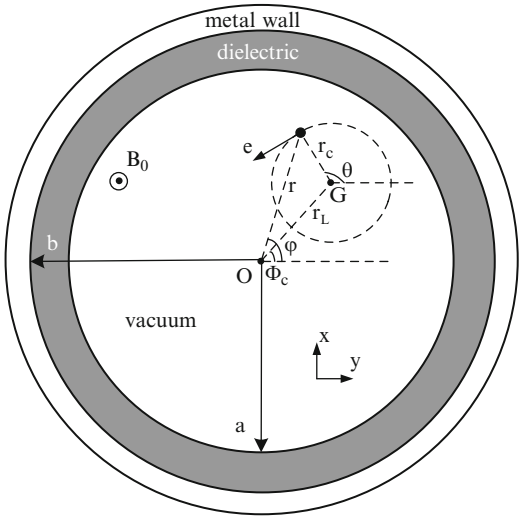

Fig. A1.1 The transverse view of the ECM system

where $\vec{E}_\theta$ is field expression in the guiding center coordinate (GCC) of the electron beam, $\vec{J}_\theta$ is the transverse beam current. In order to get the dispersion relation, we first need to obtain the express of the right side of Eq. A1.1. The following derivation includes three parts: the field expression in GCC, the perturbed current, and the Laplace transformation.

1. The Field Expression in GCC

Generally speaking, a wave in dielectric-lined waveguide exists in a hybrid mode. But what we are interested are those TE_{mn}-like modes. Hence, the following derivation is mainly devoted to deal with the TE components of the wave modes. In the waveguide cylindrical coordinate, The z component of a mode in the vacuum region is given by

$$H_z = f(z) J_m (k_{\perp 1} r)\, e^{j(\omega t - m\phi)} \tag{A1.2}$$

where the field amplitude is actually a combination of a forward-wave component and backward-wave component, as $f(z) = f_+(z)e^{-jk_z z} + f_-(z)e^{jk_z z}$. The transverse field components are given by

$$E_\perp = \frac{1}{k_\perp^2} j\omega\mu \vec{e}_z \times \nabla_\perp H_z \tag{A1.3}$$

$$H_\perp = \frac{1}{k_\perp^2} \frac{\partial}{\partial z} \nabla_\perp H_z \tag{A1.4}$$

By applying the Bessel function summation theorem [13], the z component of a mode in the waveguide cylindrical coordinate can be directly changed into GCC expression, as given by

$$H_z = f(z) \sum_{s=-\infty}^{\infty} J_s\left(k_{\perp 1} r_{\mathrm{L}}\right) J_{m-s}\left(k_{\perp 1} r_{\mathrm{c}}\right) e^{j\omega t - js\theta - j(m-s)\phi_{\mathrm{c}}} \tag{A1.5}$$

In the GCC, the operator $\nabla_{\perp}$ is

$$\nabla_{\perp} = \vec{e}_{r_{\mathrm{L}}} \frac{\partial}{\partial r} + \vec{e}_{\theta} \frac{1}{r_{\mathrm{L}}} \frac{\partial}{\partial \theta} \tag{A1.6}$$

Substituting the $\nabla_{\perp}$ and Eq. (A1.5) into the Eq. (A1.3) and Eq. (A1.4), the transverse field expressions in the GCC system are obtained,

$$E_{r_{\mathrm{L}}} = -\frac{\omega\mu}{k_{\perp}^2 r_{\mathrm{L}}} f(z) \sum_{s=-\infty}^{\infty} s J_s\left(k_{\perp 1} r_{\mathrm{L}}\right) J_{m-s}\left(k_{\perp 1} r_{\mathrm{c}}\right) e^{j\omega t - js\theta - j(m-s)\phi_{\mathrm{c}}} \tag{A1.7}$$

$$E_{\theta} = \frac{j\omega\mu}{k_{\perp}} f(z) \sum_{s=-\infty}^{\infty} J_s'\left(k_{\perp 1} r_{\mathrm{L}}\right) J_{m-s}\left(k_{\perp 1} r_{\mathrm{c}}\right) e^{j\omega t - js\theta - j(m-s)\phi_{\mathrm{c}}} \tag{A1.8}$$

$$H_{r_{\mathrm{L}}} = \frac{1}{k_{\perp}} f'(z) \sum_{s=-\infty}^{\infty} J_s'\left(k_{\perp 1} r_{\mathrm{L}}\right) J_{m-s}\left(k_{\perp 1} r_{\mathrm{c}}\right) e^{j\omega t - js\theta - j(m-s)\phi_{\mathrm{c}}} \tag{A1.9}$$

$$H_{\theta} = -\frac{j}{k_{\perp}^2 r_{\mathrm{L}}} f'(z) \sum_{s=-\infty}^{\infty} s J_s\left(k_{\perp 1} r_{\mathrm{L}}\right) J_{m-s}\left(k_{\perp 1} r_{\mathrm{c}}\right) e^{j\omega t - js\theta - j(m-s)\phi_{\mathrm{c}}} \tag{A1.10}$$

The dielectric loss makes the longitudinal wave number k_z, as well as $k_{\perp 1}$ and $k_{\perp 2}$, turn out to be complex numbers. Only the real parts of the field components are valid to describe the field distribution. The wave components in the dielectric region will not be used in the beam-wave interaction integration, hence the field components in the dielectric region is not necessary to transform into the GCC expressions.

2. The Transverse Perturbed Beam Current

Under the perturbation condition, the electron beam current $\vec{J}$ contains a DC current $\vec{J}_0$ and a perturbed current $\vec{j}$, as $\vec{J} = \vec{J}_0 + \vec{j}$. The beam current $\vec{J}$ can be described by the distribution function $f\left(\vec{x}, \vec{p}\right)$ in the phase space phase space $\langle \vec{x}, \vec{p} \rangle$.

Correspondingly, the electron distribution function $f\left(\vec{x},\vec{p}\right)$ is assumes as a linear combination of the equilibrium state $f_0\left(\vec{x},\vec{p}\right)$ and the perturbed state $f_1\left(\vec{x},\vec{p}\right)$, as $f=f_0+f_1$. The relation between the perturbed current $\vec{j}$ and the perturbed state $f_1\left(\vec{x},\vec{p}\right)$ is

$$\vec{j}=-e\int f_1\vec{v}d^3p \tag{A1.11}$$

where $-e$ indicates the charge of an electron, $\vec{v}$ indicates the velocities of the electrons. The electron dynamics follows the relativistic Vlasov Equation,

$$\frac{\mathrm{d}}{\mathrm{d}t}f=\frac{\partial}{\partial t}f+\frac{\partial}{\partial t}\vec{x}\cdot\frac{\partial}{\partial\vec{x}}f+\frac{\partial}{\partial t}\vec{p}\cdot\frac{\partial}{\partial\vec{p}}f=0 \tag{A1.12}$$

where $\frac{\partial}{\partial t}\vec{x}=\vec{v}$ and $\frac{\partial}{\partial t}\vec{p}=-e\left[\vec{E}+\vec{v}\times\left(\vec{B}+B_0\vec{e}_z\right)\right]$. The $\vec{E}$ and $\vec{B}$ indicate the electric field and magnetic field of the EM wave, and $B_0\vec{e}_z$ indicates the background static magnetic field. The linear theory assumes that the wave field is under such a weak strength that it only brings perturbation influence to the distribution function, which makes the equilibrium distribution function still meet the equation,

$$\frac{\mathrm{d}}{\mathrm{d}t}f_0=\frac{\partial}{\partial t}f_0+\vec{v}\cdot\frac{\partial}{\partial\vec{x}}f_0-e\left(\vec{v}\times B_0\vec{e}_z\right)\cdot\frac{\partial}{\partial\vec{p}}f_0=0 \tag{A1.13}$$

Substituting Eq. (A1.13) back into Eq. (A1.12), the differential perturbed state is obtained,

$$\frac{\mathrm{d}}{\mathrm{d}t}f_1=e\left[\vec{E}+\vec{v}\times\vec{B}\right]\cdot\frac{\partial}{\partial\vec{p}}f_0 \tag{A1.14}$$

where the right hand side (RHS) omits a higher order term $e\left[\vec{E}+\vec{v}\times\vec{B}\right]\cdot\frac{\partial}{\partial\vec{p}}f_1$, and the last term is given by,

$$\begin{aligned}\frac{\partial}{\partial\vec{p}}f_0&=\frac{\partial f_0}{\partial p_\perp}\vec{e}_\theta-\frac{1}{p_\perp}\frac{\partial f_0}{\partial\theta}\vec{e}_{r_\mathrm{L}}+\frac{\partial}{\partial p_z}\vec{e}_z\\&=\left[\frac{\partial f_0\left(r_\mathrm{c},p_\perp,p_z\right)}{\partial p_\perp}-\frac{\partial f_0\left(r_\mathrm{c},p_\perp,p_z\right)}{\partial r_\mathrm{c}}\frac{e^{i(\phi_\mathrm{c}-\theta)}+e^{-i(\phi_\mathrm{c}-\theta)}}{2eB}\right]\vec{e}_\theta\\&\quad+\left[\frac{1}{p_\perp}\frac{\partial f_0\left(r_\mathrm{c},p_\perp,p_z\right)}{\partial r_\mathrm{c}}r_\mathrm{L}\frac{e^{i(\phi_\mathrm{c}-\theta)}-e^{-i(\phi_\mathrm{c}-\theta)}}{2i}\right]\vec{e}_{r_\mathrm{L}}+\frac{\partial f_0\left(r_\mathrm{c},p_\perp,p_z\right)}{\partial p_z}\vec{e}_z\end{aligned} \tag{A1.15}$$

The Eq. (A1.14) further becomes,

$$\begin{aligned}\frac{\mathrm{d}}{\mathrm{d}t}f_1 &= e\left[E+\vec{v}\times B\right]\cdot\frac{\partial}{\partial\vec{p}}f_0 \\ &= F_\theta\left[\frac{\partial f_0}{\partial p_\perp}-\frac{\partial f_0}{\partial r_\mathrm{c}}\frac{e^{i(\phi_\mathrm{c}-\theta)}+e^{-i(\phi_\mathrm{c}-\theta)}}{2eB}\right] \\ &\quad + F_{r_\mathrm{L}}\left[\frac{r_\mathrm{L}}{p_\perp}\frac{\partial f_0}{\partial r_\mathrm{c}}\frac{e^{i(\phi_\mathrm{c}-\theta)}-e^{-i(\phi_\mathrm{c}-\theta)}}{2i}\right]+F_z\frac{\partial f_0}{\partial p_z}\end{aligned} \tag{A1.16}$$

where the perturbing forces from the EM wave are,

$$F_{r_\mathrm{L}} = eE_{r_\mathrm{L}}+\frac{e\mu}{\gamma m_0}\left(H_z p_t - H_\theta p_z\right) \tag{A1.17}$$

$$F_\theta = \frac{e\mu}{\gamma m_0}p_z H_{r_\mathrm{L}}+eE_\theta \tag{A1.18}$$

$$F_z = -\frac{e\mu}{\gamma m_0}p_t H_{r_\mathrm{L}} \tag{A1.19}$$

Substituting Eqs. (A1.5), (A1.6), (A1.7), (A1.8), (A1.9), and (A1.10) into Eq. (A1.16), the explicit description of the differential perturbed state is rewritten as,

$$\frac{\mathrm{d}}{\mathrm{d}t}f_1 = \sum_{s=-\infty}^{\infty}\Re_s(z)\mathrm{e}^{j\Lambda_s} \tag{A1.20}$$

where the phase factor is $\Lambda_s = \omega t-(m-s)\phi_\mathrm{c}-s\theta$, and $\Re_s(z)$ is

$$\begin{aligned}\Re_s(z) &= \frac{e\mu}{k_\perp}\frac{\partial f_0}{\partial p_\perp}\left[\frac{p_z}{\gamma m_0}f'(z)+j\omega f(z)\right]J_s'\left(k_\perp r_\mathrm{L}\right)J_{m-s}\left(k_\perp r_\mathrm{c}\right) \\ &\quad -\frac{e\mu p_t}{\gamma m_0 k_\perp}\frac{\partial f_0}{\partial p_z}f'(z)J_s'\left(k_\perp r_\mathrm{L}\right)J_{m-s}\left(k_\perp r_\mathrm{c}\right) \\ &\quad -\frac{\mu}{B_0 k_\perp}\frac{\partial f_0}{\partial r_\mathrm{c}}\left[\frac{p_z}{\gamma m_0}f'(z)+j\omega f(z)\right]J_s\left(k_\perp r_\mathrm{L}\right)J_{m-s}'\left(k_\perp r_\mathrm{c}\right) \\ &\quad +j\frac{1}{2}\frac{e\mu r_\mathrm{L}}{\gamma m_0}f(z)\frac{\partial f_0}{\partial r_\mathrm{c}}\left[\begin{array}{l}J_{s+1}\left(k_\perp r_\mathrm{L}\right)J_{m-s-1}\left(k_\perp r_\mathrm{c}\right) \\ -J_{s-1}\left(k_\perp r_\mathrm{L}\right)J_{m-s+1}\left(k_\perp r_\mathrm{c}\right)\end{array}\right]\end{aligned} \tag{A1.21}$$

It is reminded that the $f(z)$ in the Eq. (A1.21) indicates the EM wave amplitude.

A technique called Undisturbed Integration is used to calculate the perturbed state f_1 from Eq. (A1.20), which means integrating along the electron undisturbed orbit $0\sim(t,\phi_\mathrm{c},\theta)$ [26, 31, 34, 36]. The integration path $(t',\phi_\mathrm{c}',\theta')$ is defined as,

$$t' = t + \left(z' - z\right)/v_z, \phi_c' = \phi_c, \theta' = \theta + \Omega_e\left(z' - z\right)/v_z \tag{A1.22}$$

The perturbed state is given by

$$f_1 = \int_0^t \mathrm{d}t' \sum_{s=-\infty}^{\infty} \Re_s\left(z'\right) e^{j\Lambda_s'} = \sum_{s=-\infty}^{\infty} e^{j\Lambda_s} \int_0^z T_s\left(z - z'\right) \Re_s\left(z'\right) \mathrm{d}z' \tag{A1.23}$$

where $T_s\left(z - z'\right) = e^{-j\left[\omega(z-z')/v_z - s\Omega_e(z-z')/v_z\right]}/v_z$. Now, substituting the Eq. (A1.23) into Eq. (A1.11), the perturbed current $\vec{j}$ is obtained. And then substituting the beam current $\vec{J} = \vec{J}_0 + \vec{j}$ into the interaction equation (Eq. (A1.1)), the DC current makes no contribution to interaction, $\int \vec{J}_0 \cdot \vec{E}^* \mathrm{d}t = 0$. As a result, the beam-wave integration in Eq. (A1.1) considers the perturbed current $\vec{j}$ only.

3. The Laplace Transformation

Following last section, substituting the perturbed current $\vec{j}$ in Eq. (A1.11) into Eq. (A1.1), it is obtained that

$$\left(k_{zc}^2 + \frac{d^2}{dz^2}\right) f(z) G_{mn} = S(z) \tag{A1.24}$$

where

$$S(z) = -\frac{e\omega}{2\pi k_{\perp 1}^2} \int_0^{2\pi/\omega} \mathrm{d}t \int_0^{r_w} r_c \mathrm{d}r_c \int_0^{2\pi} \mathrm{d}\phi_c \int_0^{\infty} p_\perp \mathrm{d}p_\perp \int_0^{2\pi} \mathrm{d}\theta \int_0^{\infty} \mathrm{d}p_z$$
$$\cdot v_t \cdot \left(\sum_{q=-\infty}^{\infty} k_{\perp 1} J_q'\left(k_\perp r_L\right) J_{m-q}\left(k_\perp r_c\right) \mathrm{e}^{j\Lambda_q}\right)^* \cdot \sum_{s=-\infty}^{\infty} \left(\mathrm{e}^{j\Lambda_s} \int_0^z T_s\left(z - z'\right) \Re_s\left(z'\right) \mathrm{d}z'\right) \tag{A1. 25a}$$

The above equation related to integro-differential operation to $f(z)$ can be solved in the wave number space k_z by applying the Laplace Transformation, and we get,

$$G_{mn}\left[\left(k_{zc}^2 - k_z^2\right)\widehat{F}\left(k_z\right) + jk_z f(0) - f'(0)\right] = \widehat{S}\left(k_z\right) \tag{A1.25b}$$

where $\widehat{F}\left(k_z\right) = \ell\left\{f(z)\right\} = \int_0^{\infty} \mathrm{d}z\, e^{jk_z z} f(z)$, and $\ell\left\{\frac{d^2}{dz^2} f(z)\right\} = -k_z^2 \widehat{F}\left(k_z\right) + jk_z f(0) - f'(0)$.

The RHS of Eq. (A1.25) is expressed as,

$$\begin{aligned}\widehat{S}\left(k_z\right) &= \ell\left\{S(z)\right\} \\ &= -\tfrac{e\omega}{2\pi k_{\perp 1}^2}\int_0^{2\pi/\omega}\mathrm{d}t\int_0^{r_\mathrm{w}} r_\mathrm{c}\mathrm{d}r_c\int_0^{2\pi}\mathrm{d}\phi_\mathrm{c}\int_0^{\infty} p_\perp \mathrm{d}p_\perp\int_0^{2\pi}\mathrm{d}\theta\int_0^{\infty}\mathrm{d}p_z \\ &\cdot v_t\left(\sum_{q=-\infty}^{\infty} k_{\perp 1}J_q'\left(k_{\perp 1}r_\mathrm{L}\right)J_{m-q}\left(k_{\perp 1}r_\mathrm{c}\right)e^{j\Lambda_q}\right)^*\sum_{s=-\infty}^{\infty} e^{j\Lambda_s}\widehat{T}\left(k_z\right)\widehat{\Re}_s\left(k_z\right)\end{aligned} \tag{A1.26}$$

where the integration related to $\sum_{q=-\infty}^{\infty} e^{-j\Lambda_q}\cdot\sum_{s=-\infty}^{\infty} e^{j\Lambda_s}$ is nonzero only the term $q=s$, as a result, it is

$$\left(\frac{\omega}{2\pi}\right)\int_0^{2\pi/\omega}\mathrm{d}t\int_0^{2\pi}\mathrm{d}\phi_\mathrm{c}\int_0^{2\pi}\mathrm{d}\theta\sum_{q=-\infty}^{\infty}\sum_{s=-\infty}^{\infty} e^{-j\Lambda_q}e^{j\Lambda_s} = 4\pi^2 \tag{A1.27}$$

the other terms in Eq. (A1.26) are given by,

$$\widehat{T}\left(k_z\right) = \int_0^{\infty}\mathrm{d}z\, e^{jk_z z}T_s(z) = \frac{-j}{\omega - k_z v_z - s\Omega_\mathrm{e}} \tag{A1.28}$$

$$\widehat{\Re}_s\left(k_z\right) = \int_0^{\infty}\mathrm{d}z\, e^{jk_z z}\Re_s(z) = \widehat{\Re}_{s1}\left(k_z\right)\widehat{F}\left(k_z\right) + \widehat{\Re}_{s0}\left(k_z\right)f(0) \tag{A1.29}$$

where,

$$\begin{aligned}\widehat{\Re}_{s1}\left(k_z\right) = {} & j\tfrac{e\mu}{k_{\perp 1}}J_s'\left(k_{\perp 1}r_\mathrm{L}\right)J_{m-s}\left(k_{\perp 1}r_\mathrm{c}\right)\left[\left(\omega - k_z\tfrac{p_z}{\gamma m_0}\right)\tfrac{\partial f_0}{\partial p_\perp} + k_z\tfrac{p_t}{\gamma m_0}\tfrac{\partial f_0}{\partial p_z}\right] \\ & - j\tfrac{\mu}{B_0 k_{\perp 1}}J_s\left(k_{\perp 1}r_\mathrm{L}\right)J_{m-s}'\left(k_{\perp 1}r_\mathrm{c}\right)\left(\omega - k_z\tfrac{p_z}{\gamma m_0}\right)\tfrac{\partial f_0}{\partial r_\mathrm{c}} \\ & + j\tfrac{1}{2}\tfrac{e\mu r_\mathrm{L}}{\gamma m_0}\left[\begin{array}{l} J_{s+1}\left(k_{\perp 1}r_\mathrm{L}\right)J_{m-s-1}\left(k_{\perp 1}r_\mathrm{c}\right) \\ -J_{s-1}\left(k_{\perp 1}r_\mathrm{L}\right)J_{m-s+1}\left(k_{\perp 1}r_\mathrm{c}\right)\end{array}\right]\tfrac{\partial f_0}{\partial r_\mathrm{c}}\end{aligned} \tag{A1.30}$$

$$\begin{aligned}\widehat{\Re}_{s0}\left(k_z\right) = {} & -\tfrac{e\mu}{k_{\perp 1}}J_s'\left(k_{\perp 1}r_\mathrm{L}\right)J_{m-s}\left(k_{\perp 1}r_\mathrm{c}\right)\tfrac{p_z}{\gamma m_0}\tfrac{\partial f_0}{\partial p_\perp} \\ & + \tfrac{e\mu}{k_{\perp 1}}J_s'\left(k_{\perp 1}r_\mathrm{L}\right)J_{m-s}\left(k_{\perp 1}r_\mathrm{c}\right)\tfrac{p_t}{\gamma m_0}\tfrac{\partial f_0}{\partial p_z} \\ & + \tfrac{\mu}{B_0 k_{\perp 1}}J_s\left(k_{\perp 1}r_\mathrm{L}\right)J_{m-s}'\left(k_{\perp 1}r_\mathrm{c}\right)\tfrac{p_z}{\gamma m_0}\tfrac{\partial f_0}{\partial r_\mathrm{c}}\end{aligned} \tag{A1.31}$$

Substituting expressions from Eqs. (A1.25), (A1.26), (A1.27), (A1.28), (A1.29), (A1.30), and (A1.31) into the wave equation in k_z space Eq. (A1.25b), and applying

the integration by parts to eliminate the differential terms related the equilibrium distribution function, $\partial f_0/\partial p_\perp$, $\partial f_0/\partial p_z$, and $\partial f_0/\partial r_c$ [34], the simplified wave equation in $\vec{k}_z$ space is given by,

$$G_{mn}\left[\left(k_{zc}^2 - k_z^2\right)\widehat{F}\left(k_z\right) + jk_z f(0) - f'(0)\right] = \widehat{S}_1\left(k_z\right)\widehat{F}\left(k_z\right) + \widehat{S}_0\left(k_z\right) f(0) \tag{A1.32}$$

where

$$\widehat{S}_1\left(k_z\right) = \frac{4\pi^2 e^2 \mu_1}{m_0 |k_\perp|^2} \int_0^{r_w} r_c \, \mathrm{d}r_c \int_0^\infty p_\perp \, \mathrm{d}p_\perp \int_0^\infty \mathrm{d}p_z \frac{f_0}{\gamma} \times \sum_{s=-\infty}^{\infty} \left[\frac{-\beta_t^2\left(\omega^2 - k_z^2 c^2\right) H_{sm}}{\left(\omega - s\Omega - k_z v_z\right)^2} + \frac{\left(\omega - k_z v_z\right) T_{sm} - k_\perp v_t U_{sm}}{\left(\omega - k_z v_z - s\Omega_e\right)}\right] \tag{A1.33}$$

$$\widehat{S}_0\left(k_z\right) = j\frac{4\pi^2 e^2 \mu}{m_0 |k_\perp|^2} \int_0^{r_w} r_c \, \mathrm{d}r_c \int_0^\infty p_\perp \, \mathrm{d}p_\perp \int_0^\infty \mathrm{d}p_z \frac{f_0}{\gamma} \times \sum_{s=-\infty}^{\infty} \left[\frac{-k_z v_t^2 H_{sm}}{\left(\omega - k_z v_z - s\Omega_e\right)^2} + \frac{v_z T_{sm}}{\left(\omega - k_z v_z - s\Omega_e\right)}\right] \tag{A1.34}$$

where the constant terms are given by,

$$H_{sm}(x, y) = \left|J_s'(x) J_{m-s}(y)\right|^2 \tag{A1.35}$$

$$T_{sm}(x, y) = 2H_{sm} + 2\mathrm{Re}\left[x J_s'(x) J_s''(x)\right] |J_{m-s}(y)|^2 - x J_s'^*(x) J_s(x) \left[\begin{array}{l} \frac{1}{y} J_{m-s}^*(y) J_{m-s}'(y) \\ + \frac{y^*}{y} |J_{m-s}'(y)|^2 + J_{m-s}^*(y) J_{m-s}''(y) \end{array}\right] \tag{A1.36}$$

$$U_{sm}(x, y) = \left(-\tfrac{x}{2}\right) J_s'^*(x) \left\{J_{s+1}(x)\left[\tfrac{y^*}{y}|J_{m-s-1}(y)|^2 - |J_{m-s}(y)|^2\right] + J_{s-1}(x)\left[\tfrac{y^*}{y}|J_{m-s+1}(y)|^2 - |J_{m-s}(y)|^2\right]\right\} \tag{A1.37}$$

From Eq. (A1.32), the field expression in $\vec{k}_z$ space is given by,

$$\widehat{F}\left(k_z\right) = \frac{\left[\widehat{S}_0\left(k_z\right) - jk_z G_{mn}\right] f(0) + G_{mn} f'(0)}{G_{mn}\left(k_{zc}^2 - k_z^2\right) - \widehat{S}_1\left(k_z\right)} \tag{A1.38}$$

Applying the inverse Laplace Transformation to the Eq. (A1.37), the longitudinal field in real space is given by,

$$f(z)=\sum_{i=1}^{4}\left[f(0)\frac{\widehat{S}_0\left(k_{zi}\right)-jk_{zi}G_{mn}}{jD'_{\mathrm{disp}}\left(k_{zi}\right)}+f'(0)\frac{G_{mn}}{jD'_{\mathrm{disp}}\left(k_{zi}\right)}\right]e^{-jk_{zi}z} \tag{A1.39}$$

where the $D'_{\mathrm{disp}}(k_z)=\mathrm{d}D_{\mathrm{disp}}(k_z)/\mathrm{d}k_z$, the k_{zi} is the solutions to the beam-wave coupling equation,

$$D_{\mathrm{disp}}\left(k_z\right)=G_{mn}\left(k_{zc}^2-k_z^2\right)-\widehat{S}_1\left(k_z\right)=0 \tag{A1.40}$$

When assuming the equilibrium distribution function [31, 34, 35],

$$f_0=\frac{I_b}{2\pi r_{\mathrm{c}0}ev_z}\delta\left(r_{\mathrm{c}}-r_{\mathrm{c}0}\right)\delta\left(p_z-p_{z0}\right)\frac{1}{2\pi p_{t0}}\delta\left(p_t-p_{t0}\right) \tag{A1.41}$$

The explicit expression for the beam-wave coupling equation is given by,

$$\begin{aligned}D_{\mathrm{disp}}\left(k_z\right)&=\left(k_{zc}^2-k_z^2\right)G_{mn}\\&+\frac{4\pi I_b}{|k_{\perp 1}|^2I_A}\left[\frac{\beta_t^2\left(\omega^2-k_z^2c^2\right)H_{sm}}{\left(\omega-s\Omega-k_zv_z\right)^2}-\frac{\left(\omega-k_zv_z\right)T_{sm}-k_{\perp 1}v_tU_{sm}}{\left(\omega-k_zv_z-s\Omega_{\mathrm{e}}\right)}\right]=0\end{aligned} \tag{A1.42}$$

Here, the derivation process of the classic linear theory is reviewed, and also extended to deal with ECM in a dielectric-lined waveguide system. The linear theory provides two powerful solutions to ECM investigation. Since the linear theory is valid under perturbation condition, the solution of the beam-wave coupling equation (A1.40) is capable of predict the instability bandwidth and growth rate [31, 34, 35]. The longitudinal field $f(z)$ also can be predicted via Laplace Transformation. By applying proper boundary conditions, it is capable of predicting the start-oscillation thresholds of potential instabilities in a longitudinally gradually tapered circuit or cavity, which accurately takes both the axial field profile and the quality factor into consideration [36]. Even in THz wave range, using the linear theory to predict the start-oscillation thresholds of instabilities is still one of the most accurate and efficient method [37].

References

1. Chu KR (2004) The electron cyclotron maser. Rev Mod Phys 76:489–540
2. Nguyen KT, Danly BG, Levush B, Blank M, True R, Good GR, Hargreaves TA, Felch K, Borchard P (1998) Electron gun and collector design for 94 GHz gyro-amplifier. IEEE Trans Plasma Sci 26(3):799–813
3. Du CH, Chang TH, Liu PK, Yuan CP, Yu SJ, Liu GF, Bratman VL, Glyavin MY, Kalynov YK (2012) Development of a magnetic cusp gun for terahertz harmonic gyro-devices. IEEE Trans Electron Devices 59(12):3635–3640

4. Nusinovich GS (2004) Introduction to the physics of gyrotrons. The Johns Hopkins University Press, Baltimore/London
5. Du CH, Pu-Kun Liu, Qian-Zhong Xue, Ming-Hong Wang (2008) Effect of a backward wave on the stability of an ultrahigh gain gyrotron traveling-wave amplifier. Phys Plasmas 15(12):123107
6. Harrington RF (ed) (2001) Time-harmonic electromagnetic fields. Wiley/IEEE Press, Piscataway, ISBN0-471-20806-X, John Wilson, Inc, 605 Third Avenue, New York
7. Tigelis IG, Vomvoridis JL, Tzima S (1998) High-frequency electromagnetic modes in a dielectric-ring loaded beam tunnel. IEEE Trans Plasma Sci 26:922–930
8. Barnett LR, Baird JM, Lau YY et al (1980) A high gain single stage gyrotron traveling-wave amplifier. Int Electron Devices Meet 26:314–317
9. Barnett LR, Chu KR, Baird JM et al (1979) Gain, saturation, and bandwidth measurements of the NRL gyrotron travelling wave amplifier. Int Electron Devices Meet 25:164–167
10. Park GS, Choi JJ, Park SY et al (1995) Gain broadening of 2-stage tapered gyrotron traveling-wave tube amplifier. Phys Rev Lett 74:2399–2402
11. Leou KC, McDermott DB, Luhmann NC (1996) Large-signal characteristics of a wide-band dielectric-loaded gyro-TWT amplifier. IEEE Trans Plasma Sci 24:718–726
12. Chu KR, Chen HY, Hung CL et al (1998) Ultrahigh gain gyrotron traveling wave amplifier. Phys Rev Lett 81:4760–4763
13. Chu KR, Chen HY, Hung CL et al (1999) Theory and experiment of ultrahigh-gain gyrotron traveling wave amplifier. IEEE Trans Plasma Sci 27:391–404
14. Wang QS, McDermott DB, Luhmann NC (1996) Operation of a stable 200-kW second-harmonic gyro-TWT amplifier. IEEE Trans Plasma Sci 24:700–706
15. Chong CK, McDermott DB, Luhmann NC (1998) Large-signal operation of a third-harmonic slotted gyro-TWT amplifier. IEEE Trans Plasma Sci 26:500–507
16. Pershing DE, Nguyen KT, Calame JP et al (2004) A TE11 K-a-band gyro-TWT amplifier with high-average power compatible distributed loss. IEEE Trans Plasma Sci 32:947–956
17. Garven M, Calame JP, Danly BG et al (2002) A gyrotron-traveling-wave tube amplifier experiment with a ceramic loaded interaction region. IEEE Trans Plasma Sci 30:885–893
18. Denisov GG, Bratman VL, Phelps ADR et al (1998) Gyro-TWT with a helical operating waveguide: new possibilities to enhance efficiency and frequency bandwidth. IEEE Trans Plasma Sci 26:508–518
19. Bratman VL, Cross AW, Denisov GG et al (2000) High-gain wide-band gyrotron traveling wave amplifier with a helically corrugated waveguide. Phys Rev Lett 84:2746–2749
20. Denisov GG, Bratman VL, Cross AW et al (1998) Gyrotron traveling wave amplifier with a helical interaction waveguide. Phys Rev Lett 81:5680–5683
21. Sirigiri JR, Shapiro MA, Temkin RJ (2003) High-power 140-GHz quasioptical gyrotron traveling-wave amplifier. Phys Rev Lett 90:258302
22. Advani R, Hogge JP, Kreischer KE et al (2001) Experimental investigation of a 140-GHz coaxial gyrotron oscillator. IEEE Trans Plasma Sci 29:943–950
23. Dumbrajs O, Zaginaylov GI (2004) Ohmic losses in coaxial gyrotron cavities with corrugated insert. IEEE Trans Plasma Sci 32:861–866
24. Sirigiri JR, Kreischer KE, Machuzak J et al (2001) Photonic-band-gap resonator gyrotron. Phys Rev Lett 86:5628–5631
25. Lee CS, Lee SW, Chuang SL (1986) Normal modes in an overmoded circular waveguide coated with lossy material. IEEE Trans Microw Theory Tech 34:773–785
26. Liu LSG (1987) Relativistic electronics. Science Press, Beijing (In Chinese)
27. Calame JP, Garven M, Danly BG et al (2002) Gyrotron-traveling wave-tube circuits based on lossy ceramics. IEEE Trans Electron Devices 49:1469–1477
28. Du CH, Liu PK (2009) A lossy dielectric-ring loaded waveguide with suppressed periodicity for gyro-TWTs applications. IEEE Trans Electron Devices 56:2335–2342
29. Du CH, Xue QZ, Liu PK et al (2009) Modal transition and reduction in a lossy dielectric-coated waveguide for gyrotron-traveling-wave tube amplifier applications. IEEE Trans Electron Devices 56:839–845

30. Du CH, Liu PK (2009) Stability study of a gyrotron-traveling-wave amplifier based on a lossy dielectric-loaded mode-selective circuit. Phys Plasmas 16:073104
31. Du CH, Liu PK (2010) Linear full-wave-analysis of a gyrotron-traveling-wave-tube amplifier based on a lossy dielectric-lined circuit. IEEE Trans Plasma Sci 38(6):1219–1226
32. Du CH, Liu PK (2010) Nonlinear full-wave-interaction analysis of a gyrotron-traveling-wave-tube amplifier based on a lossy dielectric-lined circuit. Phys Plasmas 17:033104
33. Jiao CQ (2007) Theoretical study and numerical simulation of the gyrotron traveling wave amplifier. Doctorial dissertation (In Chinese), Chinese Academy of Science, Beijing, China
34. Chu KR, Lin AT (1988) Gain and bandwidth of the gyro-TWT and CARM amplifiers. IEEE Trans Plasma Sci 16(2):90–103
35. Kou CS, Wang QS, McDermott DB, Lin AT, Chu KR, Luhmann NC Jr (1992) High power harmonic gyro-TWT's-Part I: linear theory and oscillation study. IEEE Trans Plasma Sci 20(3):155–162
36. Kou CS, Tseng F (1998) Linear theory of gyrotron traveling wave tube with nonuniform and lossy interaction structures. Phys Plasmas 5(6):2454
37. Kao SH, Chiu CC, Chu KR (2012) A study of sub-terahertz and terahertz gyrotron oscillators. Phys Plasmas 19:023112

Chapter 3
Novel Propagation Characteristics of Lossy Dielectric-Loaded Waveguides

Abstract This chapter focuses on the propagation characteristics of the wave in strong lossy dielectric-loaded waveguide. It discovers a fundamental property of the lossy dielectric-loaded waveguide, namely, dielectric loss-induced modal transition. The modal transition indicates that the lossy dielectric material stops the electromagnetic wave from effectively penetrating into the dielectric and makes a wave mode switch from a slow wave into a fast wave. This not only enriches our understanding of the waveguide system but also promotes the application of the lossy dielectric-loaded waveguide in the gyrotron devices. A series of principles are summarized for helping intuitively understanding the complicated wave behaviors in lossy dielectric-loaded waveguide.

Keywords Dielectric-loaded waveguide • Periodic structure • Lossy ceramic • Modal transition

3.1 Introduction

The dielectric-loaded (DL) metal cylindrical waveguide is of important potential for applications as electromagnetic (EM) wave transmission system in millimeter-wave to terahertz-wave band, especially for high power EM wave. In such a waveguide, the lossy characteristics of dielectric play an important role to the waveguide propagation characteristics [1–8]. For long-range EM wave transmission applications, the influence from dielectric loss can be greatly reduced when an over-moded, or called high-order mode, metal waveguide is employed [1–3, 7, 8]. Applying the DL waveguide as the interaction circuit of a gyrotron traveling-wave-tube (gyro-TWT) amplifier, the power of spurious oscillation can be absorbed by lossy dielectric on the inner waveguide wall, and the instability competition of system can be simultaneously suppressed [9–15]. In 1998, Prof. K. R. Chu and his group reported their experiment of a gyro-TWT amplifier, which operated on TE_{11} mode in Ka-band and employed a section of Aquadag-coated cylindrical waveguide

C.-H. Du and P.-K. Liu, *Millimeter-Wave Gyrotron Traveling-Wave Tube Amplifiers*,
DOI 10.1007/978-3-642-54728-7_3, © Springer-Verlag Berlin Heidelberg 2014

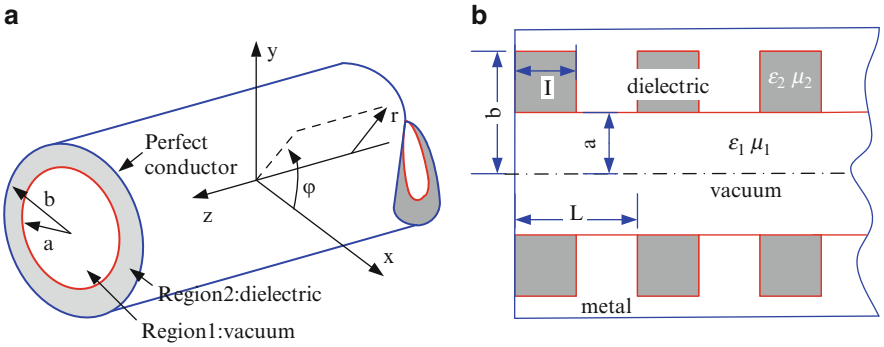

Fig. 3.1 (**a**) Uniform lossy dielectric-loaded (DL) waveguide and (**b**) periodic lossy dielectric-loaded waveguide

as the interaction circuit. It achieved performance of saturated peak power 93 kW, ultrahigh gain 70 dB, efficiency 26.5 %, and −3 dB bandwidth 3 GHz [9, 10]. In 2002, the American Naval Research Laboratory (NRL) reported the experiment of a Ka-band gyro-TWT amplifier based on the lossy ceramic-loaded circuit. It operated on the fundamental harmonic TE_{01} mode and achieved saturated peak power 137 kW, −3 dB bandwidth 3.3 % under the condition of voltage 70 kV and beam current 10 A [13, 14]. The instability competition of this experiment is well suppressed. The lossy DL waveguide not only plays an important role in interaction circuit for high power gyro-TWT amplifiers, but also can be loaded in the drifting tunnels for gyrotron amplifiers and oscillators [12, 16], as well as loading in a waveguide to filtrate unwanted modes.

The dielectric-loaded waveguide, as a typical waveguide structure, has been thoroughly investigated. Studies are normally concentrated on exploring the weak lossy transmission characteristics [1–8]. However, the gyro-devices usually adopt dielectric-loaded waveguides with strong lossy characteristics to adjust the attenuation rate of the operate mode, and it brings convenience for system stability control [10, 13, 16]. In addition, the dispersion property of the system also can be changed by loading dielectric, and it is beneficial for broadband synchronization between EM wave and cyclotron beam. The high thermal conductivity of dielectric material and waveguide structure together endows the gyro-devices high average power capability. The lossy dielectric provides advantages of suppressing oscillations in the interaction waveguide. However, it makes the system more complicated and brings disturbance to the mode distribution and transmission characteristics, which makes it more difficult to analyze the system. Hence, through investigating lossy dielectric-loaded waveguide, it brings us better understanding and promotes its application in gyro-devices.

The propagation characteristics of an EM mode in a dielectric waveguide are relatively complicated. For a high-order mode gyro-TWT, both uniform DL waveguide and the periodic DL waveguide are usually adopted, as shown in Fig. 3.1a, b respectively. When the thickness of dielectric layer is on the order of waveguide radius, the EM power in dielectric layer cannot be ignored [10, 13].

Loading a dielectric layer enlarges the transverse cross area of the waveguide, and it theoretically enriches the mode density in a given frequency band, accordingly. When the dielectric is lossless, waveguides shown in Fig. 3.1a, b are ideal slow-wave systems. While, in case of loading strong lossy dielectric, the EM wave could not effectively penetrate into dielectric layer, and the major power of the mode is confined in the hollow region. Under such a condition, the propagation characteristics of the EM wave are quite similar to that in a nonideal conductive cylindrical waveguide. When a special lossy ceramic is adopted, a given EM mode normally exists as a fast wave in the low frequency region and as a slow wave in the high-frequency region. In different waveguides with both identical structures and operation frequency band, but loading with material of different loss strength, the EM wave may exists as a slow-wave mode in one waveguide, but a fast-wave in another waveguide [17–19]. These novel phenomena of modal transition are usually ignored in other research fields, but it is significant to design a high power gyro-TWT amplifier with lossy ceramics loaded [17].

Based on the theory about lossy DL waveguide introduced in Chap. 2, two simulation programs UDW (uniform dielectric-lined waveguide program) and PDW (periodic dielectric-lined waveguide program) were coded to study lossy DL waveguides. Reliability of both programs was also verified [17–19]. In Sect. 3.2 of this chapter, the propagation characteristics, field distribution, and the phenomenon of modal transition in the uniform DL waveguide are investigated [18, 19]. Section 3.3 shows the further investigation of the periodic DL waveguide, where an important property is observed that the lossy characteristic of dielectric, to some extent, is capable of suppressing the periodicity effect of waveguide structure [17]. Mapping relations between modes in uniform DL waveguide, periodic DL waveguide, and smooth cylindrical waveguide are addressed in Sect. 3.4. Summary is given in Sect. 3.5.

3.2 Dielectric Loss-Induced Modal Transition

As shown in Fig. 3.1a, there is a special dielectric parameter region, the metal cylindrical waveguide is loaded with a layer of lossy ceramic on the inner wall. Increasing the dielectric loss tangent from 0 to the extreme lossy condition, an original slow-wave mode turns into a fast-wave mode due to dielectric loss enhancement and suppressing wave energy penetrating into dielectric layer [17–19]. In this section, the complicated characteristics of mode transition in dielectric-loaded waveguide will be addressed in depth.

3.2.1 Eigenvalue and Mode Identification

The mode identification in a waveguide originates from the eigen solutions of the eigen equation. In a simple waveguide system, such as an ideal metal cylindrical

waveguide, boundary condition generates simple eigen equations, $J_m^{'}(x_{mn}) = 0$ for a TE_{mn} mode and $J_m^{'}(x_{mn}) = 0$ for a TE_{mn} mode, in which the solutions are real numbers and independent of frequency and the waveguide dimensions. Hence a mode in an ideal metal cylindrical waveguide always keeps the same transverse field distribution. As a result, the mode identification TE_{mn} and TE_{mn} are directly related to transverse field distributions. But in a dielectric-loaded waveguide as shown in Fig. 3.1a, the eigen equation is a transcendental equation as given in Chap. 2,

$$\left[\frac{1}{k_{\perp 2}}\frac{\varepsilon_2}{\varepsilon_1}\frac{Q'(k_{\perp 2}a)}{Q(k_{\perp 2}a)} - \frac{1}{k_{\perp 1}}\frac{J_n'(k_{\perp 1}a)}{J_n(k_{\perp 1}a)}\right]\left[\frac{1}{k_{\perp 2}}\frac{\mu_2}{\mu_1}\frac{P'(k_{\perp 2}a)}{P(k_{\perp 2}a)} - \frac{1}{k_{\perp 1}}\frac{J_n'(k_{\perp 1}a)}{J_n(k_{\perp 1}a)}\right] - \frac{1}{\varepsilon_1\mu_1}\left(\frac{k_z n}{\omega a}\right)^2\left(\frac{1}{k_{\perp 1}^2} - \frac{1}{k_{\perp 2}^2}\right)^2 = 0 \tag{3.1}$$

Each region of the waveguide is limited by

$$k_{\perp 1}{}^2 + k_z^2 = k^2 = \omega^2\varepsilon_1\mu_1 \quad \text{hollow region} \tag{3.2a}$$

$$k_{\perp 2}{}^2 + k_z^2 = k^2 = \omega^2\varepsilon_2\mu_2 \quad \text{dielectric region} \tag{3.2b}$$

where the roots are related to frequency, dielectric parameters, and waveguide structure [19].

Figure 3.2a shows the dispersion map of the circular polarized TE_{01}, TE_{02}, and TE_{03} in a lossless dielectric-loaded waveguide. The phase velocity of modes between light D and light V is lower than the free space light speed, and the region between light D and light V is called slow-wave region. While the phase velocity of modes between light V and vertical coordinates is higher than free space light speed, this region is called a fast-wave region. Several characteristics should be specified. An EM mode near cutoff frequency region is a fast-wave mode and turns into a slow-wave mode after it gets across the light V at a higher frequency. For a high-order mode, there is an obvious transition region indicated by a T, locating between the fast-wave region and the slow-wave region. In Fig. 3.2b, the transverse mode distributions are given by superimposing the amplitudes of TE_{02} mode $E_\varphi(r)$ component sampled during a period. A vertical dashed line indicates the interface between vacuum region and dielectric region. The ratio of the RF power carried by the vacuum region to that carried by the whole dielectric waveguide is defined as fractional e-power (FEP). We define the FEP related to the field energy distribution; it is

$$\text{FEP} = \frac{\iint_{\text{V}} \varepsilon_{\text{r}}\vec{E}\cdot\vec{E}^*\text{d}S}{\iint_{\text{V+D}} \varepsilon_{\text{r}}\vec{E}\cdot\vec{E}^*\text{d}S} \tag{3.3}$$

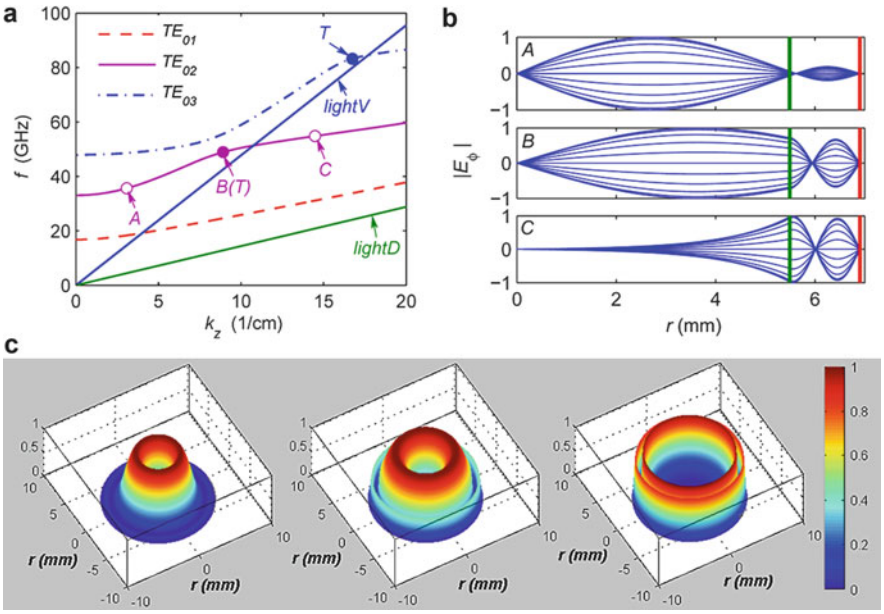

Fig. 3.2 (**a**) Dispersion relations; (**b**) TE_{02} mode normalized E_φ field distributions in a DL metal cylindrical waveguide under lossless condition. *Light V* and *light D* represent the lights traveling in uniform vacuum and dielectric, respectively, (**c**) distribution of power density. $a = 5.495$ mm, $b - a = 1.41$ mm, $\varepsilon_r = 11$, $\mu_r = 1$ (calculated by UDW)

where the numerator indicates integration of the vacuum region only and the denominator indicates integration of both the vacuum region and the dielectric region. For the TE_{02} mode shown by the mode structure A, the majority of its RF power (FEP = 81 %) is distributed in the vacuum region. The vacuum region power dominates its propagation characteristics. Hence, it behaves like a fast wave in a hollow metal cylindrical waveguide. Similarly, the field distribution C distributed about 94 % power in the dielectric region and the power in the dielectric region dominates the wave characteristics; hence it is a typical slow-wave mode.

In a lossless DL waveguide, the solution of wave equation in the above cutoff frequency region is a real number, and the mode identification is based on real solutions. When lossy material is loaded, the dielectric loss introduced complex dielectric parameter, which leads to complex eigen solutions. Hence, the mode identification in a lossy dielectric-loaded waveguide is based on the complex eigen roots of the eigen equation. In order to facilitate investigation, only axis symmetric TE_{0m} modes are considered. The mode identification principles are specified as follows [1]:

1. Use TE_{0m} and TE^{d}_{0m} to identify modes in a dielectric waveguide under lossless and lossy conditions, respectively.
2. A continuous complex propagation constant k_z with respect to frequency identifies the same TE^{d}_{0m} mode in a lossy dielectric waveguide.

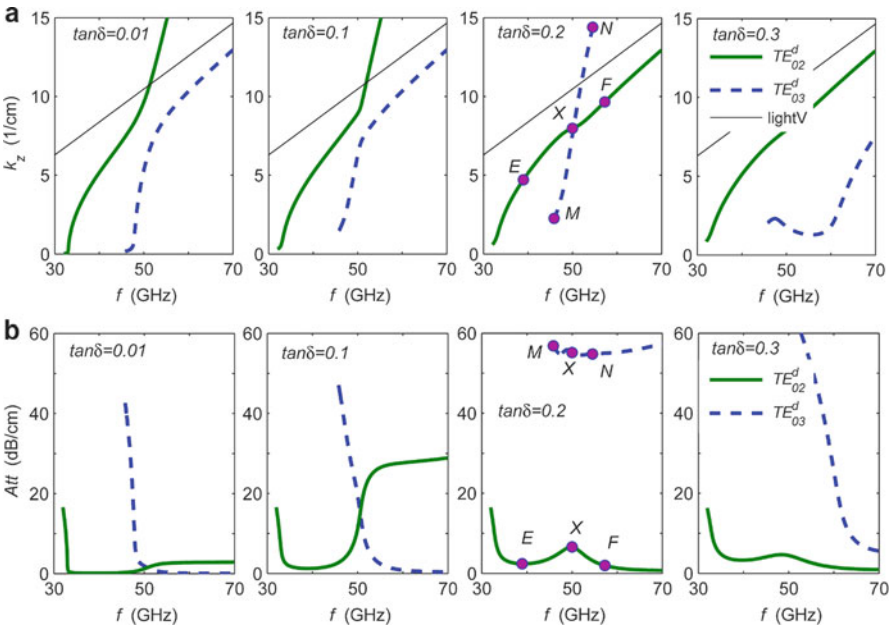

Fig. 3.3 (**a**) The dispersion relations and (**b**) the attenuation properties of TE^d_{02} and TE^d_{03} modes under different loss strength, where the k_z and *Att* are from the real part and imaginary part of the complex propagation constant, respectively

3. Reducing the lossy dielectric to lossless, under weak dielectric loss condition, a TE^d_{0m} mode degenerates into a TE_{0m} mode near its cutoff frequency.

The aforementioned definitions comply with traditional rules. The new mode identifier TE^d_{0m} brings convenient comparison between the propagation characteristics in lossless and lossy DL waveguides.

3.2.2 Modal Transition

A kind of novel transmission instability, namely, dielectric loss-induced modal transition will be addressed in this section [17–19]. The loss characteristics of dielectric leads to complex eigen solutions. Lossy dielectric may result in transmission instability, and the mode structure in a lossy DL waveguide demonstrates certain different behaviors, which are normally nonobservable in low-loss waveguide system. With material of strong loss, its skin depth is relatively small. A TE_{0m} mode in a lossless waveguide turns into a TE^d_{0m} mode in a lossy dielectric waveguide according to aforementioned mode identification principles. The dispersion relations and attenuation properties of the TE^d_{02} modes under different lossy conditions are shown in Fig. 3.3, where the k_z and *Att* are from the real and imaginary parts of the

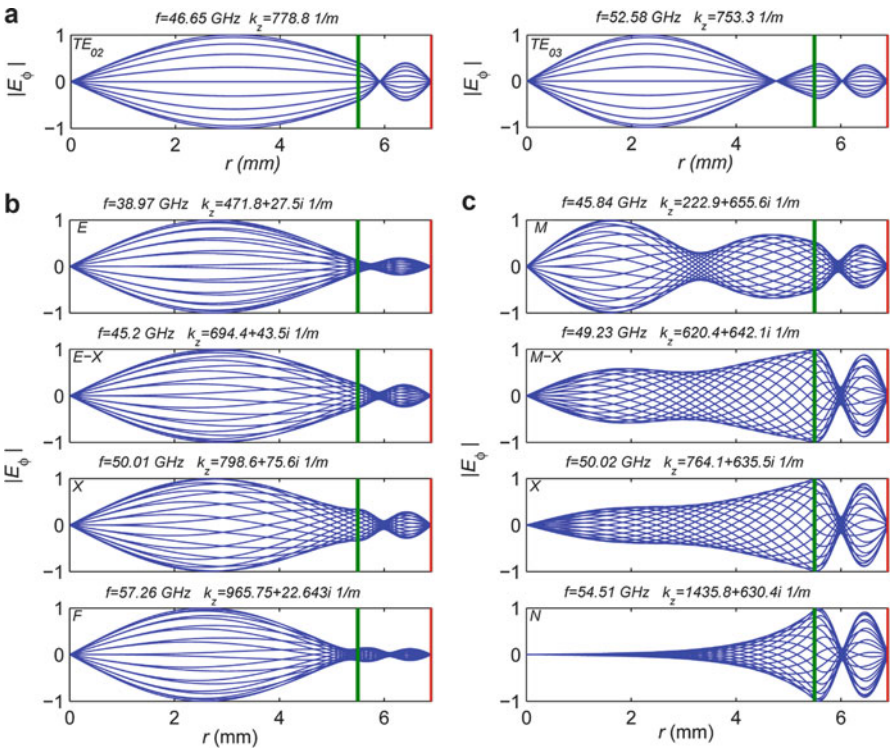

Fig. 3.4 Representative normalized E_φ field distribution in the dielectric-loaded waveguide of (**a**) TE_{02} mode and TE_{03} mode under lossless condition, and (**b**) TE_{02} mode and (**c**) TE_{03} mode under dielectric loss $\tan\delta = 0.2$. The *vertical line* on a mode structure indicates the location of the vacuum–dielectric interface

complex propagation constant, respectively. It is shown that, when loss tangent $\tan\delta$ is increased from 0.01 to 0.1, stronger dielectric loss makes the dispersion curves of the two modes get closer. With even stronger dielectric loss, the two dispersion curves get across with each other. When loss tangent $\tan\delta = 0.2$, the dispersion curve of TE_{02}^{d} mode, marked by points E–X–F, and that of TE_{03}^{d} mode, marked by points M–X–N, get across at point X. TE_{02}^{d} mode switches its dispersion curve from the normal slow-wave region under lower-loss condition into the fast-wave region in the frequency range higher than point X, while the dispersion curve TE_{03}^{d} mode accordingly switches from the normal fast-wave region into the slow-wave region. In addition, the complex propagation constants are continuous functions of frequency. With an even stronger dielectric loss, both of the two modes become fast-wave modes, indicating that the strong loss prevents the electromagnetic modes from penetrating into the dielectric layer.

The above phenomenon is explained by mode structures shown in Fig. 3.4, which is sampled from Fig. 3.3. Figure 3.4a shows the mode structures of the TE_{02} mode and TE_{03} mode in lossless dielectric-loaded waveguide. Both modes are with

fixed radial standing-wave points and are quite consistent with our experiential understanding. When a lossy dielectric of the same size is loaded, something anomalous happens. Figure 3.4 shows that, in the fast-wave region, both the mode structure E of TE_{02}^{d} mode and the mode structure M of TE_{03}^{d} mode are quite similar to that under a lossless condition. The dispersion curves of both TE_{02}^{d} and TE_{03}^{d} modes cross at point X on the dispersion map of Fig. 3.3, where each mode presents a transitional mode structure. But the mode structures of TE_{02}^{d} and TE_{03}^{d} at the point X are quite different from each other. In the frequency range above the crossing point X, the mode structure F of TE_{02}^{d} mode presents a TE_{03}-like mode, whereas the mode structure N of TE_{03}^{d} mode presents a TE_{02}-like mode. Considering together with Figs. 3.3 and 3.4, each of TE_{02}^{d} mode and TE_{03}^{d} mode under the condition of dielectric loss $\tan\delta = 0.2$ experiences continuous evolution of mode structure along the dispersion curves.

The dielectric loss results in transmission instability, namely, modal transition between a pair of modes [17–19]. Further analysis will be shown from two aspects. On one hand, the mode structures in lossy dielectric-loaded waveguide can be qualitatively classified into weak lossy mode and strong lossy mode. The former is similar to the field structure of TE_{02} in fast-wave region, where the major power of the mode is focused in vacuum region. A mode with weak lossy field structure exists as a fast-wave mode. For a strong lossy mode, major power of the mode is focused inside the lossy dielectric layer, and the mode behaves as a slow-wave mode. Here, we define the concept of modal transition in a lossy DL waveguide that a pair of independent modes in a lossy DL waveguide transfers between each other due to material changing. For each mode, study demonstrates the frequency-dependent field structures and attenuation strength. Although the dispersion curves of such a pair of modes cross at certain frequency, they still belong to different solutions of the eigen modes and demonstrate quite distinctive transverse field structures. The difference in propagation attenuation reveals the inherent mode-selecting ability of the DL waveguide. For example, in Figs. 3.3 and 3.4, the attenuation property indicates that when $\tan\delta = 0.2$, transmission attenuation of TE_{02}^{d} mode keeps lower than 6.5 dB/cm between 40 and 60 GHz, while that of TE_{03}^{d} mode keeps higher than 55 dB/cm. It is obvious that the TE_{02}^{d} mode survives, and the TE_{03}^{d} mode will be absorbed and eliminated after propagating through a short section of such lossy DL waveguide.

The characteristics of transverse field structures in a lossy DL waveguide will be further investigated. For a given mode at a specified frequency, it shows a different transverse mode structure under loss condition compared to lossless condition. Comparing Fig. 3.2 with Fig. 3.4, it reveals that the transverse field structure in traditional lossless waveguide exists in the form of pure standing wave along the radial direction, and the field demonstrates fixed standing-wave points. While, in lossy-dielectric waveguide, the transverse field structure exists in form of partial standing wave. Figure 3.5 shows the variation of TE_{02}^{d} in a half period. The transverse partial standing wave distribution demonstrates that there is a radial power flowing along the radial direction from the vacuum region into the lossy dielectric layer. Such unstable field structure could be explained as follows. In a waveguide system, the wave vector can be written as $\vec{k} = \vec{k}_z + \vec{k}_\perp$, where

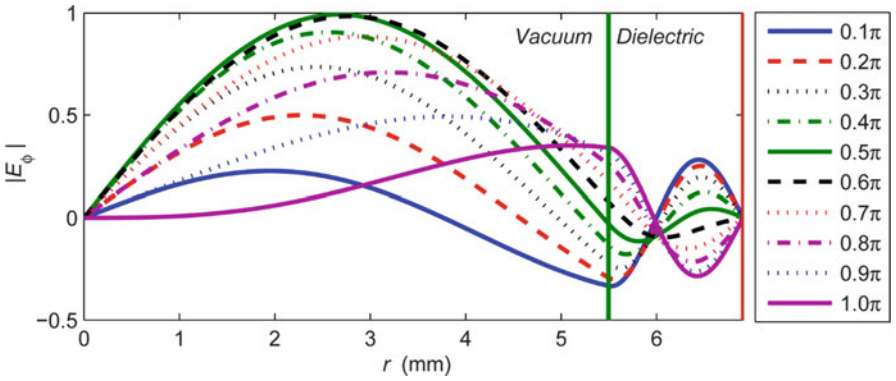

Fig. 3.5 The evolution of the normalized E_φ amplitude of TE_{02}^{d} mode in a half period (UDW calculated)

$k = \omega\sqrt{\varepsilon\mu}$ is the propagation constant in vacuum, $\vec{k}_\perp$ is the transverse wave vector, and $\vec{k}_z$ is the axial wave vector. It is concluded that the EM wave propagates along the transverse direction and axial direction. In a lossless waveguide system, electromagnetic wave is reflected totally in transverse direction and in the form of a stable standing wave. While in a lossy DL waveguide, the lossy dielectric attenuates the wave power during its propagation and results in a partial standing wave in transverse direction.

The aforementioned modal transition indicates that, due to change in dielectric material, a pair of closely independent modes transits between each other and generates a low-lossy mode and a high-lossy mode. The low-lossy mode distributes its major power in the hollow vacuum region, exists in the form of a fast wave, and its transmission property is quite similar to that of hollow metal cylindrical waveguide. While for a high-lossy mode, most of its power distributes in the lossy dielectric region and suffers from strong attenuation. To some extent, such kind of strongly attenuated mode could be regarded as eliminated, which results in decreased mode density.

3.2.3 Modal Degeneration

When the dielectric loss becomes extremely strong, the lossy DL waveguide is equivalent to a nonideal conductive metal cylindrical waveguide, and we summarize the concept as mode degeneration. Under the condition of high $\tan\delta$, heavily attenuated mode *disappears* in the slow-wave region, and it exists only in the fast-wave region. The phenomenon of this two modes degenerating into one mode is defined as mode degeneration, here. Recalling Fig. 3.3, we can find that in the condition of $\tan\delta = 0.3$, the mode TE_{03}^{d} is strongly suppressed and exists below

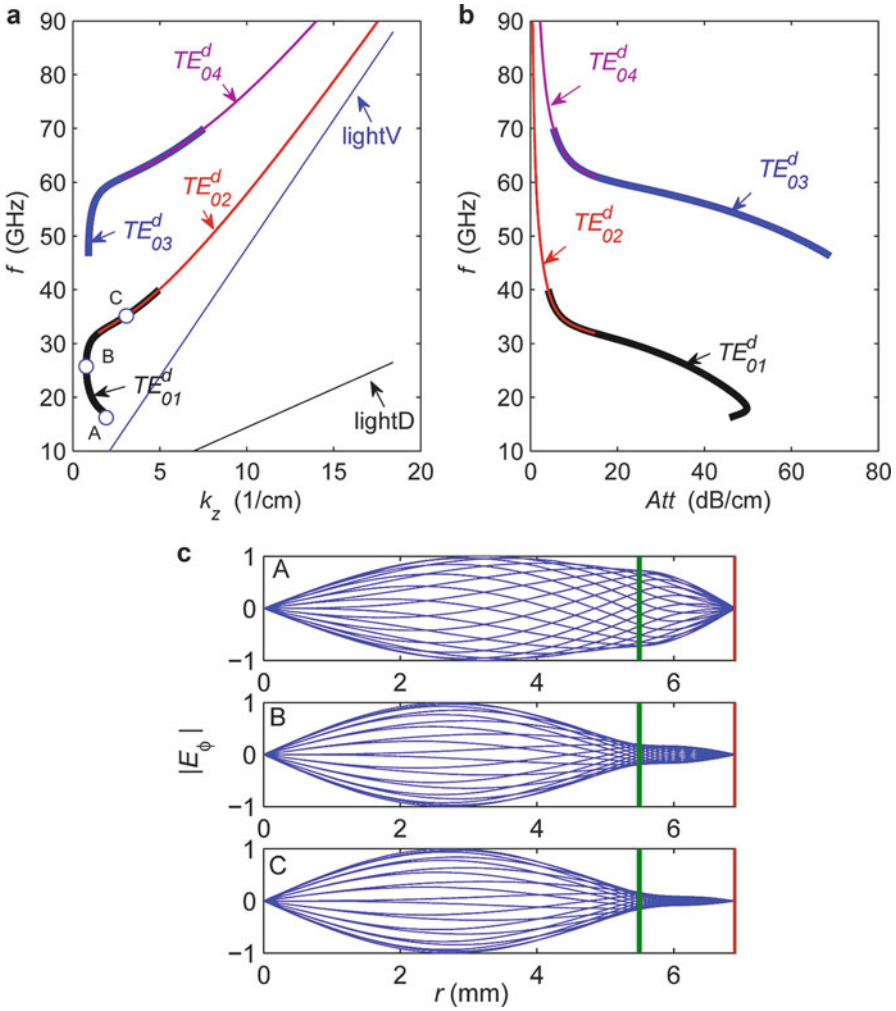

Fig. 3.6 Modes in lossy DL waveguide. (**a**) dispersion relation, (**b**) attenuation property, and (**c**) typical normalized E_φ field structure ($\tan\delta = 1$, UDW calculated)

the cutoff frequency of TE^d_{04} mode. Finally, the two modes degenerate into one, and the mode density is reduced in such a way.

The Fig. 3.6 gives the transmission property of modes under $\tan\delta = 1$. Strong loss mode TE^d_{01} is strongly attenuated. With the frequency increasing continuously, the TE^d_{01} mode transits into the TE^d_{02} mode gradually. In the pass band of the TE^d_{02} mode, the field structure and propagation property are similar to that of TE_{01} in lossy DL cylindrical waveguide. The behaviors of TE^d_{03} and TE^d_{04} mode is similar to that of TE^d_{01} and TE^d_{02} mode. According to the mode identification principles

based on continuous eigen roots, the TE_{01}^{d} mode and TE_{02}^{d} mode under such strong dielectric loss condition degenerate into a single mode. Further calculation indicates that, in the high-frequency region, the dispersion curve of TE_{02}^{d} superimposes that of the equivalent empty waveguide TE_{01} mode. Similar behavior also happens between TE_{04}^{d} and empty waveguide TE_{02} mode. Figure 3.6c gives the variation along dispersion curves (A-B-C) of TE_{01}^{d}- TE_{02}^{d}. In a DL waveguide with strong lossy material, the EM wave cannot effectively penetrate into dielectric layer, and a majority of energy is confined in the hollow vacuum region. From the above description, it is concluded that the strong attenuation property of dielectric is helpful to prevent energy from penetrating into the dielectric layer. With strong dielectric loss, lossy DL waveguide can be approximated by a hollow metal cylindrical waveguide with imperfect conducting sidewall. The radius of hollow cylindrical waveguide is equal to the radius of vacuum region of lossy DL waveguide [18, 19].

3.2.4 Modal Selection

Following study uses parameters given in Ref. [13]. The radius of vacuum region in metal cylindrical waveguide is $a = 5.945$ mm, the main content of dielectric is AlN (80 %) and SiC (20 %), the dielectric constant is $\varepsilon_r = 11 - j\ 2.2$, and the operation frequency is 35 GHz. Analysis will be concentrated on circular polarized TE_{0m}^{d} mode. Figure 3.7a shows the variation of propagation constant and attenuation property of TE_{01}^{d} and TE_{02}^{d} in lossy dielectric waveguide relative to thickness of dielectric. The calculation result has a good agreement with that in Ref. [13]. Figure 3.7b shows the field structure of four typical loading cases. In the case of A, the main energy of TE_{01}^{d} is concentrated in lossy dielectric. This high-lossy field structure is similar to that of TE_{01} in lossless DL waveguide. In the case of B, C, and D, TE_{02}^{d} transfers continuously from TE_{02}-like field structure to TE_{03}-like field structure. B and D are typical low-lossy mode. Attenuation of the conditions C and E become stronger as enhancement of the relative power in dielectric. The TE_{02}^{d} mode changes gradually from the field structure B to D, and the attenuation property increases and decreases periodically. During this process, propagate constant has no jump or singular point, which demonstrates the mode transition in lossy DL waveguide from another aspect.

The phenomenon of the modal transition is common in a lossy DL waveguide. Figure 3.8 shows the characteristics of the first seven circular electric field modes in lossy DL waveguide. The regions where modal transitions happen are marked by circles A, B, C, and D.

The major powers of TE_{02}^{d} and TE_{04}^{d} modes are in the vacuum region and exhibit quite similar to that of the TE_{01} and TE_{02} in lossless metal waveguide, respectively, which also leads to the similarity of the dispersion curves between TE_{02}^{d} and TE_{01} mode and that between TE_{04}^{d} and TE_{02}. From Fig. 3.8c, usually, minority power of TE_{01}^{d}, TE_{03}^{d}, and TE_{05}^{d} modes distributes in vacuum, and accordingly major power

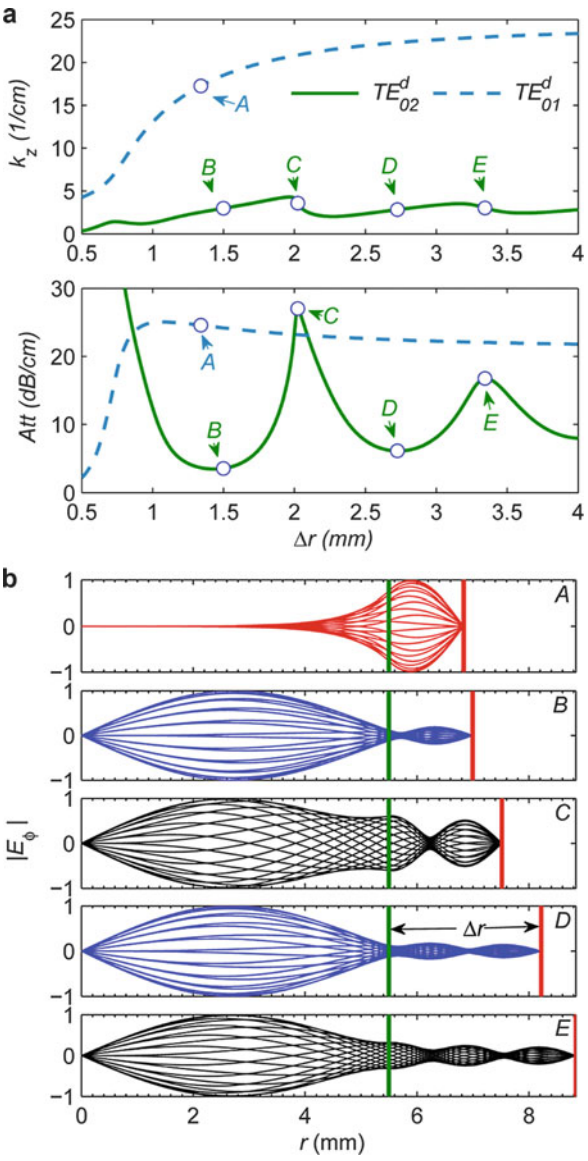

Fig. 3.7 (**a**) Propagation characteristics of modes, (**b**) variation of normalized E_φ field distributions along thickness of dielectric (UDW calculated)

distributes in dielectric layer. So these modes are strongly attenuated. Based on the above systematic analysis, principles of mode selective transmission in lossy DL waveguide can be generalized as that a mode distributing its major power in the vacuum region suffers from relative weak attenuation, while a mode distributing its major power in the dielectric region suffers from strong attenuation. This difference brings the lossy DL waveguide the ability of mode selective transmission.

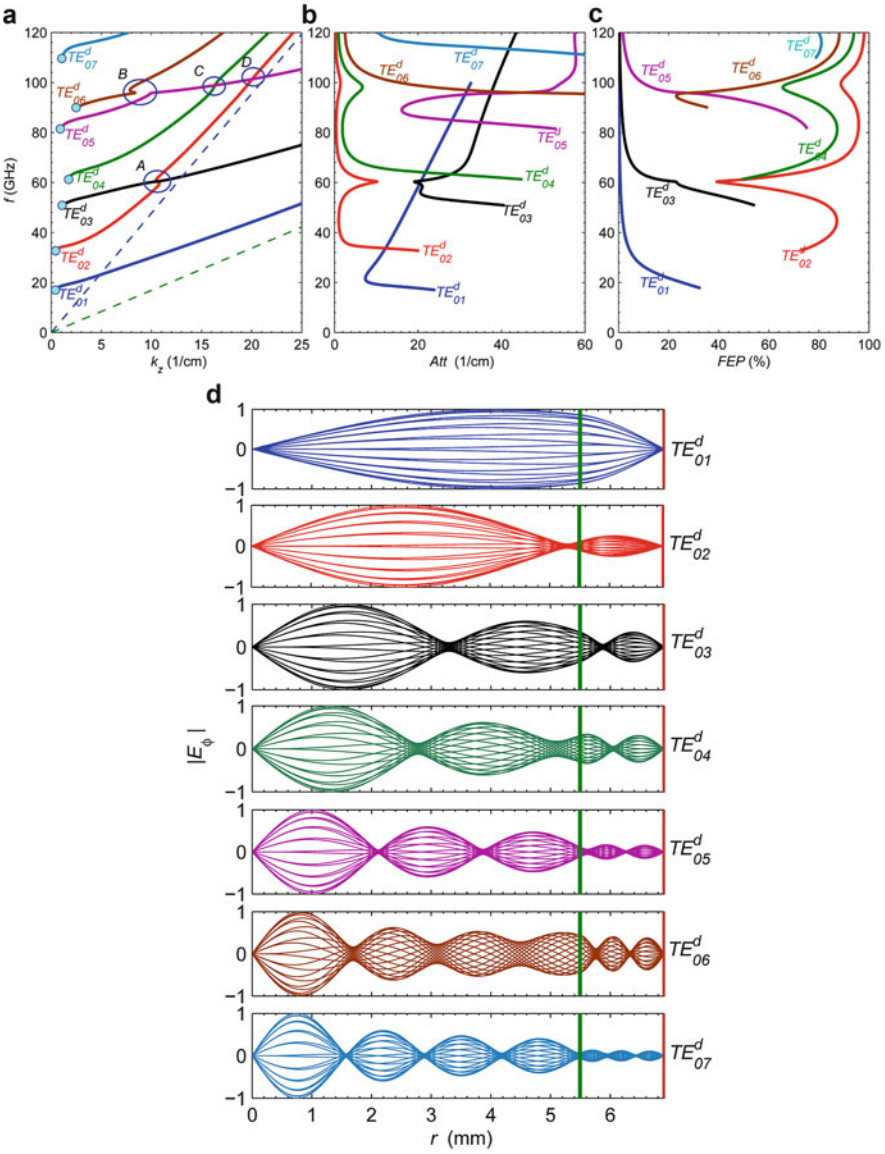

Fig. 3.8 (**a**) Dispersion relation, (**b**) attenuation property, $a = 5.495$ mm, $b = 6.905$ mm, $\varepsilon_r = 8$, $\tan\delta = 0.122$, (**c**) relative electric field power in the vacuum region, and (**d**) the normalized E_φ field distributions close to the cutoff frequency

According to the above principles, we can obtain intuitive understanding to the mode selective transmission in lossy DL waveguide:

- A fast-wave mode confines its major power in the vacuum region and suffers from relatively lower attenuation rate.

- A slow-wave mode distributes considerable power in the dielectric region and suffers from relatively higher attenuation rate.
- For a mode with its power mainly restrained in vacuum, its dispersion curve is similar to that of a fast-wave mode in simple metal cylindrical waveguide and normally propagates with low attenuation rate.
- For a mode with its power mainly restrained in dielectric, its dispersion curve is similar to that of a slow-wave mode in lossless dielectric waveguide and normally propagates with strong attenuation.

According to the analysis of mode selective property, intuitive estimation about transverse field structure and its attenuation property will be acquired by dispersion relation of lossy DL waveguide. These characteristics of mode selection of distributed lossy structure make it possible to apply in design of gyro-TWT amplifier operating on high-order modes.

In this section, the instability of modal transition and degeneration in a lossy DL waveguide are investigated. In a lossy DL waveguide, the transverse field structure behaves as a partial standing wave. When the attenuation property of dielectric material is higher than some specific values, modal transition occurs between two independent nearby modes. One is with lower attenuation rate and the other is with strong attenuation rate. The strong loss of dielectric is helpful to prevent energy from going into dielectric. With the strong lossy dielectric, DL waveguide can be equivalent to hollow waveguide with imperfect conducting walls. The cross section of lossless dielectric-loaded metal waveguide is bigger than that of corresponding metal waveguide. Hence, mode density of lossless dielectric-loaded metal waveguide is higher than that of metal waveguide. During the degeneration process of dielectric waveguide to imperfect metal waveguide, modal transition and modal degeneration reduce the mode density. Intuitive understanding of mode selection are summarized as a weak attenuated mode is restrained in the vacuum region and exists as a fast-wave mode, while a strong attenuated mode normally distributes a considerable power in the dielectric region and behaves as a slow-wave mode.

3.3 Periodic DL Waveguide with Suppressed Property of Periodicity

In practical application of a gyro-TWT, in order to adjust the waveguide transmission property, as well as avoiding dielectric charging, lossy DL waveguide with periodical structure is adopted as the interactive circuit, as shown in Fig. 3.1b [13–19]. In this section, the influence from lossy dielectric property to the transmission characteristic of periodic DL waveguide will be investigated. The specified dimensions of dielectric structure for Ka-band gyro-TWT application are inner diameter $a = 5.495$ mm, thickness of dielectric $b - a = 1.7$ mm, $\varepsilon_r = 7.11 - 1.1\,j$, $\mu_r = 1$.

3.3.1 Eigenvalue and Mode Identification

For the gyro-TWT application, in order to avoid dielectric charging, lossy dielectric also periodically loaded in the waveguide wall. The periodic DL waveguide provides additional freedom of adjusting the transmission property than a uniform DL waveguide [13–15]. As shown in Fig. 3.1b, because of high-order Bloch components, standing-wave harmonics and matching boundary conditions are introduced by periodic structure, and the eigen equation of such a system becomes the determinant of a large sparse matrix. The theorem of periodic system is already reviewed in Chap. 2. In the following study, the mode identification of periodically lossy DL waveguide is also based on the continuous eigenvalues of eigen equation. A more intuitive method for mode identification of the periodic DL waveguide will be introduced. The corresponding relations of modes in periodically lossy DL waveguide, uniformly lossy DL waveguide, and smooth cylindrical waveguide will be given in the following discussions.

3.3.2 Influence of Dielectric Slot Ratio

In Fig. 3.1b, the inner radius of waveguide is $a = 5.495$ mm, the thickness of dielectric $b - a = 1.7$ mm, the permittivity $\varepsilon_r = 7.11 - 1.1\,j$, and the permeability $\mu_r = 1$. The influence from the slot ratio l/L of the dielectric slot on the operating TE_{01} mode is considered first, as shown in Fig. 3.9. The wave numbers of the forward-wave and backward-wave components vary symmetrically besides the Brillouin Edge. Generally speaking, increasing the slot ratio l/L of the dielectric slot makes the operating TE_{01} mode in the periodic DL waveguide evolve from the TE_{01} mode distribution in a hollow waveguide toward the TE_{02}^{d} mode distribution in a uniform DL waveguide at 35 GHz. Figure 3.9 also comparatively reveals that, under full dielectric loading condition $l/L = 1$, there is some difference to the solutions between the UDW [18, 19] and PDW [15, 17]. It is caused by the difference in the physical models of the codes. The UDW solves the eigen modes of a uniform DL waveguide, while the PDW solves the eigen modes of a periodic structure. Even under full dielectric loading, $l/L = 1$, the physical model in PDW still preserves an infinite thin metal interface between a pair of nearby periods. Around the region of $l/L \approx 0.2$, due to a resonant mode in the dielectric slot, both the propagation constant and attenuation rate are sensitive to the slot ratio l/L. The vivid field distributions in Fig. 3.10 under different slot ratio conditions demonstrate the resonant and traveling characteristics of the operating mode in a periodic system. Taking both Figs. 3.9 and 3.10a consideration, there is a sharply resonant enhancement in attenuation induced by fundamental resonant mode in the dielectric region under the low slot fraction $l/L \approx 0.2$. Increasing the slot ratio from this point makes it hard to load the fundamental resonant mode and weakens the field strength in the slot. As a result,

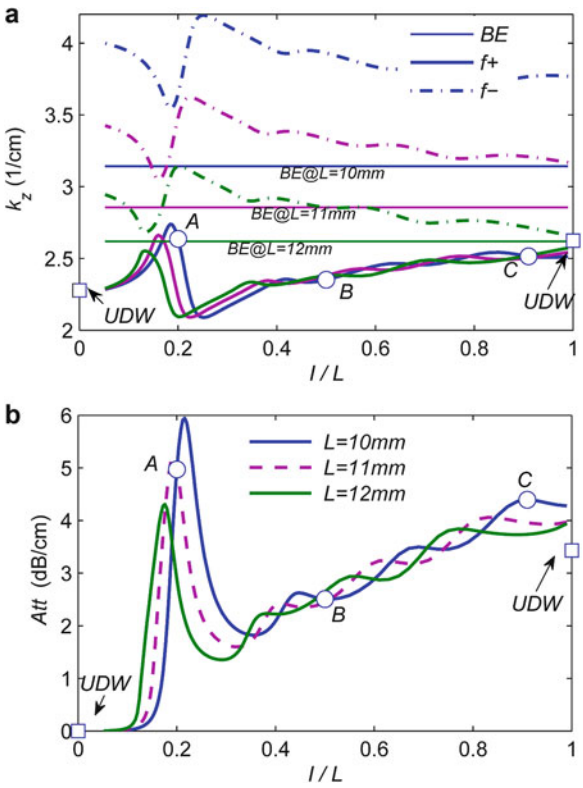

Fig. 3.9 Effect of the dielectric slot ratio *I*/*L* on (**a**) the propagation constants and (**b**) the attenuation of the operating TE_{01} mode (calculated by PDW at 35 GHz), where the *BE* indicates the first Brillouin region, f_+ indicates the k_z on the forward wave, and f_- indicates the k_z on the backward wave

the propagation characteristics return to a normal magnitude, and it behaves like a traveling wave, as shown in Figs. 3.9 and 3.10.

The normalized field distributions under several values of slot ratio *I*/*L* are shown in Fig. 3.10. The field distributions in the vacuum region are similar to TE_{01} mode distributions, while the mode distributions in the dielectric region are standing-wave distributions. The mode distributions in the dielectric region are similar to that of a TE_{02}^{d} mode in uniform DL waveguide. Hence a denotation $\sim TE_{01}$ is used to indicate such a complex mode in the periodic system. When the slot ratio *I*/*L* increases from 0.2 to 0.91, the single hump distribution in the dielectric slot evolves into a multi-hump distribution. The answers to these mode transforms can be found in the normalized harmonic magnitudes in Fig. 3.11. The standing-wave harmonic components are normalized by the strongest Bloch harmonic component in the vacuum region. The magnitudes of the higher-order harmonics decrease exponentially according to the harmonic numbers. An increased slot ratio obviously reduces the magnitudes of the high-order Bloch harmonics, indicating suppressed periodicity, while with increasing slot ratio, the higher-order standing modes reversely increase. Hence the multi-hump distribution in dielectric slots originates from the higher-order standing-wave components.

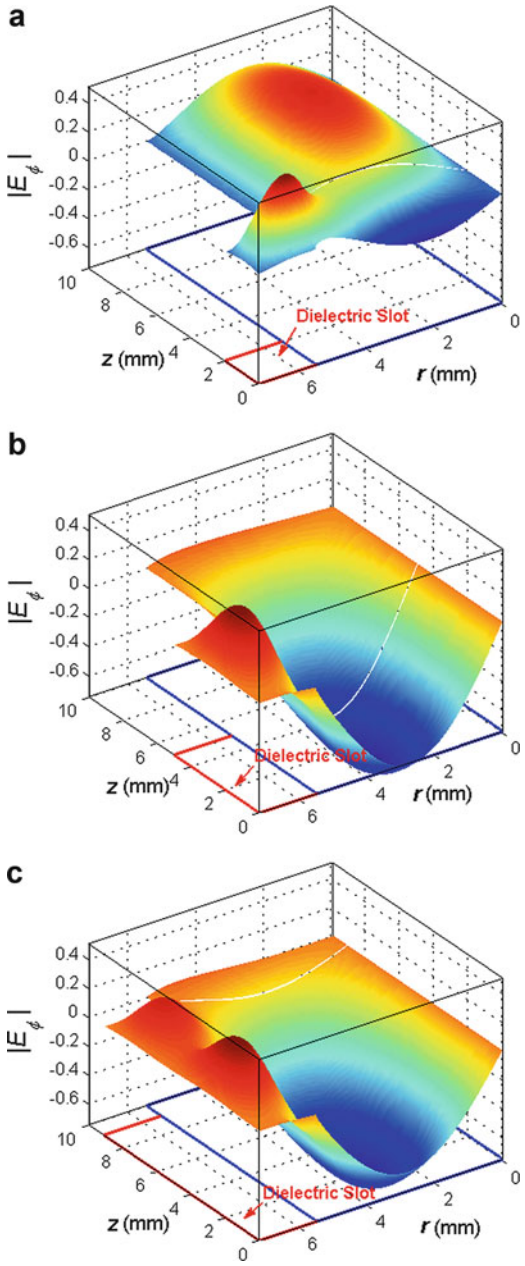

Fig. 3.10 Normalized E_φ field distributions of the three sampled schemes A, B, and C in Fig. 3.9 (calculated by PDW at 35 GHz)

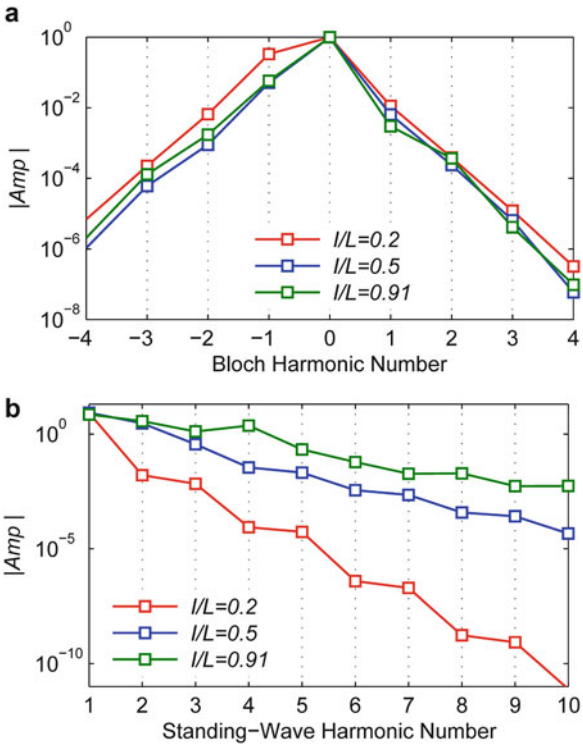

Fig. 3.11 Normalized amplitudes of (**a**) the Bloch harmonic components in the vacuum region and (**b**) the standing-wave harmonic components in the dielectric region for the operating modes. The standing-wave harmonic components are normalized to the strongest Bloch harmonic component in the vacuum region (calculated by PDW at 35 GHz based on the sampled structures A, B, and C in Figs. 3.9 and 3.10)

3.3.3 Modal Transition in a Periodic Dielectric Waveguide System

In a periodic DL waveguide, the loss dielectric can also lead to modal transition, similar to the former mentioned phenomenon in a uniform lossy DL waveguide. The modal transition in periodic DL waveguide will be investigated by comparing the mode spectrums under lossy and lossless conditions. The specific periodic waveguide structure is given in Fig. 3.1b, and parameters are given as $a = 5.495$ mm, $b - a = 1.7$ mm, $L = 11.5$ mm, $l/L = 0.87$, and $\varepsilon_r = 7.11 - 1.1\ j$. Under lossless conditions, the mode spectrum of the operating TE_{01} is shown in Fig. 3.12a. Since the mode spectrum is repeated in each Brillouin region, the entire mode spectrum can be deduced from the zeroth Brillouin region. The below cutoff attenuation is also shown in Fig. 3.12a. It is clearly demonstrated that there is a major stop band, which is further divided into three sub-stop bands. The magnitudes of the harmonic components of six sampled points in Fig. 3.12a are given in Fig. 3.12b, c, where it is clearly demonstrated that under lossless conditions each of the sampled points is composed of several major harmonics.

When the dielectric loss is present, the situation changes into that shown in Fig. 3.13, where the structure parameters are the same in both figures. In Fig. 3.13a,

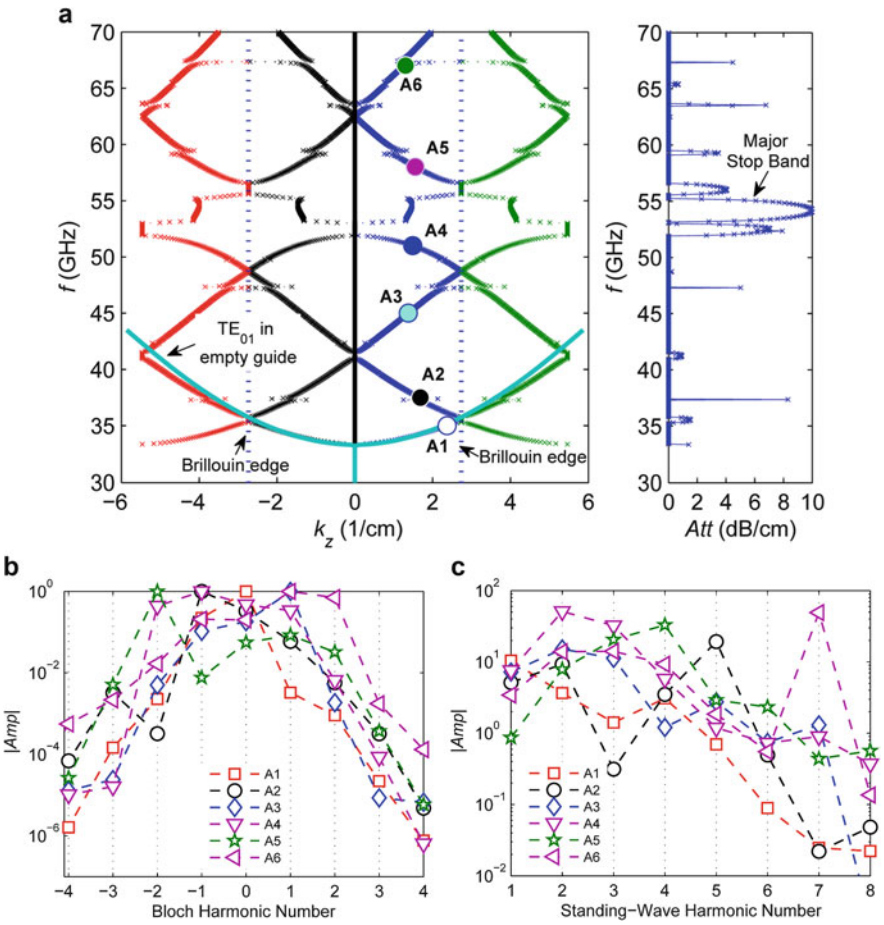

Fig. 3.12 Systematic analysis of the operating TE_{01} mode in waveguide periodically loaded with lossless dielectric material $\varepsilon_r = 7.11$, including (**a**) propagation characteristics of TE_{01} mode, (**b**) normalized amplitudes of Bloch harmonic components, and (**c**) normalized amplitudes of the standing-wave harmonic components ($I/L = 0.87$) (PDW calculated)

the most obvious phenomenon is that between 50 and 62 GHz, the stop band between two backward-wave pass bands is eliminated and the two backward-wave pass bands are unified into one. The sharp attenuation peaks in Fig. 3.12b are also eliminated and the attenuation near the original stop band is relatively stronger than those at other frequencies, as shown in Fig. 3.13a. More explicit explanations can be found in Figs. 3.12b, c. The relative magnitudes of the harmonic components in Fig. 3.13b indicate that the major power of the operating mode in the vacuum region is conveyed by some distinctive harmonic components, which are quite close to the original dispersion curve of the TE_{01} in a hollow waveguide. In other words, the operating modes in the lossy DL waveguide are quite similar to the modes in a hollow waveguide. A comparison between Figs. 3.12c and 3.13c again reveals that

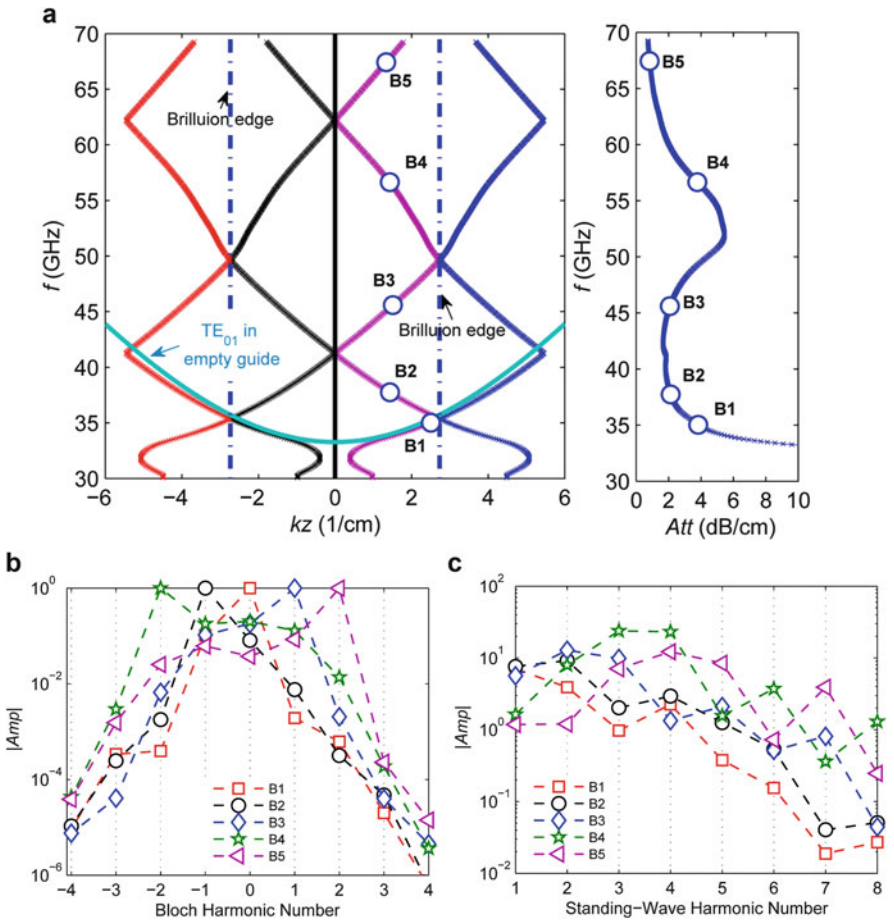

Fig. 3.13 Systematic analysis of operating TE_{01} mode in waveguide periodically loaded with lossy dielectric ($\varepsilon_r = 7.11 - 1.1\ j$) material, including (**a**) mode spectrum of TE_{01} mode and attenuation, (**b**) normalized amplitudes of Bloch harmonic components, and (**c**) normalized amplitudes of the standing-wave harmonic components ($I/L = 0.87$)

the field strength in the dielectric slot is suppressed. The previous study already revealed that strong dielectric loss would induce modal transition in a uniform DL waveguide. Here, in a periodic DL waveguide, dielectric loss also leads to obvious mode spectrum changes with respect to lossless condition, and it is also a kind of modal transition. Details about such a transition process are shown by the field distributions of the sampled points in Figs. 3.12a and 3.13a, as given in Fig. 3.14. The field distributions of the sampled modes A4 and A5 from Fig. 3.12a have similar field distributions. Dielectric loss unifies these two backward-wave modes and changes A4 and A5 distributions into B4 distribution under lossy condition.

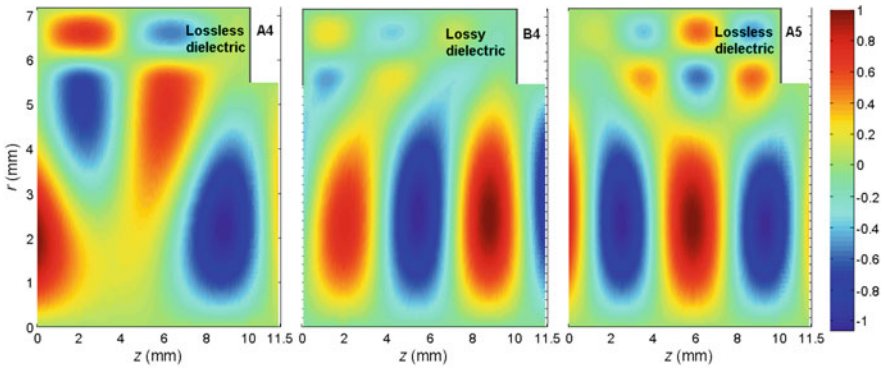

Fig. 3.14 Normalized E_φ components of the sampled points A4 and A5 in Fig. 3.12a and B4 in Fig. 3.13a to demonstrate the dielectric loss-induced modal transition in a periodic DL waveguide

3.3.4 Suppressing the System Periodicity Using Dielectric Loss

First, we define the relative ratio of the energy in the dielectric slot to the energy of a period of the waveguide:

$$\mathrm{FE} = \frac{\iiint_{\text{slot}} \varepsilon_{\mathrm{r}} \vec{E} \cdot \vec{E}^* \mathrm{d}V}{\iiint_{\text{a period}} \varepsilon_{\mathrm{r}} \vec{E} \cdot \vec{E}^* \mathrm{d}V} \tag{3.4}$$

Such a ratio is simply called as FE factor (fractional electric energy). Accurate calculations of the FE in the dielectric slot under both lossless and lossy conditions are given in Fig. 3.15. There are many high FE peaks under lossless conditions, each of which corresponds to a spurious resonant mode in the dielectric slot. When the lossless dielectric turns into lossy material, the energy in the dielectric region is much reduced and the FE in the dielectric slot is severely suppressed accordingly. The FE proximately describes the field distributions of the operating mode in the frequency domain. A comparison of FE between lossless and lossy conditions more explicitly helps us to understand the complicated transformation of the mode spectrums between Figs. 3.12a and 3.13a.

Based on analysis from Sect. 3.3.1, 3.3.2, and 3.3.3 about the transmission characteristics of a periodic DL waveguide, some important phenomena have been found that dielectric loss can cause modal transition between modes that have close dispersion curves and field structures, and simultaneously the strong lossy property can suppress the energy distribution in dielectric slot fraction which makes transmission characteristics in periodic DL waveguide similar to that in hollow

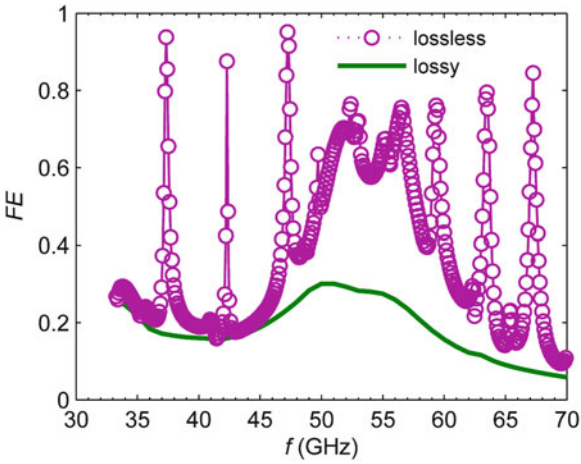

Fig. 3.15 Fractional electric field energy (FE) in the dielectric slot under both lossy and lossless conditions. The *peaks* indicate the resonant modes in the dielectric slots

metal cylindrical waveguide. Hence, the loss property in dielectric layers builds a bridge relation between the DL waveguide and the hollow metal cylindrical waveguide.

3.4 Mode Mapping

In this section, a DL waveguide with inner radius fixed to be $a = 5.495$ mm will be specially investigated for a Ka-band TE_{01} mode gyro-TWT application, especially the mode mapping relation between the empty metal cylindrical waveguide, uniform DL waveguide, and periodic DL waveguide. In order to transmit a wave in the DL waveguide with TE_{01}-like mode distribution in the hollow vacuum region, the operating mode in the DL waveguide is actually a TE_{02}^{d} mode.

An experiment about X-band gyro-TWT loaded with dielectric in rectangular waveguide to suppress dispersion of modes and extend the bandwidth was performed at UC Davis in 1990s [20]. It achieved output power 55 kW, efficiency 11 %, gain 27 dB, and frequency band 11 %. NRL reported their Ka-band gyro-TWT experiment in 2002 [14]. The fundamental harmonic TE_{01} mode in cylindrical waveguide was adopted. It achieved saturated peak power 137 kW, −3 dB band about 3.3 %, voltage 70 kV, and current 10 A. Hence, using periodic lossy ceramic-loaded waveguide as the interaction circuit of a gyro-TWT, it provides multidimensional freedoms to adjust interaction system, including dielectric permittivity, loss tangent $\tan\delta$, material conductivity, and flexible ways to load the dielectric structure. But introducing the lossy dielectric makes the system more complicated and also leads to mode transmission instability. In this section, a method called mode mapping is introduced to figure out the relation between metal cylindrical waveguide, uniform lossy DL waveguide, and periodic lossy DL waveguide.

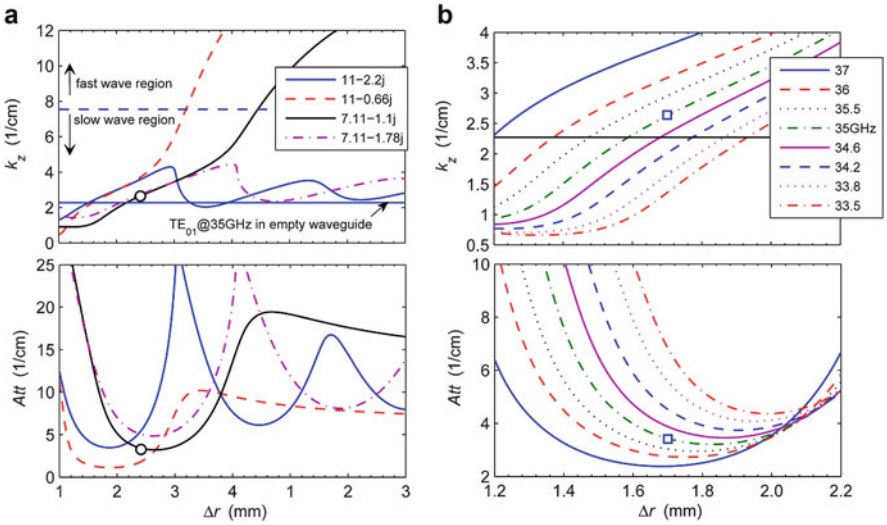

Fig. 3.16 Effect of the dielectric thickness on the propagation characteristic of TE_{02}^{d} mode at 35 GHz (calculated by UDW), where $\varepsilon_r = 11$ indicates the AlN and $\varepsilon_r = 7$ indicates the BeO

Figure 3.16 shows the effect of the dielectric thickness on the propagation characteristics of the TE_{02}^{d} mode, in which both AlN–SiC and BeO–SiC dielectrics with different loss tangents are included. The TE_{02}^{d} mode is inherently under cutoff at 35 GHz when the dielectric layer is relatively thin. With adding the dielectric thickness, the propagation characteristics are changed. For the material with a lower permittivity, the first low attenuation region is corresponding to a thicker dielectric layer. A distinctive feature conveyed by Fig. 3.16 is that, with thicker dielectric layer, stronger dielectric loss prevents the mode from distributing its energy into the dielectric layer and the TE_{02}^{d} mode remains a fast wave. Otherwise, if the material is not lossy enough, it turns into a slow wave. Here, whether a waveguide mode is a fast-wave or a slow-wave mode is determined by whether its phase velocity is faster or slower than that of the speed of free space light. The real part of the wave number is insensitive to the dielectric loss tangent variation, which is important for beam-wave synchronization and helpful to overcome the parameter fluctuation induced by elevated environmental temperature in a real device. In a Ka-band gyro-TWT, the operating TE_{02}^{d} mode should have a wave number almost the same as that of the TE_{01} mode in the hollow waveguide, and a reasonable amount of attenuation is also required to suppress the potential competing instabilities. Taking both factors into consideration, the preliminary dielectric layer thickness is set to be $\Delta r = 1.7$ mm, indicated by the circles in Fig. 3.16.

From the above analysis, the following rules are obtained:

- When the dielectric lay is too thin, TE_{02}^{d} mode is below cutoff ($\varepsilon_r = 11$ AlN: $\Delta r < 0.9$ mm, BeO: $\Delta r < 1.2$ mm).

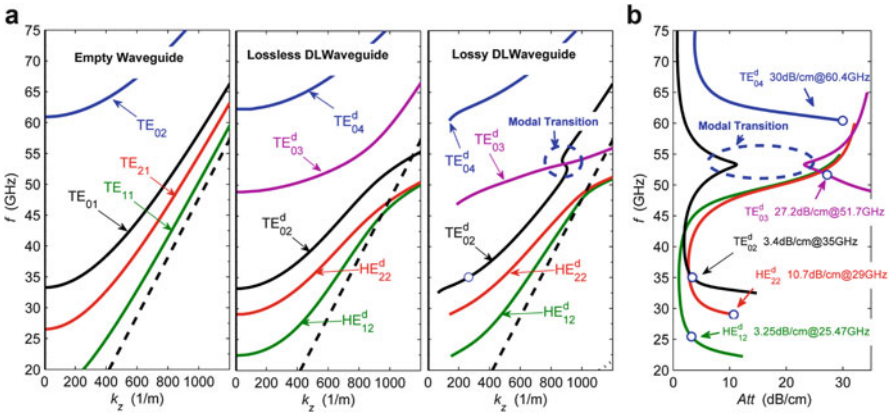

Fig. 3.17 (**a**) Mapping relationship between modes in the hollow waveguide, the lossless DL waveguide, and the lossy DL waveguide as calculated by UDW. (**b**) Attenuation property of lossy DL waveguide ($\Delta r = 1.7$ mm) (UDW is calculated)

- Increasing the thickness of dielectric layer, the TE^d_{02} mode becomes propagating and reaches the lowest attenuation in specific thickness (AlN: 1.1 mm $< \Delta r <$ 1.8 mm, BeO: 1.4 mm $< \Delta r <$ 2.2 mm).
- Further increasing the thickness, the TE^d_{02} mode becomes a slow wave in condition of weak lossy material, while in strong lossy material, TE^d_{02} mode becomes a high-order and low-lossy-type mode. Its attenuation and dispersion fluctuate with the thickness of dielectric material.

If the lossy material BeO–SiC is selected and its parameters are assumed as $\mu_r = 1$, $\varepsilon_r = 7.11 - 1.1\,j$, $\Delta r = 1.7$ mm. In this case, the attenuation of TE^d_{02} mode is 3.4 dB/cm at the frequency of 35 GHz in lossy DL waveguide. Its propagating constant $k_{zr} = 2.64$ 1/cm is a little bigger than that of metal cylindrical waveguide $k_{zr} = 2.27$ 1/cm. The uniform DL waveguide will be further adjusted to compensate such difference.

Figure 3.17 shows the mapping relationship between the hollow waveguide, the lossless DL waveguide, and the lossy DL waveguide. According to the dispersion relations and the field structures, the key modes HE^d_{12}, HE^d_{22}, TE^d_{02}, and TE^d_{04} in the uniform DL waveguide are mapped to TE_{11}, TE_{21}, TE_{01}, and TE_{02} in the hollow waveguide, respectively. The loss-induced modal transition happens between the TE^d_{02} and TE^d_{03} modes near the fast-wave boundary, where both modes are with similar phase velocities and field distributions. After modal transition, the TE^d_{02} mode couples to the original TE^d_{03} mode at frequencies higher than the transition point, and it changes into a fast wave at all frequencies. On the other hand, the TE^d_{03} mode directly couples into the slow-wave region through the transition point. More details about the loss-induced modal transition are addressed in Ref. [17–19]. In addition, since the current structure is optimized to support a stable TE^d_{02} mode, the TE^d_{03} mode and the lower-order HE^d_{12} and HE^d_{21} modes become absorbed into

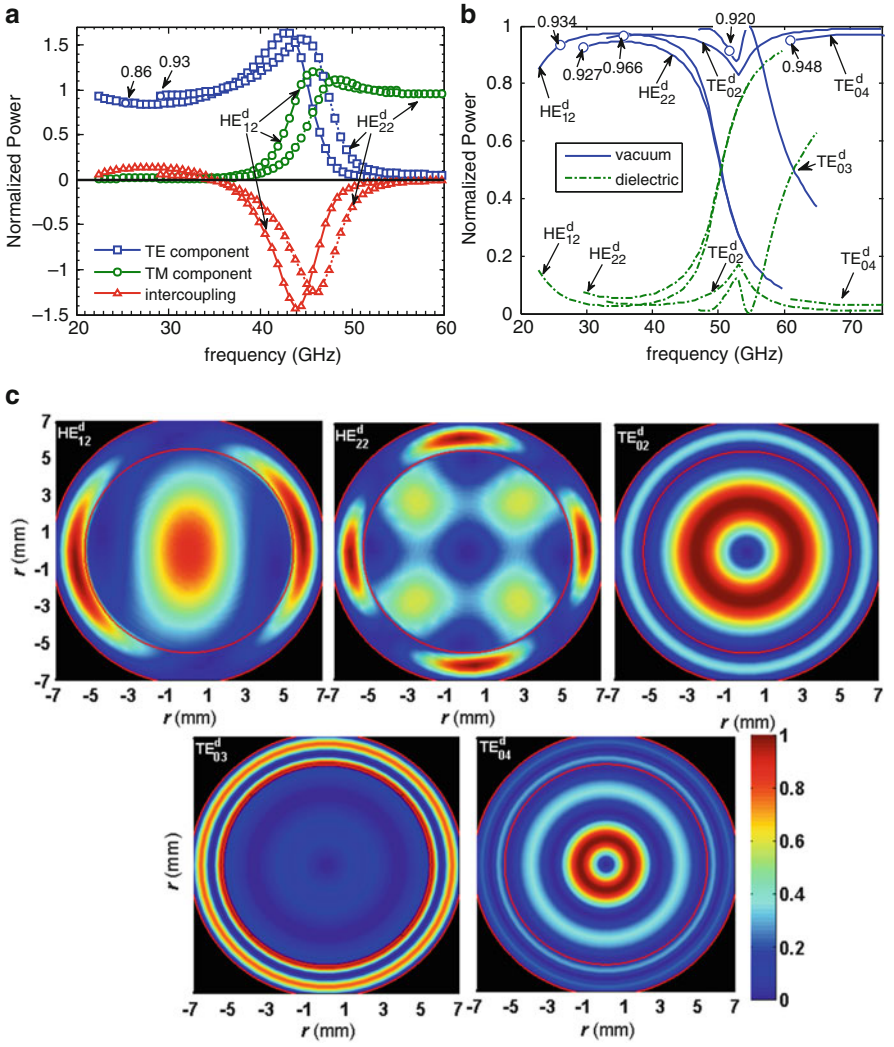

Fig. 3.18 (**a**) Normalized power ratio of TE and TM components in HE^d_{12}, HE^d_{22}, (**b**) mode distributions in space, and (**c**) normalized transverse distributions of the electric energy density of the key modes in the lossy DL waveguide as calculated by UDW

the dielectric layer and experience strong attenuation. As a result, these three modes HE^d_{12}, HE^d_{21}, and TE^d_{03} pose no danger of self-oscillation in the gyro-TWT.

Figure 3.18 shows the normalized transverse distributions of the electric energy density of the key modes in the lossy DL waveguide. The boundary condition introduced by dielectric material makes the noncircular polarized modes to be hybrid modes which can be analytically expressed as a linear combination of TE and TM components. As shown in Fig. 3.18a, the main energy of mixed modes

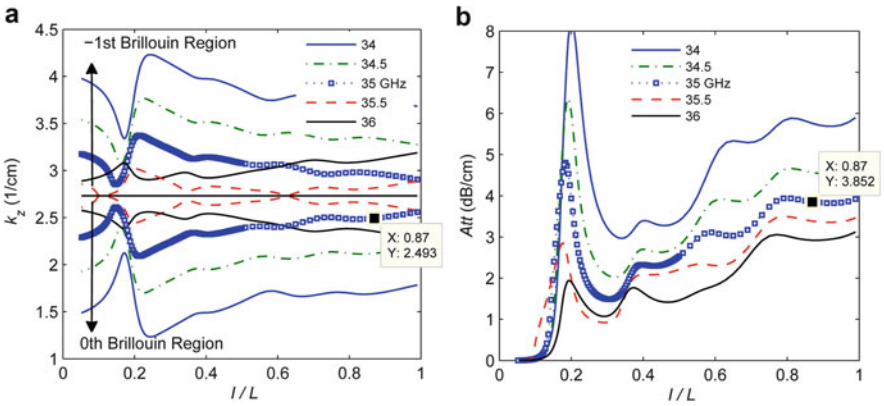

Fig. 3.19 Influence of the dielectric slot fraction on (**a**) the propagation constants and (**b**) the attenuation of the operating TE_{01} mode (calculated by PDW at 35 GHz) (BeO − SiC, $L = 11.5$ mm, $\Delta r = 1.7$ mm)

HE_{12}^{d} and HE_{22}^{d} in fast-wave region is concentrated in TE mode, and in slow-wave region, the main energy is transferred to TM mode. In fast-wave region, the energy of about 95 % is focused in hollow region, as indicated in Fig. 3.18b. Figure 3.18c shows the transverse field distribution of several main modes which are similar to the corresponding modes in metal cylindrical waveguide. The main power of several critical modes in fast-wave region near the electron beam cyclotron resonance is distributed in hollow region (HE_{12}^{d} 93.4 %, HE_{22}^{d} 92.7 %, TE_{02}^{d} 96.6 %, and TE_{04}^{d} 94.8 %). It can be deduced that using metal rings to make truncations periodically on lossy dielectric can enhance relative energy of RF field in hollow region.

According to the transmission property of uniform lossy DL waveguide, the transmission property of periodic lossy DL waveguide is calculated. The influence of the dielectric slot fraction on the operating TE_{01} mode is considered first, as shown in Fig. 3.19. In a periodic system, the propagating constant of operating mode TE_{01} changes symmetrically about Brillouin edge. In the range of $I/L < 0.2$, because of a parasitical oscillation fundamental mode, the curve of attenuation property appears a peak value at $I/L = 0.2$. When the ratio $I/L = 0.87$ is selected, the propagating constant of TE_{01} in zeroth Brillouin region is $k_{zr} = 2.49$ 1/cm at 35 GHz, while in empty waveguide it is $k_{zr} = 2.27$ 1/m.

The lossy dielectric makes the primary power of modes concentrated in the vacuum region in a periodic DL waveguide, as shown in Figs. 3.14 and 3.15. In other words attenuation property of dielectric in periodic system makes the main energy of modes be carried by special harmonic and makes such a mode similar to modes in a smooth waveguide. Considering the special harmonic carrying majority of energy, the dispersion relation and attenuation property of periodic system are shown in Fig. 3.20. By comparing the dispersion relations, it is revealed that modes in periodic lossy DL waveguide and metal smooth cylindrical waveguide are with a one-to-one mapping relation, as recorded in Table 3.1.

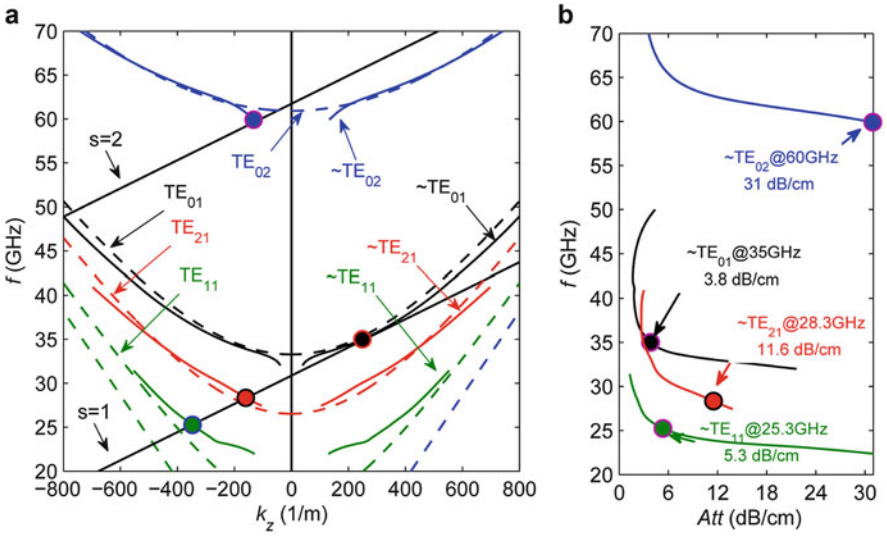

Fig. 3.20 (**a**) Cold dispersion relation and (**b**) attenuation property of interactive circuit with periodic lossy dielectric of Ka-band, TE_{01} mode gyro-TWT

Table 3.1 The mapping relations between the empty waveguide, the uniform DL waveguide, and the periodic DL waveguide

Empty waveguide	TE_{11}	TE_{21}	TE_{01}	TE_{02}
Uniform DL waveguide	HE^{d}_{12}	HE^{d}_{22}	TE^{d}_{02}	TE^{d}_{04}
Periodic DL waveguide	$\sim TE_{11}$	$\sim TE_{21}$	$\sim TE_{01}$	$\sim TE_{02}$

3.5 Conclusion

In this chapter, based on the theory of dielectric waveguide, the influence of the waveguide propagation characteristics from lossy dielectric is systematically investigated. A series of wave mode transmission instabilities are revealed [17–19]:

- When the loss tangent tan δ of dielectric material is higher than certain thresholds, modal transition happens between two nearby modes and generates a pair of independent modes. One suffers from relatively lower attenuation and the other is strongly attenuated.
- The dielectric loss prevents EM wave from effectively penetrating into the dielectric layer. When strong loss dielectric is loaded, the DL waveguide can be equivalent to cylindrical waveguide with imperfect conducting wall. Hence, mode density of lossless DL waveguide is reduced.

Principles of mode selection are summarized as the modes in a uniform or a periodic lossy DL waveguide could be qualitatively divided into two kinds,

namely, weak attenuated modes and strong attenuated modes. A weak attenuated mode distributes major power in the hollow region. A strong loss mode distributes considerable power in the dielectric layer, and it can be suppressed and eliminated by dielectric loss. For a periodic DL waveguide with high slot ratio, the strong dielectric loss can prevent wave mode from distributing power in the dielectric slot; hence, the system periodicity would be suppressed by the lossy dielectric. Hence, periodic lossy property in dielectric layers can be regarded as a bridge between a DL waveguide and a hollow metal cylindrical waveguide. This is very important for the application in gyro-TWTs. In designing an interaction circuit for a Ka-band TE_{01} mode gyro-TWT with periodic lossy DL waveguide, the mode mapping relation between the empty waveguide and the DL waveguide provides important evidence to simplify theoretical investigation of the ECM beam-wave interaction based on the DL waveguide circuit.

References

1. Lee CS, Lee SW, Chuang SL (1986) Normal modes in an overmoded circular waveguide coated with lossy material. IEEE Trans Microw Theory Tech 34:773–785
2. Carlin JW, D'Agostino P (1971) Low-loss modes in dielectric lined waveguide. Bell Syst Tech J 50:1631–1643
3. Miyagi M, Kawakami S (1984) Design theory of dielectric-coated circular metallic waveguides for infrared transmission. J Lightwave Technol 2:116–126
4. Yeh P, Yariv A, Marom E (1978) Theory of bragg fiber. Opt Soc Am 68:1196–1201
5. Ibanescu M, Fink M, Fan S (2000) An all-dielectric coaxial waveguide. Science 289:415–419
6. Ibanescu M, Johnson SG, Soljacic M (2003) Analysis of mode structure hollow dielectric waveguide fibers. Phys Rev E 67:046608
7. Miyagi M, Hongo A, Kawakami S (1983) Transmission characteristics of dielectric-coated metallic waveguide for infrared transmission: slab waveguide model. IEEE Trans Microw Theory Tech 19:136–145
8. Carlin JW, D'Agostino P (1973) Normal modes in overmoded dielectric-lined circular waveguide. Bell Syst Tech J 52:453–486
9. Chu KR, Chen HY, Hung CL et al (1998) Ultrahigh gain gyrotron traveling wave amplifier. Phys Rev Lett 81:4760–4763
10. Chu KR, Chen HY, Hung CL et al (1999) Theory and experiment of ultrahigh-gain gyrotron traveling wave amplifier. IEEE Trans Plasma Sci 27:391–404
11. Chou RC, Lee SW (1988) Modal attenuation in multilayered coated waveguides. IEEE Trans Microw Theory Tech 36:1167–1176
12. Levush B, Blank J, Calame J (1999) Modeling and design of millimeter wave gyroklystron. Phys Plasmas 6:2233–2240
13. Calame JP, Garven M, Danly BG et al (2002) Gyrotron-traveling wave-tube circuits based on lossy ceramics. IEEE Trans Electron Devices 49:1469–1477
14. Garven M, Calame JP, Danly BG et al (2002) A gyrotron-traveling-wave tube amplifier experiment with a ceramic loaded interaction region. IEEE Trans Plasma Sci 30:885–893
15. Tigelis IG, Vomvoridis JL, Tzima S (1998) High-frequency electromagnetic modes in a dielectric-ring loaded beam tunnel. IEEE Trans Plasma Sci 26:922–930
16. Blank M, Danly BG, Levush B (2000) Experimental demonstration of W-band gyroklystron amplifiers with improved gain and efficiency. IEEE Trans Plasma Sci 28:706–711

17. Du CH, Liu PK (2009) A lossy dielectric-ring loaded waveguide with suppressed periodicity for gyro-TWTs applications. IEEE Trans Electron Devices 56:2335–2342
18. Du CH, Xue QZ, Liu PK et al (2009) Modal transition and reduction in a lossy dielectric-coated waveguide for gyrotron-traveling-wave tube amplifier applications. IEEE Trans Electron Devices 56:839–845
19. Du CH, Xue QZ, Liu PK (2008) Loss-induced modal transition in a dielectric-coated metal cylindrical waveguide for gyro-traveling-wave-tube applications. IEEE Electron Device Lett 29:1256–1258
20. Leou KC, McDermott DB, Luhmann NC (1996) Large-signal characteristics of a wide-band dielectric-loaded gyro-TWT amplifier. IEEE Trans Plasma Sci 24:718–726

Chapter 4
Instability Competition in an Ultrahigh Gain Gyro-TWT Amplifier

Abstract In a gyrotron traveling-wave tube amplifier (gyro-TWT) circuit, one of the cyclotron harmonic couples with an eigen wave mode. Such a beam-wave coupling forms a growing instability mechanism. Under the condition that the absolute instabilities are not strong enough to build up oscillations, a convective instability is capable of amplifying a driving wave. In order to achieve high power and high gain, a gyro-TWT is normally with the interaction circuit exceeding tens of wavelengths. In such a long interaction circuit, it is extremely challenging for the convective instability to survive, simultaneously suppressing all competing absolute instabilities. This chapter takes a Ka-band gyro-TWT as an example. It presents a series of basic concepts and a general analyzing process. Studying the instability competition is relatively complicated, but the related principles are very interesting and are generally applicable to all kinds of gyro-devices.

Keywords Gyro-TWT • Absolute instability • Convective instability • Instability competition

4.1 Introduction

High-power coherent millimeter-wave sources attract worldwide intense attention due to its potential value in a series of important applications, including high-resolution radar, millimeter-wave electronic countermeasure, high data rate communication, nonlethal weapons, nondestructive detection, accelerator, plasma heating in fusion, industry heating, ceramic sintering, and so on [1]. A gyrotron traveling-wave tube (gyro-TWT) amplifier based on the relativistic electron cyclotron maser (ECM) is capable of radiating electromagnetic (EM) power on the level of hundreds of kilowatts, which makes it the first-choice candidate source for the radiating transmitter of next-generation high-power millimeter-wave radar. Since the 1970s, a series of experiments have adopted various kinds of interaction circuits to improve the instability and performance of gyro-TWTs [1]. In 1998, Prof. K. R. Chu

C.-H. Du and P.-K. Liu, *Millimeter-Wave Gyrotron Traveling-Wave Tube Amplifiers*,
DOI 10.1007/978-3-642-54728-7_4,

and his research group reported a Ka-band TE_{11} mode gyro-TWT experiment based on lossy Aquadag-loaded distributed loss circuit. The excellent experiment achievement, especially ultrahigh gain up to 70 dB, proved the feasibility of distributed wall lossy to suppress the instability competition and leaded to a research upsurge focusing on gyro-TWTs [2]. Later, a series of lossy circuits based on various kinds of lossy schemes were tested in experiments [3–5]. These encouraging achievements proved the general feasibility of strong lossy scheme to stabilize the serious instability competition in a gyro-TWT. In other words, during the past half century, suppressing the instability competition by strong lossy material is the major breakthrough in gyro-TWT research, which promotes the gyro-TWTs transferring from lab to applications.

4.1.1 Analysis Method of the Instability Competition

A gyro-TWT employs a helically traveling electron beam to interact with an EM mode in the waveguide circuit. Under amplification state, a gyro-TWT operates on the convective instability, and the EM wave injected by input power is amplified along the direction electron beam is traveling. Once the driving power is switched off, the zero-drive stability requires the system turn off the output power immediately [1, 6]. In the interaction circuit of a gyro-TWT, the ECM resonance happens anywhere when a cyclotron mode harmonic gets resonant with a waveguide mode on a specified frequency and wavelength. If the electron beam-wave coupling exceeds certain threshold strength, the absolute instability of the ECM resonance builds up a self-exciting oscillation [7]. Besides, refection on both ports of the interaction circuit may induce oscillation based on regenerative amplification of reflected EM power [6], which belongs to oscillation from convective instability. In a word, if beam-wave coupling strength exceeds certain threshold, an absolute instability or convective instability becomes the origin of an oscillation. The self-excited oscillation from absolute instability is the inherent characteristic of the interaction system, while the regenerative amplification-induced oscillations is a technique factor which could be suppressed by improving matching conditions on both wave ports. Exploring solutions to suppress various kinds of oscillations is the major subject to study the instability competition.

The threshold parameters of an oscillation, such as the threshold current and critical length, are normally employed to identify the system stability. These parameters are among the primary considerations to maintain amplification and simultaneously suppress oscillation. A gyro-TWT amplifier with operating current lower than the threshold current, or with interaction circuit length shorter than the critical length, will operate without self-excited oscillation.

After decades of theoretical and experimental research on gyro-TWTs, three investigation methods are proposed here, namely, linear theory based on plasma kinetics, self-consistent nonlinear theory based on frequency domain particle tracking, and particle-in-cell simulation (PIC). The first one, the linear theory, is concise

and of high simulation efficiency, but it is valid only under perturbation condition. Therefore, it is suitable for primary diagnosis and start-oscillation investigation. Especially, it is efficient in determining the threshold parameters of a simple system. The second method, the self-consistent nonlinear theory, is a method of semi-analytical and semi-numerical method of high accuracy and mediate simulation speed. It employs analytical solution to describe the transverse distribution of the EM field and numerical integration to calculate the longitudinal amplitude evolution. Hence, it is suitable for most of the traveling-wave circuit-based gyro-TWTs. The third method, the PIC simulation, is a full numerical FDTD method with charged particles, and it performs the approximation of highest accurately to the real condition. Unfortunately, a gyro-TWT is of relatively oversized system which takes too much computational resources. So it is proposed to carry out preliminary large-scale parameter investigation based on the linear theory and nonlinear theory and the final stage verification based on PIC simulation. This chapter focuses on the linear theory and nonlinear theory only. Both theoretical tools are efficient in estimating the threshold parameters of the system.

The linear theory, after proper approximation, would generate stability criteria for a simple and homogeneous system. However, the real situation is that the instability competition in the interaction circuit has strong dependence on the electron beam parameter distribution, nonuniform circuit, and boundary condition. The linear theory is of relative inability to manage all of these complicated factors. The nonlinear theory is capable of taking most of the sensitive factors in to consideration. Especially, it is capable of modeling a circuit of multistage structure and efficiently calculating both amplification and self-exciting oscillation. Taking advantage of the outstanding simulation efficiency of the linear theory and nonlinear theory to investigate the system performance and oscillation thresholds is the major topic of this chapter.

4.1.2 The Key Factors of Instability Competition

It is complicated to systematically study the instability competition in the interaction circuit. A gyro-TWT is a multi-degree freedom system. A systematic method to analyze the instability competition is conveyed through investigating the fundamental harmonic TE_{11} mode gyro-TWT, parameters are from Refs. [6, 8]. Since the TE_{11} mode is the lowest order cylindrical waveguide, it is the simplest example, and this chapter considers the absolute instability from the $TE_{11}^{(1)}$ mode and the $TE_{21}^{(2)}$ mode only, where the superscript (n) indicates nth cyclotron harmonic interaction. The internal feedback influence of the backward wave plays an important role in the absolute instability [6]; therefore, this chapter explores the backward-wave influence first [8]. A gyro-TWT is normally constituted of several stages. In order to achieve global zero-drive stability, each stage should be locally stabilized first. Local stability investigation focuses on the potential oscillations in each stage, including backward-wave oscillation in the input coupler stage, distributed-loss-loaded linear

stage oscillation, and unloaded nonlinear stage oscillation. Other problems are also investigated, such as multi-steady states of the instability, reflection-induced oscillations, and influence from magnetic tapering. An important conclusion will be finalized that the distributed wall loss linear stage inherently imposes bunching onto the electron beam, and such a kind of pre-bunching is an essential condition for efficient interaction in the downstream nonlinear stage. Based on this, a conceptual design scheme called pre-bunching exciting amplification will be proposed for further improving the performance of a gyro-TWT.

4.2 Balance Between the Backward Wave and Forward Wave in an Absolute Instability

This section mainly addresses how to determine the threshold parameters of a self-exciting oscillation in the beam-wave interaction system and reveals the role a backward wave played in the absolute instability oscillation. A gyro-TWT normally operates with zero-drive stability, which means the output power will immediately shut down once the input driving power is turned off, demonstrating no oscillation. To achieve the zero-drive stability, the operating parameters of a gyro-TWT should be carefully balanced during the design stage, as a way to explore an oscillation-free operation-parameter window and to achieve reasonable amplification performance. The threshold parameters of oscillation, normally absolute instability oscillation, will be determined first to estimate the safe parameter window for amplification. When a cyclotron electron beam is injected into an interaction system and a spurious oscillation is excited, outgoing EM waves propagate out of both upstream port and downstream port. Theoretical investigation in frequency domain searches for converged solutions meeting outgoing boundary condition on both ports. A converged solution means a set of parameters to determine all of the system freedoms. Such a solution is a possible oscillation state of the system. Linear theory based on the linearized Vlasov equation and Laplace transformation is capable of determining the axial field profile of the system. By applying outgoing boundary condition, it could be employed to determine an oscillation state. Since the linear theory is built up based on perturbation assumption, it only converges on system solutions of perturbation influence. Hence, each converged solution from the linear theory indicates a start-oscillation state. The operating parameters of such a solution are the thresholds of this oscillation. It is relatively more complicated to determine the thresholds by nonlinear theory. Since nonlinear theory can converge on solutions of any interaction strength, such a solution indicates a real system case, which may be under perturbation condition, linear interaction, saturated condition, or even oversaturated condition. The beam-wave interaction efficiency is applied to qualitatively identify the beam-wave interaction strength. According to enormous simulation experiences, a system state with interaction efficiency between 10^{-6} and 10^{-3} normally becomes most sensitive to operating parameters. Hence, in nonlinear theory investigation, any system state with interaction efficiency between 10^{-6} and

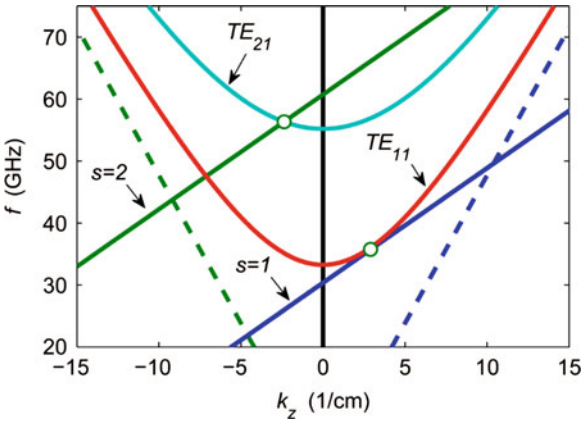

Fig. 4.1 The beam-wave cold dispersion relation of a Ka-band TE_{11} mode gyro-TWT interaction system

Table 4.1 The operating parameters of a Ka-band fundamental harmonic TE_{11} mode gyro-TWT

Operation mode	TE_{11}
Cyclotron harmonic	Fundamental
Waveguide inner radius	$r_w = 0.264$ cm
Lossy layer thickness	$\Delta r = 0.08$ mm
Lossy material resistivity	$\rho = 30,000\rho_{cu}$
Beam voltage	100 kV
Beam current	5 A
Beam velocity ratio	$v_\perp/v_z = 1.0$
Guiding center	$r_c = 0.36\, r_w$
Applied magnetic field	$B_0 = 1.28$ T (tangential magnetic field $B_g = 1.31$ T)

10^{-3} is identified as the start-oscillation state. According to former experiences, threshold parameters predicted by both linear theory and nonlinear theory are well consistent between each other when such an experiential threshold is defined.

A Ka-band gyro-TWT is employed as an example for theoretical investigation. The interaction circuit and dispersion relation of a millimeter-wave Ka-band fundamental harmonic TE_{11} mode gyro-TWT of ultrahigh gain is shown in Fig. 4.1, and parameters are given in Table 4.1. The circuit structure and operating parameters originate from the experiment published in the paper of Prof. K. R. Chu in 1999 [6], but not exactly the same.

From the cold dispersion relation in Fig. 4.1, it is found that the absolute instabilities could happen in the tangential region between the fundamental harmonic and the TE_{11} mode, which is quite close to the cutoff frequency or happens close to the cross point between the second harmonic and the TE_{21} mode. Oscillations from this pair of absolute instabilities are called $TE_{11}^{(1)}$ forward-wave oscillation and $TE_{21}^{(2)}$ backward-wave oscillation, respectively. Before investigating the performance of the amplifier, the $TE_{11}^{(1)}$ absolute instability will be set as an example to investigate some fundamental dynamics about self-excited oscillations in a gyro-TWT.

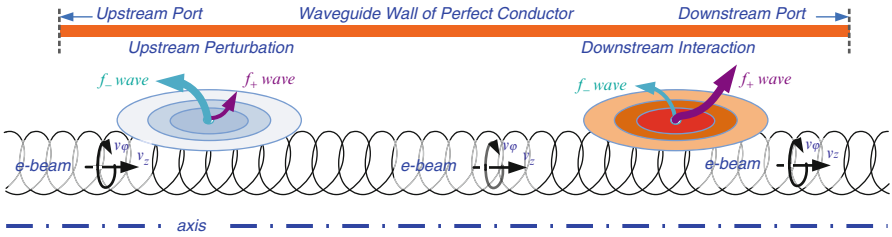

Fig. 4.2 A schematic demonstration of the internal feedback dynamics in an absolute instability oscillation

4.2.1 Internal Feedback Dynamics of an Absolute Instability

When a wave gets synchronized with the cyclotron electron beam, a self-excited oscillation can be excited originating from the absolute instability. For such an oscillation under start-oscillation condition, the operating current I_b and circuit length L of the system are identified as the threshold current I_{st} and critical length L_C of the oscillation, respectively. Both parameters, I_{st} and L_C, are the popular ones employed to identify the stability of the system. In other words, it is the up limit of the parameter window maintaining the oscillation-free state. Before studying the complicated beam-wave interaction in a real gyro-TWT circuit, a simple uniform waveguide of perfect conductor, displayed in Fig. 4.2, is investigated first to understand the fundamental physics of an absolute instability oscillation.

Figure 4.3 shows the dispersion relation, the field profile, and the normalized electron beam efficiency of the start-oscillation state of $TE_{11}^{(1)}$ absolute instability. Simulation automatically converges on a solution with an oscillation frequency right close to the cutoff frequency, as shown in Fig. 4.3a. The oscillation is excited by the $TE_{11}^{(1)}$ absolute instability in such a simple circuit, and propagates toward both directions, as indicated by a forward-wave component f_+ and a backward-wave component f_-. From the complex total field distribution, the forward-wave component and backward-wave component can be determined via

$$f_+ = \frac{-jk_z f(z) + f'(z)}{-2jk_z} e^{+jk_{zr}z} \tag{4.1}$$

$$f_- = \frac{jk_z f(z) + f'(z)}{2jk_z} e^{-jk_{zr}z} \tag{4.2}$$

where $f(z)$ indicates the total field profile and k_z is the complex propagation constant $k_z = k_{zr} + ik_{zi}$. The field profiles under start-oscillation condition are shown in Fig. 4.3b. The total fields from both the linear theory and nonlinear theory are exactly the same. In Fig. 4.3b, the total field $f(z)$ decomposes into a smooth forward growing wave and a backward strengthened wave. Especially, the backward wave demonstrates reduced field strength close to the downstream port. Here a detuning

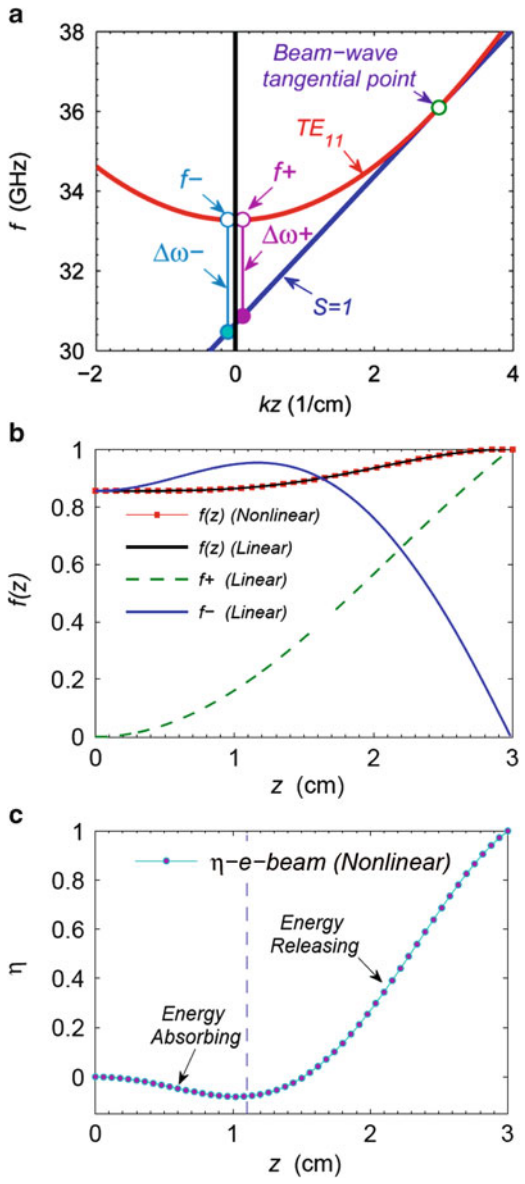

Fig. 4.3 (**a**) The beam-wave synchronization relation of the forward-wave f_+ and backward-wave f_- with respect to the fundamental harmonic $s = 1$. Magnetic field $B_0 = B_g = 1.31$ T is applied. (**b**) Axial field profile of the $TE_{11}^{(1)}$ absolute instability oscillation, where the square red line indicates the nonlinear theory calculated total field, other lines are calculated by linear theory, and f_+ and f_- indicate the forward wave and backward wave, respectively. The start-oscillation solution frequency is $(f_{osc} - f_c)/f_c = 1.190 \times 10^{-4}$. The threshold beam current is $I_{st} = 0.5074$ A, other parameters are as given in Table 4.1. (**c**) The normalized electron beam efficiency under start-oscillation condition

frequency defined as $\Delta\omega = \omega - k_z v_z - s\Omega_e/\gamma$ is introduced to qualitatively identify the detuning condition from ideal beam-wave synchronization. Taking both Figs. 4.2 and 4.3a into consideration, the detuning conditions of both wave components are positive and approximately equal to each other $\Delta\omega_+ \approx \Delta\omega_- \geq 0$, which means that both the wave components are capable of synchronizing with the fundamental harmonic $s = 1$ and maintaining positive energy deposition phase to draw power

from the electron beam. From the normalized electron beam efficiency in Fig. 4.3c, it is easy to understand the field profiles in Fig. 4.3b. When an undisturbed cyclotron electron beam is injected from the upstream port, it encounters the backward wave of the highest strength and will be modulated to get synchronizing in phase space. During this initial modulation, some electrons will be decelerated to gain higher angular frequency, and others will be accelerated to slow down angular frequency. The overall effect of such initial modulation stage demonstrates electron absorbing energy, as shown in Fig. 4.3c that the electron efficiency initially grows in the minus region. Since both wave components meet energy-releasing condition $\Delta\omega_+ \approx \Delta\omega_- > 0$, after the initial bunching stage, both forward wave and backward wave are capable of continuously extracting energy from electron beam-based electron cyclotron maser (ECM) interaction.

It is generally summarized that the EM wave from disturbance of the absolute instability propagates toward both upstream and downstream directions. For a wave close to the cutoff frequency region, it is of extremely low group velocity and of the highest beam-wave coupling strength. Hence, a close-to-cutoff oscillation originating from an absolute instability is easy to be excited, and both wave components therein are with low group velocity and approximately equal detuning conditions. In other words, both wave components in the oscillation are capable of continuously modulating the electron beam. In a uniform interaction circuit without any additional disturbance on both wave ports, the forward wave and backward wave in the oscillation are both essential traveling waves and grow along inverse directions. The backward wave bunches the incoming electron beam, and the forward wave also could bunch the forward traveling electron beam. Keep in mind that the group velocity v_g of the wave is normally much slower than the axial velocity of the electron beam v_z. The downstream electron beam becomes better modulated and normally more strongly interacts with both the wave components. If the beam-wave coupling is strong enough, interaction from such internal feedback is capable of growing up from noise-level perturbation into efficient strong radiation.

4.2.2 Magnetic Tuning

Magnetic tuning is constantly applied to optimize the performance of a gyrotron. The magnetic field directly determines the electron cyclotron frequency Ω_e and the detuning condition $\Delta\omega$ from ideal beam-wave synchronization. Hence, it is also one of the most sensitive parameters influencing the thresholds of a potential oscillation. Figure 4.4 demonstrates the influence of the magnetic tuning to the threshold current I_{st} and critical length L_C of the $TE_{11}^{(1)}$ oscillation in a uniform circuit. From Fig. 4.4a, for a circuit of fixed length $L = 3$ cm, stronger magnetic field strength results a higher start-oscillation current I_{st} and higher oscillation frequency f_{osc}. From Fig. 4.4b, for a fixed beam current of $I_b = 5$ A, stronger magnetic field strength also leads to longer critical length L_C. Taking both figures into consideration, generally speaking, either higher beam current or longer interaction circuit makes positive

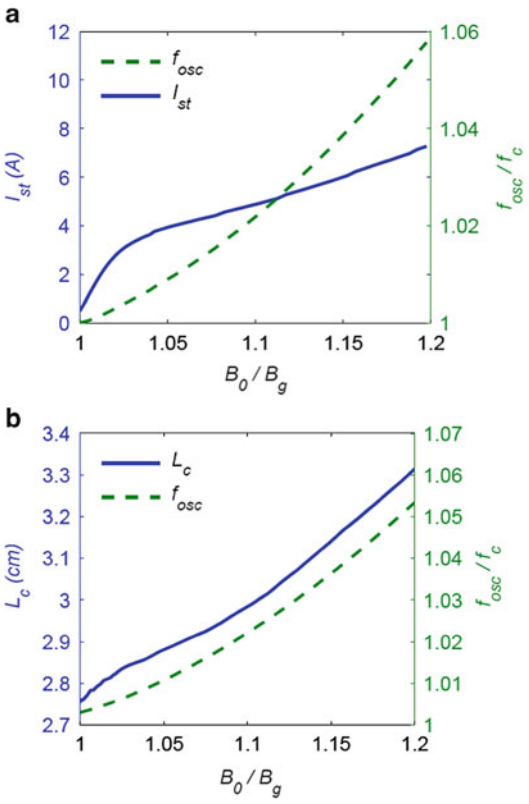

Fig. 4.4 The influence from the magnetic tuning to the start-oscillation thresholds of the $TE_{11}^{(1)}$ absolute instability, (**a**) threshold current I_{st}, assuming circuit length $L = 3$ cm, and (**b**) critical length L_C, assuming current $I_b = 5$ A. Other operation parameters are as given in Table 4.1, where B_g is the tangential magnetic field strength

contribution to enhance the internal feedback strength of an absolute instability and to raise an oscillation from noise-level perturbation into strong radiation.

In order to further look into the dynamics of the magnetic tuning, Figure 4.5 shows the cold beam-wave dispersion relations and the start-oscillation field profiles of $TE_{11}^{(1)}$ absolute instability under different magnetic field strengths B_0. From the condition Fig. 4.5a to condition Fig. 4.5d, the magnetic field B_0 increases from below tangential magnetic field strength $B_0 = 0.98\ B_g$ to above tangential magnetic field strength $B_0 = 1.15\ B_g$, the beam-wave resonance automatically converges at specified frequencies during this process. Since an oscillation contains a forward-wave component and backward-wave component, both wave components under different conditions are also shown in the dispersion maps from Figs. 4.5a–d. The field profiles of the start-oscillation conditions change accordingly, as shown in Figs. 4.5e–h. Under the below tangential condition in Fig. 4.5a, the forward wave is with obviously smaller detuning than the backward wave $0 < \Delta\omega_+ < \Delta\omega_-$; hence, the forward wave becomes dominant in the overall field profile, as shown in Fig. 4.5e. Under the tangential condition in Fig. 4.5b, absolute instability oscillation converges at frequency very close to the cutoff frequency. Both wave components are with extremely low group velocity and both with

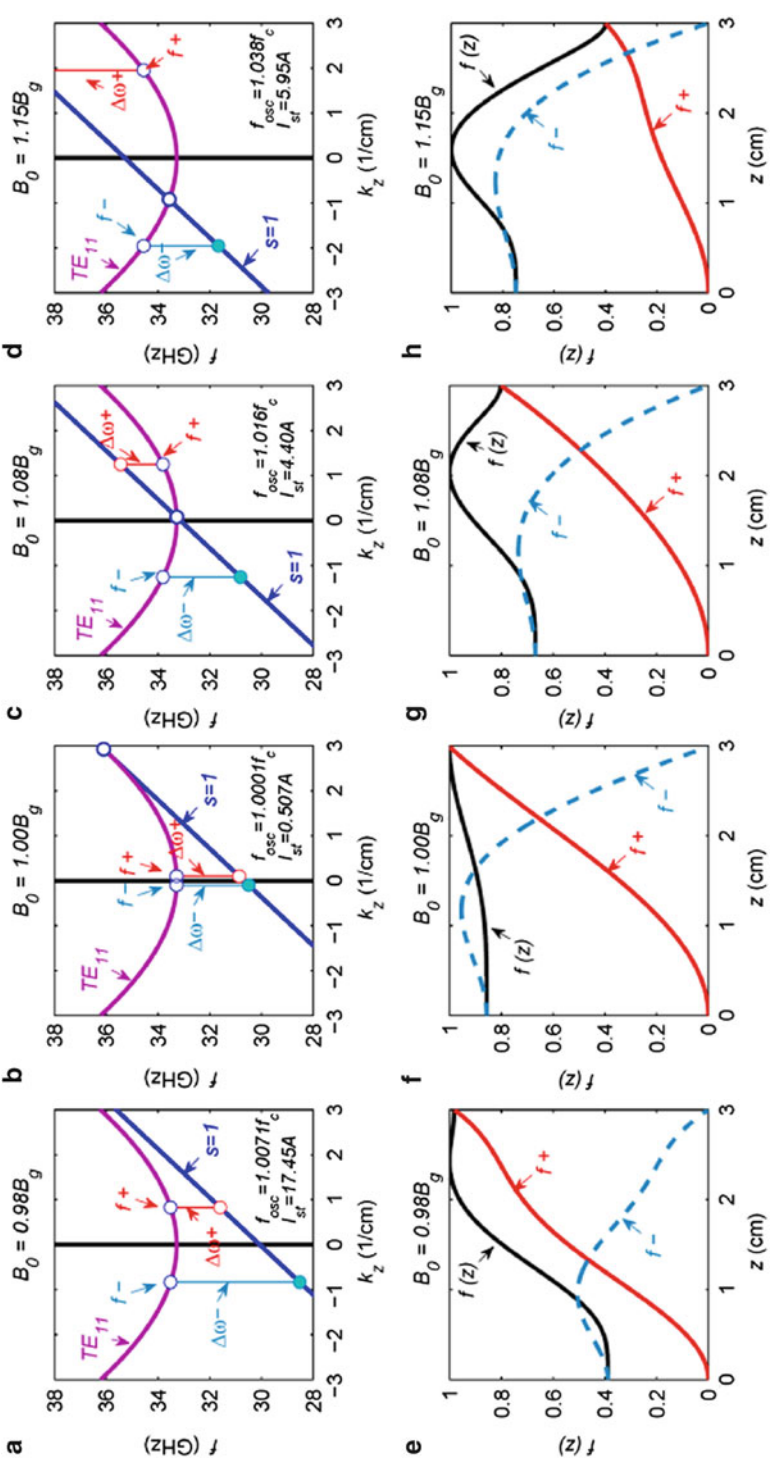

Fig. 4.5 The evolution process of the cold dispersion map and field profiles of the absolution instability oscillation during the magnetic tuning from beam-wave bellow-tangential condition to beam-wave crossing in backward-wave region

almost approximately equal detuning conditions $0 < \Delta\omega_- \approx \Delta\omega_+$. Hence, the start-oscillation fields are with comparable forward-wave and backward-wave profiles, and it reaches the lowest threshold current $I_{st} = 0.507$ A. As the magnetic field becomes stronger $B_0 = 1.08\ B_g$ in Fig. 4.5c, where the cyclotron beam mode crosses the TE_{11} mode around the cutoff frequency. The backward wave still maintains a normal positive detuning $\Delta\omega_- > 0$, but the forward wave becomes a negative detuning $\Delta\omega_+ < 0$. Under even stronger magnetic field $B_0 = 1.15\ B_g$ in Fig. 4.5d, the cyclotron beam and wave cross in the backward-wave region. Stronger magnetic field also leads to higher oscillation frequency, where both wave components are with higher propagation constants.

The backward wave is still with a normal positive detuning $\Delta\omega_- > 0$. The forward wave is located far below the cyclotron beam mode and becomes seriously detuning $\Delta\omega_+ < 0$ from the synchronization. As result, start-oscillation profile of beam-wave resonance in backward-wave region becomes backward-wave dominant. It is summarized that when magnetic field strength is tuned from below tangential condition to beam-wave crossing in the backward-wave region, the oscillation field profiles of the absolute instability change from a forward-wave dominant distribution to a backward-wave dominant distribution. During this process, the backward-wave component always maintains a positive detuning $\Delta\omega_- > 0$, while the forward-wave component changes from a positive detuning $\Delta\omega_+ > 0$ in a forward-wave dominant field profile into a negative detuning $\Delta\omega_+ < 0$ in a backward-wave dominant field profile. Hence, the overall field profile of an oscillation results from the balance between the backward wave and forward wave in an absolute instability.

4.2.3 High-Order Axial Mode

Both linear theory and nonlinear theory are suitable to determine the threshold parameters of electron cyclotron maser (ECM) interaction in a uniform circuit. The analytical linear theory is the more efficient one to calculate the start condition, while the nonlinear theory is also capable of calculating the saturated state. From Figs. 4.3, 4.4, and 4.5, the $TE_{11}^{(1)}$ absolute instability has been systematically investigated, but confined to only the 1st axial mode. Similar to the eigen solutions in a closed cavity with high-order axial modes, an absolute instability oscillation in a gyro-TWT circuit also possibly turns out to be an high-order axial mode distribution. Fixing all the operating parameters, and applying the outgoing boundary condition on both upstream port and downstream ports, the first three-order axial modes of both $TE_{11}^{(1)}$ forward-wave oscillation and $TE_{21}^{(2)}$ backward-wave oscillation in lossless circuit are obtained by using both linear and nonlinear theories to solve the oscillation frequency and critical length, as demonstrated in Fig. 4.6. There are also axial mode solutions higher than 3rd order, but not listed here. The field profiles from both theories excellently agree with each other. A higher-order axial mode normally requires a higher threshold current I_{st} and a longer critical length L_C to

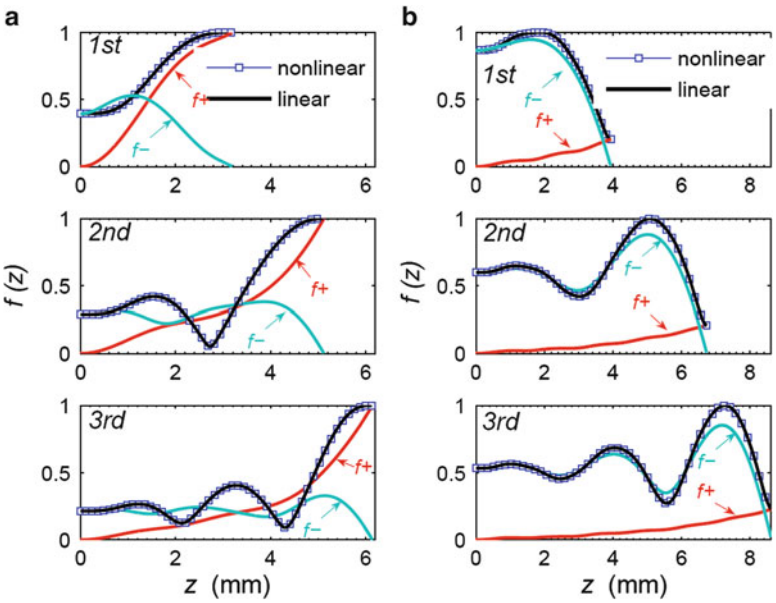

Fig. 4.6 The normalized field profiles of the first three orders of (**a**) $TE_{11}^{(1)}$ oscillation and (**b**) $TE_{21}^{(2)}$ oscillation, where the f_+ and f_- indicate the forward-wave component and backward-wave component, respectively, assuming waveguide of perfect conductor and beam current $I_b = 10$ A. Other parameters are the same as in Table 4.1. Both the red lines and the square lines indicate the total field profiles of the absolute instabilities

build up oscillation. One axial mode is just a possible solution of the oscillation. It means that if the oscillation is built up, it may steadily exhibit in one of the axial mode or may iteratively switch between several axial modes. If the beam-wave coupling strength exceeds the critical strength, such as operation current I_b higher than the threshold current I_{st}, or if the circuit length L is longer than the critical length L_C to enhance the internal feedback influence, one axial mode or iteratively several axial modes may be built up. Oscillation of each axial mode also can be decomposed into a forward-wave component and a backward-wave component and meets the outgoing boundary condition at both ports. Several methods could be applied to determine the order of the axial mode, such as the transit angle [9], electron beam energy deposition rate [9], and axial field profile [8]. Applying the field profile shape to determine the order of an axial mode is more intuitional and convenient. In this chapter, the order of the axial mode will be determined based on the numbers of the concave-convex shapes of the field profile. Figure 4.6 reveals that a forward-wave oscillation generated by $TE_{11}^{(1)}$ forward-wave absolute instability is dominated by the forward-wave component, and a backward-wave oscillation generated by the $TE_{21}^{(2)}$ backward-wave absolute instability is dominated by the backward-wave component. For both kinds of oscillations, a high-order axial mode is with a longer critical length L_C and oscillates at a higher frequency. Normally, a high-order axial mode is with a larger wave number k_z.

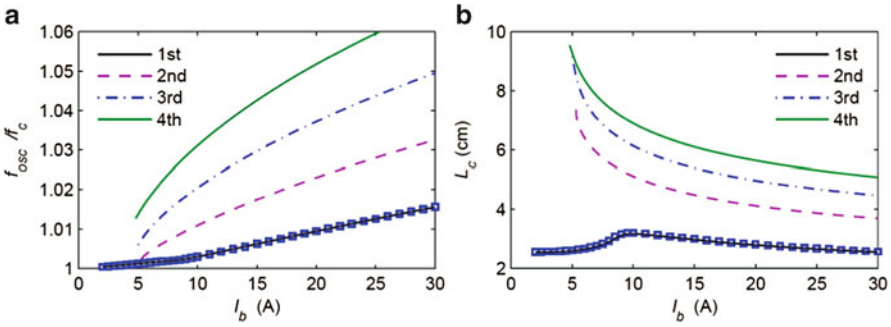

Fig. 4.7 (**a**) Oscillation frequency and (**b**) critical length vs. beam current of the $TE_{11}^{(1)}$ mode gyro-TWT forward-wave absolute instabilities, where the 1st-order axial mode is calculated by both the linear theory (*real linear*) and nonlinear theory (*squares*)

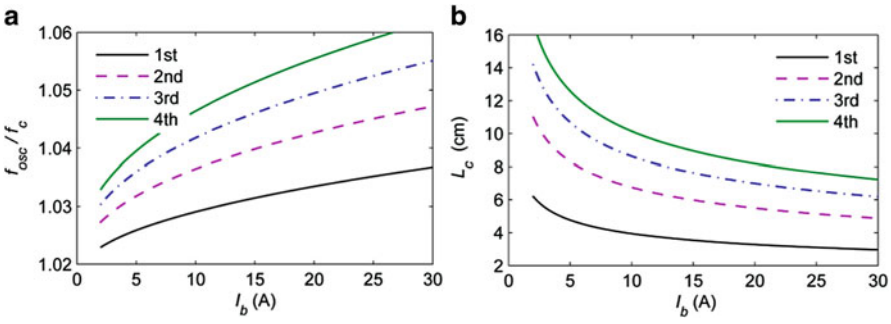

Fig. 4.8 (**a**) Oscillation frequency and (**b**) critical length vs beam current of the $TE_{21}^{(2)}$ mode gyro-TWT backward-wave absolute instabilities, where f_c indicates the cutoff frequency of the TE_{21} in unloaded waveguide

The influence of the beam current I_b to the first three axial modes of both $TE_{11}^{(1)}$ oscillation and $TE_{21}^{(2)}$ oscillation are given in Figs. 4.7 and 4.8, respectively. Generally speaking, a higher-order axial mode is of higher oscillation frequency and requires a longer interaction circuit to build up oscillation. From the beam-wave coupling voltage defined in Chap. 3, the beam-wave coupling strength is linearly proportional to the beam current. A smaller beam current usually requires a circuit of longer critical length to build up an oscillation. However, the 1st axial mode of $TE_{11}^{(1)}$ oscillation is an exception. Under small beam current ($I_b < 10$ A), as shown in Fig. 4.7a, b, it requires a shorter critical length to build up oscillation. The 1st axial mode of the $TE_{11}^{(1)}$ oscillation is of the smallest wave number and the lowest frequency. Once its wave number becomes smaller, the backward-wave component becomes better synchronized to the fundamental cyclotron mode, and both forward-wave and backward-wave components could more effectively distract electron beam energy. Stronger coupling leads to shorter start-oscillation threshold length. Such an abnormal phenomenon of shorter start-oscillation threshold length under lower beam current is called self-induced constriction [8].

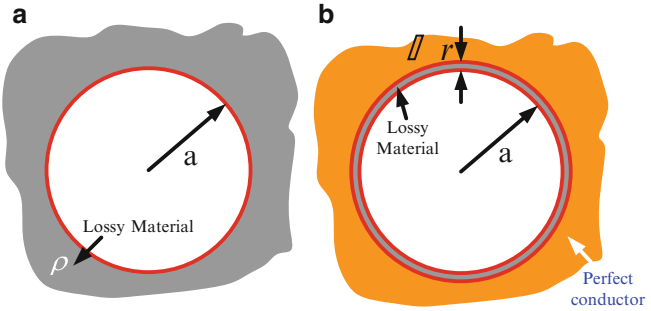

Fig. 4.9 (**a**) Lossy material-loaded cylindrical waveguide, and (**b**) a thin lossy layer-coated cylindrical waveguide

4.2.4 Waveguide Wall Loss

In the 1980s, the initial theoretical and experimental works in NRL revealed the positive influence of lossy circuit on improving the gyro-TWT performance [10]. Until 1990s, under strong theory and experiments backup, the ultrahigh gain experiments of Ka-band distributed loss-loaded gyro-TWTs reported by Prof. K. R. Chu fully realized the positive effect of loss loading to enhance the system stability [6, 7, 11]. The principle of loading distributed wall loss is that the loading material imposes minimum influence on the operation mode and could maintain stable electron beam interaction. Especially, strong wall loss imposes strong attenuation on the potential competing instabilities. There are two kinds of waveguide wall loss loading as shown in Fig. 4.9. One is to use a lossy material with finite conductivity to construct the interaction circuit, and the other is to coat a negligibly thin layer of lossy material on the inner metal wall. The propagation constant in Fig. 4.9a waveguide is approximated by [6]

$$k_z^2 = \frac{\omega^2}{c^2} - \left(\frac{x_{\mathrm{mn}}}{a}\right)^2 \left(1 - (1+i)\,\frac{\delta}{a}\left(1 + \frac{m^2}{x_{\mathrm{mn}}^2 - m^2}\,\frac{\omega^2}{\omega_{\mathrm{c}}^2}\right)\right) \tag{4.3}$$

where ω is the angular operating frequency, x_{mn} is the eigen root of Bessel function $J_m'(x_{\mathrm{mn}}) = 0$, c is the vacuum light speed, ω_{c} is the cutoff frequency of the operation mode $\omega_{\mathrm{c}} = cx_{\mathrm{mn}}/r_{\mathrm{w}}$, and δ is the skin depth. When a negligibly thin layer of the lossy material is loaded, as shown in Fig. 4.9b, the propagation constant is estimated by [12]

$$k_z^2 = \frac{\omega^2}{c^2} - \left(\frac{x_{\mathrm{mn}}}{a}\right)^2 \left(1 - (1-i)\tan\left(\Delta r\,\frac{1+i}{\delta}\right)\frac{\delta}{a}\left(1 + \frac{m^2}{x_{\mathrm{mn}}^2 - m^2}\,\frac{\omega^2}{\omega_{\mathrm{c}}^2}\right)\right) \tag{4.4}$$

where the Δr is the thickness of the lossy material. If the circuit is unloaded, beam-wave coupling reaches highest strength close to cutoff frequency region, due to low

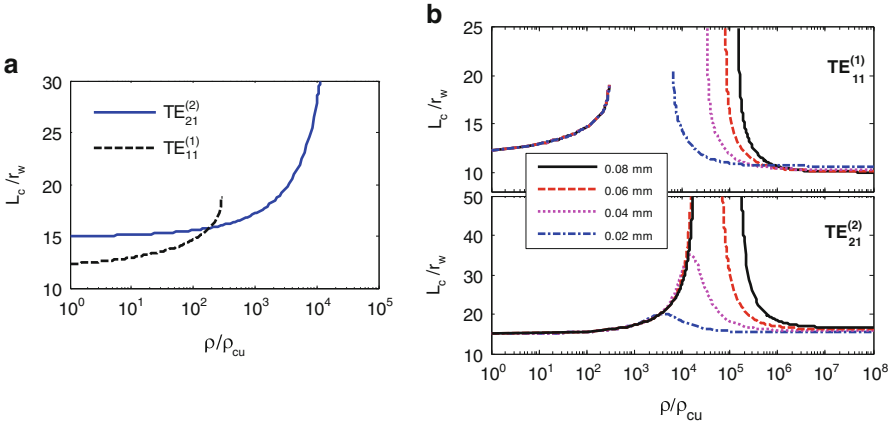

Fig. 4.10 Linear theory calculated influence of lossy material resistivity to start-oscillation length of absolute instabilities. (**a**) Model of lossy material-loaded circuit, and (**b**) model of lossy layer-coated circuit. $I_b = 10$ A, and ρ_{cu} indicates the copper resistivity

group velocity, where the oscillation normally is of smallest threshold current. When distributed wall loss is loaded, the attenuation to the wave also reaches most strength near the cutoff frequency. The absolute instability threshold current will be boosted into a higher value. For a convective instability, its growth rate will be reduced to a lower strength, but still acceptable. As a result, the amplification works well, but oscillation is effectively suppressed. Hence, the waveguide wall loss is an excellent candidate solution to suppress absolute instability oscillations.

The EM field encounters attenuation from the lossy circuit. As a result, the absolute instability requires a longer circuit to build up strong enough feedback for an oscillation. The linear theory defines the resistivity ρ of lossy material leading to sharp growth of start-oscillation length L_c, even growing to infinite, as the loss threshold of suppressing an absolute instability. As shown in Fig. 4.10a, the start-oscillation length L_c increases with resistivity ρ of lossy material. When resistivity exceeds $\rho = 3 \times 10^2 \rho_{cu}$, the L_c of $TE_{11}^{(1)}$ sharply grows. From Fig. 4.1, since the absolute instability on $TE_{21}^{(2)}$ mode is with larger wave number than that of $TE_{11}^{(1)}$ mode absolute instability, and its attenuation rate is much weaker, which leads to L_c sharp growth when resistivity exceeds a higher strength $\rho = 2 \times 10^4 \rho_{cu}$. Figure 4.10b shows a more complicate relation between the material resistivity ρ and start-oscillation length L_c in a lossy layer-coated ECM system. At first, it needs to be stressed that the attenuation rate of a mode does not always grow with the increase strength of the lossy material resistivity and it is strongly associated with the thickness Δr of the loss layer. Under low resistivity or high conductivity condition, the wave skin depth is much smaller than the lossy layer thickness Δr; hence, attenuation rate to the EM field grows respecting to increasing material resistivity ρ, and critical length L_C grows accordingly. However, under strong resistivity or low conductivity condition, the skin depth is comparable to the

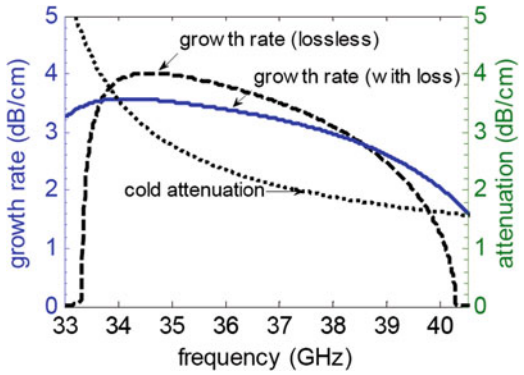

Fig. 4.11 Linear growth rate and attenuation rate $\Delta r = 0.08$ mm, $\rho = 3 \times 10^4 \rho_{cu}$

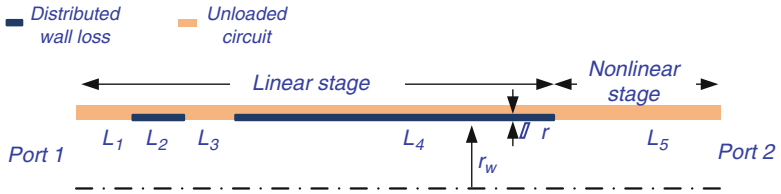

Fig. 4.12 The multistage interaction circuit of a gyro-TWT amplifier loaded with distributed wall loss, axial structure $L_1 = L_2 = L_3 = 2$ cm, $L_4 = 13$ cm, and $L_5 = 2 \sim 5$ cm

thickness Δr, and it leads to not-enough attenuation to wave. Hence, the critical length L_C returns to smaller value under stronger resistivity ρ condition. It is concluded that under lossy layer coating condition, special coating thickness Δr is required according to material resistivity ρ.

Figure 4.11 comparatively shows the linear growth rates of the traveling-wave amplifier circuit under lossy and lossless conditions, with zero electron beam velocity spread assumption. It is found that distributed wall loss brings the growth rate with better uniformity in wider frequency band. Linear growth rate study provides guidance for determining a set of preliminary parameters for amplifier design and nonlinear investigation.

4.2.5 A Multistage Interaction Gyro-TWT Circuit

Self-consistent nonlinear theory is employed to investigate the multistage interaction circuit shown in Fig. 4.12. A possible absolute instability oscillation is determined by applying outgoing boundary conditions on both ports. Figure 4.13 shows the oscillation field profiles of $TE_{11}^{(1)}$ and $TE_{21}^{(2)}$ modes. The field profiles of both oscillations in L_5 stage are similar to that of fundamental axial modes in Fig. 4.2, where beam-wave energy transferring is limited in a single cycle. Hence, such oscillations are called local first axial mode. However, due to the

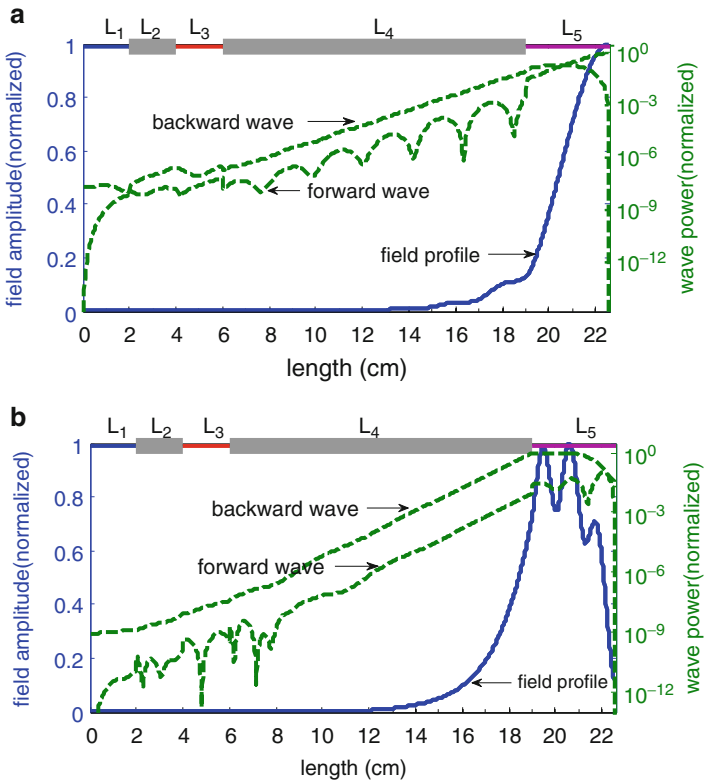

Fig. 4.13 Oscillation field profiles of absolute instabilities from (**a**) $TE_{11}^{(1)}$ and (**b**) $TE_{21}^{(2)}$ modes

connection between L_4 stage and L_5 stage, both oscillations penetrate into the upstream lossy stages. Beam-wave interaction of oscillations experience multiple energy transferring cycles during electron beam passing through upstream stages; hence, such oscillations are also called global high-order axial modes (HOAMs) [13–16]. As shown in Fig. 4.13, oscillations of $TE_{11}^{(1)}$ mode and $TE_{21}^{(2)}$ mode are actually global 9th and 6th HOAM, respectively.

In nonlinear instability study, the threshold of an oscillation is a transition state between linear perturbation and strong nonlinear interaction. The influence of the beam current I_b to the oscillation efficiency is displayed in Fig. 4.14. The efficiency grows with current in a certain range. Under lower efficiency stage, $\eta < 10^{-3}$, the oscillation is under disturbance of low strength, and the interaction efficiency is quite sensitive to the beam current variation. While, under higher efficiency stage, $\eta > 10^{-3}$, the oscillation switches from linear disturbance into nonlinear interaction state, and the efficiency growth rate respect to beam current slows down. Nonlinear instability study monitors the various steady states of an absolute instability under different system parameters, as a way to understand the system stability. For a gyro-TWT, the threshold currents of all kinds of oscillations should be higher than the operation current to obtain zero-drive stability.

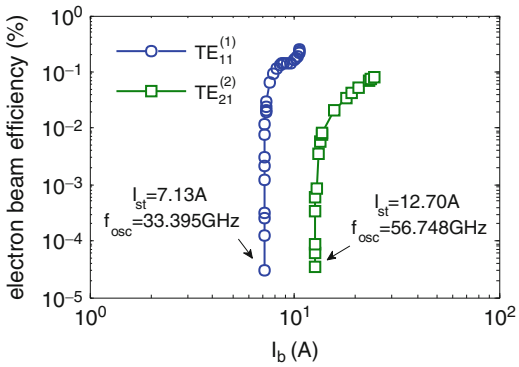

Fig. 4.14 The influence of beam current to interaction efficiency of absolute instability oscillations of $TE_{11}^{(1)}$ and $TE_{21}^{(2)}$ modes

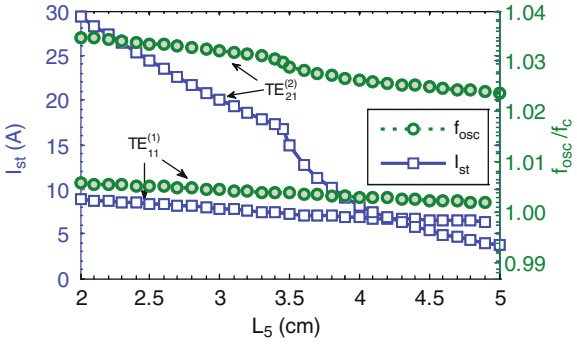

Fig. 4.15 The influence of the nonlinear stage length to absolute instability oscillations

An oscillation gains the highest field strength in the downstream unloaded nonlinear stage L_5, which makes the nonlinear stage a key factor to system stability and performance. From the point of view of efficiency and average power, the nonlinear stage should be as long as possible, to make sure strong EM field confined in the unloaded nonlinear stage. However, the requirement of strong system stability favors a short nonlinear stage to avoid self-excited oscillation. Optimizing the parameters in nonlinear stage is the major task of nonlinear stability study. It is enough to diagnose the threshold of the local 1st axial mode, normally, the most dangerous one. Figure 4.15 demonstrates that shorter nonlinear stage length would improve the thresholds of both oscillations. Taking Fig. 4.13 into consideration, the difference between $TE_{11}^{(1)}$ and $TE_{21}^{(2)}$ oscillations is that the relative field strength at the connection between the L_4 stage and L_5 stage differs from each other obviously. In other word, the lossy material of L_4 stage is more effective to absorb the power from $TE_{21}^{(2)}$ oscillation. Optimization determines the length $L_5 = 3.6$ cm.

Figure 4.16 shows the performance of the interaction circuit as shown in Fig. 4.12. From Fig. 4.16a, it is found that even under amplification condition, the backward wave grows in the nonlinear stage and penetrates into the lossy stages. From Fig. 4.16b, the 1 dB saturated bandwidth is larger than 3.5 GHz. At 34.06 GHz, the system obtains the highest output power of 152 kW, gain of

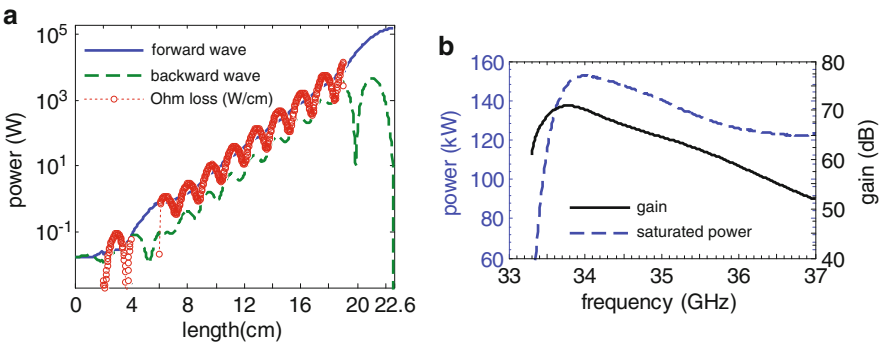

Fig. 4.16 (**a**) Amplification field profile and (**b**) bandwidth and gain, electron beam velocity spread is $\Delta v_z = 5$ %

71 dB, and electron beam efficiency of 32.72 %, and about 2.2 % of beam energy is absorbed by lossy material. It needs to be stressed that the strongest ohmic loss happens close to the end of L_4 stage. Hence, to develop lossy scheme capable of high average power operation is meaningful.

4.3 Oscillation with Multi-steady States

The challenging problems of suppressing absolute instability oscillations hinder the development of the gyro-TWTs. The above section revealed an oscillation existed in a high-order axial mode (HOAM). The following section will focus on the complicate multi-steady states of absolute instability and solutions to stabilize them. The stability-oriented design principle is conveyed in a start-to-end design flow of a Ka-band TE_{11} mode gyro-TWT.

The circuit of an engineering Ka-band TE_{11} mode gyro-TWT is shown in Fig. 4.17, and parameters are given in Table 4.2. The circuit consists of a coupler stage, a linear stage, and a nonlinear stage, and each is with a specific function. The radius-tapered coupler stage is for input power coupling. The loss material linear stage is employed for suppressing absolute instability oscillations and providing major gain of the system. The nonlinear stage is of highest power and plays a key role to the performance.

4.3.1 Self-Consistent Nonlinear Instability Study

The tapered coupler stage reduces the cutoff frequency of TE_{11} mode, and it constitutes an ideal TE_{11} mode fundamental harmonic gyro-BWO circuit. Hence, the coupler stage design considers both limitations from the broadband coupler

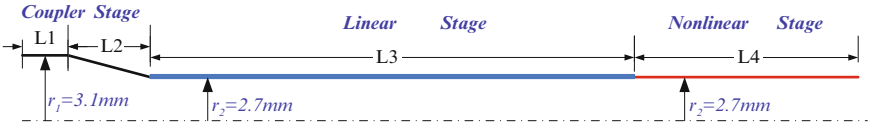

Fig. 4.17 The axial configuration of an engineering Ka-band TE_{11} mode gyro-TWT circuit

Table 4.2 Ka-band TE_{11} mode gyro-TWT design parameters

Operation frequency	Ka-band
Operation mode	TE_{11}
Cyclotron harmonic	$s = 1$
Waveguide inner radius	$r_w = 2.7$ mm
Guiding center	$r_c = 0.36\, r_w$
Lossy material	$\rho = 50,000\rho_{cu}$
Beam voltage	$V = 80$ kV
Beam current	$I_b = 8$ A
Beam velocity ratio	$v_\perp / v_z = 1.0$
Applied magnetic field	$B_0 = 0.99B_g$
Magnetic tapering	$B_{end} = 0.9B_g$ (linearly tapered in the last 2 cm of the circuit)
Axial structure	$L_1 = 7.2$ mm, $L_2 = 15$ mm, $L_3 + L_4 = 180$ mm

design and suppressing the $TE_{11}^{(1)}$ mode gyro-BWO oscillation. The oscillation frequency is under cutoff in the lossy linear stage; hence, gyro-BWO analysis considers $L_3 = 1$ cm only. Figure 4.18 shows the oscillation field profile and sensitivity of the threshold to taper length L_2. Longer taper results in lower start-oscillation threshold. In order to maintain a margin safe enough, the taper length $L_2 = 1.5$ cm is chosen, corresponding to the threshold $I_{st} = 23$ A of the TE_{11} mode gyro-BWO. Furthermore, the $TE_{21}^{(2)}$ gyro-BWO happens on the second cyclotron harmonic, its beam-wave coupling is much weaker, and will not be consideredhere.

4.3.2 Attenuation Strength of the Lossy Linear Stage

A thin layer of lossy material, shown in Fig. 4.9b, is loaded to suppress the instability oscillation in the linear stage. Figure 4.19a shows the relation between the start-oscillation lengths of the first three-order axial modes versus material resistivity. When the resistivity of the material grows higher than a certain value, start-oscillation length of all the instability grows toward infinite, as a way to determine the minimum lossy strength of the circuit. From the linear growth rate shown in Fig. 4.19b, it is estimated that the linear stage of 15 cm would generate the highest gain about 55 dB under operation current of 6 A.

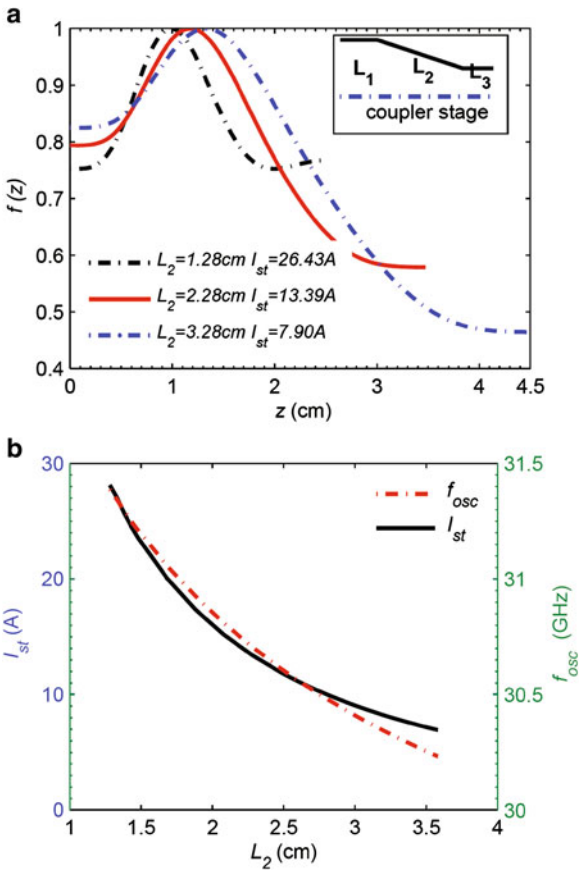

Fig. 4.18 Potential Gyro-BWO oscillation in the coupler stage, (**a**) oscillation field profiles, and (**b**) the sensitivity of the threshold to taper length L_2

4.3.3 Multi-steady States of Absolute Instability Oscillation

In a gyro-TWT interaction circuit, an absolute instability-induced oscillation exists in the form of a high-order axial mode (HOAM), which is sensitive to the system parameters, such as distributed loss strength, circuit radius, circuit length, magnetic field strength, electron beam parameters, and so on. An absolute instability would induce one of the HOAMs; hence, such oscillation constantly switches from one of these HOAM to another during the parameter tuning. To find out the one with the lowest threshold is the key to determine the system threshold.

Figure 4.20 displays the first three local axial modes in the nonlinear stage induced by $TE_{11}^{(1)}$ mode forward-wave absolute instability and $TE_{21}^{(2)}$ mode backward-wave absolute instability. Here, the order of an axial mode is determined by the numbers of the concave-convex shapes on the field profile [13–16]. Since the

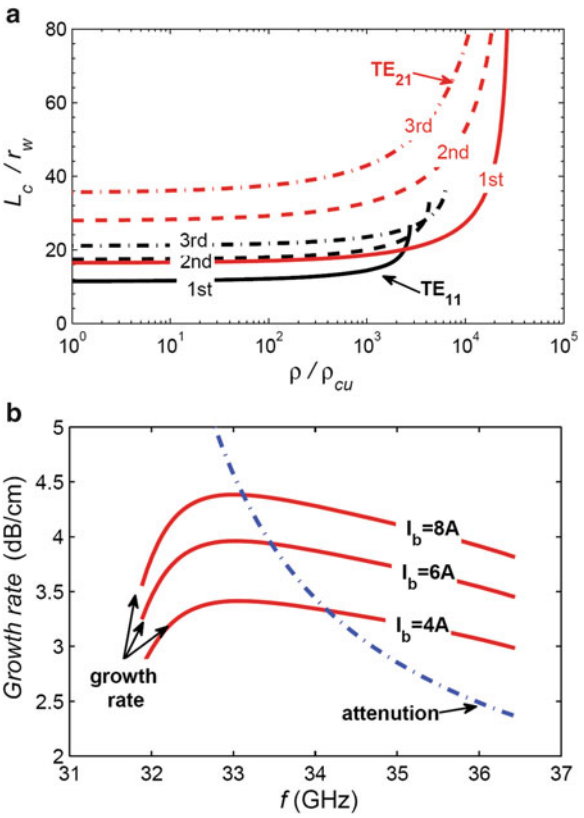

Fig. 4.19 (**a**) Influence of the lossy material resistivity to start-oscillation length under $I_b = 10$ A condition, and (**b**) linear growth rate of different beam current under $\rho/\rho_{cu} = 5 \times 10^4$ condition

highest strength of the field of an oscillation always locates in the nonlinear stage, the nonlinear stage length is the most important factor to system threshold. Using a long nonlinear stage, $L_4 = 8$ cm, the lowest threshold current of both oscillations are much lower than the operation 8 A. Keep the circuit length constant $L_3 + L_4 = 18$ cm and increase the length of the lossy stage L_3, as a way to decrease the nonlinear stage L_4. Figure 4.21 shows the length of the nonlinear stage to the threshold currents. A general rule is that a shorter nonlinear stage corresponds to a higher threshold current. The tendency for both kinds of oscillations is similar. Due to much weaker beam-wave coupling on the second cyclotron harmonic, the threshold for a $TE_{21}^{(2)}$ mode oscillation is much higher than a corresponding $TE_{11}^{(1)}$ mode oscillation. Figure 4.21 also shows that during the tuning process of decreasing the nonlinear stage length L_4, the threshold current of the second and the third local axial mode exhibits fluctuation to some extent. Because of shortening the length L_4, the field of a HOAM is pushed into the lossy stage L_3. As a result, the third local axial mode turns into the second local axial mode. In other word, the number of beam-wave energy transferring cycles in the nonlinear stage becomes smaller, but the order of such a HOAM is unchanged from a global view. When the circuit configuration, especially the nonlinear stage length L_4, is favored by a certain

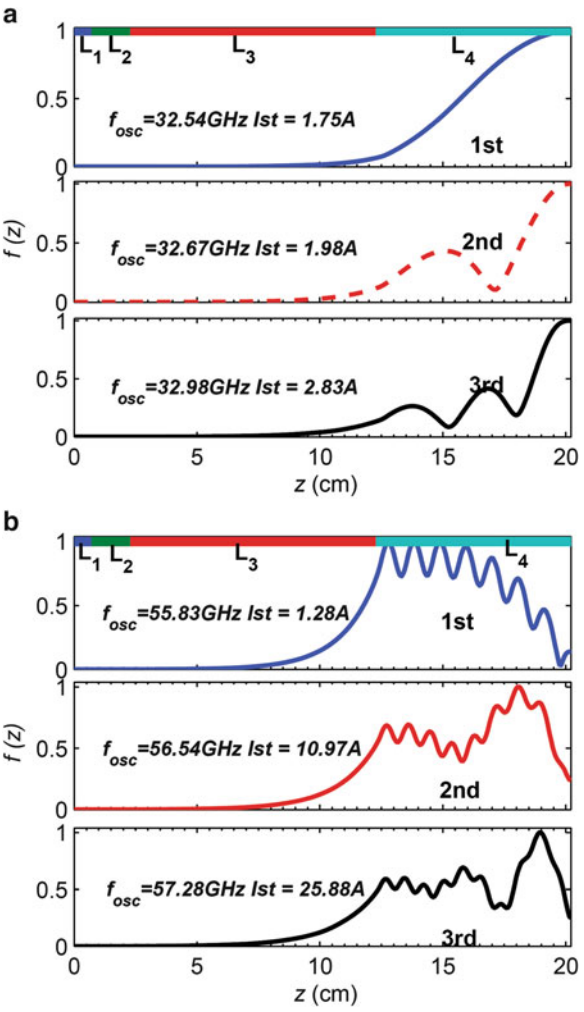

Fig. 4.20 The first three local axial modes in the nonlinear stage induced by (**a**) $TE_{11}^{(1)}$ mode forward-wave absolute instability and (**b**) $TE_{21}^{(2)}$ mode back-ward wave absolute instability

HOAM, the corresponding threshold current is relatively lower. On the other hand, if the circuit configuration is not favored, it corresponds to a high threshold current. Hence, the threshold current of a higher local axial mode exhibit fluctuation during changing the nonlinear stage length.

Figure 4.21 also reveals that a HOAM is not stable enough. During the system parameter tuning, it might mislead us to omit tracking the most dangerous axial mode. An objective view requires us to diagnose all the HOAMs and to find out the most dangerous one, meaning time-consuming and complicated calculation. Fortunately, after enormous of nonlinear calculation, the fundamental local axial mode in the nonlinear stage is usually the most dangerous one under normal parameters and should be focused on.

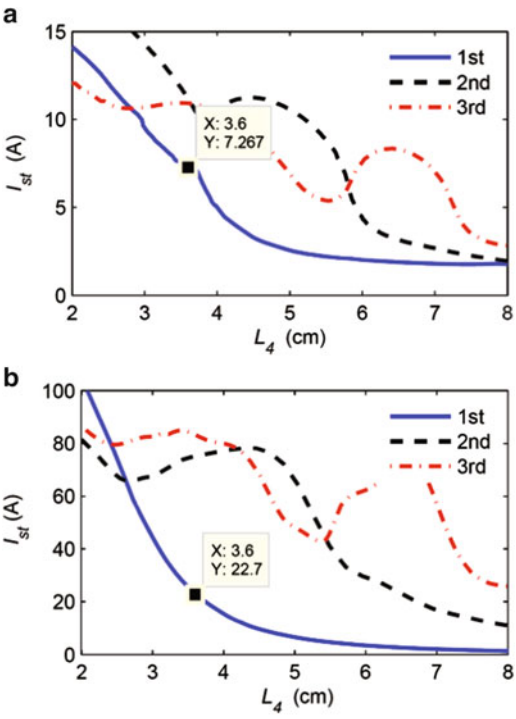

Fig. 4.21 Influence of the nonlinear stage length L_4 to thresholds of the first-order oscillation from (**a**) $TE_{11}^{(1)}$ and (**b**) $TE_{21}^{(2)}$ absolute instabilities ($L_3 + L_4 = 18$ cm)

Nonlinear stage of suitable length is required due to performance and stability consideration. The nonlinear stage is chosen to be $L_4 = 3.6$ cm. Under such a length, the local 1st axial modes from $TE_{11}^{(1)}$ and $TE_{21}^{(2)}$ absolute instabilities are the 9th and 6th HOAMs, respectively. But the threshold current I_{st} of the $TE_{11}^{(1)}$ 9th HOAM is 7.27 A, lower than the operation current 8 A. Additional technology is needed to stabilize this fundamental mode oscillation.

4.3.4 Applying Magnetic Field Tapering to Enhance Nonlinear Stage Stability

Tuning the magnetic field strength and profile has long been considered as a major solution to optimize the interaction performance of an ECM system [17–19]. Loading strong lossy material or modifying the circuit length is constantly applied to enhance the system stability. But nonlinear stage is an exception. The ECM interaction emits the strongest radiation in the nonlinear stage, and the nonlinear stage should be maintained to guarantee high efficiency and high average power. Both the two aspects require the nonlinear stage of reasonable length. Magnetic field tapering could simultaneously enhance the system stability and improve the amplification performance. For example, the magnetic field of the last 2 cm in the

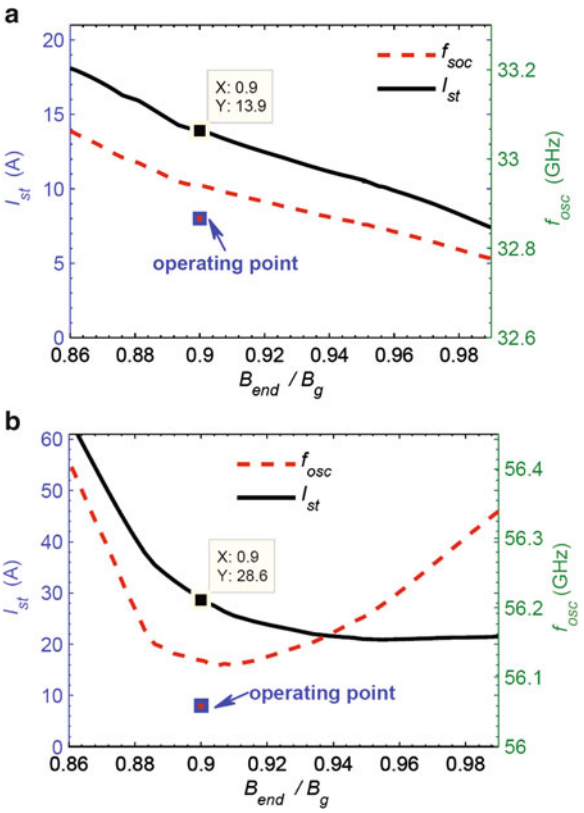

Fig. 4.22 Influence of the magnetic field tapering to (**a**) 9th HOAM of $TE_{11}^{(1)}$ absolute instability and (**b**) 6th HOAM of $TE_{21}^{(2)}$ absolute instability

nonlinear stage is down tapered, and others maintain $B_0 = 0.99\ B_g$ unchanged. For amplification consideration, the bunched electron beam maintains strong radiation in the former half of the nonlinear stage, and, in the latter half stage, the electron γ factor becomes smaller, the down tapered B_{z0} could push the cyclotron electron back into energy-losing phase and gain higher radiation efficiency. For stability consideration, strong magnetic field tapering leads to varying beam-wave synchronizing condition with respect to local absolute instability, and it shortens the effective feedback length of an oscillation, as a way to enhance the threshold current.

Figure 4.22 shows the influence of magnetic field tapering to the most dangerous HOAM of $TE_{11}^{(1)}$ and $TE_{21}^{(2)}$ absolute instabilities. For the oscillation of $TE_{11}^{(1)}$ absolute instability, since the detuning between fundamental cyclotron harmonic and the TE_{11} mode is almost linearly increased according to magnetic field tapering, the threshold current is increased accordingly, as shown in Fig. 4.22a. The $TE_{21}^{(2)}$ mode is more complicated. When the tapering strength is weaker, the beam-wave synchronization is shifted toward the lower propagation constant region, leading to stronger beam-wave coupling. Under stronger tapering, the effect of the nonhomogeneous synchronization overcomes the stronger beam-wave coupling in lower propagation constant region; hence, threshold current increases obviously.

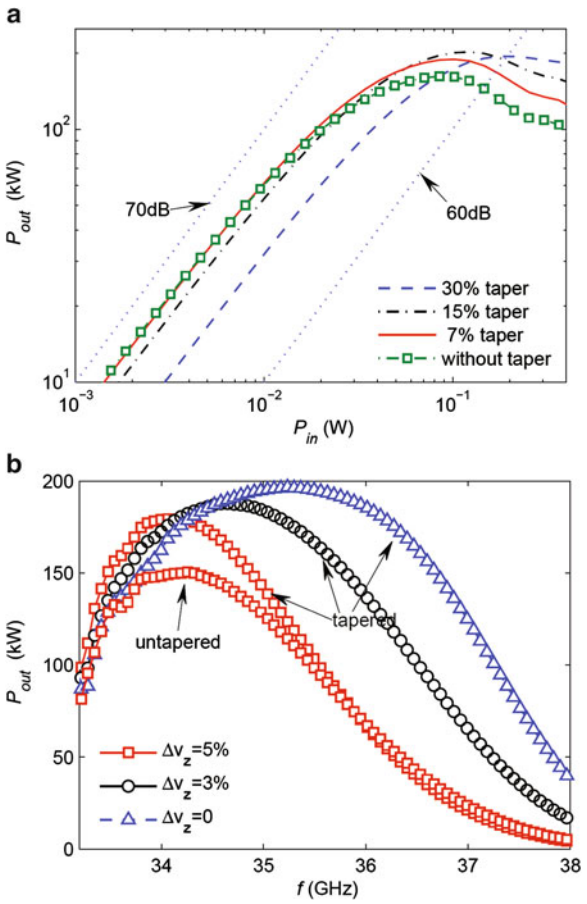

Fig. 4.23 Influence of the magnetic tapering to (**a**) amplification characteristics (33.67 GHz, $\Delta v_z = 0$) and (**b**) bandwidth characteristics ($B_{end}/B_g = 0.9$, $p_{in} = 0.1$ W)

From Fig. 4.22, it is found that the threshold currents of both modes are enhanced obviously when magnetic field tapering is stronger than 10 % ($B_{end}/B_g < 0.9$). Figure 4.23 shows the results of investigating magnetic field tapering to the gyro-TWT amplification. As shown in Fig. 4.23a, even the tapering reach 30 %, the saturated output power is still stronger than the condition of uniform magnetic field. Certainly, magnetic tapering reduces the gain. Generally speaking, magnetic tapering could enhance the system stability and increase the saturated output power.

4.3.5 Influence of the Downstream Port Reflection

Reflection from the both ends of a gyrotron amplifier is also one of the reasons inducing oscillations. In the circuit of a distributed loss-loaded gyro-TWT, no matter under amplification or self-excited oscillation, the highest power is normally

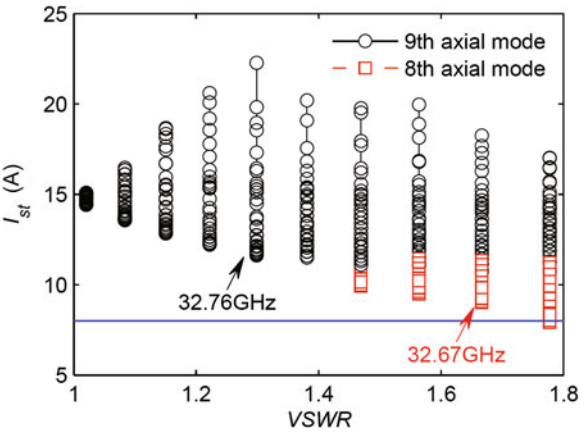

Fig. 4.24 Influence of the output port reflection on the $TE_{11}^{(1)}$ absolute instability oscillation

confined in the output stage. The influence from the reflected power of output port will be studied here. Reflection oscillation boundary condition is applied to find out the possible steady states of the system, given as

$$f(L) = f_+ e^{-ik_z L}\left(1 + |\Gamma_L| e^{i\varphi_L}\right), \text{(Downstream port)} \tag{4.5}$$

$$f'(L) = -ik_z f_+ e^{-ik_z L}\left(1 - |\Gamma_L| e^{i\varphi_L}\right), \text{(Downstream port)} \tag{4.6}$$

where $f(L)$ is the field amplitude at the downstream port and $z = L$, $|\Gamma_L|$, and φ_L indicate the reflection amplitude and phase, respectively. Based on the magnetic field tapering circuit, Fig. 4.24 shows the influence of the downstream port reflection on $TE_{11}^{(1)}$ absolute instability oscillation. Simulation assumes reflection of voltage standing wave ratio VSWR $= 1 \sim 1.8$ and the phase $\varphi_L = 0 \sim 2\pi$. From Fig. 4.24, it is found that the threshold current I_{st} is phase sensitive at a given reflection strength. Sweeping all the phases $\varphi_L = 0 \sim 2\pi$ between reflection range VSWR $= 1 \sim 1.8$, it is obviously demonstrated that reflection would reduce the start-oscillation threshold current I_{st}. An interesting result is that strong reflection leads to the 8th HOAM with lower threshold current than that of the 9th HOAM. When the reflection exceeds a certain value VSWR ≥ 1.8, the I_{st} of the 8th HOAM becomes smaller than the operation current 8 A.

4.3.6 Pre-bunched ECM Radiation

The influence of the lossy stage on the amplification of a gyro-TWT is studied here. Figure 4.25 shows the amplification power profile under three different conditions. The real-blue line indicates a normal amplification. The dash-black line indicates the amplification profile of a linear stage bunched electron beam, but the power at the nonlinear stage is suddenly turned off, and the power is induced from noise level.

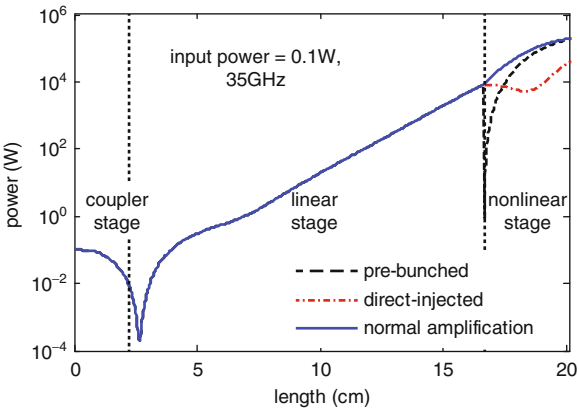

Fig. 4.25 Comparative study of the influence of the electron beam bunching to amplification

The dash-dot-red line in the nonlinear stage indicates amplification profile driven by the power generated in the linear stage, but the electron beam is an undisturbed monolithic beam, or called cold beam. Comparing the three conditions, it reveals that the linear stage bunched electron beam would induce power from the noise level in the nonlinear stage and the final output power is almost equivalent to that of a normal amplification. The non-bunched cold beam, even under high power driven, experiences an energy absorbing stage to get in phase with the wave, and the output power is obviously lower. It is summarized that the necessary condition of high-efficiency amplification in nonlinear stage is the bunching effect of the lossy linear stage to electron beam, not the power generated in the linear stage. In other words, the actual role the distributed loss-loaded linear stage played is to impose a pre-bunch effect to the electron beam.

Since the linear stage provides the major total gain, the total gain is tightly related to the electron beam bunching condition. The pre-bunched radiation indicates a well-bunched electron beam inducing high-efficiency radiation in the nonlinear stage. The distributed loss-loaded scheme is generally applicable to gyro-TWT as a way of oscillation suppression and the system stability enhancement. The ohmic loss is always a hidden danger to high average power operation. Hence, the concept of pre-bunched radiation opens a new research field that is to explore new solutions to provide stable and broadband bunching to electron beam, as a way to replace the distributed loss scheme and endow the system with high average power or continuous wave operation capability.

4.4 Summary

The Ka-band TE_{11} mode gyro-TWT is taken as an example to describe the general stability-related problems. Many issues are addressed. The forward-wave component and backward-wave component of an oscillation are decomposed from

the total field throughout the circuit, through which the physical feeding-back mechanism of all the absolute instability-induced oscillations is clearly analyzed. In an engineering gyro-TWT circuit, the oscillation of an absolute instability exists in a form of HOAM, which would present in different orders due to parameter tuning and shows multi-steady states. Based on the start-to-end design principle, in order to guarantee high stability of each circuit section, the stability study of a gyro-TWT is introduced in detail. Sharp magnetic field tapering is introduced to improve the nonlinear stage stability as well as the performance. The concept of pre-bunching amplification is proposed. It is revealed that the necessary condition of high-efficiency amplification in the nonlinear stage is a well pre-bunched electron beam provided by the loss-loaded linear stage. Systematic exploring of these physical principles is very helpful for understanding the instability competition and developing a gyro-TWT of high stability.

References

1. Chu KR (2004) The electron cyclotron maser. Rev Mod Phys 76:489–540
2. Chu KR (2002) Overview of research on the gyrotron traveling-wave amplifier. IEEE Trans Plasma Sci 30:903–908
3. Calame JP, Garven M, Danly BG et al (2002) Gyrotron-traveling wave-tube circuits based on lossy ceramics. IEEE Trans Electron Devices 49:1469–1477
4. Pershing DE, Nguyen KT, Calame JP et al (2004) A TE11 K-a-band gyro-TWT amplifier with high-average power compatible distributed loss. IEEE Trans Plasma Sci 32:947–956
5. Sirigiri JR, Shapiro MA, Temkin RJ (2003) High-power 140-GHz quasioptical gyrotron traveling-wave amplifier. Phys Rev Lett 90:258302
6. Chu KR, Chen HY, Hung CL et al (1999) Theory and experiment of ultrahigh-gain gyrotron traveling wave amplifier. IEEE Trans Plasma Sci 27:391–404
7. Chu KR, Barnett LR, Chen HY et al (1995) Stabilization of absolute instabilities in the gyrotron traveling-wave amplifier. Phys Rev Lett 74:1103–1106
8. Du CH, Liu PK, Xue QZ et al (2008) Effect of a backward wave on the stability of an ultrahigh gain gyrotron traveling-wave amplifier. Phys Plasmas 15:123107
9. Chang TH, Chen NC (2006) Transition of absolute instability from global to local modes in a gyrotron traveling-wave amplifier. Phys Rev E 74:017402
10. Barnett LR, Baird JM, Lau YY et al (1980) A high gain single stage gyrotron traveling-wave amplifier. Int Electron Devices Meet 26:314–317
11. Chu KR, Chen HY, Hung CL et al (1998) Ultrahigh gain gyrotron traveling wave amplifier. Phys Rev Lett 81:4760–4763
12. Luo JR, Jiao CQ (2006) Effect of the lossy layer thickness of metal cylindrical waveguide wall on the propagation constant of electromagnetic modes. Appl Phys Lett 88:1–8
13. Chang TH, Chen SH, Barnett LR et al (2001) Characterization of stationary and nonstationary behavior in gyrotron oscillators. Phys Rev Lett 87(6):064802
14. Chang TH, Fan CT, Pao KF et al (2007) Stability and tunability of the gyrotron backward-wave oscillator. Appl Phys Lett 90:191501
15. Chen SH, Chu KR, Chang TH (2000) Saturated behavior of the gyrotron backward-wave oscillator. Phys Rev Lett 85:2633–2636
16. Pao KF, Chang TH, Fan CT et al (2005) Dynamics of mode competition in the gyrotron backward-wave oscillator. Phys Rev Lett 95:185101

17. Dumbrajs O, Nusinovich GS, Pavelyev AB (1988) Mode competition in a gyrotron with tapered external magnetic-field. Int J Electron 64:137–145
18. Gantenbein G, Borie E (1990) Gyrotron with a tapered external magnetic-field. Int J Infrared Millim Waves 11:837–850
19. Chang TH, Idehara T, Ogawa I et al (2009) Frequency tunable gyrotron using backward-wave components. J Appl Phys 105:063304

Chapter 5
A Lossy Ceramic-Loaded Millimeter-Wave Gyro-TWT Amplifier

Abstract Loading lossy ceramic of high thermal conductivity is a proposed scheme for developing a high-power millimeter-wave gyro-TWT amplifier for engineering application. This chapter focuses on investigating lossy ceramic-loaded gyro-TWTs. It addresses proper approximation methods to simplified analyzing ceramic-loaded gyro-TWTs. The propagation characteristics approximation considers only the influence from the ceramic to the wave dispersion and attenuation properties while assuming ideal empty waveguide mode distribution. On the other hand, by using full-wave interaction method, it could relatively accurately consider influence from the ceramic to both dispersion and mode distribution. Finally, the concept of the beam-wave coupling strength in a gyro-TWT is investigated. It brings some new explanations to the amplifier performance.

Keywords Lossy ceramic • High power • Gyro-TWT • Coupling impedance

5.1 Introduction

A high-power and broadband millimeter-wave gyrotron traveling-wave tube amplifier (gyro-TWT) is of great prospects in applications, including high-resolution radar, electron countermeasure system, outer space detection, and high data rate communication [1]. Based on the interaction of electron cyclotron maser (ECM), a gyro-TWT employs a helically traveling electron beam to interact with a fast wave, transfers the kinetic energy to wave through transverse interaction, and induces coherent radiation in broadband. Since it is based on fast wave interaction, a gyro-TWT could radiate power higher than normal rectilinear vacuum electronic devices (VEDs). During the past half century, international researchers carried out extensive investigations focusing on the subject of instability competition in a gyro-TWT and tried to explore solutions to suppress these unfavorable competitions.

It is found that introducing proper attenuation to waves in the interaction circuit is capable of absorbing oscillation and maintaining amplification [1, 2]. At the end

C.-H. Du and P.-K. Liu, *Millimeter-Wave Gyrotron Traveling-Wave Tube Amplifiers*,
DOI 10.1007/978-3-642-54728-7_5, © Springer-Verlag Berlin Heidelberg 2014

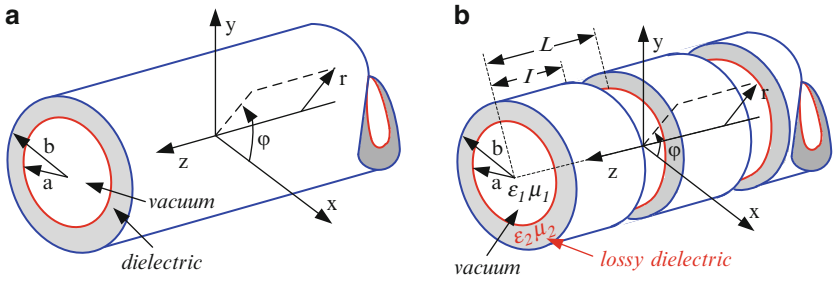

Fig. 5.1 (**a**) Uniform dielectric-loaded waveguide and (**b**) periodic dielectric-loaded waveguide

of the last century, the Ka-band gyro-TWT experiment carried out in National Tsing Hua University (NTHU) employed lossy Aquadag loading in the inner circuit wall, and it obtained 93 kW peak power, 70 dB ultrahigh gain, and 8.6 % bandwidth [3, 4]. Later, American Naval Research Laboratory (NRL) carried out Ka-band periodic dielectric-loaded gyro-TWT experiment and achieved 137 kW peak power [5, 6]. A Ka-band experiment carried out in Beijing Vacuum Electronics National Laboratory, China, achieved a peak power of 290 kW and −3 dB bandwidth of 2.1 GHz [7]. A Q-band experiment based on a periodic lossy ceramic-loaded circuit is recently carried out in the University of Electronic Science and Technology of China, and it achieved highest gain of 41 dB, peak power of 152 kW, and especially a bandwidth of 2 GHz with power exceeding 100 kW [8]. The W-band experiment carried out in American University of California Davis (UC Davis) obtained output power of 80 kW and bandwidth of 2 GHz [9]. American MIT employed confocal waveguide with open side walls taken as the interaction circuit of a 140 GHz gyro-TWT, and it achieved output power about 30 kW [10].

The Ka-band lossy ceramic-loaded gyro-TWT experiment carried out in American NRL exhibits excellent stability to the self-excited oscillations. The schematic plot of the interaction circuit is shown in Fig. 5.1b. The linear stage of the circuit is loaded with a layer of lossy ceramic on the inner wall. In order to avoid dielectric charging, the ceramic tube is cut into a series of rings which are separated by metal rings. Finally, the interaction circuit becomes a periodic dielectric-loaded waveguide [5, 6]. The structure of lossy ceramic-loaded circuit is specially designed, which makes the competition modes strongly attenuated and the operating mode relatively less disturbed. Since the structure of the interaction circuit is relatively complicated, the problem is that the past theoretical design approximated the circuit as a traditional cylindrical waveguide with attenuation strength the same as that of the dielectric waveguide [6, 11]. Other influences from loading ceramic to ECM interaction are omitted. Involving the lossy ceramic, the dispersion relation of the operation mode could be regulated to broaden the interaction bandwidth, and it is called dispersion shaping (DS) [12–14]. Until now, ref. [12] studied about the DS via perturbation method to take the dispersion characteristics into consideration with linear theory and studied the influence to the amplifier bandwidth only omitting

the influence to the field structure and material attenuation. Actually, early ECM instability study developed linear theory of dielectric-loaded ECM interaction system [15, 16]. But early studies omitted the positive effect of the dielectric loss to suppress the instability competition; as a result, the early developed linear theory could predict the instability bandwidth, but lacking the capability of analyzing the instability competition. This chapter employs the special theory developed in Chap. 3 to study lossy ceramic-loaded ECM system [17, 18].

This chapter introduces three different research methods and a concept of beam-wave coupling impedance to deal with instability competition in a dielectric-loaded TE_{01} mode gyro-TWT. The concept of beam-wave coupling impedance provides a general standard for measuring beam-wave coupling strength between different cyclotron harmonics and waveguide modes, and it builds up an intuitive understanding of the competition between operating TE_{01} mode and competing TE_{11}, TE_{21} and TE_{02} modes. Three different methods of studying dielectric-loaded gyro-TWT are introduced, namely, propagation characteristics approximation [11], linear full-wave interaction analysis [17], and nonlinear full-wave interaction analysis [18]. The method of propagation characteristics approximation fully explores the relation mapping between modes in dielectric-loaded waveguide and that of empty waveguide. It omits the complexity of the dielectric-loaded structure and considers the dispersion characteristics of waveguide modes in beam-wave instability study. This efficient method provides preliminary reference for engineering design. The second method, linear full-wave interaction analysis, is based on the linear ECM theory of uniform dielectric-loaded waveguide. The third nonlinear full-wave interaction analysis is based on the nonlinear theory of uniform dielectric-loaded waveguide, and it is capable of predicting the system performance with better accuracy.

5.2 Propagation Characteristics Approximation

This section takes the Ka-band TE_{01} mode gyro-TWT experiment carried by American Naval Research Laboratory as an example [5, 6]. The amplifier employed a lossy linear waveguide loaded with periodic lossy ceramic rings and metal rings, and unloaded empty nonlinear waveguide. The lossy ceramic is made from 80 % AlN − 20 % SiC, and its dielectric permittivity is measured to be $\varepsilon_r = 11 - 2.2\,i$ in the Ka-band. The operating parameters are as shown in Table 5.1.

5.2.1 The Propagation Characteristics of the Dielectric-Loaded Waveguide

The propagation characteristics of the three different kinds of waveguides are, namely, smooth empty waveguide, uniform dielectric-loaded (DL) waveguide, as shown in Fig. 5.1a, and periodic DL waveguide, as shown in Fig. 5.1b. The uniform

Table 5.1 The operating parameters of the NRL Ka-band $TE_{01}^{(1)}$ mode gyro-TWT

Operating frequency	Ka-band
Operating mode	TE_{01}
Cyclotron harmonic	Fundamental
Inner radius	$a = 5.495$ mm
Outer radius	$b = 6.905$ mm
Period structure	$L = 11.5$ mm, $I = 10$ mm
Lossy ceramic	$\varepsilon_r = 11 - 2.2j$, $\mu_r = 1$
Linear stage	$L_1 = 230$ mm
Nonlinear stage	$L_2 = 40$ mm
Beam voltage	$V = 70$ kV
Beam current	$I_b = 10$ A
Applied magnetic field	$B_0 = 1.26$ T
Beam velocity ratio	$\alpha = 1.0$

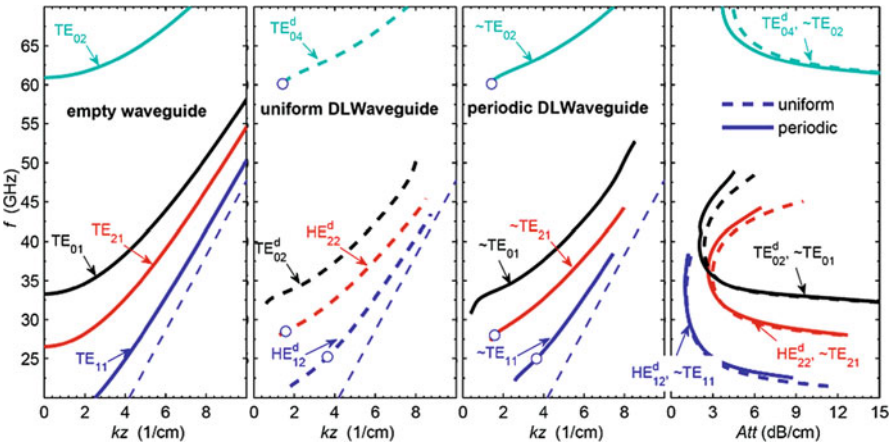

Fig. 5.2 The mode mapping relation between a smooth empty waveguide, a uniform DL waveguide, and a periodic DL waveguide

DL waveguide and the periodic DL waveguide are with the same inner radius. The dispersion relations and propagation attenuations are comparatively shown in Fig. 5.2. It is clearly revealed that there is ideal mapping relation between the modes in three different kinds of waveguides. In the uniform DL waveguide, since the dielectric layer enlarges the effective waveguide cross area, the modes TE_{11}, TE_{21}, TE_{01} and TE_{02} in smooth empty waveguide map to the high-order modes HE_{12}^d, HE_{22}^d, TE_{02}^d and TE_{04}^d, respectively. In the periodic DL waveguide, the modes in the metal section map to the TE_{11}, TE_{21}, TE_{01} and TE_{02} in smooth empty waveguide, and the modes in the lossy ceramic section map to HE_{12}^d, HE_{22}^d, TE_{02}^d and TE_{04}^d in a uniform DL waveguide. Hence, modes in the periodic DL waveguide are defined as $\sim TE_{11}$, $\sim TE_{21}$, $\sim TE_{01}$, and $\sim TE_{02}$, respectively. Figure 5.3a shows the amplitudes of azimuthal electric component of $\sim TE_{01}$ and $\sim TE_{02}$ modes in the

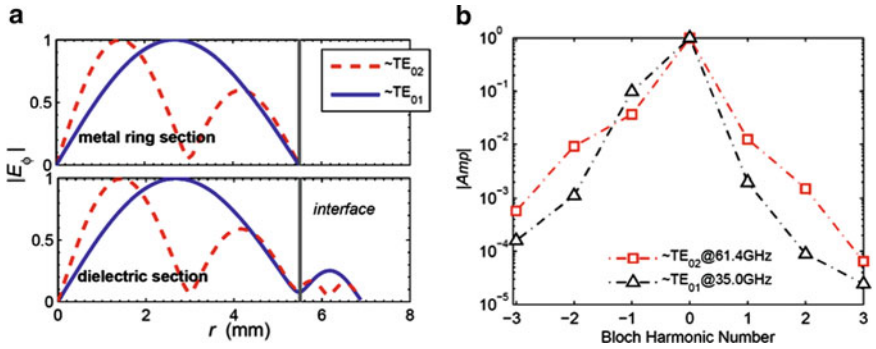

Fig. 5.3 The $\sim TE_{01}$ and $\sim TE_{01}$ mode of the periodic DL waveguide, (**a**) normalized azimuthal electrical components and (**b**) normalized Bloch components

Table 5.2 Modes in DL waveguide for NRL Ka-band *gyro-TWT* experiment

Mode	$\sim TE_{11}$	$\sim TE_{21}$	$\sim TE_{01}$	$\sim TE_{02}$
Frequency(GHz)	25.2	28.6	35	61.4
Power ratio[a] (inner region)	0.968	0.962	0.982	0.978
Attenuation rate(dB/cm)	2.93	9.8	3.44	15.3
Equivalent skin depth[b](mm)	0.721	0.829	0.245	0.560

Note: [a]The power ratio indicates the ratio of the partial power in the inner vacuum region to the total power of the waveguide

[b]Equivalent skin depth means the lossy periodic DL waveguide equal to a lossy waveguide made from special lossy material with equivalent skin depth for the given mode

metal ring section and lossy ceramic section, respectively. Figure 5.3b shows the normalized Bloch components of the special harmonic of the periodic waveguide. It is stressed that the lossy ceramic forces the energy of the wave distributed in the inner vacuum region and conveyed by the fundamental Bloch harmonic. Hence, the dispersion curve of the periodic DL waveguide shown in Fig. 5.2 considers only the major Bloch component.

The propagation characteristics of the modes in the periodic DL waveguide used in NRL experiment are shown in Table 5.2. These data further indicates that higher than 96 % of the wave powers are propagating in the inner vacuum region for all the modes. Hence, it is, to some extent, reasonable to omit the power in the lossy material, and the key of the problem is to take the accurate ohmic loss into consideration. As a result, the periodic DL waveguide is considered as a lossy smooth waveguide of equivalent propagation characteristics.

Applying the method of propagation characteristic approximation, Fig. 5.4 shows the numerical simulation of the NRL Ka-band gyro-TWT experiment [6]. Generally speaking, the calculation coincides well with experimental result. However, reasons from three aspects are estimated to be the origins of the remaining differences [6]: the electron beam is reported to be around 8–10 %, while calculation used electron beam velocity spread of 8.5 %, omitted the electron beam guiding center spread,

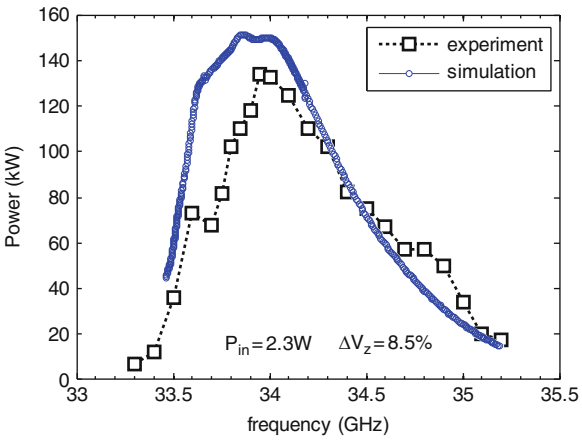

Fig. 5.4 The calculated performance comparing to the NRL Ka-band gyro-TWT experiment ($a = 5.4$ mm, $b = 6.8$ mm)

and it was assumed to be perfectly matched on both ends of the gyro-TWT circuit. Uncertainty of the above three aspects leads to the acceptable differences, and it indicates the reliability of the approximation method of equivalent propagation characteristic.

5.2.2 *Linear and Nonlinear Instability Study*

Based on the study in the above section, traditional linear theory is employed to analyze the threshold of instability oscillation in the TE_{01} mode interaction system, only considering the dispersion and attenuation. Since oscillations are suppressed by the loss material-loaded linear stage, the highest power is confined in the nonlinear stage of a traveling-wave amplifier circuit. The threshold of the nonlinear stage mainly determines the power level of the amplifier. According to the operation parameters in ref. [6], the threshold of the absolute instability of TE_{01} mode is shown in Fig. 5.5. It is found that increasing the magnetic field strength, the frequency of the TE_{01} mode oscillation gets closer to the cutoff frequency. Figure 5.6 displays the axial power profiles of the TE_{01} mode oscillation. Since the oscillation of the TE_{01} mode absolute instability is close to the cutoff frequency, both forward-wave and backward-wave components get synchronizing with the cyclotron beam. The electron beam is modulated in the upstream of the circuit and transfers energy to both components during traveling toward the downstream, which makes the forward wave and the backward wave grow in reverse directions. The total field exhibits a zero point, where the net backward-wave power right balances the forward-wave power. It is obvious that the forward-wave component dominates the TE_{01} mode absolute instability.

Figures 5.7 and 5.8 show the influence of the beam current to the TE_{01} mode oscillation frequency and critical length. Generally speaking, the oscillation frequency increases with beam current. But the critical length exhibits some

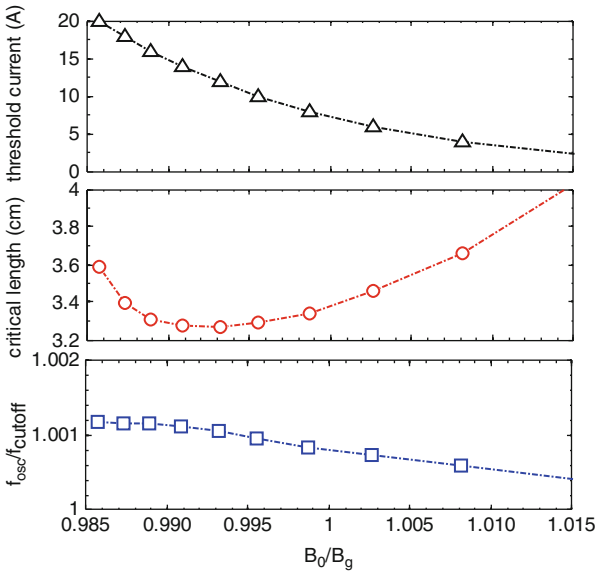

Fig. 5.5 Thresholds of the TE_{01} mode oscillation

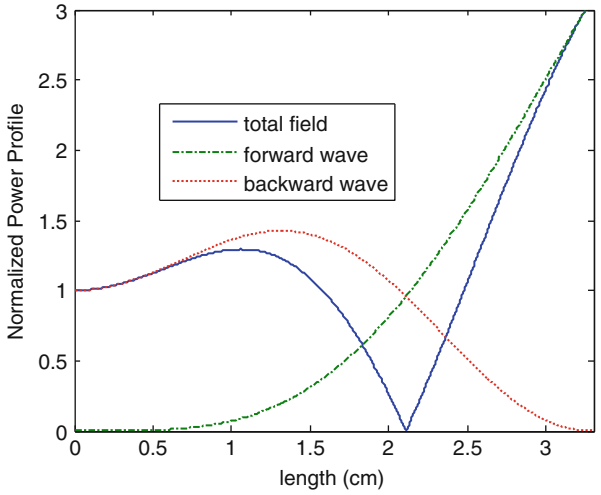

Fig. 5.6 Fields of the TE_{01} mode oscillation

abnormal behaviors. There also is a gradual transition between $B_0/B_g = 1.005$ and $B_0/B_g = 0.990$. Under the magnetic strength of $B_0/B_g = 1.005$, the critical length decreases with increasing current, which is consistent with our common sense. But for the condition of $B_0/B_g = 0.990$, under lower current $I_b < 25$ A, the critical length abnormally becomes shorter under lower current. Comparison indicates

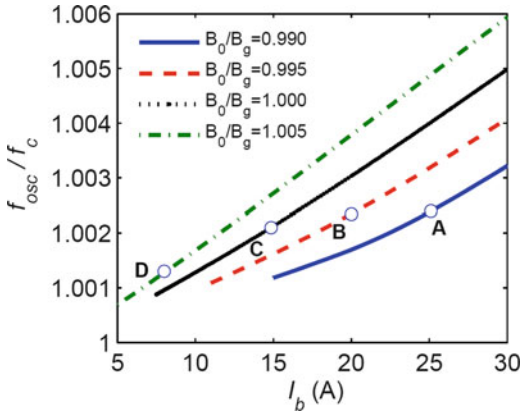

Fig. 5.7 Influence of current to oscillation frequency

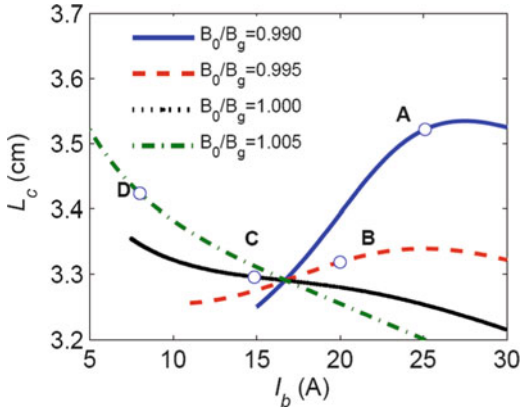

Fig. 5.8 Influence of current to critical length

that under the same beam current and the magnetic field strength maintaining $B_0/B_g = 0.990$, the oscillation frequency is smaller than other conditions, which means the backward-wave component plays a relatively more important role in the oscillation and enhances the feedback strength accordingly. This is obviously revealed in Fig. 5.9. The oscillation of an absolute instability is a result of complicated balance between forward-wave component and backward-wave component. This abnormal reduction in the critical length under lower current condition is due to the same reason as revealed in self-induced constriction in the TE_{11} interaction system [19].

Figure 5.10 displays the power profiles of the self-induced oscillation in the backward-wave region, where it is found that the backward wave plays a dominant role. Figure 5.11 reveals that comparing TE_{11} mode with other modes, the critical length of a backward-wave oscillation becomes less sensitive to the magnetic field strength in the deep backward-wave region. Taking all the possible oscillations into consideration, oscillation from the TE_{01} mode absolute instability is with the lowest threshold and is the most dangerous one.

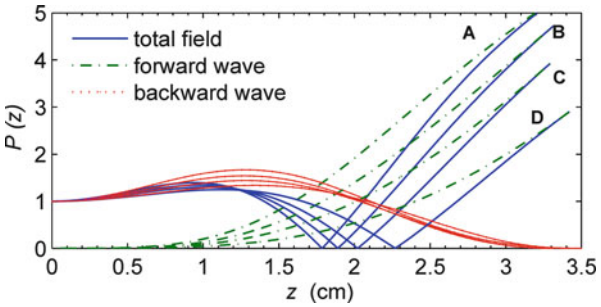

Fig. 5.9 The balance between forward-wave component and backward-wave component of the sampled conditions

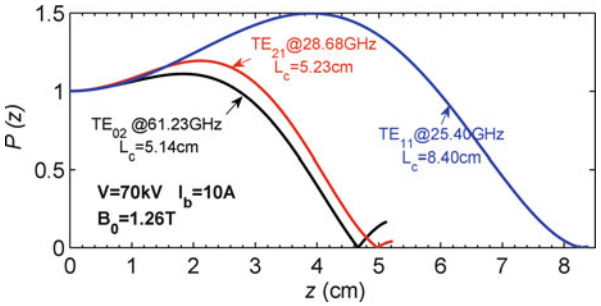

Fig. 5.10 Normalized axial power profile of oscillation in backward-wave region

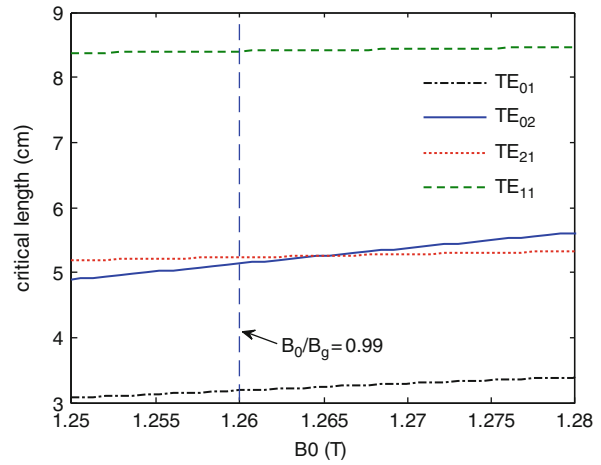

Fig. 5.11 Influence of magnetic field to the critical length

The nonlinear self-consistent theory could take both the linear stage and the nonlinear stage into consideration [11, 19, 20]. Figure 5.12 shows the axial field profiles of the four oscillations in the circuit, under both lossy dielectric and Aquadag ($\rho = 8\ e\ 4\rho_{cu}$) conditions. The lossy material suppresses the fields of oscillations, and the high power of each mode is limited in the nonlinear stage. These oscillations are also called local axial modes [21]. Comparatively study Figs. 5.5, 5.9, 5.10, and 5.12, it is found that the oscillation profiles in the nonlinear stage, or called local fundamental axial modes, are quite consistent with that of

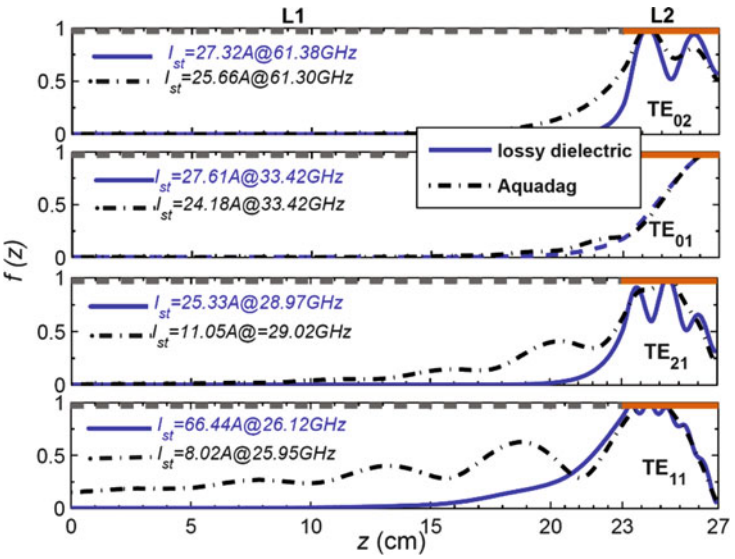

Fig. 5.12 The influence of the loss to the axial field distribution of the competing modes under start-oscillation condition

the uniform empty waveguide. Still the local axial mode, the TE_{01} oscillation is dominated by the forward-wave component. The TE_{02} mode, TE_{21} mode, and TE_{11} mode are dominated by backward-wave components. From the field profiles on the TE_{02} mode, TE_{21} mode and TE_{11} mode, it is revealed that the backward-wave components are also reflected by the interface between the lossy stage and the unloaded nonlinear stage, which results in field ripples in nonlinear stage. The thresholds of the dielectric-loaded circuit are apparently higher than the Aquadag-loaded circuit, which is consistent with the NRL experiment. It is stressed that the Aquadag-loaded circuit could not impose strong enough attenuation to the TE_{11} oscillation, and it makes the threshold current limited to only 8.02 A.

Study of the influence of the operation parameters and structure of the system stability is important to gyro-TWT experiment. The influence of the magnetic field strength and the nonlinear stage length to the thresholds is shown in Figs. 5.13 and 5.14. Increasing the magnetic field strength, the TE_{01} oscillation gets closer to the cutoff frequency, and the backward-wave component enhances the internal feedback strength. The threshold current is reduced, accordingly, which is consistent with the empty waveguide. Comparatively, the TE_{02} gets farther away from the cutoff frequency, and its threshold current increases with respect to increasing magnetic field strength. Since both the TE_{11} and TE_{21} modes are located in the deep backward-wave region, their oscillations are less sensitive to magnetic tuning. The length of the nonlinear stage is a major structure parameter to be optimized. Taking both Figs. 5.10 and 5.14 into consideration, since the critical length of TE_{11} mode is the longest, it is relatively stable to the change of L_2 stage. Under $L_2 > 5.2$ cm,

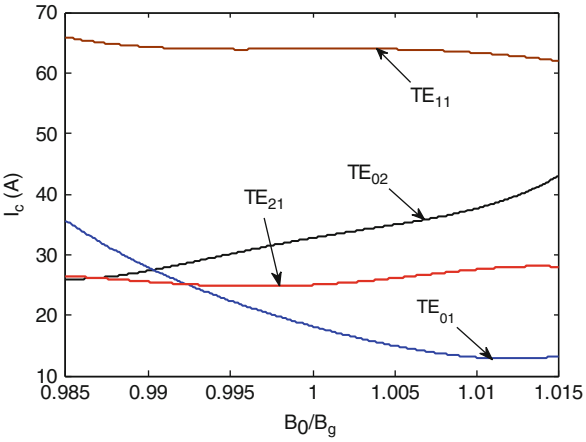

Fig. 5.13 Influence of magnetic field to threshold current

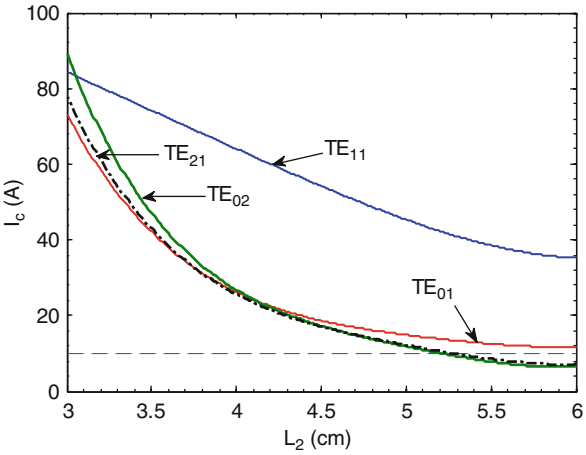

Fig. 5.14 Influence of the nonlinear stage length to threshold current

the threshold currents of both TE_{21} and TE_{02} mode oscillations are smaller than 10 A, and the threshold currents of TE_{01} mode oscillation become quite close to the 10 A. During the engineering design of a gyro-TWT, a margin safe enough should be maintained between the operation current and the threshold current to guarantee zero-drive stability.

The amplification performances of the system under velocity spread of 3 % are demonstrated in Figs. 5.15 and 5.16. The amplification profile in Fig. 5.15 shows that the backward wave grows inversely in the nonlinear stage and seriously attenuated in the lossy linear stage during propagating toward upstream. The forward-wave component exponentially grows along with the forward traveling electron beam. The dissipated power by ohm loss primarily concentrates in the downstream end of the lossy stage, which determines the average power level of the system. The amplification profile in Fig. 5.16 shows that the system could generate 223 kW at frequency of 33.59 GHz under 3 W drive power and efficiency about

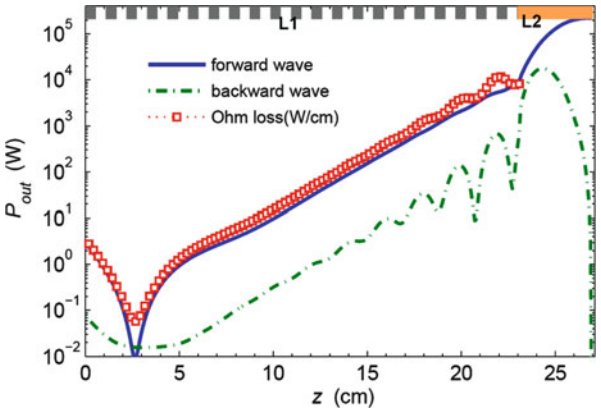

Fig. 5.15 The axial field profile of amplification

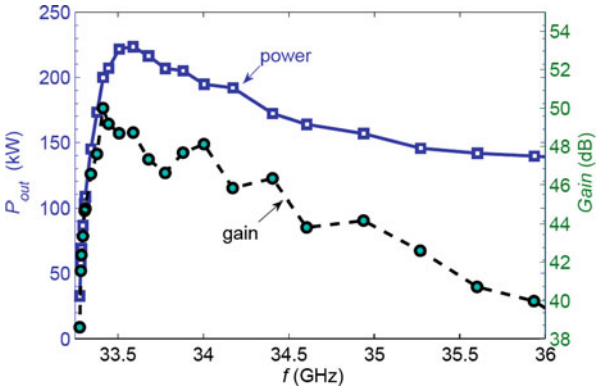

Fig. 5.16 The bandwidth of saturated amplification

32 %. Figure 5.16 shows the bandwidth of the system under beam velocity spread of 3 %. The bandwidth higher than 150 kW reaches 3 GHz, and gain is between 40 and 50 dB. Comparing the performance between simulation and NRL experiment, it is found that the improvement in the electron velocity spread is a major method to improve the performance [6].

5.3 Linear Study of Full-Wave Interaction in Dielectric-Loaded Waveguide

In the above section, the method of propagation characteristics approximation is applied to study the beam-wave interaction of the NRL periodic lossy dielectric-loaded gyro-TWT [5, 6]. It is simple and efficient, but it is valid only under some special conditions that the power which propagates in the dielectric region is negligibly small, and the dielectric imposes little influence on the field distribution of the inner vacuum region. In order to study linear behavior of ECM interaction

Table 5.3 The system parameters of dielectric-loaded gyro-TWT system

Operating mode	TE_{01} (empty waveguide), TE^{d}_{02} (DL waveguide)
Cyclotron harmonic	Fundamental
Radius	$a = 5.495$ mm, $b = 7.195$ mm
Dielectric material	$BeO - SiC(\varepsilon_r = 7.11 - j\ 1.1, \mu_r = 1)$
Beam voltage	$V = 70$ kV
Beam current	$I = 10$ A
Velocity ratio	$\alpha = 1$
Velocity spread	$\Delta v_z = 0$
Magnetic field	$B_0 = 1.26$ T
Guiding center	$r_c = 0.48\ a$

in a dielectric-loaded (DL) circuit in wider range of parameters, the linear theory of full-wave ECM interaction in dielectric-loaded circuit developed in Chap. 3 is applied. Here the DL circuit specially indicates the simple uniform DL circuit. The theory in Chap. 3 considers only the TE mode component of a mode in dielectric-loaded waveguide which is absolutely accurate for circularly polarized modes TE^{d}_{02} and TE^{d}_{04}, which only contain TE mode components. For competing hybrid modes HE^{d}_{12} and HE^{d}_{22}, the TM components are omitted [11, 22, 23]. Under present design, such approximation is valid. Since, from former analysis, the hybrid HE^{d}_{12} and HE^{d}_{22} modes are respectively with 85.3 % (25.7 GHz) and 93.4 % (29.2 GHz) of the power conveyed by the TE mode components this means the TE mode component approximation could calculate the circularly polarized TE^{d}_{02} and TE^{d}_{04} modes in ECM interaction and evaluate the thresholds of HE^{d}_{12} and HE^{d}_{22} oscillations with reasonable accuracy.

5.3.1 Linear Instability Competition Study

The discussion in this section is based on the uniform dielectric-loaded waveguide for gyro-TWT interaction circuit. Instability competition from operation TE^{d}_{02} mode and competing HE^{d}_{12}, HE^{d}_{22}, and TE^{d}_{04} modes is considered. Reference [24] provides analytical criteria of an absolute instability in uniform interaction system, and, for a lossy system, numerical simulation is applied to monitor the roots of the beam-wave-coupled dispersion relation to determine the thresholds of an absolute instability. Laplace transformation applied in the linear theory could obtain axial field profile of the ECM interaction, and monitoring the influence of parameters to the starting oscillation can determine the thresholds. Keep in mind that the linear theory here could study the circuit with uniform parameter only and the oscillation would be suppressed only when the interaction circuit is shorter than the start-oscillation length.

The parameters of the gyro-TWT are shown in Table 5.3. Under lossless condition, the first three axial modes of operation TE^{d}_{02} mode and competing HE^{d}_{12}, HE^{d}_{22}, and TE^{d}_{04} modes are shown in Fig. 5.17. Each could be decomposed into a

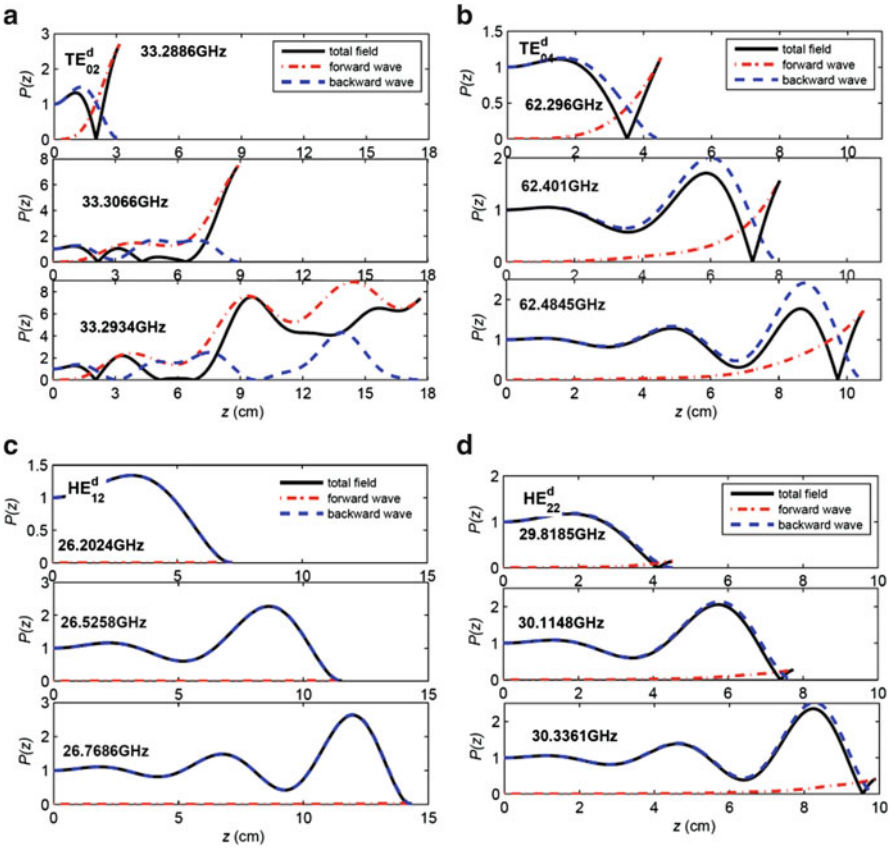

Fig. 5.17 The first three axial modes of the four modes. (**a**) TE^d_{02} mode, (**b**) TE^d_{04} mode, (**c**) HE^d_{12} mode, and (**d**) HE^d_{22} mode

forward-wave component and a backward-wave component, matching the outgoing boundary condition on both ports. The total field shows a zero power flow point when both the forward-wave and the backward-wave components are with identical amplitude. The relative amplitudes of both wave components are determined by beam-wave synchronizing point on the dispersion curve. Figures 5.17a, b indicate the instability oscillations from TE^d_{02} and TE^d_{04} modes, which are quite close to the cutoff frequencies. Both forward-wave component and backward-wave component can get synchronized with respective harmonic; hence both components are with comparative amplitudes. The absolute instability of competing HE^d_{12} and HE^d_{22} modes is in the deep backward-wave region; hence, backward-wave components of these modes are the dominant components. The total field profile in an absolute instability is the result of balance between forward-wave and backward-wave components.

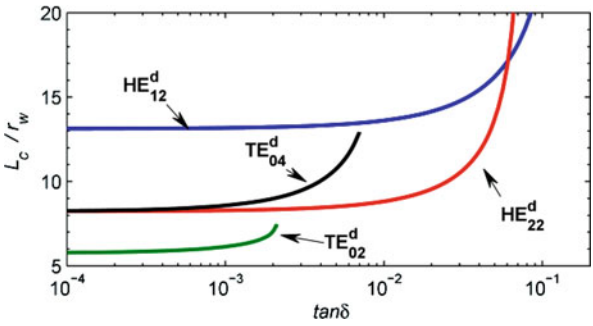

Fig. 5.18 Influence from the loss tangent to start-oscillation length

The linear study is used to determine the loss strength the linear stage required. From Fig. 5.17, it is found that the fundamental axial modes of all the instabilities are with the shortest length and are the most dangerous ones. Figure 5.18 shows the influence of dielectric loss tangent $\tan\delta$ to the start-oscillation length. For a given mode, when the loss $\tan\delta$ reaches to a certain strength, the start-oscillation length grows sharply; such a growing tendency indicates the effectiveness of the loss strength to influencing the threshold. Since the TE^d_{02} and TE^d_{04} absolute instabilities are close to the cutoff frequency, where loss-loaded waveguide imposes strongest attenuation to wave, they are suppressed under even low-loss condition $\tan\delta \approx 0.01$. The HE^d_{12} and HE^d_{22} absolute instabilities located in the deep backward-wave region, the influence from the material loss are relatively weak to suppress the oscillation, so only when the loss tangent reaches strength $\tan\delta \approx 0.1$, the oscillation is suppressed. The material adopted here is about $\tan\delta \approx 0.15$; hence, the linear stage is of high stability.

5.3.2 *Linear Growth Rate Study*

Under the driven power of 1 W, the power profile of amplification in uniform dielectric-loaded circuit is shown in Fig. 5.19. The result from nonlinear theory is also included. From calculation, there is excellent consistency between both theories [17, 18], indicating the reliability of the ECM in dielectric-loaded waveguide. Figure 5.20a shows the influence from the power in dielectric layer to amplification growth rate. It indicates that the growth rate without considering power in dielectric layer is about 1.4 % higher than the condition considered. Further calculation indicates that about 3.5 % power flows in the dielectric layer at 35 GHz. It indicates interaction without considering that the power in dielectric layer would generate power with error of several percent. Tuning the magnetic field strength and beam current in gyro-TWT is important hot test technologies. Figures 5.20b, c respectively show the growth rates under different magnetic strengths and currents. Based on the linear growth rate in Fig. 5.20, the linear stage length of the interaction circuit could be approximately determined.

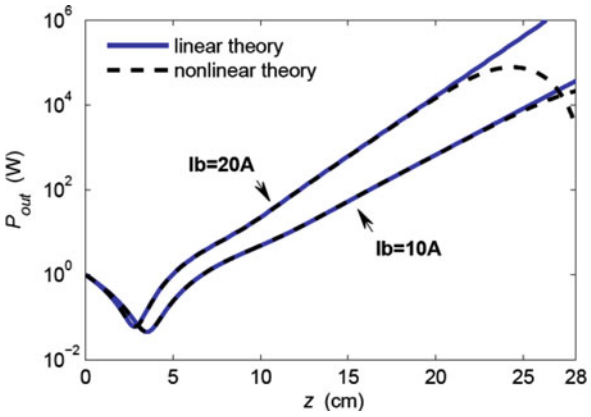

Fig. 5.19 The TE_{02}^{d} mode amplification profile in dielectric-loaded circuit (verified by nonlinear theory at frequency 35.67 GHz)

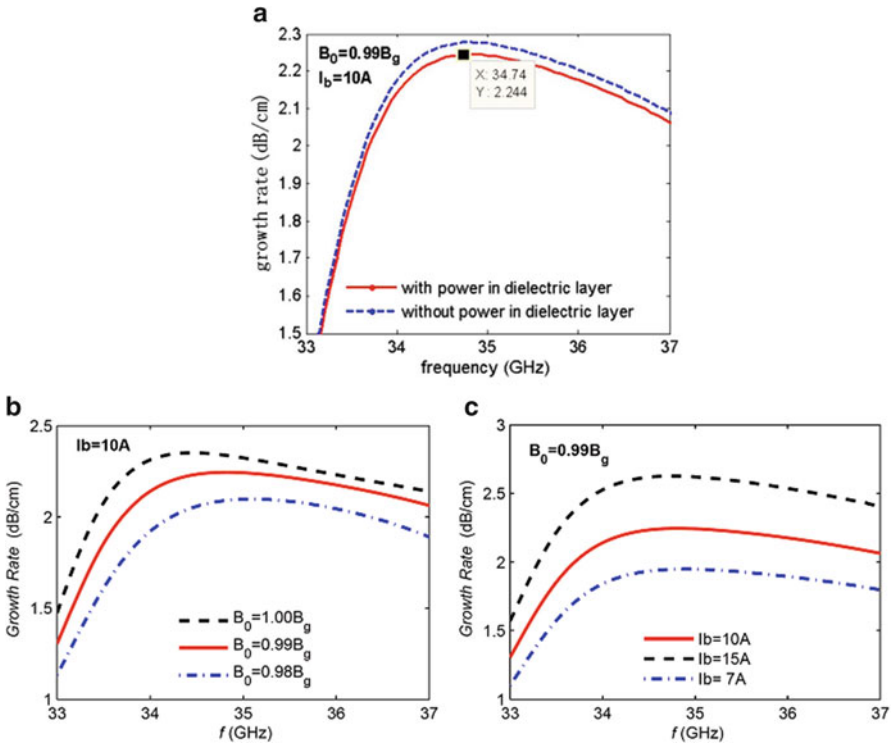

Fig. 5.20 The linear growth rates of (**a**) considering the power in dielectric layer or not, (**b**) magnetic field, and (**c**) electron beam current

5.4 Nonlinear Study of Full-Wave Interaction in Dielectric-Loaded Waveguide

The lossy dielectric-loaded (DL) interaction structure of a gyro-TWT is shown in Fig. 5.21. The interaction circuit contains three main stages, namely, input coupler stage, uniform DL circuit, and smooth output stage. The parameters of the interaction system are given in Table 5.4. The dispersion relation between the DL waveguide and empty waveguide is shown in Fig. 5.22. Since the dielectric layer extends the transverse cross area, each of the corresponding modes in the DL waveguide is with added radial index, which indicates additional field distribution in the dielectric layer, as shown in Fig. 5.23. The mode distributions in the inner vacuum region strongly correlate to that in the empty waveguide.

Here we address more detailed assumptions about the nonlinear theory of the DL waveguide [11, 17, 18, 22]. At first, the interaction considers only the TE mode

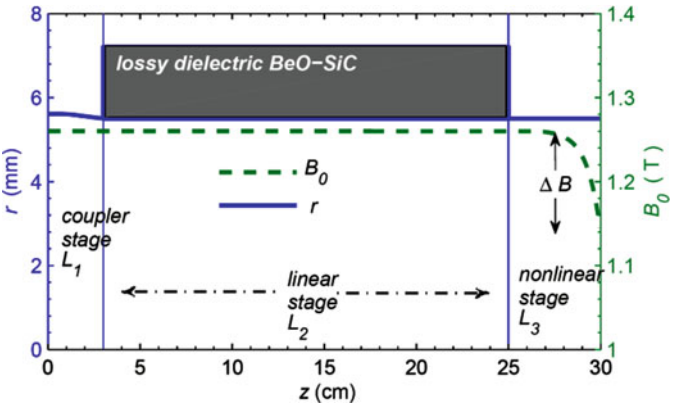

Fig. 5.21 The circuit of the uniform dielectric-loaded interaction circuit

Table 5.4 The design parameters of a gyro-TWT with a uniform DL linear stage

Operating mode	TE_{01} (empty waveguide)➔TE^{d}_{02} (DL waveguide)
Competing modes	$TE_{02}, TE_{21}, TE_{11}$ (empty waveguide) ➔$TE^{d}_{04}, HE^{d}_{22}, HE^{d}_{12}$ (DL waveguide)
Cyclotron harmonic	Fundamental
Radius	$a = 5.5$ mm, $b = 7.2$ mm
Length	$L_1 = 30$ mm, $L_2 = 225$ mm, $L_3 = 45$ mm
Dielectric material	BeO − SiC($\varepsilon_r = 7.11 - j\ 1.1, \mu_r = 1$)
Beam voltage	$V = 70$ kV
Beam current	$I = 10$ A
Velocity ratio	$\alpha = 1$
Velocity spread	$\Delta v_z = 0$
Magnetic field	$B_0 = 1.26$ T (10 % down tapered near the end)
Guiding center	$r_c = 0.48\ a$

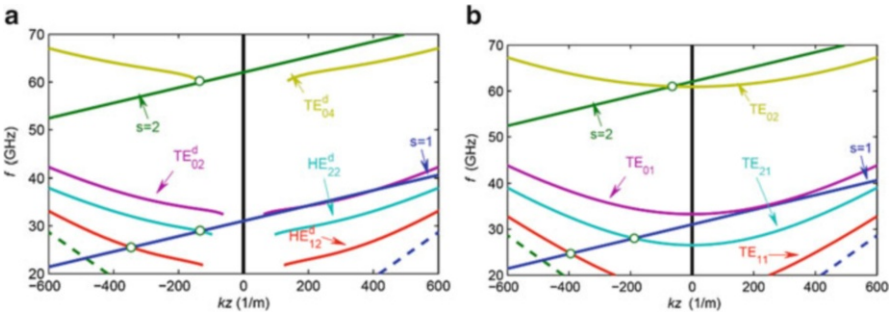

Fig. 5.22 The dispersion relations in (**a**) a uniform dielectric-loaded circuit and (**b**) empty waveguide

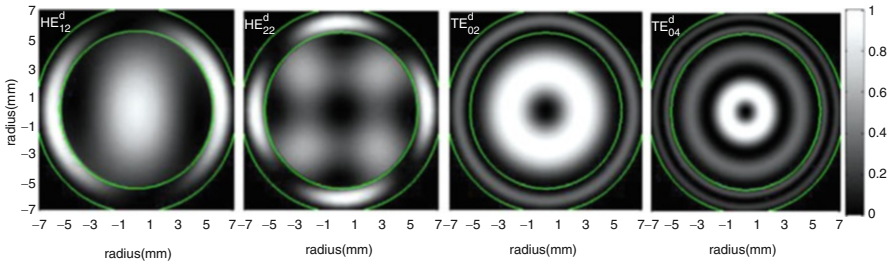

Fig. 5.23 Field distribution of the modes in DL waveguide

component, which is addressed in the last section. Secondly, the field amplitude is assumed to be continuous at a connection between the dielectric waveguide and empty waveguide. Reasons are as follows: inner radius of the connection is continuous and the boundary matching condition at a connection leads to high-order components which are much weaker than the major mode; the power of a mode is concentrated in the inner vacuum region. The ratios of the power in the vacuum region-to-total power are respectively HE^{d}_{12} mode 0.934 (26 GHz), HE^{d}_{22} mode 0.927 (29.6 GHz), TE^{d}_{02} mode 0.965 (35 GHz), and TE^{d}_{04} mode 0.948 (61 GHz). Thirdly, the axial field strength at a connection is relatively weak comparing to that of the nonlinear stage. The error from the assumption is with relative small influence. In a word, nonlinear theory could evaluate the interaction in the DL circuit with acceptable accuracy.

5.4.1 Nonlinear Instability Competition Study

Due to the mapping relation between the modes in DL waveguide and smooth waveguide, a lot of the Ka-band DL gyro-TWT studies focus on instability competition between the mode pairs $TE^{d}_{02} - TE_{01}$, $TE^{d}_{04} - TE_{02}$, $HE^{d}_{12} - TE_{11}$, and $HE^{d}_{22} - TE_{21}$. From the cold dispersion relation in Fig. 5.22, it is found that

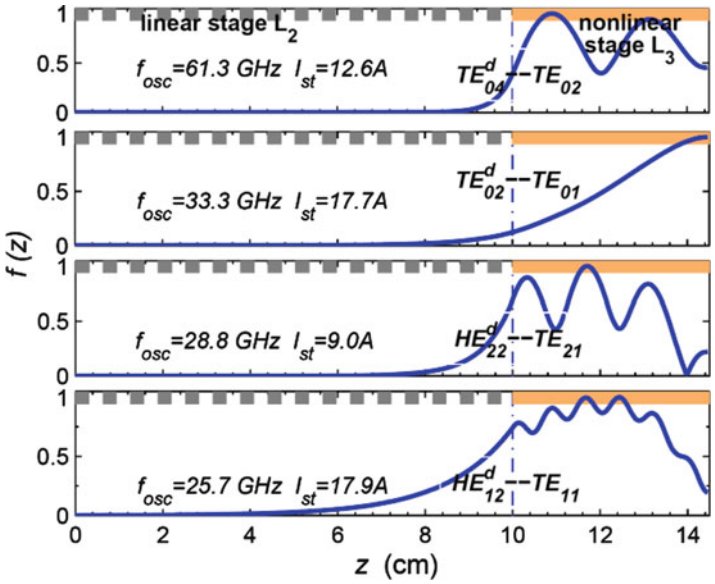

Fig. 5.24 Normalized axial field profiles of oscillations $L_1 = 0, L_2 = 10$ cm, $L_3 = 4.5$ cm, $B_0 = 1.26$ T

the potential absolute instabilities in the backward-wave region are fundamental harmonic $\mathrm{HE}_{12}^{\mathrm{d}} - \mathrm{TE}_{11}$ and $\mathrm{HE}_{22}^{\mathrm{d}} - \mathrm{TE}_{21}$ and second harmonic $\mathrm{TE}_{04}^{\mathrm{d}} - \mathrm{TE}_{02}$. The absolute instability from the operation mode $\mathrm{TE}_{02}^{\mathrm{d}} - \mathrm{TE}_{01}$ also possibly leads to oscillation. Analysis in the above section indicates that the lossy ceramic $\mathrm{BeO} - \mathrm{SiC}(\varepsilon_{\mathrm{r}} = 7.11 - j\ 1.1, \mu_{\mathrm{r}} = 1)$ is with loss strong enough to guarantee the stability in the linear stage. Here the study of the nonlinear instability competition focuses on the oscillation in the whole circuit.

Nonlinear study of the instability competition is to determine the threshold current in the whole circuit. Figure 5.24 shows the axial profiles of the self-excited oscillations from potential modes. Due to the continuous field at the connection between DL waveguide and smooth waveguide, the oscillation profiles are quite similar to that of the distributed loss-loaded gyro-TWT circuit [11, 21]. Figure 5.25 further shows the influence of the nonlinear stage length to the start-oscillation current. It indicates that a longer nonlinear stage is obviously with a lower threshold current. For an engineering design of gyro-TWT circuit, a nonlinear stage as long as possible is required to reduce the ohm loss at the end of the lossy section. In order to achieve a balance between stability and performance, the nonlinear stage $L_3 = 4.5$ cm is chosen. Under such condition, the modal pairs $\mathrm{HE}_{22}^{\mathrm{d}} - \mathrm{TE}_{21}$ and $\mathrm{TE}_{04}^{\mathrm{d}} - \mathrm{TE}_{02}$ are with threshold currents not high enough to provide a safe margin. Additional technology is required to enhance the system stability.

Based on the experience of ultrahigh gain TE_{11} gyro-TWT, magnetic tapering at the output stage is applied to enhance the system stability, without expense of

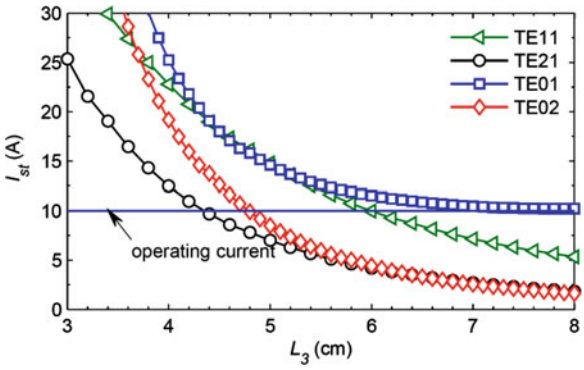

Fig. 5.25 Influence of the nonlinear stage to threshold currents of the four modes $L_1 = 0$, $L_2 = 10$ cm, $B_0 = 1.26$ T

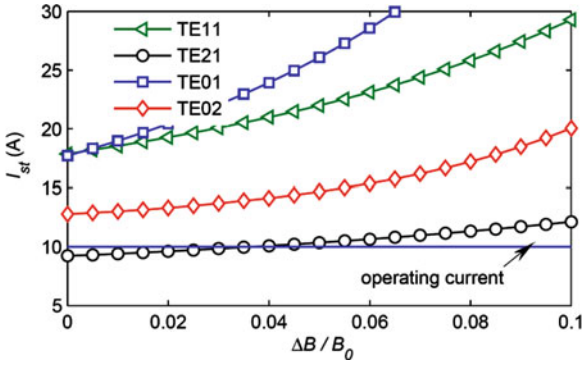

Fig. 5.26 The influence of the magnetic tapering strength of the output stage to the threshold currents, $L_1 = 0$, $L_2 = 10$ cm, $L_3 = 4.5$ cm

the amplification performance. The magnetic tapering is already given in Fig. 5.21. Figure 5.26 shows the influence from magnetic tapering $\Delta B/B_0$ to system stability. It indicates that magnetic tapering enhances the threshold currents of all the modes. When the tapering strength reaches to $\Delta B/B_0 > 5$ %, all the threshold currents are higher than the operation current 10 A. It meets the condition of zero-drive stability. In order to keep a safe margin, the magnetic tapering strength $\Delta B/B_0 = 10$ % is selected.

5.4.2 *Amplification Characteristics*

For a gyro-TWT with lossy ceramic-loaded scheme, a series of possibilities from the sintering, measuring, machining, and temperature fluctuation would introduce errors. All the above factors may lead to errors in dielectric parameter between design and engineering development. Design considerations need to be specially spent on the performance sensitivity to material and structure errors.

Figure 5.27 shows the influence of the lossy material permittivity, loss tangent, and loss layer thickness to the propagating characteristics of the operation TE_{02}^{d} mode. It is concluded that increasing both the permittivity and dielectric thickness

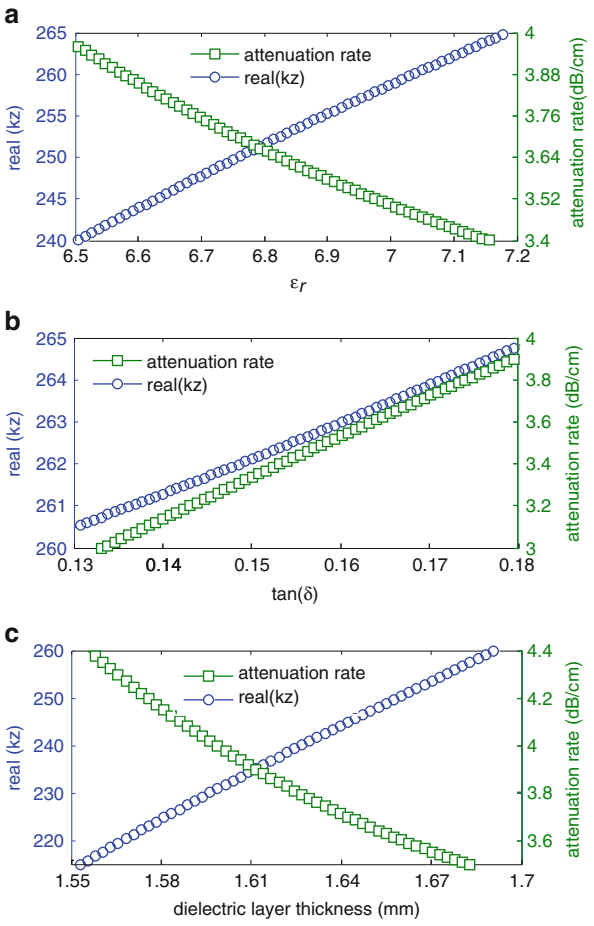

Fig. 5.27 The sensitivity of the TE_{02}^{d} propagation constant to (**a**) dielectric permittivity ε_r, (**b**) loss tangent tan δ, and (**c**) dielectric thickness (inner radius maintains unchanged 35 GHz)

leads to higher propagation constant and lower attenuation rate. Attenuation rate is almost linear related to loss tangent, and the propagation constant is relatively insensitive to loss tangent variation. Hence, employing changing the $BeO-SiC$ composition proportion to control the attenuation rate has little influence on the beam-wave synchronizing condition.

Figure 5.28 shows the sensitivity of beam-wave interaction to dielectric permittivity ε_r, loss tangent tan δ and dielectric thickness. As shown in Figs. 5.28a–c, the bandwidth and growth rate are relatively sensitive to dielectric permittivity ε_r and dielectric thickness Δr. Increasing both the ε_r and Δr would downshift dispersion curve and extend the bandwidth of the convective instability. The loss tangent mainly influences the growth rate, as shown in Fig. 5.28b. Figure 5.28c comparatively shows the growth rate of the lossy and lossless condition; it indicates the lossy material could achieve amplification rate of better uniformity in the operating frequency band.

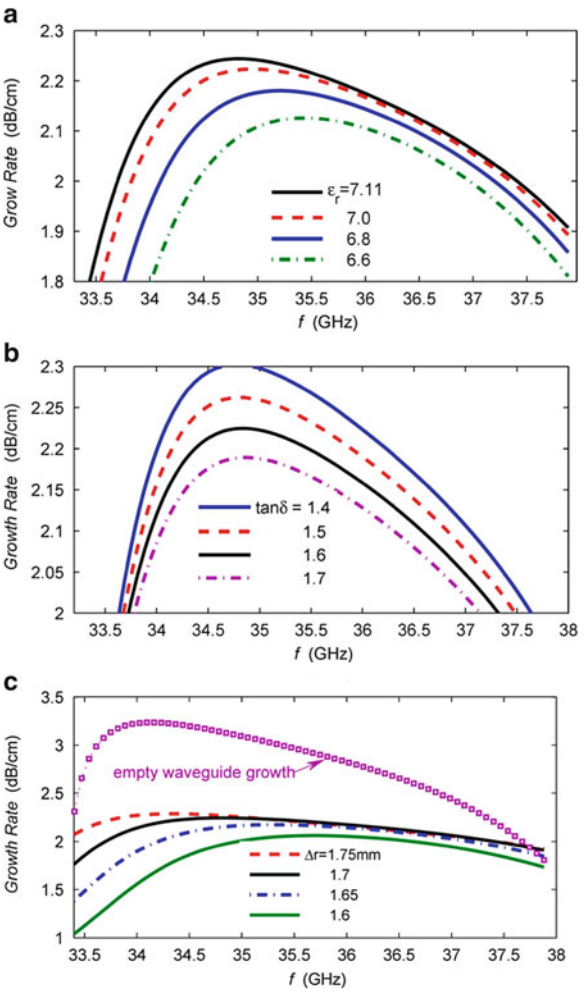

Fig. 5.28 The sensitivity of growth rate to (**a**) dielectric permittivity ε_r, (**b**) loss tangent $\tan\delta$, and (**c**) dielectric thickness Δr

The performance of the gyro-TWT based on DL linear stage is shown in Fig. 5.29. The length of the linear stage is linearly related to the total gain, but it has little influence on the saturated amplification power. The influence of the loss tangent $\tan\delta$ is quite similar to that of the linear stage length. Because both the linear stage length and loss tangent $\tan\delta$ affect the total attenuation of circuit, and they have little influence on the beam-wave synchronizing condition. Hence, their influences to the total performance are similar. Similar to other gyro-TWTs, the Doppler-shifted ECM resonance in a DL gyro-TWT is with reduced growth rate when the beam velocity spread increases. From both Figs. 5.28 and 5.29, it is concluded that the material parameters mainly affect the linear performance and introduce less influence on saturated power.

Figures 5.27 and 5.28 show similar influences of ceramic permittivity and ceramic thickness Δr to propagation constant. Under the driving power of 0.55 W,

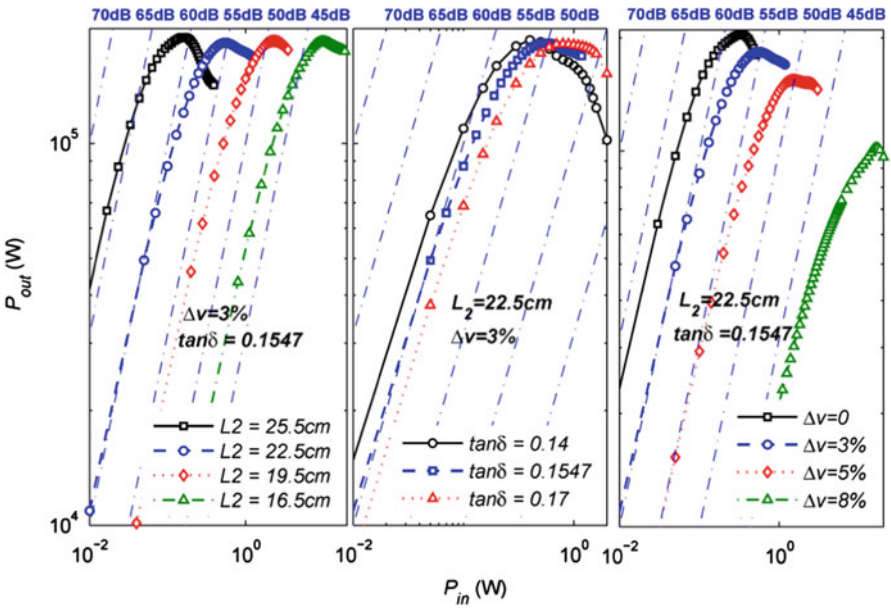

Fig. 5.29 Influence of the ceramic length L_2, loss tangent tan δ, and electron beam velocity spread Δv_z to beam-wave interaction at 35 GHz

Fig. 5.30a shows the bandwidth under different permittivity values. It shows that the permittivity value affects both the output power and bandwidth. From both Figs. 5.27 and 5.28, the propagation constant is approximately with linear relation with the ceramic permittivity. Under fixed fundamental cyclotron harmonic, variation of the ceramic permittivity changes the beam-wave resonance bandwidth. It affects the performance accordingly. Figure 5.30b shows the amplification field axial profile at the 35 GHz. Under the velocity spread $\Delta v_z = 3$ %, the interaction efficiency reaches 29.6 %, and about 3.3 % is absorbed close to the end of the lossy stage. The summation of the field power and ohm loss power right balances the electron beam efficiency, indicating the energy conservation of the system. The saturated power is shown in Fig. 5.30c. Under velocity spread of $\Delta v_z = 3$ %, the output power is about 220 kW, −3 dB bandwidth reaches 10 %, total gains about 40–55 dB.

5.5 Beam-Wave Coupling Strength

Investigation in former sections indicates that the threshold of a start-oscillation state can be described by a series of different parameters, such as threshold current I_{st}, critical length L_C, the electron beam pitch factor $\alpha = v_t/v_z$, and the critical attenuation strength. All these threshold parameters are directly related to the

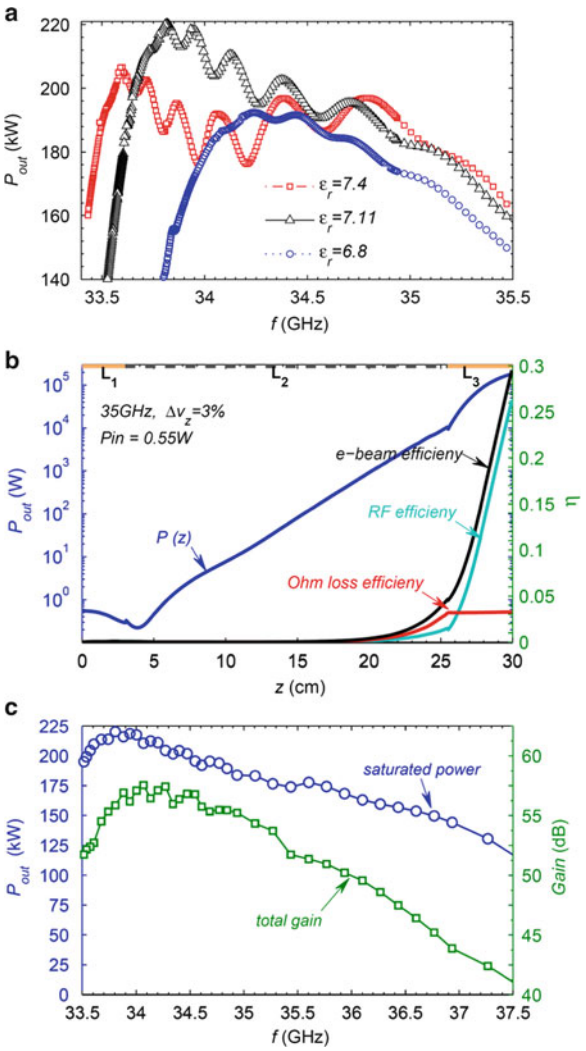

Fig. 5.30 (**a**) Sensitivity of the output power to ceramic permittivity, (**b**) amplification profile and interaction efficiency, and (**c**) saturated power and efficiency (velocity spread $\Delta v_z = 3$ %)

beam-wave coupling strength. Once the beam-wave coupling strength exceeds the critical strength of start-oscillation state, the ECM system turns into efficient self-excited oscillation from perturbation. A gyro-TWT is a complicated system of multiple dimensions of freedoms, and the beam-wave coupling strength involves factors of various aspects, including the transverse kinetic energy of the electron beam, beam velocity spread, guiding center location, the EM wave impedance, and waveguide wall loss. Not only beam current I_b, voltage V, and pitch factor α affect the transverse beam kinetic energy but also the beam velocity spread $\Delta v_z/v_z$ influences the effective energy interacting with the wave. In a cavity circuit, the quality factor Q is applied to describe the ratio between the energy stored inside and

the dissipation power. While in a gyro-TWT, there is not only the mainly traveling-wave circuit but also some unavoidable disturbance, which may excite small local reflection and rise low-Q spurious mode in the circuit. Keep in mind that a self-excited oscillation in a gyro-TWT circuit oscillates at a frequency decided by both the *traveling-wave* circuit and beam condition, not exactly the oscillation frequency of the low-Q spurious mode in an electron-free circuit. How to describe the beam-wave coupling strength to include the major factors? Former a dimensionless coupling factor is defined as [1–3]

$$H_{sm}(x, y) = \left|J_s'(x) J_{m-s}(y)\right|^2 \tag{5.1}$$

where $x = k_\perp r_\mathrm{L}$, and $y = k_\perp r_\mathrm{c}$, $k_\perp$ indicates the transverse wave number, r_L and r_c indicate the Larmor radius and guiding center radius of the electron beam, s indicates the harmonic number, and m indicates the order of the Bessel Function of the first kind. Actually, in the field of vacuum electronic devices (VEDs), beam-wave coupling impedance K is applied to describe the beam-wave coupling strength of a rectilinear VED

$$K = \frac{|U|^2}{2P} \tag{5.2}$$

where U is an equivalent voltage from the $\overrightarrow{E}$ of the field and P is the power flows in the circuit. To make the impedance K suitable to describe an ECM system, the equivalent voltage is defined as the azimuthal integration of the synchronized EM field component on the Larmor circle

$$U = \int_0^{\frac{\pi}{2s}} E_{s\theta} \cos(s\theta)\, r_\mathrm{L} \mathrm{d}\theta \tag{5.3}$$

where s is the cyclotron harmonic number and $E_{s\theta}$ is the synchronized component of angular electric field on the Larmor circle

$$E_{s\theta} = \frac{j\omega\mu_1}{k_{\perp 1}} f(z) J_s'(k_{\perp 1} r_\mathrm{L})\, J_{m-s}(k_{\perp 1} r_\mathrm{c}) \tag{5.4}$$

In a uniform dielectric-loaded waveguide, the coupling impedance is defined as [25]

$$K = \mu_1 |k_{\perp 1}|^2 \frac{r_\mathrm{L}^2}{s^2} \frac{v_\mathrm{p}}{G_{mn}} H_{sm} \tag{5.5}$$

where the phase velocity of the wave is $v_\mathrm{p} = \omega/k_z$ and the geometer factor is defined as $G_{mn} = K_a$ in a uniform empty waveguide

$$K_a = \frac{2\pi}{|k_{\perp 1}|^2} \int_0^a \left[\left|J_m'(k_{\perp 1} r)\right|^2 + \left| \frac{m}{k_{\perp 1} r} J_m(k_{\perp 1} r) \right|^2 \right] r \mathrm{d}r \tag{5.6}$$

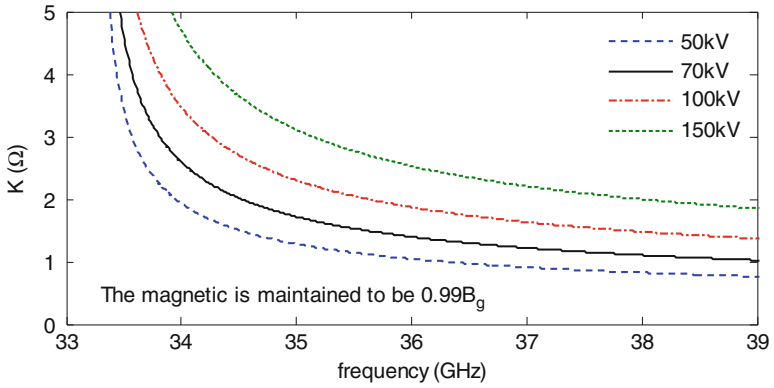

Fig. 5.31 Influence of the beam voltage to beam-wave coupling strength of TE_{01} mode

While in uniform dielectric-loaded waveguide, it is defined as $G_{mn} = K_a + K_b$, where

$$K_b = \frac{2\pi}{|k_{\perp 2}|^2} \int_a^b \left[\begin{array}{l} \left| \left[\alpha J'_m (k_{\perp 2} r) + \beta N'_m (k_{\perp 2} r) \right] \right|^2 \\ + \left| \frac{m}{k_{\perp 2} r} \left[\alpha J_m (k_{\perp 2} r) + \beta N_m (k_{\perp 2} r) \right] \right|^2 \end{array} \right] r \mathrm{d}r \tag{5.7}$$

Further, a coupling voltage to describe the effective beam energy which has been coupled with operating mode is defined as

$$V = \alpha I_b K \tag{5.8}$$

where I_b is the beam current. The coupling impedance K could be used to measure the modulating ability of the EM mode to electron beam, and the coupling voltage V can be applied to measure the exciting ability of the harmonic cyclotron electron mode to the EM field. The coupling impedance K and the coupling voltage V bring a general frame to measure beam-wave coupling strength between different harmonics and operation modes.

The parameters for numerical investigation are as given in Table 5.4. The beam-wave coupling strength in a smooth waveguide is studied first. Figure 5.31 shows the influence of the beam voltage to the beam-wave coupling impedance K. Increasing beam voltage leads to higher beam energy, and the beam-wave coupling strength is enhanced accordingly. In addition, since the coupling strength is proportional to wave phase velocity, the coupling strength becomes higher when it gets closer to the cutoff frequency.

The magnetic tuning is capable of changing the synchronization between cyclotron harmonics and operation modes. Figure 5.32 shows the influence of the magnetic tuning to the beam-wave coupling impedance of TE_{01} and TE_{02}, TE_{21} and TE_{11} modes. Increasing the magnetic B_0 between $1.00B_g$ and $1.12B_g$,

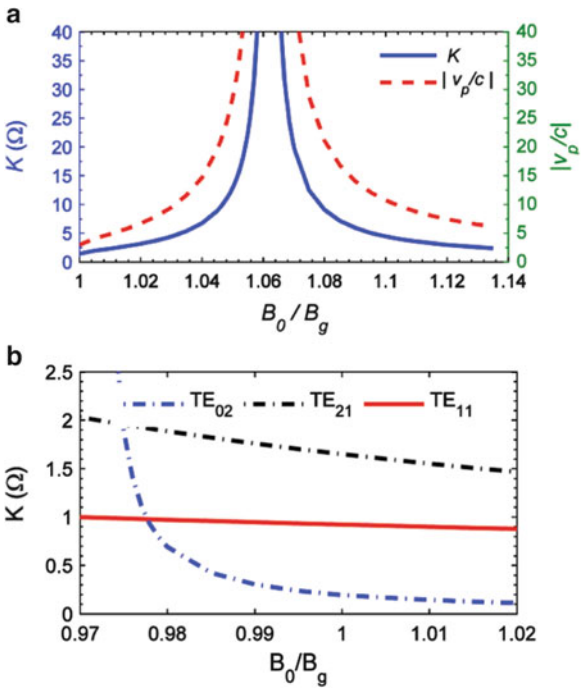

Fig. 5.32 The influence of the magnetic tuning to the coupling impedance of (**a**) TE_{01} mode and (**b**) TE_{02}, TE_{21}, and TE_{11} mode, where the (ω, k_z) at the beam-wave cross points are adopted

the synchronization between fundamental cyclotron harmonic and operation TE_{01} moves from the forward-wave interaction region toward the cutoff region and finally into the backward-wave region. The phase velocity mainly affects the beam-wave coupling impedance, and K grows toward infinite at the cutoff frequency. Since the TE_{11} and TE_{21} modes synchronize to the fundamental harmonic in the deep backward-wave region, the K of the two modes is less sensitive to magnetic tuning. Increasing magnetic strength shifts the beam-wave cross point from the cutoff frequency toward the backward-wave region. Hence, the K of the TE_{02} mode reaches highest strength close to the low magnetic region.

For a Ka-band DL gyro-TWT, its linear stage employs DL waveguide, and nonlinear stage employs smooth waveguide. Figure 5.33 comparatively shows the beam-wave coupling impedance of modes at specific synchronizing frequencies in DL waveguide and smooth waveguide. Since the dielectric layer of the DL waveguide conveys part of the power, the electron beam encounters lower field strength in the DL waveguide if both waveguides propagate identical power. For other modes, the differences of the coupling impedance between the DL waveguide and the smooth waveguide primarily originate from the differences of beam-wave cross points on the cold dispersion map.

Figure 5.34 comparatively shows the beam-wave coupling impedance and the growth rate of the convective instability. Due to the lossy property and modification to the dispersion of the operating TE_{01} mode, the circuit based on the lossy DL waveguide is of wider instability bandwidth and better uniformity. Similarly,

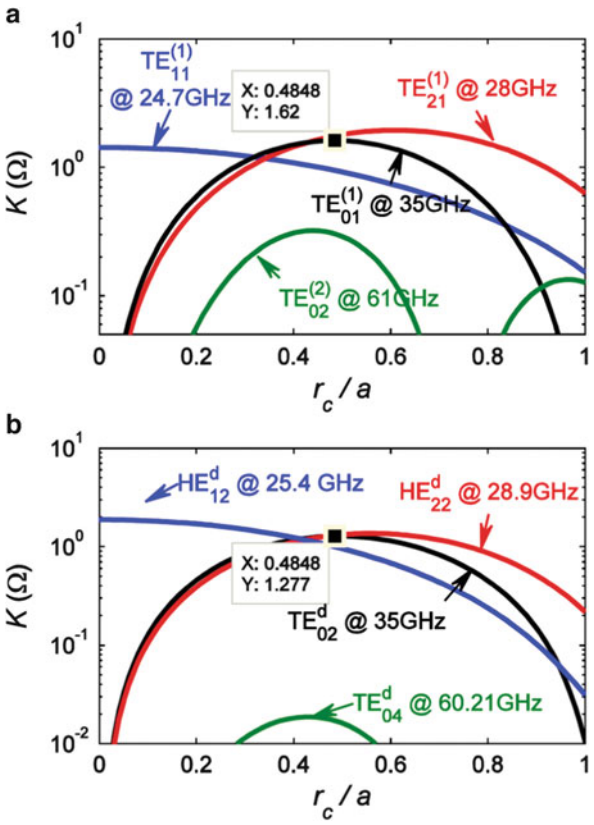

Fig. 5.33 Beam-wave coupling strength in (**a**) smooth waveguide and (**b**) dielectric-loaded waveguide

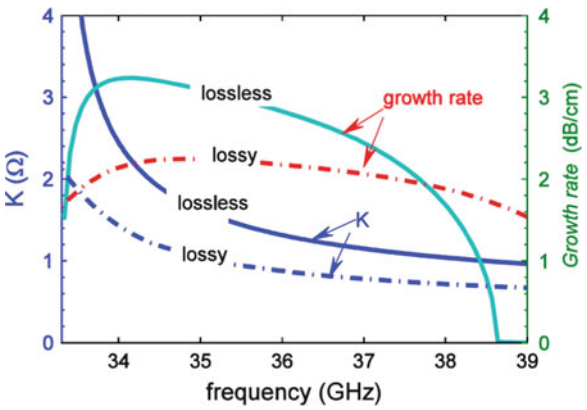

Fig. 5.34 The coupling impedance and convective instability growth rate in lossy DL waveguide and smooth waveguide

the lossy DL waveguide is of smaller but flatter beam-wave coupling impedance than that of the empty waveguide. In addition, since the coupling impedance is proportional to the phase velocity, the impedance gets stronger when it gets close to the cutoff frequency.

Summarizing the study on the beam-wave coupling impedance, we conclude the following rules. Firstly, the coupling impedance K is proportional to the phase velocity of the mode and grows toward infinite when the frequency gets close to the cutoff frequency in lossless waveguide. Secondly, stronger coupling impedance leads to higher instability growth rate. Thirdly, under the same frequency, a lower order mode is with stronger coupling impedance than a higher-order mode. Comparing the beam-wave synchronization of these three kinds of device, namely, gyrotron, gyroklystron, and gyro-TWT, we can get an intuitional understanding of the beam-wave coupling strength in three different gyrotron devices. A gyrotron operates on a frequency quite close to the cutoff frequency. Hence, it is with highest beam-wave coupling strength. A gyroklystron is a kind of cavity-based narrow band amplifier, and its working band is generally closer to the cutoff frequency than a gyro-TWT, but not as close as a gyrotron. It is generally true that a gyroklystron is with a weaker coupling strength than a gyrotron, but stronger than that of the gyro-TWT. A gyro-TWT operates in broad bandwidth away from the cutoff frequency, and it is, generally speaking, with the lowest beam-wave coupling strength than other gyro-devices.

5.6 Summary

This chapter employs three different methods to study the DL gyro-TWTs. The first is applying propagation characteristics approximation to simplify the DL interaction circuit as a smooth waveguide and considers the attenuation and dispersion characteristics of the wave in the DL waveguide. The simple model of this method provides very efficient evaluation during the preliminary design of the gyro-TWT design. The second method and the third method are respectively the linear theory and nonlinear theory of the full-wave DL waveguide interaction. Both methods consider the influence of the lossy dielectric layer to field distribution. The last section simply devotes to study the beam-wave coupling strength of ECM system and brings some simple and intuitive conclusions for understand the ECM interaction.

The conclusion of this chapter includes that the performance of a DL gyro-TWT is stable to dielectric parameters and structure parameters in a reasonable range and lossy dielectric combined with metal structure to construct DL waveguide is capable of selectively suppressing the instability competition. The full-wave interaction theory also could be applied to study the gyrotron slow-wave amplifier and to explore the ultra-broadband width characteristics.

References

1. Chu KR (2004) The electron cycltron maser. Rev Mod Phys 76:489–540
2. Chu KR (2002) Overview of research on the gyrotron traveling-wave amplifier. IEEE Trans Plasma Sci 30:903–908

3. Chu KR, Chen HY, Hung CL et al (1998) Ultrahigh gain gyrotron traveling wave amplifier. Phys Rev Lett 81:4760–4763
4. Lau YY, Barnett LR, Granatstein VL (1982) Gyrotron traveling wave amplifier: IV. Analysis of launching losses. Int J Infrared Millim Waves 3:45–62
5. Calame JP, Garven M, Danly BG et al (2002) Gyrotron-traveling wave-tube circuits based on lossy ceramics. IEEE Trans Electron Devices 49:1469–1477
6. Garven M, Calame JP, Danly BG et al (2002) A gyrotron-traveling-wave tube amplifier experiment with a ceramic loaded interaction region. IEEE Trans Plasma Sci 30:885–893
7. Wang E, Zeng X, Liu BT, Qian LJ, Li ZL, Feng JJ, Zhu SQ (2012) Experimental study of high power gyrotron traveling wave tube with periodic lossy material loading. IEEE Trans Plasma Sci 40(7):1846–1853
8. Yan R, Luo Y, Liu G, Pu YL (2012) Design and experiment of a Q-band gyro-TWT loaded with lossy dielectric. IEEE Trans Electron Devices 59(12):3612–3617
9. Song HH, McDermott DB, Hirata Y et al (2004) Theory and experiment of a 94 GHz gyrotron traveling-wave amplifier. Phys Plasmas 11:2935–2941
10. Sirigiri JR, Shapiro MA, Temkin RJ (2003) High-power 140-GHz quasioptical gyrotron traveling-wave amplifier. Phys Rev Lett 90:258302
11. Du CH, Liu PK (2009) Stability study of a gyrotron-traveling-wave amplifier based on a lossy dielectric-loaded mode-selective circuit. Phys Plasmas 16:073104
12. Rao SJ, Jain PK, Basu BN (1996) Broadbanding of a gyro-TWT by dielectric-loading through dispersion shaping. IEEE Trans Electron Devices 43:2290–2299
13. Singh G, Chandra SMSR, Bhaskar PV et al (2004) Analysis of a vane-loaded gyro-TWT for the gain-frequency response. IEEE Trans Plasma Sci 32:2130–2138
14. Singh G, Basu BN (2005) Improved approach for gain-frequency response of vane-loaded gyro-TWT. IEEE Trans Plasma Sci 33:1443–1446
15. Chu KR, Ganguly AK, Granatstein VL et al (1981) Theory of a slow wave cyclotron amplifier. Int J Electron 51:493–502
16. Choe JY, Uhm HS, Ahn S (1981) Analysis of the wide band gyrotron amplifier in a dielectric loaded waveguide. J Appl Phys 52:4508–4516
17. Du CH, Liu PK (2010) Linear full-wave-analysis of dielectric-lined waveguide. IEEE Trans Plasma Sci 38(6):1219–1226
18. Du CH, Liu PK (2010) Nonlinear full-wave-analysis dielectric loaded gyro-TWT. Phys Plasmas 17:033104
19. Du CH, Liu PK, Xue QZ et al (2008) Effect of a backward wave on the stability of an ultrahigh gain gyrotron traveling-wave amplifier. Phys Plasmas 15:123107
20. Du CH, Liu PK (2009) Stabilization of the potential multi-steady-state absolute instabilities in a gyrotron traveling-wave amplifier. Phys Plasmas 16:103107
21. Chang TH, Chen NC (2006) Transition of absolute instability from global to local modes in a gyrotron traveling-wave amplifier. Phys Rev E 74:016402
22. Du CH, Liu PK (2009) A lossy dielectric-ring loaded waveguide with suppressed periodicity for gyro-TWTs applications. IEEE Trans Electron Devices 56:2335–2342
23. Du CH, Xue QZ, Liu PK et al (2009) Modal transition and reduction in a lossy dielectric-coated waveguide for gyrotron-traveling-wave tube amplifier applications. IEEE Trans Electron Devices 56:839–845
24. Chu KR, Lin AT (1988) Gain and bandwidth of the gyro-TWT and CARM amplifiers. IEEE Trans Plasma Sci 16:90–104
25. Du CH, Liu PK (2010) Beam-wave coupling strength analysis in a gyrotron traveling-wave amplifier. J Infrared Millim Terahz Waves 31:714–723

Chapter 6
Exploring New Mechanisms for High Power Millimeter-Wave Gyrotron Amplifiers

Abstract A complex gyrotron amplifier, namely, gyrotron-cascaded pre-bunching amplifier (gyro-CPA), is proposed in this chapter. The amplifier employs three interesting schemes, which are called electron cyclotron maser (ECM)-cascaded amplifier, high-order mode drift tube, and bi-mode operation. These topics are intended for providing solutions to the challenges related to lossy material error control, suppressing instability competitions, and high-power capability in engineering developing a gyrotron amplifier.

Keywords High power • Millimeter-wave • Gyrotron amplifier • High-order mode • Lossy ceramic

6.1 Introduction

This section presents some considerations related to dielectric-loaded circuits of gyrotron amplifier. The major aim is to address some interesting physics in some novel circuits and provide stimulating ideas for engineering applications. Reviewing the past gyro-TWTs experiments, various kinds of beam-wave interaction structures and schemes are innovated, as a way to continuously promote the amplifier development. These novel interaction circuits include [1–3]:

- *Broadband interaction circuit based on tapered waveguide cross section*: In the 1980s and 1990s, the Naval Research Laboratory (NRL) employed tapered rectangular waveguide as interaction circuit and adjusted the magnetic field profile to ensure the beam-wave synchronization along the circuit. Experiments successfully explored the broadband operation capability of the gyro-TWTs and obtained bandwidth up to 33 % [3–5].
- *Interaction circuit based on the wall loss*: In the 1990s, K. R. Chu and his group from National Tsing Hua University (NTHU) carried out experiments based on distributed wall loss interaction circuit. It successfully demonstrated the potential of the wall loss to improve the system stability. Ultrahigh gain and high output

C.-H. Du and P.-K. Liu, *Millimeter-Wave Gyrotron Traveling-Wave Tube Amplifiers*,
DOI 10.1007/978-3-642-54728-7_6, © Springer-Verlag Berlin Heidelberg 2014

power were achieved [6, 7]. The wall loss mechanism was also adopted in a series of other interaction systems, including slotted waveguide [8, 9], sliced waveguide [10, 11], periodic lossy DL cylindrical waveguide [11–14], and quasi-optical confocal waveguide [15].

- *High-order mode circuit*: A high-order mode circuit is of larger transverse space than a low-order mode system, corresponding to higher power capacity. The MIT carried out gyro-TWT experiment based on the high-order HE_{06} mode in a confocal waveguide. An interaction circuit based on photonic band-gap (PBG) structure is also another candidate to achieve high-order mode operation. Its feasibility was approved by a 140 GHz TE_{04}-like mode gyrotron [16].
- *Helically corrugated waveguide*: In the 1990s, an impressive progress was made on developing gyro-TWTs-based helically corrugated waveguide [17–21]. In a helically corrugated waveguide, a pair of counterrotating modes meeting Bragg resonant condition couple into a new mode, and it is of approximately constant group velocity near the region $k_z \approx 0$ on the cold dispersion map, which means that the interaction is insensitive to velocity spread.

Gyrotron amplifiers based on the principle of electron cyclotron maser (ECM) are generally divided into two classes, namely, the gyro-TWT amplifier and the gyroklystron amplifier. The broadband Doppler-shifted beam-wave synchronization provides a gyro-TWT broadband operation capability. A cavity-based gyroklystron is capable of generating higher power, but the bandwidth is relatively limited. There are also other amplifier schemes which were investigated. A gyrotwystron is a kind of hybrid amplifier, which is a combination of cavity-bunching stage and traveling-wave output stage [22]. A harmonic-multiplying gyrotron amplifier was created by combining a fundamental harmonic stage and a higher harmonic stage, and it can generate high output power with the frequency as s times as the driving signal, where s is harmonic number of the output stage [23].

Above introduction indicates that the interaction circuit of a gyrotron amplifier is not limited to traveling-wave circuit or cavity circuit. From various kinds of tapered circuit, wall loss-loading schemes, helically corrugated waveguide, and combination of the traveling circuit and cavity circuit, it is concluded that there is a high flexibility of selecting an interaction circuit for a gyrotron amplifier. Through properly combining a cavity circuit and a traveling-wave circuit, a trade-off can be made between output power and bandwidth to obtain high stability and overall performance. For a gyrotron traveling-wave amplifier, since the lossy material must be loaded in a gyrotron amplifier to suppress instability competition, it brings the interaction circuit discontinuities and may induce reflection in the interaction system. To some extent, such discontinuities function as the boundaries of cavities. In other words, a *cavity* of low-quality factor is normally unavoidable in the circuit of a gyro-TWT amplifier. In order to achieve high power for millimeter-wave gyrotron amplifier, the following considerations are proposed. First, an interaction circuit based on a high-order operation mode is proposed to ensure high-power capacity. For a gyrotron amplifier, a high-order mode circuit with relatively larger cross section also brings convenience in fabrication. Second, mode control

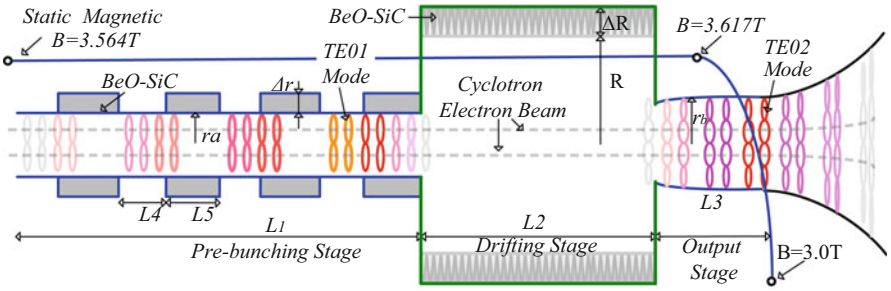

Fig. 6.1 A schematic demonstration of a gyrotron-cascaded pre-bunching amplifier (gyro-CPA)

mechanism should be introduced to suppress instability competition and guarantee high efficiency interaction on the operating mode. A certain kind of loss mechanism, such as loading loss material, or including a diffraction-loss slice or slot on the circuit wall, is normally proposed to bring strong disturbance to competing mode as well as maintain amplification on the operating mode. Third, in order to achieve broadband operation, traveling-wave circuit should play a major contribution to beam-wave interaction.

Based on the above-proposed principles, a scheme for high-power millimeter-wave gyrotron amplifiers is introduced in this chapter, as is shown in Fig. 6.1. Such a schematic amplifier is called gyrotron-cascaded pre-bunching-excited amplifier (gyro-CPA). The interaction circuit of a gyro-CPA includes three stages, namely, pre-bunching stage, high-order mode drift stage, and output stage. For the pre-bunching stage, a section of metal tube followed by a lossy ceramic tube constitutes a single ECM stage; several ECM stages build a multi-ECM-cascaded bunching circuit. The cyclotron electron beam gains bunching in phase space after traveling through such a bunching stage and injects into a high-order mode drift stage. Finally, the cyclotron electron beam induces high-power radiation in the output stage via convective instability of a high-order-mode interaction.

The scheme of the gyro-CPA shown in Fig. 6.1 contains some interesting physics which will be useful for engineering development. Before investigate beam-wave interaction in a gyro-CPA, special topics will be addressed in detail, including ECM-cascaded pre-bunching stage, high-order mode drift stage, and multimode matching technology. Finally, preliminary estimation on the stability and performance of the proposed gyro-CPA is discussed. The following sections will separately discuss the physics in each part of the system.

6.2 An ECM-Cascaded Amplifier

Comparing between a traditional gyro-TWT and a gyroklystron, it is found that a gyro-TWT based on a traveling-wave interaction circuit is capable of achieving broad bandwidth, but special mode control mechanism should be employed

to suppress potential instability competitions. A gyroklystron based on cavity interaction in a narrow band is easier to achieve higher power and better stability. Is there a solution to achieve broadband operation, high-power output, and good stability by combining together a traveling-wave circuit and cavity circuit? In this section, a gyrotron ECM-cascaded amplifier is introduced to study the physics in the ECM-cascaded circuit, a kind of circuit between a gyroklystron and a gyro-TWT.

6.2.1 The Concept of ECM-Cascaded Amplifier

A gyrotron amplifier normally encounters the problem of instability competition [1, 24]. Normal solutions to suppressing instability competition include lossy cutoff drift tube, as usually adopted in a gyroklystron, and distributed wall loss, as normally loaded in a gyro-TWT. The lossy drift tube in a gyroklystron provides space to enhance electron inertial bunching and cuts off the electromagnetic (EM) field between a pair of adjacent cavities. But there is something worthy of attenuation for a high-order mode gyroklystron. The operating high-order mode is under cutoff in the drift tube, but this is usually not the case for a low-order spurious mode in the drift tube. Such a spurious mode couples from one cavity to the next and possibly leads to oscillation. Lossy material loaded in the drift tube also helps to suppress the low-order mode coupling. In a gyro-TWT, lossy material is usually loaded in the linear stage to suppress instability competition, as a way to achieve a higher threshold current and higher output power [25–27]. The bottleneck for a lossy material-loaded gyro-TWT is that the dissipated power density exponentially grows along with growing wave strength toward downstream, and, near the nonlinear stage, it reaches such a strength that may be beyond the cooling capability and generate outgassing due to overheating. This hinders the average power capacity of a normal gyro-TWT. These problems lead us to find out solution of suppressing instability competition in a high-power broadband gyrotron amplifier.

Investigation reveals that wall loss technique in a gyro-TWT brings a mechanism to stabilize instability competition in electron cyclotron maser, ensures effective interaction between cyclotron electron beam and operation mode, and, finally, induces high-power radiation in the unloaded nonlinear stage. Besides, instability competition investigation of a wall loss-loaded system usually concentrates on mode attenuation in a gyro-TWT system, while much less attention is paid on the beam-wave detuning $\Delta\omega = \omega - k_z v_z - s\Omega_e/\gamma$ from ideal synchronization $\Delta\omega = 0$. In the interaction system, the propagation constant k_z and magnetic field B_0 are key factors to influence the beam-wave detuning $\Delta\omega$, as a way to influence the competing instability. Special magnetic field profile is not easy to build, but modification of the propagation constant k_z can be easily realized by adjusting waveguide radius or lossy material parameters. Investigation in this section focuses the influence of the propagation constant k_z to system performance. A schematic plot of lossy material-loaded ECM-cascaded gyrotron amplifier is shown in Fig. 6.2. It is a kind of circuit between a gyroklystron and a gyro-TWT.

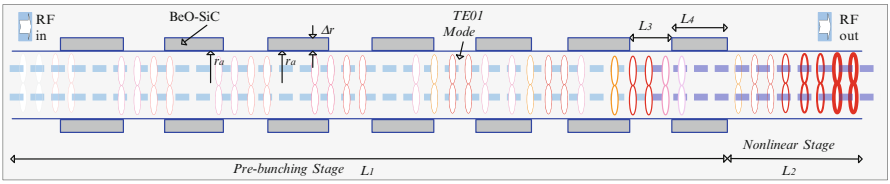

Fig. 6.2 A schematic plot of lossy material-loaded ECM-cascaded gyrotron amplifier, where operating mode TE_{01} in metal stage and TE^{d}_{02} in ceramic-loaded waveguide, and $r_a = r_b = 1.99$ mm, $\Delta r = 0.615$ mm, ceramic parameters $\varepsilon_r = 6.3 - 0.85\,j$, and $\mu_r = 1$, voltage 70 kV, current 6 A, pitch factor $\alpha = 1.5$, electron beam with velocity spread $\Delta v_z = 5$ %, and fundamental harmonic operation with magnetic field strength $B_0 = 0.99\,B_g$

The design of lossy dielectric is similar to that in the experiment of Ka-band periodic lossy-dielectric-loaded gyro-TWT in NRL [28], but the beam-wave detuning conditions are carefully designed. In each of the unloaded metal waveguide, it maintains a positive detuning condition as $\Delta\omega \geq 0$. While in each of the lossy ceramic section, the beam-wave detuning $\Delta\omega$ could be adjusted via changing the radial thickness to achieve positive or negative detuning according to the instability competition requirement.

6.2.2 *Beam-Wave Interaction in an ECM-Cascaded Amplifier*

The ECM-cascaded scheme in Fig. 6.2 is similar to a gyroklystron that the beam-wave interaction is enhanced in each of the metal stage, while the lossy ceramics function as energy wells to absorb EM power, as a way to keep system from oscillation. Since there is no below-cutoff drift tube, it is also similar to a gyro-TWT. The traveling wave is still dominant in the interaction.

A W-band example of the ECM-cascaded amplifier is shown in Fig. 6.2. The normalized field profiles in the W-band ECM-cascaded gyrotron amplifier are shown in Fig. 6.3. Although the metal waveguide and the ceramic tube are iteratively loaded, the length of each stage is on the scale of several wavelength. Hence, it is reasonable to omit the periodicity effect of the circuit during simulation. The total field $f(z)$ demonstrates ripples along electron beam traveling direction. The total field $f(z)$ normally reaches highest strength in each metal stage. Each of the metal stage functions as low-quality factor cavity, located between a pair of lossy ceramic tubes. If the quality factor Q is applied to describe the energy stored in each of the metal section, the Q is much lower than that of a gyroklystron cavity. When forward-wave component $f_+(z)$ and backward-wave component $f_-(z)$ are derived from the total field $f(z)$, it is found that after the initial lunching loss in the first stage, the forward-wave $f_+(z)$ gains obvious growth along traveling direction in each metal stage and damped by the lossy ceramic tubes. The bunched electron beam excites backward-wave $f_-(z)$ in the unloaded nonlinear stage and inversely injected into

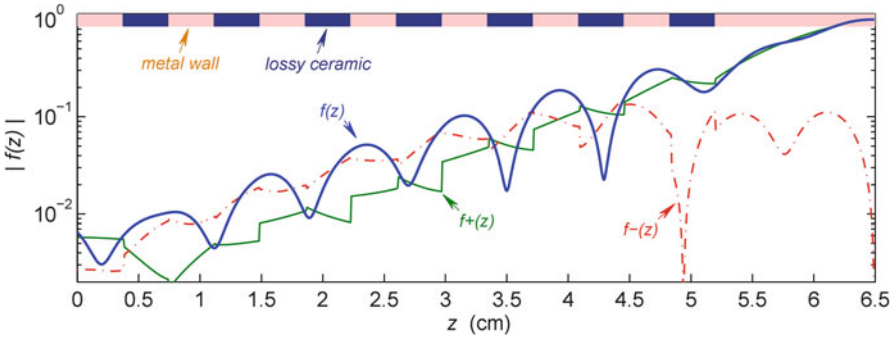

Fig. 6.3 Normalized field profiles in a W-band ECM-cascaded gyrotron amplifier, where $f(z)$ indicates the total field, $f_+(z)$ indicates the forward wave, and the $f_-(z)$ indicates the backward wave

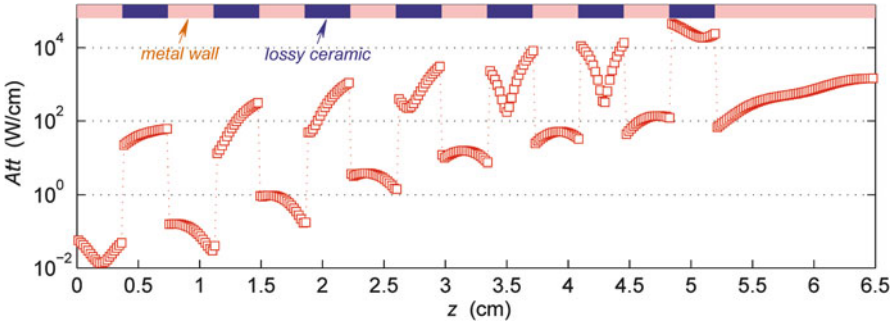

Fig. 6.4 Longitudinal loss strength distribution under saturation amplification at 94 GHz, input power $p_{in} = 5$ W, output power $p_{out} = 151.3$ kW, and the total ohmic loss power $p_{loss} = 13.7$ kW

the loss-loaded linear stag. During $f_-(z)$ travels toward upstream, it is damped in each of the lossy stage. After the backward-wave $f_-(z)$ travels through all of the energy wells, it turns to be several times lower than the input power at the upstream port. Figure 6.4 shows the ohm power absorbed by the lossy ceramic under saturated amplification. Since the metal waveguide is assumed to be copper, ohm loss in metal stage is several orders lower than that of the close lossy stages. The ohm-loss peak power exceeds 10 kW/cm in the last lossy stage, which constitutes the up-limit of high average power operation.

A comparison reveals the difference between traditional periodic lossy-dielectric-loaded (DL) scheme [12–14, 28] and the proposed ECM-cascaded scheme. A pair of different lossy ceramic-loaded schemes is demonstrated in Fig. 6.5, where the scheme A indicates the traditional ones [12–14, 28], and scheme B is the one proposed in this section. Both schemes are periodically loaded with lossy ceramic. But scheme A is periodically truncated by narrow metal rings, which is similar to that of the Ka-band experiments [12–14, 28]. Scheme B is with half of the linear stage occupied by metal wall. In scheme A, traveling-wave

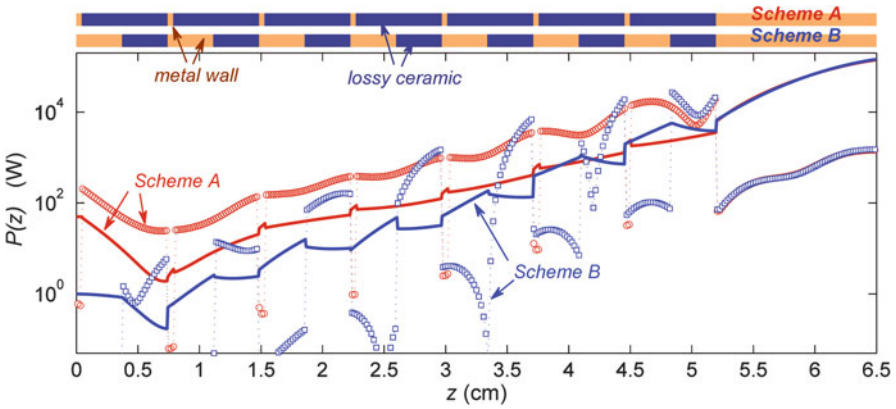

Fig. 6.5 Comparative demonstration of the saturated amplification at 93.7 GHz of a pair of schemes. The loading structures along z direction are shown on the *top* of the figure. *Real lines* indicate the growing profiles of the driving waves. *Circle-dashed line* and *square-dashed line* indicate the ohm loss power density (W/cm). Other parameters are the same as Fig. 6.2

interaction in the lossy ceramic tube mainly contributes to linear amplification, while in scheme B, the driving wave is mainly amplified in the metal stages and is either damped or without obvious growth in ceramics stages. Since there is more lossy ceramic loaded, scheme A requires driving power about one order higher than that of scheme B. The saturated amplifications in the output stage are almost identical for both schemes.

6.2.3 Discussion

It is concluded that in traditional periodic DL gyro-TWT as scheme A in Fig. 6.5, the lossy ceramic circuit simultaneously plays the roles of amplifying and suppressing oscillations. While in an ECM-cascaded amplifier, these two functions are carried by metal stage and lossy stage, respectively. Each metal stage plays the role of amplification, and the lossy ceramic absorbs the power and suppressing oscillations. According to engineering experience, the ceramic sintering is quite difficult to achieve product of monolithic parameters, and it is also very difficult to achieve high accuracy during ceramic machining. The traditional DL gyro-TWT requires accurate beam-wave synchronizing in circuit, but engineering experiment is relatively challenging to realize the designed condition due to errors from ceramics. An obvious advantage is that the performance of the ECM-cascaded amplifier is quite stable to lossy ceramic parameter errors and dimension errors, because it absorbs power only.

In an EMC-cascaded gyrotron amplifier, a metal tube and a lossy ceramic tube are combined to build an ECM stage, and multi-ECM stages constitute the bunching

stage. In each of the ECM stage, the cyclotron electron beam synchronizes with the EM wave to enhance its phase bunching characteristics. The periodically loaded ceramic tubes function as energy wells for EM wave power and enhance the system stability. Since the electron beam gains excellent phase bunching characteristics, it induces hyper-exponential amplification in the output stage. Amplification test shows that the system is inherent with broadband capability.

6.3 High-Order Mode Drift Tube

Investigation on the effect of wall loss on a gyro-TWT circuit reveals that loss-loaded linear stage brings pre-bunching to the electron beam in broad operating frequency band. Such kind of pre-bunching is the precondition of high efficiency interaction in the downstream unloaded nonlinear stage. This section focuses on an overmoded drift tube between the lossy linear stage and unloaded nonlinear stage [29].

6.3.1 The Concept of High-Order Mode Drift Tube

In a loss-loaded traveling-wave interaction circuit, the EM field exponentially grows [25–27]. As a result, the dissipated energy also reaches highest strength at the downstream end of the lossy stage, as demonstrated in Fig. 6.5. The thermal conductivity there determines the average power capability of the interaction system. Former investigation shows that the lossy stage brings necessary pre-bunching to electron beam. Hence, the problem is whether there is a solution which simultaneously bunches the electron beam and is capable of enduring high-power capability. Former solution in a gyroklystron is to load a below-cutoff drift tube to cutoff coupling between a pair of nearby cavities. The below-cutoff drift tube is with smaller radius than a normal circuit, and it encounters danger of intercepting electron beam and becomes overheated.

One high average power solution proposed here is to add an overmoded drifting tube, a section of circuit with very high-order mode, to separate the bunching stage from the output stage. A gyrotron amplifier loaded with a section of overmoded drift tube is shown in Fig. 6.6. In the pre-bunching stage, the driving power imposes bunching onto the electron beam, and it is enhanced to reasonable strength via linear beam-wave interaction in wall loss stage. The bunched electron beam injects into the lossy material loaded overmode drift tube, and the transition space there further enhances the bunching strength. Finally, efficient radiation is induced in the output stage. This scheme is, to some extent, similar to a traditional gyrotwistron, but also with some inherent differences. Firstly, other than the narrow band staggered tuning cavities in a gyrotwistron, the pre-bunching stage adopts broadband wall loss-loaded stage. Secondly, a loss-loaded overmoded drift tube is employed to replace the

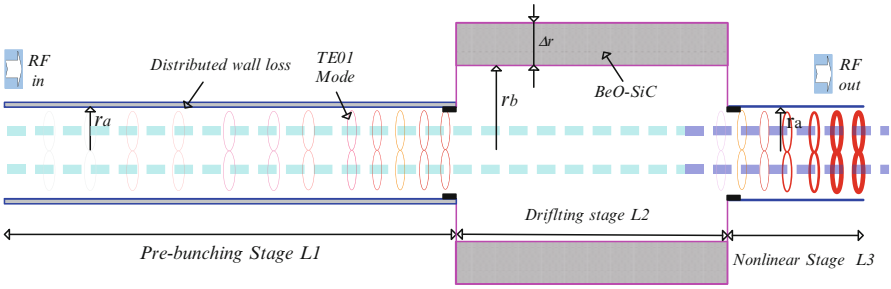

Fig. 6.6 The system structure of the overmoded drift tube-loaded gyrotron amplifier, where operating mode TE_{01} in metal stage and TE^{d}_{07} in ceramic-loaded waveguide, pre-bunching stage wall loss strength $\rho = 2.5 \times 10^5 \rho_{cu}$, and $r_a = 1.99$ mm, $r_b = 5.35$ mm, $\Delta r = 2.00$ mm, ceramic parameters $\varepsilon_r = 6.3 - 0.85\,j$, and $\mu_r = 1$, voltage 70 kV, current 6 A, pitch factor $\alpha = 1.5$, electron beam with velocity spread $\Delta v_z = 5$ %, and fundamental harmonic operation with magnetic field strength $B_0 = 0.99\,B_g$

cutoff drift tube. The distributed lossy stage is shorter than a normal gyro-TWT, which results in much lower power level in this lossy stage and brings higher power capability here. The overmoded drifting tube extends the thermal dissipation area and simultaneously enhances the beam bunching characteristics.

6.3.2 *Beam-Wave Interaction in Overmoded Drift Tube*

The key of this section is to investigate the physics in the overmoded drift tube. In the scheme as shown in Fig. 6.6, the operating modes in both the pre-bunching stage L_1 and nonlinear stage L_3 are the TE_{01} mode. The overmoded drift tube is designed to convey a propagating TE^{d}_{06} mode, which is with close propagation constant k_z with that of TE_{01} mode in L_1 and L_3. In addition, a TE^{d}_{0n} mode, $(n \leq 5)$ is also above cutoff in the overmoded drift tube. As a result, other than the drift tube of *zero-field strength* in a gyroklystron, the overmoded drift tube here is inherently a high-order mode interaction circuit. Figure 6.7 demonstrates the power density distributions of the modes in the circuit. Due to special design, the cyclotron electron beam bears simultaneous strongest coupling with TE_{01} mode in L_1 (and L_3) and TE^{d}_{06} mode in overmoded circuit. Since a TE^{d}_{0n} mode $(n \leq 5)$ is with k_z larger than the TE_{01} mode and with strongest field strength shifting away from electron beam location, theoretical simulation only considers TE^{d}_{06} mode in the drift tube and assumes field amplitude and phase continuous at the interfaces between L_1, L_2, and L_3.

In order to understand the beam-wave interaction in the gyrotron amplifier with overmoded drift tube, Fig. 6.8 demonstrates the field profiles under saturated amplification. Comparing with a normal gyro-TWT, the forward-wave field profile in the pre-bunching stage L_1 is under conventional traveling-wave amplification. Considering larger waveguide transverse cross and strong loss, the growth rate in

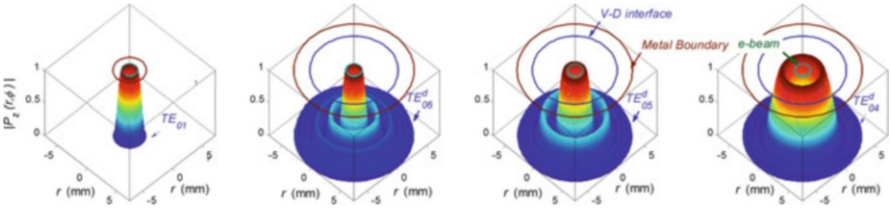

Fig. 6.7 The power density distribution of the operating mode TE_{01} in pre-bunching stage L_1 and nonlinear stage L_3, and TE^{d}_{06}, TE^{d}_{05}, and TE^{d}_{04} modes in overmoded stage L_2. The locations of the electron beam guiding center, vacuum-dielectric interface, and waveguide inner metal boundary are indicated by e-beam, V-D interface, and metal boundary, respectively

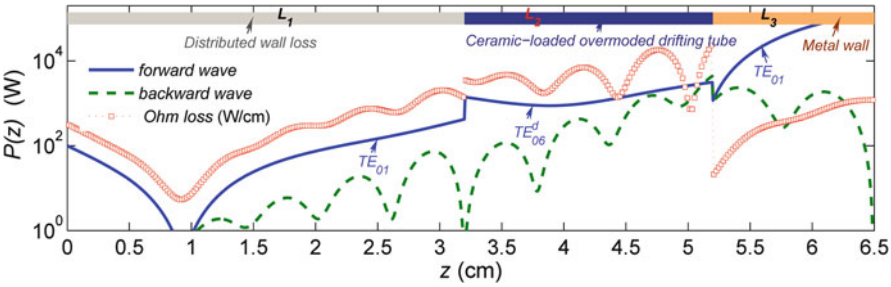

Fig. 6.8 Axial power profiles of the gyrotron amplifier with a high-order mode drift tube. Operation parameters are given in Fig. 6.6. Input power is 100 W, total gain is about 30.8 dB at 94 GHz

the L_2 stage is obviously lower than that of the L_1 stage. When the pre-bunched electron injects into the overmoded stage L_2 at $z = 3.2$ cm, due to a tiny mismatch of k_z between TE_{01} (L_1) mode and TE^{d}_{06} (L_2) mode, electron beam readjusts to synchronize with the traveling wave of TE^{d}_{06} mode, which is an energy absorbing process and makes the field profile gradually decay. Starting at $z = 4.0$ cm, the forward wave of TE^{d}_{06} mode gains a gradually growth rate obviously lower than that of the L_1 stage. Due to low growth rate in high-order mode L_2 stage, general estimating indicates that the major contribution of stage L_2 is to enhance the electron bunching and amplifying TE^{d}_{06} mode is the minor one. The bunched electron beam excites hyper-exponential amplification in the output nonlinear stage L_3. In addition, due to the assumption of single TE^{d}_{06} mode interaction and continuous phase-amplitude variation at the interfaces, the wave power sharply steps up and steps down at the upstream end and downstream end of the overmoded stage L_2. Reviewing Fig. 6.8, the backward wave is excited in the output stage L_3, and backwardly injects into the overmoded stage L_2 and is exponentially decayed by the lossy material. The ohm loss rate in the overmoded stage L_2 is averaged to approximately constant, but with growing ripples which is the result of backward-wave interference.

6.3.3 Discussion

Reconsidering the field profiles in Fig. 6.8, the original intention of introducing a high-order mode drift tube to gyrotron amplifier is to replace the bellow cutoff drift tube in a gyroklystron or to replace a section of wall loss section close to output stage. The high-order mode L_2 stage, as is called drift tube, is mainly to bunch the electron beam and maintains the wave growth rate as low level as possible. The high-order mode circuit is with larger inner radius, and it extends the interference space between the lossy material and wave, as a way to enhance the average power operation capability. The convective instability in the overmoded circuit is with low growth rate, and it also can effectively absorb backward wave. As a result, the ohm loss in the overmoded drift tube is relatively spread out with better improved longitudinal uniformity than that of a distributed wall-loaded gyro-TWT. It is estimated that for a traditional wall-loaded gyro-TWT, there is about 5 % electron energy dissipated on the lossy circuit under saturated amplification, especially, confined at the downstream end of the lossy circuit. Here, the proposed amplifier with an overmoded drift tube is with overall ohm loss power comparable to a gyro-TWT, but with dissipation area about 10 times larger. It is concluded that for the proposed overmoded drift tube scheme, the loss material-loaded circuit no more turns to be the bottleneck of heat dissipation in the gyrotron amplifier.

6.4 High-Power Gyrotron Amplifier Based on Bi-modes Operation

High-order mode interaction [29] much enhances system power capacity which is the inherent advantage for a gyrotron device over a traditional linear-beam vacuum tube [30]. But if without special mode control mechanism, there will be challenges to high-order mode interaction, such as instability competition and high-order mode excitation. We will discuss a compromising approach, the bi-modes operation. The design is based on a low-order pre-bunching stage and a high-order mode output stage. The concept of bi-modes operation is based on the high stability of the wall loss-loaded linear stage and high-power capacity of the high-order mode output stage.

6.4.1 The Concept of Bi-modes Operation

In an ECM system, the cyclotron beam is with inherent cyclotron frequency, which makes it possible to operate on a high-order mode and generate much higher power than a rectilinear beam vacuum tube. Hence, higher-order mode interaction is a major development tendency for gyrotron devices. A gyrotron oscillator operates on a cavity mode and generates radiation based on a single frequency. During the

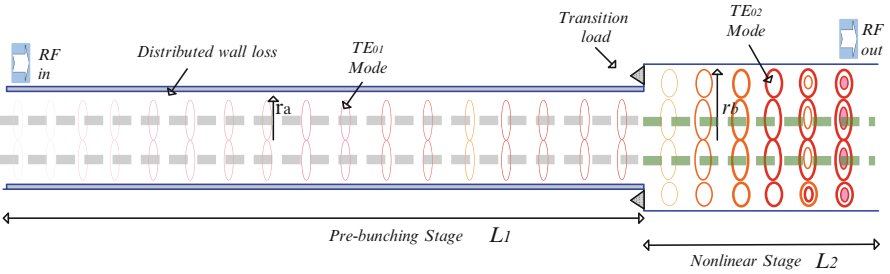

Fig. 6.9 Schematic plot of a bi-modes operation gyrotron amplifier, where operating mode TE_{01} in pre-bunching stage and TE_{02} in nonlinear stage, the wall loss strength $\rho = 2.5 \times 10^5 \rho_{cu}$, and $r_a = 1.99$ mm, $r_b = 3.64$ mm, voltage 70 kV, current 6 A, pitch factor $\alpha = 1.5$, electron beam with velocity spread $\Delta v_z = 5$ %, and fundamental harmonic operation with magnetic field strength $B_0 = 0.99\, B_g$

development of high-power gyrotron, it experienced operation on circular modes, whispering-gallery modes, and high-order volume mode [3]. This, to some extent, also demonstrates the great potential of high-order mode operation for a gyrotron amplifier. However, a gyrotron amplifier is based on the Doppler-shifted synchronization. To achieve broadband radiation, it encounters the challenge of suppressing instability competition in the traveling wave circuit.

The zero-drive stability is the basic requirement for a gyrotron amplifier, which means high-power radiation is induced by the driving power only, and it switches off once the driving power is turned off. A high-order mode gyrotron amplifier relies on fundamental technologies, including a high-order mode excitation and stable interaction. Normal input couplers can effectively excite a low-order mode and circular polarized mode. But when the mode order index increases, it encounters much serious problems of low excitation efficiency, poor mode purity, and parasitic modes. In a high-order mode system, abundant beam-wave coupling happens between cyclotron harmonics and waveguide modes. Hence, a high-power gyrotron amplifier needs a circuit to convey a high-order mode interaction and simultaneously suppressing instability competition. Now available interaction circuits for high-power gyrotron includes cavity, wall loss-loaded structure with mode selection ability, and other structures.

The concept of bi-modes operation is proposed for application in a gyrotron amplifier. The bi-modes operation means combination of a low-order mode in pre-bunching stage and a high-order mode in the nonlinear stage, as is shown in Fig. 6.9. The linear stage L_1 bunches the electron beam and provides main gain for the amplifier. The nonlinear stage L_2 generates the major high power. The lower-order mode is easier to be excited and to achieve zero-drive stability. The excitation of the higher-order mode much relies on the bunched electron beam. The upstream lower-order mode and the downstream high-order mode constitute a mode pair. The selection of such a mode pair must meet a condition that the location of the electron beam simultaneously couples with both modes at their highest strength. A mode pair is usually with the same azimuthal index and different radial index.

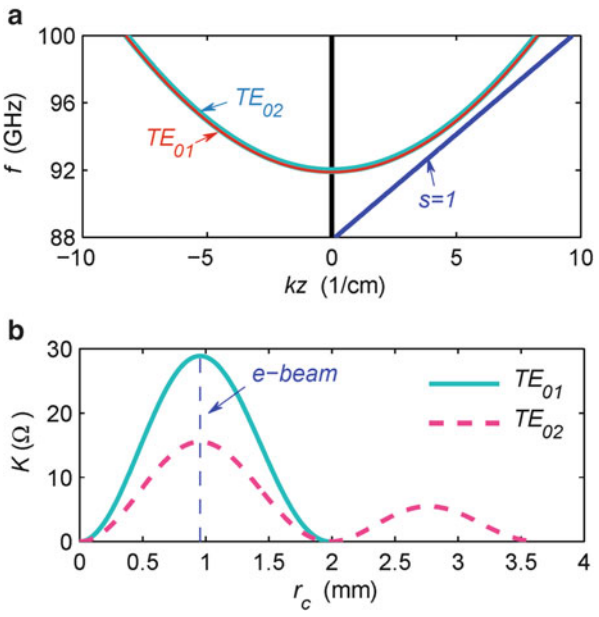

Fig. 6.10 (**a**) Cold dispersion relation and (**b**) beam-wave coupling impedance of the $TE_{01} - TE_{02}$ interaction system. The *vertical dashed line* in (**b**) indicates the location of electron beam guiding center

6.4.2 The Principle of Bi-modes Operation

This section focuses to investigate the feasibility of the bi-modes operation. The schematic circuit is demonstrated in Fig. 6.9. The pre-bunching stage is distributed wall loss-loaded stage, and it operates on cylindrical waveguide TE_{01} mode. The unloaded nonlinear stage operates on TE_{02} mode. Since a TE_{0n} mode is from the nth root of $J_0'(x_{0n}) = 0$, all the TE_{0n} $(n = 1, 2, 3, \ldots)$ modes of equal cutoff frequency f_c will be with almost identical field distribution between $0 < r_w < x_{01} \cdot c/(2\pi f_c)$, where $x_{01} = 3.832$. Hence, electron beam could simultaneously couple with the $TE_{01} - TE_{02}$ mode pair, which is based on the same principle of complex cavity gyrotron [31]. The design parameters are given in Fig. 6.9. From the cold dispersion relation in Fig. 6.10a, the dispersion curves of both TE_{01} and TE_{02} overlap each other and are under identical detuning condition with respect to fundamental harmonic. The beam-wave coupling impedance shown in Fig. 6.10b reveals that both modes simultaneously couple with the electron beam, but due to TE_{02} mode of higher radial index and larger waveguide radius, the coupling impedance K in the nonlinear stage is about half of the strength of the TE_{01} mode circuit. It is a double-edge sword for lower K in nonlinear stage, corresponding to higher threshold current I_{st} of a self-excited oscillation, but lower interaction efficiency.

Theoretic prediction of the beam-wave interaction in the bi-mode operation system assumes single mode in each stage of the circuit, that is, only TE_{02} mode in the nonlinear stage. The saturated amplification profile is shown in Fig. 6.11. The wall loss-loaded linear stage brings the system high stability and simultaneously

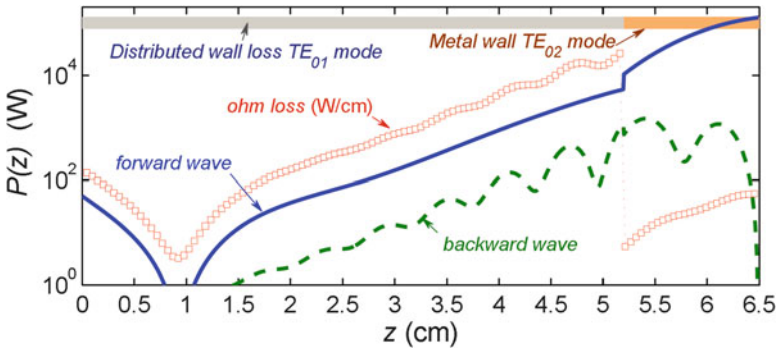

Fig. 6.11 Saturated amplification profile of a bi-mode gyrotron amplifier operating on TE_{01} ─ TE_{02} mode pair. Operating parameters are given in Fig. 6.9

bunches the electron beam in phase space. Then the well-bunched beam induces a high-order mode in nonlinear stage and excites high-power radiation. The overall profile in the circuit is similar to the normal amplification profile in a gyro-TWT. The distributed wall loss-loaded linear stage works in a low-order mode, which makes the system easier to suppress instability competition. The nonlinear stage operates on a high-order mode and is with higher power capacity. In addition, although the single-mode assumption leads to a minor power step up at the interface between the lossy stage and output stage as shown in Fig. 6.11, it, fortunately, brings little influence to revealing the major physics of the ECM interaction.

6.5 High-Power Gyrotron Amplifier Based on ECM-Cascade and Pre-bunching Scheme (Gyro-CPA)

Former sections discussed three concepts, including cascaded ECM stages, over-moded drift tube, and bi-modes operation. Each of these concepts tends to solve some of the challenges related to gyrotron amplifier, and there is no conflict between each other. This section combines these three technologies to form a new advanced complex scheme for high-power millimeter-wave gyrotron amplifier, which is simply called gyro-CPA as shown in Fig. 6.1.

6.5.1 Key Technologies Related to a Gyro-CPA

A gyrotron-cascaded pre-bunching amplifier (gyro-CPA) as shown in Fig. 6.1 contains three key technologies. The pre-bunching stage is built by ECM-cascaded interaction circuit, which is constructed by multistage of metal-dielectric cascading waveguides. It is with the advantage of high stability as in lossy dielectric-load interaction circuit. Since electron beam bunching is enhanced in the metal sections,

Table 6.1 The design parameters of the W-band gyro-CPA

Operating mode	TE_{01} @ $L_1(L_4)$, TE^{d}_{03} @ $L_1(L_5)$, TE^{d}_{06} @ L_2, TE_{02} @ L_3
Cyclotron harmonic	Fundamental
Radius	$r_a = 1.99$ mm, $\Delta r = 1.25$ mm, $R = 5.30$ mm, $\Delta R = 2.0$ mm, $r_b = 3.65$ mm
Length	$L_1 = 40$ mm, $L_2 = 20$ mm, $L_3 = 25$ mm, $L_4 = 3.2$ mm, $L_5 = 4.8$ mm
Loss ceramic	$BeO - SiC - W(\varepsilon_r = 6.3 - 0.85j, \mu_r = 1)$
Electron beam	$V = 70$ kV, $I = 10$ A, $\alpha = 1.3$, $\Delta v_z = 5$ %
Magnetic field	$B_g = 3.5713$ T(down tapered at the output end)
Guiding center	$r_c = 0.48$ r_a

beam-wave interaction is much more insensitive to dielectric and structure errors. An overmoded drift stage can be flexibly loaded with various lossy structures to suppress instability competition, and it is capable of high-duty factor operation, even under continuous wave operation. Efficient ECM interaction happens between well-bunched electron beam and a high-order mode in nonlinear stage, and the large transverse size enables high-power capacity.

6.5.2 Principle of Amplifier Based on ECM Cascade and Pre-bunching Excitation

A set of high-power operation parameters for the W-band gyro-CPA is given in Table 6.1, and the configuration of the amplifier circuit is shown in Fig. 6.1. The cyclotron electron beam travels through the circuit, and it experiences a series of different modes. The cold dispersion relation between fundamental harmonic and these interaction modes is shown in Fig. 6.12. The pre-bunching stage is constructed by four ECM-cascaded stages, where the operating mode is TE_{01} mode in a metal section and TE^{d}_{03} mode in a lossy ceramic-loaded section. The operating mode in the overmoded drift stage is actually TE^{d}_{06} mode. The unloaded output stage operates on a higher-order TE_{02} mode. The output stage is actually a low-Q cavity, as a way to enhance the beam-wave coupling and mode selection ability. In order to improve the stability from oscillation in the output stage, the magnetic field is sharply down tapered to reduce the effective feedback length of an absolute instability. Considering the cathode emitting capability, the electron beam is designed to be with voltage $V = 70$ kV and current $I = 10$ A, pitch factor $\alpha = 1.3$, and velocity spread $\Delta v_z = 5$ %. The following investigation will study the instability competition and amplification. Theoretical investigation still assumes single-mode interaction in each stage of circuit, and amplitude and phase continuous at the connections.

6.5.2.1 Instability Competition

Although the W-band gyro-CPA, as shown in Fig. 6.1, and the dispersion curves, as shown in Fig. 6.12, are loaded with lossy ceramic, the systematic investigation on

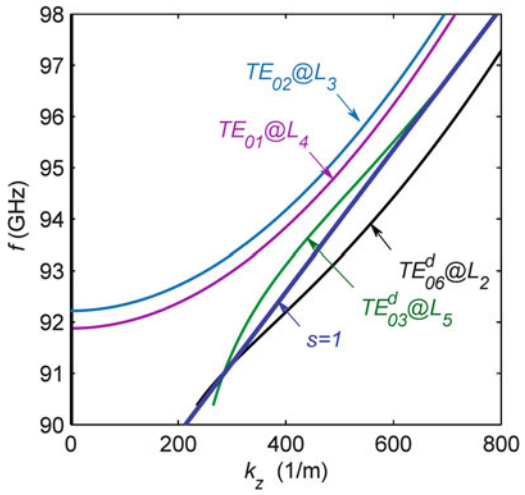

Fig. 6.12 Cold dispersion relation between the fundamental harmonic and modes in the gyro-CPA

the instability competitions in each stage should be carried out. The drift stage L_2 operates on a very higher-order TE^d_{06} mode which makes the beam-wave coupling strength much weaker than that in pre-bunching stage L_1 and output stage L_3, and it is also loaded with strong lossy material. Considering above factors, the lossy drift stage L_2 is assumed to be with unconditional stability. More details are addressed in former Sect. 6.3. Instability competition focuses on pre-bunching stage L_1 and output stage L_3.

For the pre-bunching stage, since the circuit is periodically loaded with metal waveguide and ceramic-loaded waveguide, the self-excited oscillation of the operating mode may exhibit in a high-order axial mode. Figure 6.13 demonstrates the influence of the ceramic-loading factor $D_f = L_5/(L_4 + L_5)$ to the field profiles and start-oscillation current. The first four axial modes are with quite close frequencies, close to TE_{01} mode cutoff frequency. As a result, each of the start-oscillation current I_{st} behaves similarly, and linearly increasing loading factor D_f leads to exponentially growing I_{st}. The operating parameters in Table 6.1 choose $D_f = 0.6$ to ensure high stability from oscillation in the pre-bunching stage.

For the TE_{02} mode output stage, both the circuit radius and magnetic profile are tapered to balance between the stability and amplification performance. The output system configuration is shown in Fig. 6.14a, where the tapered radius extended the effective interaction length for the upper band frequency and the tapered circuit reduced the effective feedback length for the competing self-excited oscillation. For the present electron beam guiding-center location $r_c = 0.48\ r_a$, the electron beam almost simultaneously couples with the TE_{02} and TE_{22} mode of highest strength. Because both TE_{02} and TE_{22} modes are with close eigenvalues 7.016 and 6.706 and beam-wave synchronization conditions, the tapering parameters impose similar influence on both modes. Tapering either circuit radius or magnetic field leads to higher start-oscillation current I_{st}. Figures 6.14b, c show the influence of the

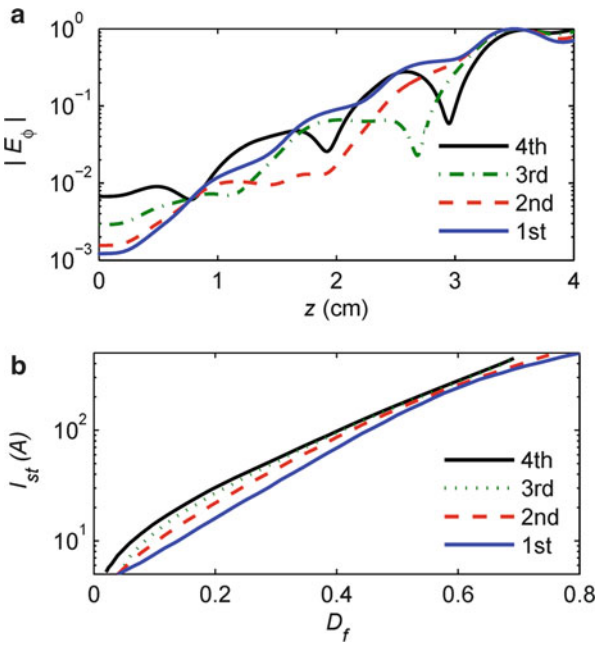

Fig. 6.13 The first four axial modes of the operating TE_{01} mode in the pre-bunching stage under self-excited oscillation condition, (**a**) field profiles at $D_f = 0.3$ and (**b**) start-oscillation current, where the factor D_f is defined by $D_f = L_5/(L_4 + L_5)$

radius tapering angle θ and magnetic tapering $\Delta B/B_g$ to threshold currents of TE_{02} and TE_{22} mode. Finally, the optimized circuit chooses radius taper angle 0.8° and magnetic field taper $\Delta B/B_g = 0.1$, and the start-oscillation current is about $I_{st} = 19$ A for both modes, about twice the operating current $I_b = 10$ A.

6.5.2.2 Amplification Simulation

The design parameters of gyro-CPA in Fig. 6.1 are given in Table 6.1. The simulation structure of the interaction system is given in Fig. 6.15. The parameters are specially selected to achieve close beam-wave synchronization for the operating modes in each stage, as the cold beam-wave dispersion relation shown in Fig. 6.12. Hence, amplification simulation assumes single mode in each stage of the circuit to approximate the overall behavior of the system. Keep in mind that there may be a little bit power transferring to other spurious TE_{0n} modes around the discontinuity interfaces due to modal interference. Such spurious TE_{0n} modes are detuning from synchronization with cyclotron harmonic and will be absorbed by lossy material. As a result, nonlinear single-mode simulation assumes no influence from the spurious TE_{0n} modes.

The parameter evolutions of the beam-wave interaction on 95.1 GHz are shown in Fig. 6.16. Figure 6.16a demonstrates the axial wave power distribution. Both the forward power $P_+(z)$ and backward power $P_-(z)$ are derived from the total wave power distribution $P(z) = \oint E \times H^* \mathrm{d}s$. The cold attenuation rate Att(dB/cm)

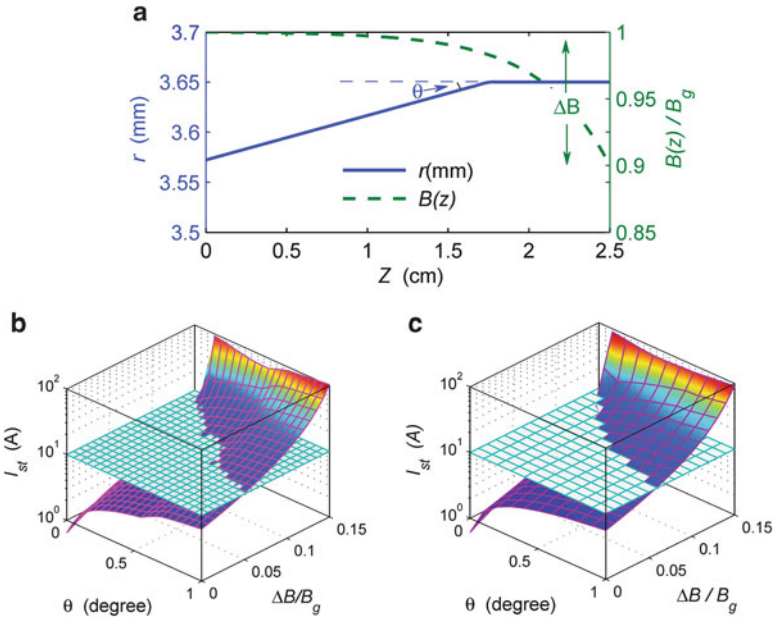

Fig. 6.14 (**a**) Circuit configuration of the output stage and influence of the circuit radius taper and magnetic field taper to the start-oscillation current of (**b**) the operating TE_{02} mode and (**c**) the competing TE_{22} mode

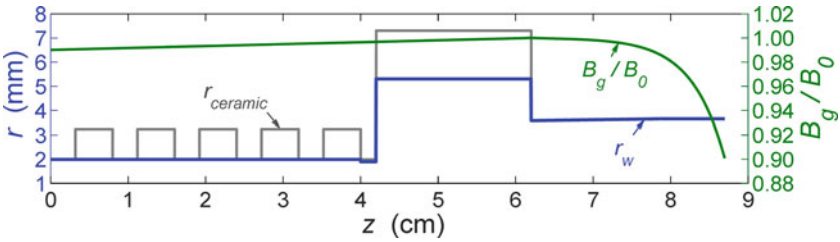

Fig. 6.15 The interaction structure of the W-band gyro-CPA, parameters are given in Table 6.1

shows the lossy strength of the lossy ceramic-loaded circuit. The hot attenuation rate P_{loss}(W/cm) demonstrates the real power dissipation condition under amplification. In the pre-bunching stage $z < 4$ cm, the electron beam iteratively travels through the metal-ceramic circuit. High growth rate on the forward-wave power $P_+(z)$ is achieved in metal stages, while the field strength is suppressed in the lossy ceramic stages. There is a below-cutoff sever at $4.0 \sim 4.3$ cm to suppress the downstream interference, especially the influence of the downstream backward wave to the upstream amplification. In the drift tube, 4.3 cm $< z <$ 6.3 cm, the high-order mode circuit reduces the beam-wave coupling strength and also introduces waves of different propagation constant k_z from that of the pre-bunching stage. Both lead

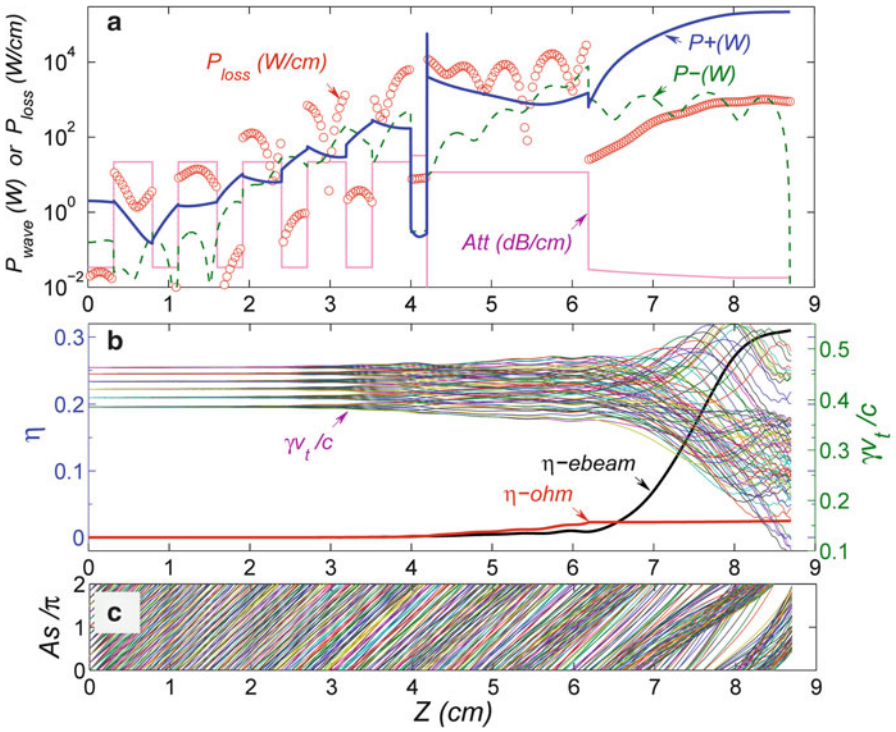

Fig. 6.16 The beam-wave interaction of the W-band gyro-CPA. (**a**) The axial distribution of the field power and ohm loss, (**b**) the axial evolution of the electron beam efficiency and transverse gamma factor, and (**c**) axial evolution of the phase. The input power is $p_{in} = 2$ W, and the operating frequency is $f_0 = 95.1$ GHz

to the electron beam readjusting to synchronize with the wave in the drift tube, resulting in gradual decaying in $P_+(z)$. As a result, the field does not gain too much growth. When the well-bunched electron beam injects into the *loss-free* output stage, $z > 6.3$ cm, the beam-wave interaction strength is instantly enhanced, and the $P_+(z)$ experiences a nonlinear amplification process until to saturation. A review indicates that the backward-wave $P_-(z)$ is excited in the output stage and is severely suppressed in the lossy drift tube. The below-cutoff short $4.0 \sim 4.3$ cm reflects the $P_-(z)$ into $P_+(z)$. The remaining $P_-(z)$ in the lossy pre-bunching stage travels through a series of cascaded lossy ceramics and is finally reduced to at least one order lower than the input power $P_-(z) < 0.1P_+(z)$ at the upstream entrance $z = 0$. Low-level reflection power in the input port reduces the danger of the oscillation from regenerated amplification [6, 7]. The field attenuation strength P_{loss} in each lossy ceramic stage is several orders higher than that of the close-by metal waveguide. For each of the lossy ceramic tube, the $P_+(z)$ and the $P_-(z)$ inject from the both sides, as a result the $P_{\text{loss}}(z)$ normally exhibits *V-shapes* in the pre-bunching stage.

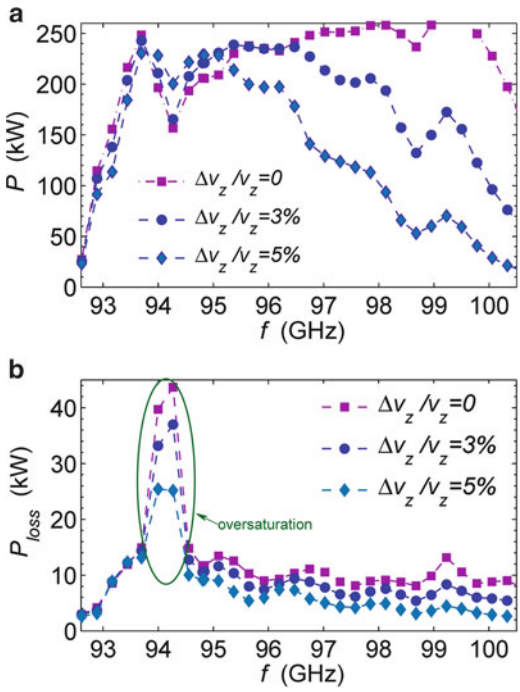

Fig. 6.17 (**a**) The output power and (**b**) the dissipated power of the W-band gyro-CPA under driving power of 1 W

The evolutions of the electron parameters are shown in Figs. 6.16b, c. Since there is a small velocity spread $\Delta v_z/v_z = 5$ % and all of the electrons are accelerated by the same voltage of 70 kV, it leads to a small spread on the transverse velocity Δv_t, as is indicated by the $\gamma v_t/c$ in Fig. 6.16b. The relative beam-wave phase in the phase space in Fig. 6.16c is defined by $A_{si} = \omega t_i - s\theta_i - (m-s)\phi_{ci}$, the same as that in Chap. 3. The low power level linear interaction in the pre-bunching stage $z < 4$ cm modulates the electron beam and imposes exponential growing disturbance to the beam parameters. The beam parameters do not demonstrate obvious changes until the below-cutoff region. In the drift tube, 4.3 cm $< z <$ 6.3 cm, the field power does not obviously grow, but the electron beam bunching strength is self-consistently enhanced. Such bunching influence could be revealed by both the disturbance on the $\gamma v_t/c$ in Fig. 6.16b and phase evolution As/π in Fig. 6.16c. In the output stage, the interaction grows to highest strength, and most of the particles positively deposit transverse kinetic energy to wave. Simultaneously, electrons also concentrate into a tight bunch in the phase space, as shown in Fig. 6.16c. For the ohm loss power P_{loss} in Fig. 6.16a and $\eta_{-ohm} = P_{loss}/(V \cdot I_b)$ in Fig. 6.16b, most of the power absorbed by the lossy ceramic is relatively uniformly dissipated in the drift tube, 4.3 cm $< z <$ 6.3 cm. The drift tube is overmoded and with large circuit radius, which means the interaction circuit is capable of high average power operation.

The amplification bandwidth of the W-band gyro-CPA under driving power of 1 W is shown in Fig. 6.17a. The corresponding ohm loss power is shown in

Fig. 6.17b. Similar to a gyro-TWT, the bandwidth of the gyro-CPA depends on ECM interaction with Doppler-shifted beam-wave synchronization and is relatively sensitive to electron beam velocity spread. It is predicted that the constant driving bandwidths with power higher than 200 kW under the conditions of velocity spreads $\Delta v_z/v_z$ of 0, 3 %, and 5 % are about 7 GHz, 5 GHz, and 3 GHz, respectively. The gyro-CPA has the similar bandwidth characteristic to gyro-TWT amplifier which is sensitive to beam velocity spread, and, as the spread increases, the bandwidth decreases obviously. From the ohm loss power in bandwidth Fig. 6.17b, there is a region around 94.2 GHz, where the P_{loss} is higher than other frequencies and the bandwidth demonstrates a concave in Fig. 6.17a. Further simulation indicates this strong loss is induced by oversaturated amplification. From Fig. 6.17b, it is predicted that other than the overdrive frequency around 94 GHz, the system is normally with dissipated power P_{loss} less than 2 % of the electron beam energy.

6.5.3 Discussion

A W-band gyro-CPA based on ECM-cascaded pre-bunching excitation is discussed in detail in this section, and the analyzed method of instability competition and amplification is presented. The research reveals that interaction system based on ECM-cascaded circuit and high-order mode drift stage is inherent with the feature of high stability. Since the lossy-dielectric material functions merely as EM wave attenuation and ECM interaction occurs mainly in the smooth metal waveguide, the system performance is insensitive to dielectric parameter errors. Since the bandwidth of the device depends on Doppler-shifted ECM interaction, a gyro-CPA is similar to a gyro-TWT, and it is sensitive to the electron beam velocity spread. The 3 dB bandwidth of the device about 4 %, which is much superior to a gyroklystron.

6.6 Conclusion

This chapter discusses preliminary investigation on three novel lossy ceramic-loaded configurations for further enhancing the gyrotron amplifier performance. The operation principle, advantage, and disadvantage of the three technologies are as follows:

1. ECM-cascaded interaction circuit: each section of interaction circuit is made of a metal tube and a lossy-dielectric tube, and several periods are cascaded to constitute the bunching stage. The cyclotron beam interacts with the EM field in the metal circular waveguide. When the EM field propagates into the lossy-dielectric waveguide, it decays due to disturbance from the waveguide discontinuity and detuning from the beam-wave synchronization. The ECM-cascaded circuit is not sensitive to the errors from the lossy material and structure. The ECM-cascaded gyrotron amplifier features high stability.

2. High-order mode drift tube: a drift tube which absolutely cuts off all kinds of the EM fields is difficult to be realized, especially, in a high-order mode gyrotron amplifier. The high-order mode drift tube introduces a loss-loaded high-order mode waveguide as the drift tube. Due to the loss material in the drift tube, it is highly stable to self-excited oscillation. Since the mode density in the overmoded drift tube is relatively high, there is always a mode approximately synchronizing with the cyclotron electron beam. The phase bunching of the electron beam would be enhanced by the joint influence from the inertia drift and a synchronizing mode interaction.
3. Bi-modes operation: for a gyrotron amplifier, the pre-bunching stage operates on a low-order mode, and the output stage operates on another high-order mode. The low-order mode bunching stage maintains low-level interaction strength, which provides the major gain of the system and is with high stability. The high-order mode output stage is with larger power capacity and generates the major high power. The high-order mode excitation relies on the bunched electron beam.

Combining the three technologies, a W-band gyrotron-cascaded pre-bunching amplifier (gyro-CPA) is investigated. The output circuit of the gyro-CPA is similar to an open cavity with low-quality factor. Self-excited oscillations in output circuit are suppressed by adjustment of structure and magnetic field. A gyro-CPA adopts the similar mechanism to traditional gyrotwystron, but it is realized with different technologies. A gyro-CPA has the equivalent output power level to a gyroklystron and comparable bandwidth to a gyro-TWT.

This chapter introduced three interaction structures to the gyrotron amplifier, namely, ECM-cascaded bunching stage, high-order mode drift tube, and Bi-modes operation. The feasibility of each is preliminarily verified. They provide helpful inspirations for future gyrotron amplifier development.

References

1. Chu KR (2004) The electron cyclotron maser. Rev Mod Phys 76:489–540
2. Chu KR (2002) Overview of research on the gyrotron traveling-wave amplifier. IEEE Trans Plasma Sci 30:903–908
3. Thumm M (2013) State-of-the-art of high power gyro-devices and free electron masers, Update 2012. KIT Scientific Report 7641, KIT Scientific Publishing
4. Park GS, Choi JJ, Park SY et al (1995) Gain broadening of 2-stage tapered gyrotron traveling-wave tube amplifier. Phys Rev Lett 74:2399–2402
5. Barnett LR, Lau YY, Chu KR et al (1981) An experimental wideband gyrotron traveling-wave amplifier. IEEE Trans Electron Devices 28:872–875
6. Chu KR, Chen HY, Hung CL et al (1998) Ultrahigh gain gyrotron traveling wave amplifier. Phys Rev Lett 81:4760–4763
7. Chu KR, Chen HY, Hung CL et al (1999) Theory and experiment of ultrahigh-gain gyrotron traveling wave amplifier. IEEE Trans Plasma Sci 27:391–404
8. Wang QS, McDermott DB, Luhmann NC (1996) Operation of a Stable 200-kW second-harmonic gyro-TWT amplifier. IEEE Trans Plasma Sci 24:700–706

9. Chong CK, McDermott DB, Luhmann NC (1998) Large-signal operation of a third-harmonic slotted gyro-TWT amplifier. IEEE Trans Plasma Sci 26:500–507
10. Pershing DE, Nguyen KT, Calame JP et al (2004) A TE11 K-a-band gyro-TWT amplifier with high-average power compatible distributed loss. IEEE Trans Plasma Sci 32:947–956
11. Nguyen KT, Calame JP, Pershing DE et al (2001) Design of a Ka-band gyro-TWT for radar applications. IEEE Trans Electron Devices 48:108–115
12. Liu BT, Feng JJ, Wang EF, Li ZL, Zeng X, Qian LJ, Wang H (2011) Design and experimental study of a Ka-band gyro-TWT with periodic dielectric loaded circuit. IEEE Trans Plasma Sci 39(8):1665–1672
13. Wang E, Zeng X, Liu BT, Qian LJ, Li ZL, Feng JJ, Zhu SQ (2012) Experimental study of high power gyrotron traveling wave tube with periodic lossy material loading. IEEE Trans Plasma Sci 40(7):1846–1853
14. Yan R, Luo Y, Liu G, Pu YL (2012) Design and experiment of a Q-band gyro-TWT loaded with lossy dielectric. IEEE Trans Electron Devices 59(12):3612–3617
15. Sirigiri JR, Shapiro MA, Temkin RJ (2003) High-power 140-GHz quasioptical gyrotron traveling-wave amplifier. Phys Rev Lett 90:258302
16. Sirigiri JR, Kreischer KE, Machuzak J et al (2001) Photonic-band-gap resonator gyrotron. Phys Rev Lett 86:5628–5631
17. Denisov GG, Bratman VL, Phelps ADR et al (1998) Gyro-TWT with a helical operating waveguide: new possibilities to enhance efficiency and frequency bandwidth. IEEE Trans Plasma Sci 26:508–518
18. Burt G, Samsonov SV, Ronald K et al (2004) Dispersion of helically corrugated waveguides: analytical, numerical, and experimental study. Phys Rev E 70:046402
19. Bratman VL, Cross AW, Denisov GG et al (2000) High-gain wide-band gyrotron traveling wave amplifier with a helically corrugated waveguide. Phys Rev Lett 84:2746–2749
20. Denisov GG, Bratman VL, Cross AW et al (1998) Gyrotron traveling wave amplifier with a helical interaction waveguide. Phys Rev Lett 81:5680–5683
21. Cross AW, He W, Phelps ADR et al (2007) Helically corrugated waveguide gyrotron traveling wave amplifier using a thermionic cathode electron gun. Appl Phys Lett 90:253501
22. Blank M, Danly BG, Levush B (1999) Experimental demonstration of a W-band (94 GHz) gyrotwystron amplifier. IEEE Trans Plasma Sci 27(2):405–411
23. Baik CW, Jeon SG, Kim DH, Sato N, Yokoo K, Park GS (2005) Third-harmonic frequency multiplication of a two-stage tapered gyrotron TWT amplifier. IEEE Trans Electron Devices 52(5):829–838
24. Lau YY, Chu KR, Barnett LR et al (1981) Gyrotron traveling wave amplifier.1. Analysis of oscillations. Int J Infrared Millim Waves 2:373–393
25. Du CH, Liu PK (2009) A lossy dielectric-ring loaded waveguide with suppressed periodicity for gyro-TWTs applications. IEEE Trans Electron Devices 56:2335–2342
26. Du CH, Xue QZ, Liu PK et al (2009) Modal transition and reduction in a lossy dielectric-coated waveguide for gyrotron-traveling-wave tube amplifier applications. IEEE Trans Electron Devices 56:839–845
27. Du CH, Xue QZ, Liu PK (2008) Loss-induced modal transition in a dielectric-coated metal cylindrical waveguide for gyro-traveling-wave-tube applications. IEEE Electron Device Lett 29:1256–1258
28. Garven M, Calame JP, Danly BG et al (2002) A gyrotron-traveling-wave tube amplifier experiment with a ceramic loaded interaction region. IEEE Trans Plasma Sci 30:885–893
29. Tsai WC, Chang TH, Chen NC et al (2004) Absolute instabilities in a high-order-mode gyrotron traveling-wave amplifier. Phys Rev E 70:056402
30. Chen SH, Chang TH, Pao KF et al (2002) Linear and time-dependent behavior of the gyrotron backward-wave oscillator. Phys Rev Lett 89:268303
31. Fliflet AW, Lee RC, Read ME (1988) Self-consistent field model for the complex cavity gyrotron. Int J Electron 65(3):273–283

Chapter 7
Technologies Related to Gyrotron Amplifiers

Abstract This chapter presents some key technologies related to engineering development of millimeter-wave gyrotron amplifiers, including input power couplers, output windows, electron gun, and lossy material measurement. The design methods and considerations are helpful for developing millimeter-wave gyrotron amplifier of high-power capability.

Keywords Gyrotron amplifier • Input coupler • Output window • Electron gun • Lossy material

7.1 Introduction

A gyrotron traveling-wave tube (gyro-TWT) amplifier is characterized by high-power, high gain, and broad bandwidth, but it is sensitive to electron beam velocity spread. In order to fully realize the potential of a gyro-TWT, the challenges related to a series of technologies need to be overcome [1, 2]. A gyro-TWT primarily consists of an electron gun, an input coupler, an interaction circuit, a tapered output waveguide, a collector, a broadband output window.

The electron gun is employed to generate a high-power cyclotron electron beam [3–14]. There are two main kinds of electron gun applied in gyrotrons, namely, the magnetron injection gun (MIG) and the magnetic CUSP gun [12]. The cycling electron beam guiding center r_c, the Larmor radius r_L, velocity ratio $\alpha = v_\perp/v_z$, and velocity spread $\Delta v_z/v_z$ are important parameters of an electron gun. A MIG is used to generate small-orbit electron beam $r_c > r_L$, while a CUSP gun is used to generate a large orbit electron beam $r_c \approx 0$. Moreover, there is also strict limitations on the electron gun structure, including building the required electric field and simultaneously avoiding high-voltage arcing.

The input coupler not only injects the driving power into the interaction circuit and builds up a required EM mode, but also can separate the inner vacuum environment from outside atmospheric surroundings by vacuum sealing [15, 16].

C.-H. Du and P.-K. Liu, *Millimeter-Wave Gyrotron Traveling-Wave Tube Amplifiers*,
DOI 10.1007/978-3-642-54728-7_7,

Due to the high gain and broad bandwidth characteristics of a gyro-TWT, the input coupler should be of high transmission efficiency and broadband, as a way to avoid imposing limitation on the amplifier performance. In order to facilitate precision machining and ceramic sealing, the mechanical structure of the input coupler should be carefully designed.

The interaction circuit amplifies the driving power via convective instability. During engineering fabricating of the interaction circuit, special attention should be paid on a series of problems, including minimizing the machining error, realizing high thermal conductive lossy material, maintaining ideal alignment, and so on.

A nonlinear tapered output waveguide [17] is a transition stage connecting between the interaction circuit and the collector. Since the interaction circuit operates close to the cutoff frequency, the tapered output waveguide is with small radius r_0 and high wave impedance. Due to the high-power requirement of the downstream collector, the collector is normally with radius r_1 about one order larger than the interaction circuit radius, as $r_1/r_0 \sim 10$. It is relatively challenging to design a good tapered waveguide simultaneously suppressing the parasitic modes interacting with after-interaction electron beam, broadband low reflection, and compact size.

A collector is used to collect the spent electron beam. It is better to adjust the magnetic field profile to homogeneously distribute the electron beam on the collector wall, and simultaneously maintains the peak power on the collector surface as low as possible.

A broadband output window [18] is used to transmit the generated high power to the external transmission system, and it keeps the system vacuum isolation. An output window is required to meet the basic requirements of broad bandwidth, low standing wave ratio, the ability to bear high power, and reliable vacuum sealing. An output window employs multilayer window chips to extend the bandwidth. The material of the window chip is usually ceramic of high purity and high thermal conductivity. Sapphire and diamond are excellent materials to enhance the high-power capability.

The gyro-TWT manufacturing is also limited by some basic technical problems, including cathode technology, precision machining, assembly error, welding and sealing technology, and so on. This chapter provides a simple discussion about the input coupler, output window, electron gun, and the measurement of dielectric materials.

7.2 Input Coupler

An input coupler transfers the external driving power to the operation mode in the circuit. It also functions as a vacuum isolation between the inner vacuum condition and the outer atmosphere. The requirement of vacuum isolation makes it indispensable to seal a piece of dielectric chip on the coupler. The configuration

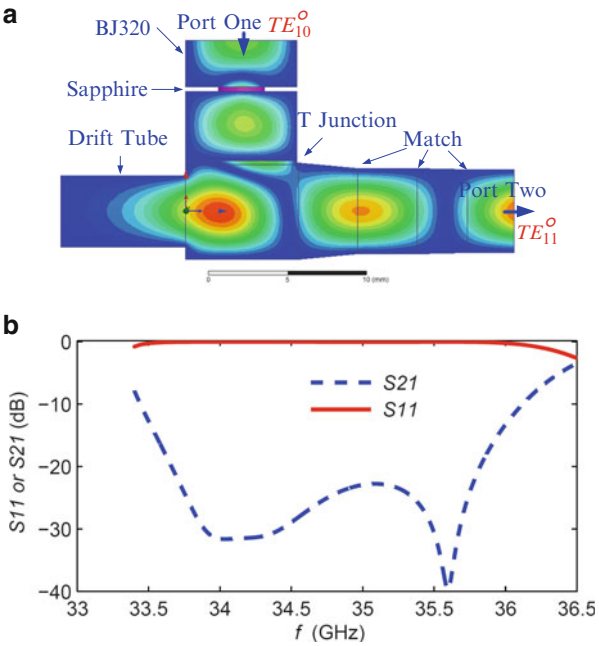

Fig. 7.1 TE_{11} mode input coupler of gyro-TWT (**a**) simulation structure (**b**) transmission characteristic

of input coupler is determined by the operating mode, frequency, and bandwidth of the gyro-TWT. This section provides the design and experiment of two Ka-band couplers, one for a TE_{11} mode gyro-TWT and another for a TE_{01} mode gyro-TWT and another W-band TE_{01} mode converter.

7.2.1 A Ka-Band TE_{11} Mode Input Coupler

A Ka-band fundamental TE_{11} mode gyro-TWT adopts a TE_{11} mode cylindrical waveguide as the interaction circuit. The amplifier bandwidth locates in the range of the single-mode propagation of the waveguide. In other words, any EM power couples into the circuit will be converted to the TE_{11} mode. As shown in Fig. 7.1a, in order to simplify the design of input coupler, the structure of a 90° *T* rectangular waveguide is vertically loaded on the circular waveguide. A BJ320 rectangular waveguide is used by external transmission system, and a piece of sapphire is used to keep the external transmission system isolating from inner vacuum condition. Because the operating frequency is under cutoff in the drift tube, the operating mode propagates along the direction the electron beam travels in. As shown in Fig. 7.1b, commercial HFSS is used to simulate the transmission characteristic,

an input coupler with the transmission characteristics of −3 dB and bandwidth of 9 % is designed which provides a precondition for the broadband characteristics of fundamental TE_{11} mode gyro-TWT.

It is stressed that increasing the radius of circular waveguide near the position of the *T* junction would improve the bandwidth of the coupler, but this also enables beam-wave synchronization in the backward-wave region. So coupler length and the instability competition of input coupler must be specially studied. Reference [18] provides a design scheme of a TE_{11} mode input coupler using array-apertures coupling which can obtain a cold transmission of −3 dB bandwidth about 9 %. Because the length of the input coupler in Ref. [18] is relatively long, backward-wave oscillation becomes dangerous.

7.2.2 A Ka-Band TE_{01} Mode Input Coupler

The TE_{01} mode input coupler for a gyro-TWT is a very classic structure. As shown in Fig. 7.2, a single BJ320 rectangular waveguide drives a combined coaxial/cylindrical cavity system. The coaxial cavity resonates in the TE_{411} mode. The EM power is coupled into the inner cavity with equal phase through four slots and excites a TE_{011} mode. Figure 7.2b shows the port one reflection characteristic.

Figure 7.3 shows the measured transmission characteristic of TE_{01} mode input coupler by vector network analyzer. It can be seen from the measurement result that the −3 dB bandwidth of S_{21} is 1.5 GHz and the −6 dB is 3 GHz. It is necessary to explain that in the process of the measurement, a mode converter must be used to connect the circular waveguide (TE_{01} mode) and the rectangular waveguide BJ320 (TE_{10}). Due to the error from the mode converter, the measurement result shows that the bandwidth of S_{21} is not so good as predicted from Fig. 7.2b. Based on the tendency of the S_{21} curve, it is concluded that the measurement results and the design results are relatively consistent.

7.2.3 A W-Band Multichannel TE_{01} Mode Converter

For a W-band gyrotron amplifier, the circuit diameter is relatively small. The input coupler injects the driving power from the rectangular waveguide TE_{10} mode into the interaction circuit, and builds up the operating TE_{01} mode in the interaction circuit, where the diameter is about 4 mm. Here, a novel multichannel mode converter, as shown in Fig. 7.4, is presented to alleviate the problem of mechanical machining [19]. The input mode converter is also sealed with a sapphire disc to maintain vacuum insulation, and structures are optimized to minimize the reflection in the operating band. In the input coupler, the driving power experiences a series of conversions [20]. Firstly, it goes through a broadband pill-box window and is further split into four traveling waves of identical phase by two stages cascaded

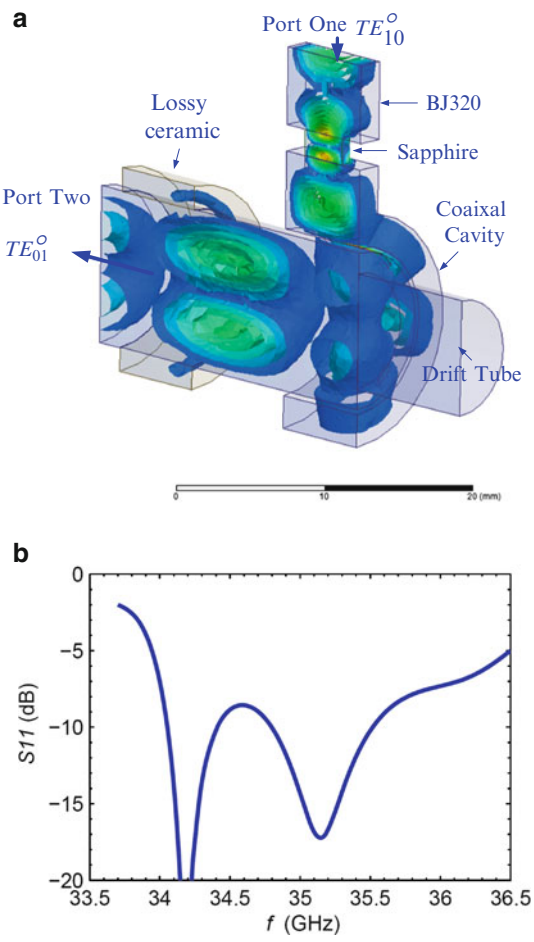

Fig. 7.2 TE_{01} mode input coupler of gyro-TWT (**a**) simulation structure and (**b**) port one reflection

Y-power dividers. And then, such four-way powers excite axis-symmetrical TE_{01} mode in the interaction circuit. Since the TE_{01} mode could not propagate in the below-cutoff drift tube, it travels along positive z direction, as shown in Fig. 7.4. The sapphire disc of the pill-box window is obviously with radius bigger than that of the besides cylindrical cavities. Such a design enlarges the sapphire-to-metal seal area and much improves the welding success rate. The insertion loss and reflection of the input coupler is shown in Fig. 7.5. The input coupler maintains a low reflection S_{11} lower than −15 dB from 90 to 100 GHz, and the insertion loss S_{21} is better than −0.08 dB. Previous experiments adopt input coupler of coaxial-cavity structure with azimuthal slots to build cylindrical TE_{01} mode for Ka-band gyro-TWTs [21–25] and W-band gyrotron amplifiers [15, 26]. The input coupler presented here employs two stage cascaded Y-power dividers [20] to split the input power into four waves other than the previous coaxial-cavity structure with slots, as a way to alleviate the problems of narrow band and high sensitivity to fabrication errors.

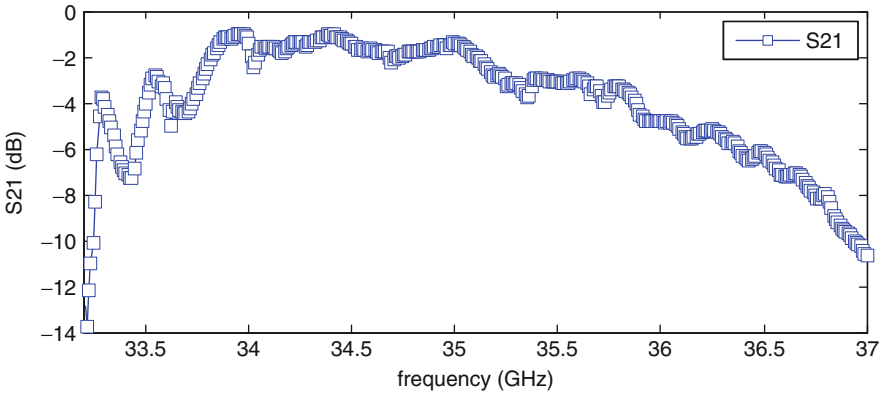

Fig. 7.3 TE_{01} mode input coupler

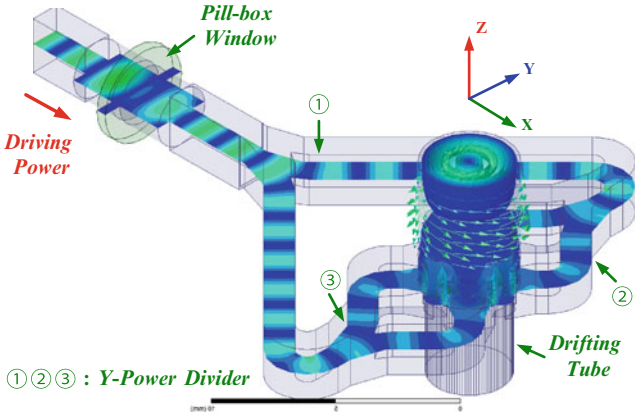

Fig. 7.4 A novel W-band multichannel TE_{01} mode converter

Fig. 7.5 The HFSS simulated performance of the W-band multichannel TE_{01} mode converter

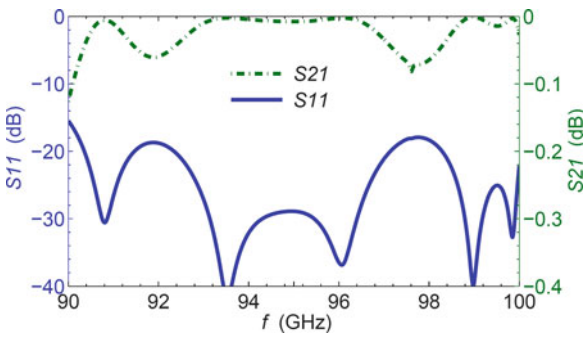

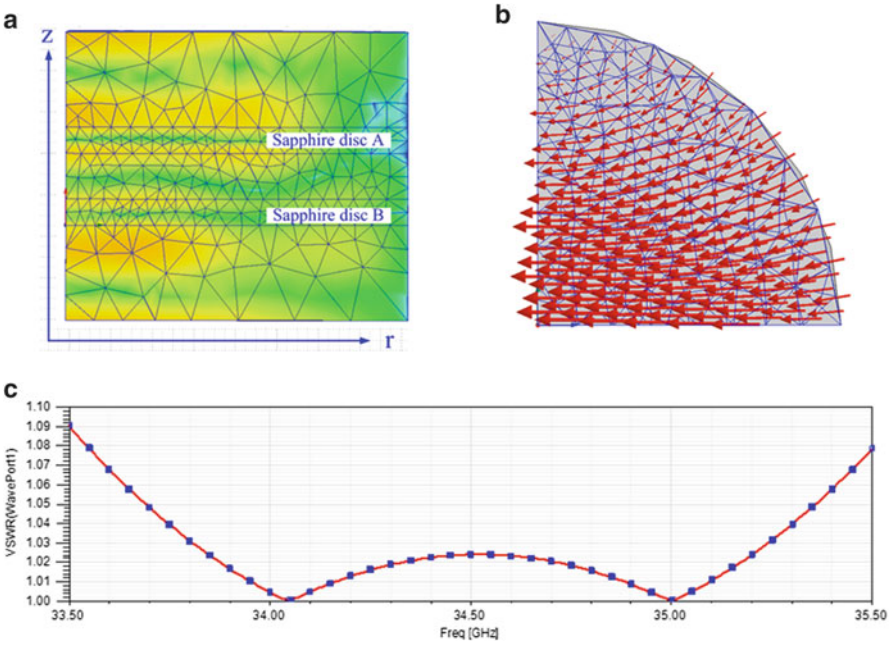

Fig. 7.6 TE_{11} mode output window using two pieces of sapphire (**a**) HFSS simulation structure (**b**) the mode of the port (**c**) VSWR

7.3 Broadband Output Window

Broadband output window transfers the high power out of the tube and also maintains vacuum isolation. The broadband output window needs to keep low reflection in the operation band, usually $S_{11} \leq -30$ dB is needed. Otherwise reflection may induce unstable operation. In order to enhance the high-power capacity of the window, the dielectric materials with high thermal conductivity and low loss are chosen, such as high purity BeO ceramics, sapphire, and diamond. Generally, multilayer window chips are used to extend the bandwidth. This section provides the design method and experiment of Ka-band TE_{01} mode and TE_{11} mode output window.

7.3.1 A Ka-Band TE_{11} Mode Output Window

This section discusses the design method of a Ka-band TE_{11} mode output window using two pieces of sapphire disks. Figure 7.6 shows the simulation structure diagram of HFSS. Since the electrical size of the output window structure is relatively large, 1/4 symmetrical structure is used in the simulation, as shown in Fig. 7.6b. Sapphire window sealed in circular waveguide is a resonant window structure. For a structure fixed resonant window, the V-shaped transmission characteristics will be

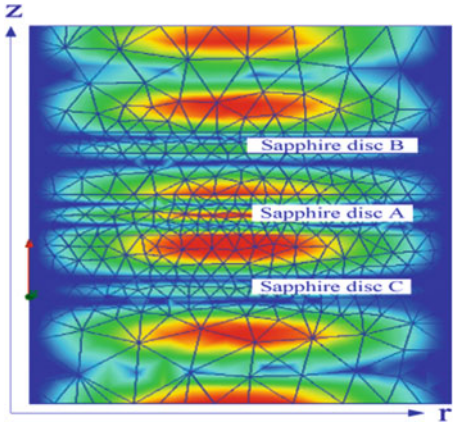

Fig. 7.7 The HFSS simulation structure of the TE_{01} mode output window using three pieces of sapphire

obtained in a specific frequency range. In the design process of TE_{11} mode output window, the resonance frequency of sapphire should be 35 GHz. Then adjust the distance between two sapphire to ensure them matching at 34 GHz. Figure 7.6 shows the simulation result using software HFSS. The SWR of the output window is less than 1.03 and the bandwidth is about 1.5 GHz.

7.3.2 A Ka-Band TE_{01} Mode Output Window

The design method of Ka-band TE_{01} mode output window using three pieces of sapphire is present here. Simulation structure is shown in Fig. 7.7. The design method of the window with three pieces of sapphire is similar to a double-piece window. When compared with the double-piece window, the bandwidth of triple-piece window is wider because the transmission curve of the triple-piece window has one pole more than the double-piece window. The resonant frequency of the three sapphire chips is around 35 GHz; adjusting the distance between the three sapphires, broadband matching characteristics can be obtained. Finite element method is used to optimize the SWR of the output window. The simulated result and the measurement result are shown in Fig. 7.8a, b, respectively. It is revealed from the tendency of the curves that the simulated result is in good agreement with the measurement result.

7.4 A Small-Orbit Gun

The magnetron injection gun (MIG) is capable of generating electron beam for beam-wave interaction in a gyro-TWT and is a key component of gyrotron. This section provides the design method of MIG used in the Ka-band TE_{01} mode

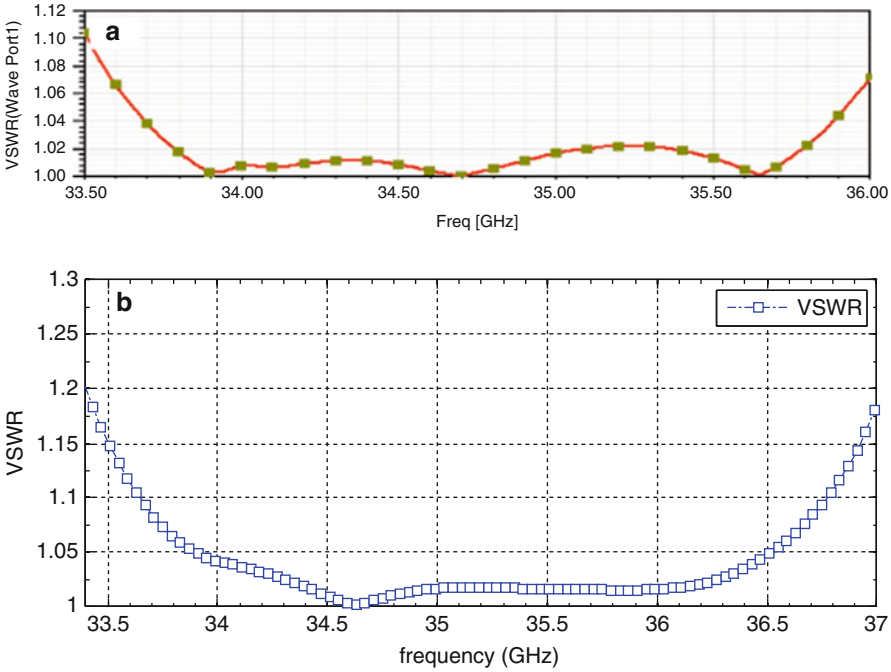

Fig. 7.8 VSWR of output window using three pieces of sapphire (**a**) designed curve (**b**) measurement curve

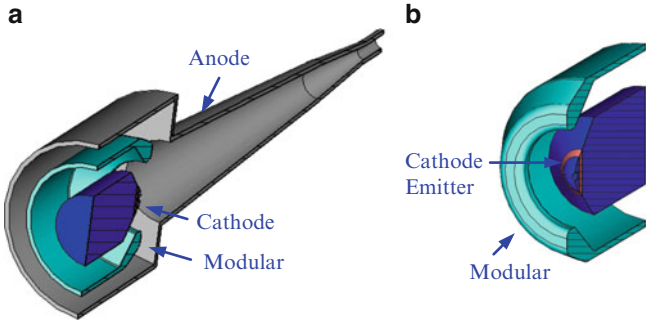

Fig. 7.9 The MIG for a Ka-band TE_{01} mode gyro-TWT (**a**) structure profile (**b**) the designed cathode

gyro-TWT. It is well known that the optimal performance of gyrotron requires high-quality beams. The gun of this section is designed on the basis of the parameters used in Ref. [22]. It can be seen from Fig. 7.9 that the gun consists of three parts, cathode, modular, and anode.

In order to understand the physics in an electron gun, let us review the theory related to electron traveling in an axis-symmetry system [27]. The Lagrangian L

describing the motion of an electron in an axial symmetrical system is independent of the generalized angular coordinate ϕ, which leads to the law of angular generalized momentum (AGM) P_ϕ conservation,

$$P_\phi = \frac{\partial L}{\partial \dot{\phi}} = \gamma m_0 r v_\phi - \frac{e}{2\pi}\Psi = \text{const} \tag{7.1}$$

where γ, v_ϕ, m_0, and $-e$ are the electron relativistic factor, angular velocity, static mass, and charge, respectively. The Ψ is the net magnetic flux inside the circle, radius of which equals the instantaneous electron radial location r. The initially emitted electron beam on the cathode surface is assumed to be with no velocity. A first-order approximation of the motion could be described by

$$B_{zc} {r_c}^2 = B_{z0}\left(r_g^2 - r_L^2\right) \tag{7.2}$$

where r_c and B_{zc} are the cathode emitter radius and axial magnetic field strength, respectively. r_g, r_L, and B_{z0} are the electron guiding center radius, Larmor radius, and the magnetic field strength in the cavity region. The electron transverse-to-axial velocity ratio α in the cavity region is

$$\alpha = \left(\frac{2\gamma V_0}{\eta B_{z0}\left(B_{z0} r_g^2 - B_{zc} r_c^2\right)} - 1\right)^{-\frac{1}{2}} \tag{7.3}$$

where V_0 is the anode voltage and $\eta = e/m_0$. From Eq. (7.3), we can determine all the other parameters of an electron gun.

The geometries of the cathode and modular are sensitive factors for the design of an electron gun. A gyrotron requires an electron gun with high current, high duty factor and long lifetime, so it is necessary to increase the area of emission surface. The bigger the emission surface, the more difficult to control the beam velocity spread. It is needed to made trade-off between these problems. Figure 7.9 shows the sketch map of electron gun. The designed current of this gun is 10 A.

The distributions of the MIG potential distribution are cathode 0 V, modulation 28 kV, and anode 70 kV. Actually, for experimental test, the tube anode is grounded and the cathode is connected with negative potential. Gyrotron devices require beams with high-velocity ratio and low-velocity spread. So the geometries of cathode, modulation, and anode have to be adjusted repeatedly to optimize the parameters. It is normally helpful to keep the magnetic field constant near cathode emitter, as a way to reduce the beam parameter sensitivity to location errors between gun and magnetic field.

Figure 7.10a shows the 3D simulation trajectory of electron beam, and Fig 7.10b shows the guiding center radius is about 2.64 mm. Figure 7.11 shows the distribution

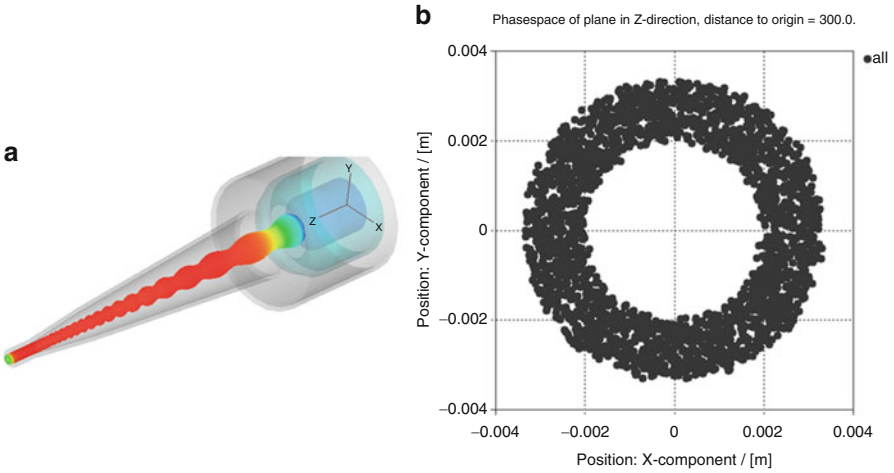

Fig. 7.10 (**a**) Trajectory of electron (**b**) distribution of electrics in the entrance of the interaction circuit

of energy. It indicates that the energy spread is about 0.3 %. Figure 7.11b, c shows that the average speeds along the traverse direction and the axial direction are nearly the same, the value of them are about 10^8 m/s. Figure 7.11c also shows that the axial velocity spread is about 5 %. The 3D simulation results are also verified by SLAC Egun code [28].

An optimal electron not only can generate high-quality beam but also need to bear the characteristic of relative stability to parameter errors. Figure 7.12 shows the gun performance versus the modular voltage, current, and minor error between the cathode location and magnetic field profile. It is revealed that increase in the modular voltage leads to accordingly increase in velocity ratio and velocity spread. The electron gun parameters were relatively stable with current between 7 and 13 A, while the parameters will change obviously when changing the position of the emitter locating in the magnetic field.

7.5 Measurement of Lossy Dielectric Materials

The lossy ceramic is an important material for the construction of a high stability gyro-TWT. How to measure the parameters of ceramic is also very important for designing the interaction circuit. Many methods can be used to measure the parameters. In this section, transmission and reflection measurement method is chosen. The physical model of this method is shown in Fig. 7.13; loading the dielectric in a rectangular waveguide, the relative permittivity is calculated from the measured *S* parameter.

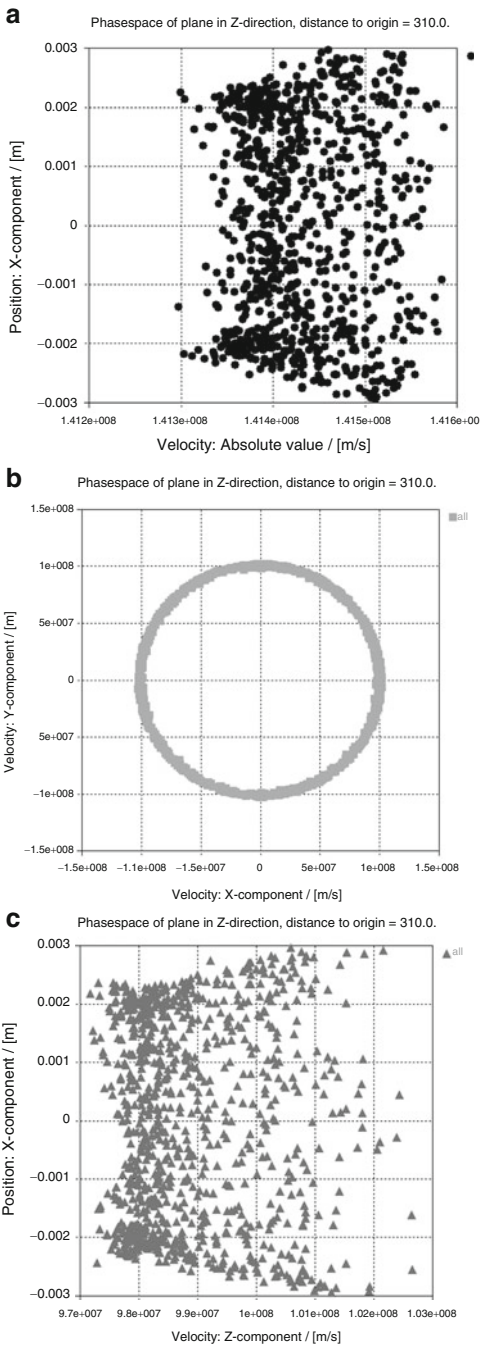

Fig. 7.11 Velocity spread of electron in drift tube (**a**) overall velocity distribution (**b**) transverse velocity distribution (**c**) axial velocity distribution

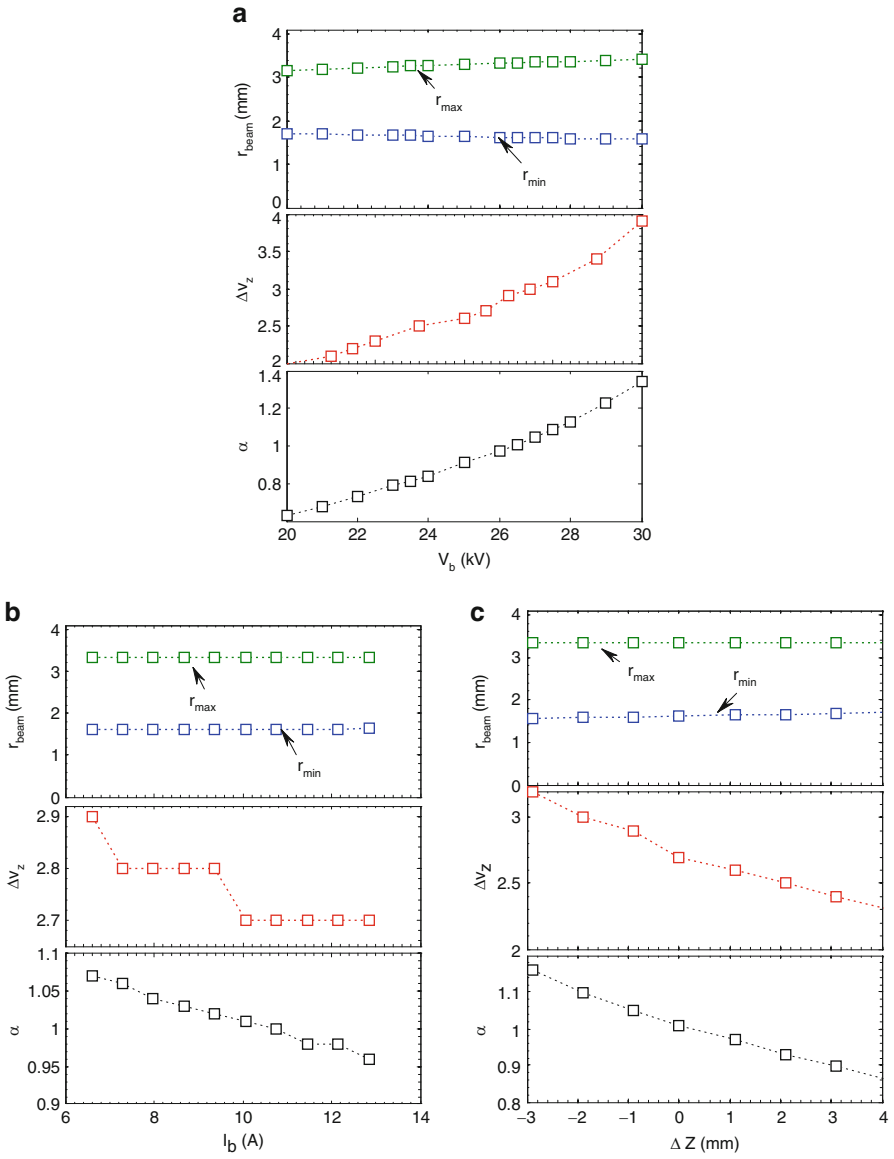

Fig. 7.12 (**a**) Voltage of mode anode (**b**) working current (**c**) position of the device versus the gun parameters

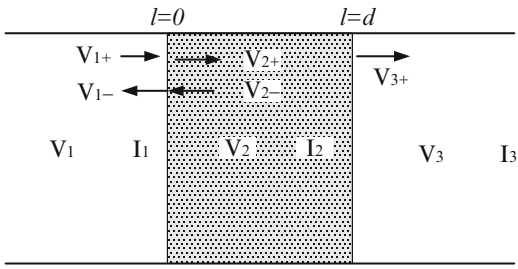

Fig. 7.13 Physical model of transmission and reflection measurements method

Equivalent voltage and equivalent current of each region can be deduced from telegraph equation:

$$V_1 = V_1^+ e^{-j\gamma_0 l} + V_1^- e^{j\gamma_0 l} \tag{7.4a}$$

$$I_1 = \frac{1}{Z_0}\left(V_1^+ e^{-j\gamma_0 l} - V_1^- e^{j\gamma_0 l}\right) \tag{7.4b}$$

$$V_2 = V_2^+ e^{-j\gamma_1 l} + V_2^- e^{j\gamma_1 l} \tag{7.4c}$$

$$I_2 = \frac{1}{Z_\mathrm{d}}\left(V_2^+ e^{-j\gamma_1 l} - V_2^- e^{j\gamma_1 l}\right) \tag{7.4d}$$

$$V_3 = V_3^+ e^{-j\gamma_0 (l-d)} \tag{7.4e}$$

$$I_3 = \frac{1}{Z_0} V_3^+ e^{-j\gamma_0 (l-d)} \tag{7.4f}$$

where Z_0 and Z_d are characteristic resistance of rectangular hollow waveguide and dielectric-loaded rectangular waveguide separately. γ_0 and γ_1 are transmission constant of rectangular waveguide and dielectric-loaded rectangular waveguide, respectively.

$$\gamma_0 = \sqrt{\left(\frac{\omega}{c}\right)^2 - (k_{mn})^2} \tag{7.5a}$$

$$\gamma_1 = \sqrt{\left(\frac{\omega}{c}\right)^2 (\varepsilon_r \mu_r) - (k_{mn})^2} \tag{7.5b}$$

For TE_{01} mode of rectangular waveguide, $k_{mn} = \pi/a$, where a is the broadside length of rectangular waveguide. The characteristic resistance is defined by

$$Z = \frac{U}{I} = \frac{\int_0^a E_y \mathrm{d}y}{\int_0^b - H_x \mathrm{d}x} \tag{7.6}$$

We can obtain that

$$\frac{Z_{\mathrm{d}}}{Z_0} = \frac{\gamma_0}{\gamma_1}\mu_r \tag{7.7}$$

According to the boundary condition of dielectric surface

$$V_1 = V_2, I_1 = I_2 \qquad l = 0 \tag{7.8a}$$

$$V_2 = V_3, I_2 = I_3. \qquad l = d \tag{7.8b}$$

We get

$$4\frac{1}{S_{21}} = \frac{1}{T}\left(1 + \frac{1+\Gamma}{1-\Gamma}\right)\left(1 + \frac{1-\Gamma}{1+\Gamma}\right) + T\left(1 - \frac{1+\Gamma}{1-\Gamma}\right)\left(1 - \frac{1-\Gamma}{1+\Gamma}\right) \tag{7.9a}$$

$$4\frac{S_{11}}{S_{21}} = \frac{1}{T}\left(1 + \frac{1+\Gamma}{1-\Gamma}\right)\left(1 - \frac{1-\Gamma}{1+\Gamma}\right) + T\left(1 - \frac{1+\Gamma}{1-\Gamma}\right)\left(1 + \frac{1-\Gamma}{1+\Gamma}\right) \tag{7.9b}$$

where $T = e^{-j\gamma_1 d}$ is transmission factor and $\Gamma = (Z_{\mathrm{d}} - Z_0)/(Z_{\mathrm{d}} + Z_0)$ is reflection coefficient. Solving Eq. (7.6), expression of material parameters is

$$\mu_{\mathrm{r}} = \pm\sqrt{\frac{Y^2}{k^2 - (\pi/a)^2}\left[\frac{\ln(X)}{jd}\right]^2} \tag{7.10a}$$

$$\varepsilon_{\mathrm{r}} = \frac{\left[\frac{\ln(X)}{jd}\right]^2 + (\pi/a)^2}{\mu_{\mathrm{r}} k^2} \tag{7.10b}$$

where X and Y are

$$X = \frac{S_{21}(1 - Y)}{1 + S_{11} + (S_{11} - 1)Y} \tag{7.11a}$$

$$Y = \pm\sqrt{\frac{S_{21}^2 - S_{11}^2 - 1 - 2S_{11}}{S_{21}^2 - S_{11}^2 - 1 + 2S_{11}}} \tag{7.11b}$$

We need to pay attention to some problems. Generally speaking, the result must satisfy the condition of real$(\mu_r) > 0$ and real$(\varepsilon_r) \geq 1$. When using transmission and reflection method to measure the material with thickness thicker than half of the guided wave wavelength, the measurement result normally turns to be ill conditioned, and it leads to multi roots due to measured complex parameters.

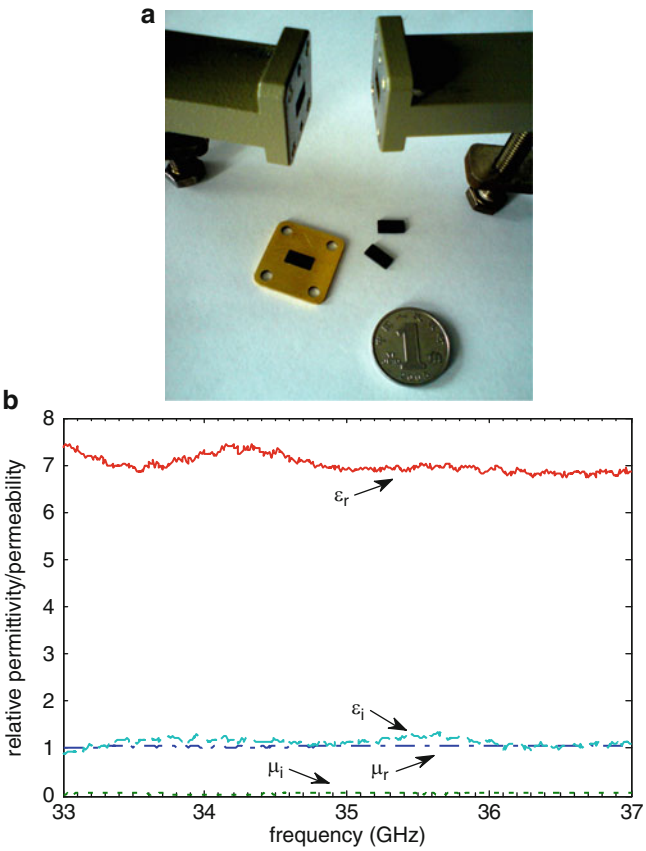

Fig. 7.14 (**a**) Measurement devices and (**b**) the measured parameters of the BeO–SiC

In an actual measurement case, the size of the measured sample is 7.12 mm × 3.56 mm × 1 mm for the Ka-band measurement. Measurement device and curve are given in Fig. 7.14. It can be estimated that the relative permeability of BeO–SiC is about $\mu_r \approx 1$ and the relative permittivity is about $\varepsilon_r \approx 7.11 - 1.1j$. According to experience, repeated measurements shows that the fluctuation of the result in the lower frequency is caused by the error of the vector network analyzer.

7.6 Summary

This chapter discusses some key components during developing a gyro-TWT, including the input and output coupler, the electron gun, and the lossy dielectric material. The actual manufacturing works are far beyond the abovementioned

complicity. The process of a gyrotron device manufacture includes electrical design, mechanical design, machining, welding, degasification, cold test, and hot test and may require refurbishment. The designers, engineers, and the technicians should keep well communication with each other to fully understand the mutual limitations and balance relation between the theory design and engineering practice. Generally, minor deviation between the measurement result and the design value is unavoidable. The solution is to bring these deviations under control.

References

1. Chu KR (2004) The electron cyclotron maser. Rev Mod Phys 76:489–540
2. Chu KR, Chen HY, Hung CL et al (1999) Theory and experiment of ultrahigh-gain gyrotron traveling wave amplifier. IEEE Trans Plasma Sci 27:391–404
3. Yuan CP, Chang TH, Chen NC et al (2009) Magnetron injection gun for a broadband gyrotron backward-wave oscillator. Phys Plasmas 16:073109
4. Fu WJ, Yan Y, Yuan XS et al (2009) Two-beam magnetron injection guns for coaxial gyrotron with two electron beams. Phys Plasmas 16:23103
5. Barroso JJ, Montes A, Silva CAB (1985) The use of a synthesis method in the design of gyrotron electron guns. Int J Electron 59:33–47
6. Lygin VK, Manuilov VN, Kuftin AN et al (1995) Inverse magnetron injection gun for a coaxial 1.5mw, 140 Ghz gyrotron. Int J Electron 79:227–235
7. Lygin VK, Piosczyk B, Dammertz G et al (1997) A diode electron gun for a 1 MW 140 GHz gyrotron. Int J Electron 82:193–201
8. Kartikeyan MV, Borie E (2000) Design of an electron gun for a 42 GHz, 200 kW, TE5,2 mode gyrotron using the BFCRAY code. IETE Tech Rev 17:275–281
9. Piosczyk B (2001) A novel 4.5-MW electron gun for a coaxial cavity gyrotron. IEEE Trans Electron Devices 48:2938–2944
10. Anderson JP, Korbly SE, Temkin RJ et al (2002) Design and emission uniformity studies of a 1.5-MW gyrotron electron gun. IEEE Trans Plasma Sci 30:2117–2123
11. Einat M, Jerby E, Rosenman G (2002) Spectral measurements of gyrotron oscillator with ferroelectric electron gun. Appl Phys Lett 81:1347–1349
12. Harriet SB, McDermott DB, Gallagher DA et al (2002) Cusp gun TE21 second-harmonic Ka-band Gyro-TWT amplifier. IEEE Trans Plasma Sci 30:909–914
13. Manuilov VN, Idehara T, Kamada M et al (2006) Electron gun for large orbit gyrotron (LOG) with decreased influence of cathode plasma on electron beam properties. Int J Infrared Millim Waves 27:343–353
14. Piosczyk B (2006) A coaxial magnetron injection gun (CMIG) for a 2 MW, 170 GHz coaxial cavity gyrotron. Int J Infrared Millim Waves 27:1041–1061
15. Song HH, McDermott DB, Hirata Y, Barnett LR, Domier CW, Hsu HL et al (2004) Theory and experiment of a 94 GHz gyrotron traveling-wave amplifier. Phys Plasmas 11:2935–2941
16. McDermott DB, Song HH, Hirata Y et al (2002) Design of a W-Band TE01 mode gyrotron traveling-wave amplifier with high power and broad-band capabilities. IEEE Trans Plasma Sci 30:894–902
17. Lawson WG (1990) Theoretical evaluation of nonlinear tapers for a high-power gyrotron. IEEE Trans Microw Theory Tech 38:1617–1622
18. Pershing DE, Nguyen KT, Calame JP et al (2004) A TE11 K-a-band Gyro-TWT amplifier with high-average power compatible distributed loss. IEEE Trans Plasma Sci 32:947–956

19. Chao-Hai Du, Tsun-Hsu Chang, Pu-Kun Liu, Yi-Cheng Huang, Pin-Xian Jiang, Shou-Xi Xu, Zhi-Hui Geng, Bao-Liang Hao, Liu Xiao, Gao-Feng Liu, Zheng-Di Li, Shao-Hui Shi (2013) Design of a W-band Gyro-TWT amplifier with a lossy ceramic loaded circuit. IEEE Trans Electron Devices 60(7):2388–2394
20. Chang TH, Lee CS, Wu CN, Yu CF (2008) Exciting circular TEmn modes at low terahertz region. Appl Phys Lett 93(11):111503
21. Garven M, Calame JP, Danly BG, Nguyen KT, Levush B, Wood FN (2002) A gyrotron-traveling-wave tube amplifier experiment with a ceramic loaded interaction region. IEEE Trans Plasma Sci 30:885–893
22. Calame JP, Garven M, Danly BG, Levush B, Nguyen KT (2002) Gyrotron-traveling wave-tube circuits based on lossy ceramics. IEEE Trans Electron Devices 49:1469–1477
23. Liu B, Feng J, Wang E, Li Z, Zeng X, Qian L, Wang H (2011) Design and experimental study of a Ka-band gyro-TWT with periodic dielectric loaded circuits. IEEE Trans Plasma Sci 39(8):1665–1672
24. Yan R, Luo Y, Liu G, Pu Y (2012) Design and experiment of a Q-band gyro-TWT loaded with lossy dielectric. IEEE Trans Electron Devices 59(12):3612–3617
25. Wang E, Liu B, Qian L, Li Z, Feng J, Zhu S (2012) Experimental study of high-power gyrotron traveling-wave tube with periodic lossy material loading. IEEE Trans Plasma Sci 40(7): 1846–1853
26. Blank M, Danly BG, Levush B (2000) Experimental demonstration of W-band gyroklystron amplifiers with improved gain and efficiency. IEEE Trans Plasma Sci 28:706–712
27. Du C-H, Chang TH, Liu PK, Yuan CP, Yu SJ, Liu GF, Bratman VL, Glyavin MY, Kalynov YK (2012) Development of a magnetic cusp gun for terahertz harmonic gyro-devices. IEEE Trans Electron Devices 59(12):3635–3640
28. Herrmannsfeldt WB (1988) EGUN, an electron optics and gun design program [M]. Stanford Linear Accelerator Center, Stanford University, Menlo Park